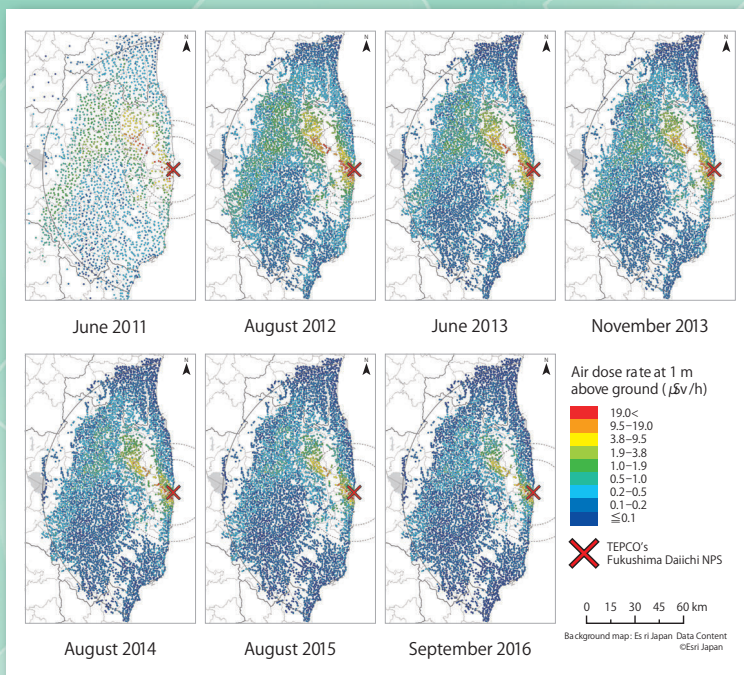
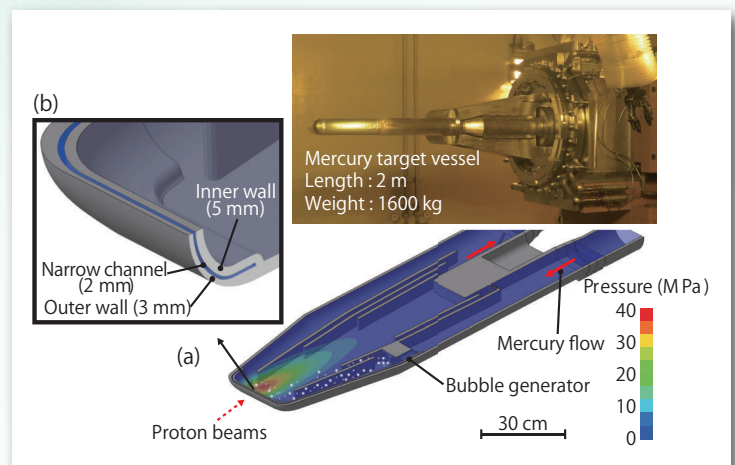


JAEA R&D Review

2020-21



Air dose rate maps around the TEPCO's Fukushima Daiichi NPS from 2011–2016 (Topic 1-17)



Mercury target vessel which adopted double-walled structure (Topic 5-3)



Message from the President

児玉 敏雄

President Toshio KODAMA

We sincerely thank you for your understanding and continuous support regarding the research and development (R&D) activities of the Japan Atomic Energy Agency (JAEA).

JAEA's mission, as the only comprehensive nuclear R&D institution in Japan, is to contribute to the welfare and prosperity of human society through nuclear science and technology (S&T). In order to achieve this, JAEA works on the response to the accident at the Fukushima Daiichi Nuclear Power Station (NPS) operated by the Tokyo Electric Power Company Holdings, Inc., researches the improvement of nuclear safety, carries out R&D on the nuclear fuel cycle and on radioactive waste treatment and disposal technology, and engages in basic and fundamental research in the nuclear field.

In response to the accident at the Fukushima Daiichi NPS, and based on the Mid-and-Long-Term Roadmap towards the Decommissioning, etc., we are working on R&D for both decommissioning and environmental recovery. This includes preparation for analysis of fuel debris, environmental radiation monitoring for the lifting of evacuation orders in areas where it is difficult to return, and activities to improve safety through accident investigation in cooperation with the Nuclear Regulation Authority. Additionally, based on the "Backend Roadmap" and "Medium-/Long-Term Management Plan of JAEA Facilities", we will continue to safely and steadily advance decommissioning and backend measures for, among others, Monju, Fugen, and Tokai Reprocessing Plant.

In addition, we will conduct R&D on fast reactors and advanced reactors, as well as basic and fundamental research aimed at creating new uses of atomic energy; we will also proceed with measures for the resumption of the operation of experimental research reactors. In the future, in conjunction with the resumption of operation of JRR-3, we will operate a service platform that adds general equipment to large-scale facilities which can only be provided by JAEA. We will also promote joint research and collaboration with industry, academia, and government institutions to create innovation.

In October 2019, JAEA set forth a future vision entitled "JAEA 2050 +" which outlines its future profile, namely the goals to be set and the actions to be taken toward these goals in order to continue its social contribution into the future. The future vision envisages progress toward fusion of the nuclear energy field with other fields with the aim of realizing a "new-era nuclear S&T" that can contribute to resolving global climate change, securing energy supply, and achieving the ideal future society (Society 5.0).

This work aims to introduce topics that are representative of our latest R&D achievements. We hope that this publication will help you understand our R&D activities.

We appreciate your continued encouragement and cooperation.

About This Publication and the JAEA Organizational Outline	10
--	----

1 Research and Development Related to the Accident at the TEPCO's Fukushima Daiichi NPS

Highlight Assistance in Environmental Restoration and Decommissioning	13
--	----

1-1 Evaluation of Uranium Leaching from Fuel Debris in Water – Leaching Rate Evaluation Considering Effects of Concrete Components, and Comparison with Spent Fuel – Akira Nakayoshi	14
1-2 Distribution of Components in Fuel Debris – Segregation of Gadolinium and Iron during Solidification Using Simulated Molten Debris – Ayako Sudo	15
1-3 50x Increase in Plasma Emission Intensity by Microwave – Advanced Remote Analysis Technology for Fuel Debris Using Laser-Induced Breakdown Spectroscopy – Masaki Oba	16
1-4 Clarifying the Warming Behavior of a Robot Test Pool – Measurement and Analysis toward Facility Utilization with User Needs – Ryoki Arakawa	17
1-5 3D Reconstruction of Structures from Images – Development of Image Analysis Method to Support Remote Operation – Toshihide Hanari	18
1-6 Chemisorption of Cesium on Structural Materials during SA – Prediction and Verification of Thermodynamic Properties of Cesium Compounds – Chikashi Suzuki	19
1-7 Hydrogen Release from Geopolymer by Gamma Irradiation – Reduced Hydrogen Yield of Bulky, Solidified, Water-Saturated Waste – Isao Yamagishi	20
1-8 Accident Progression Analysis: Units 1–3 at the Fukushima Daiichi NPS – Insights from International Benchmark Analysis Project – Hitoshi Tamaki	21
1-9 Cause of Cesium Concentration Change in Fish – Three Transport Pathways from Forests to Fish – Hiroshi Kurikami	22
1-10 Fast and Easy Analysis of Tritium in Plants and Animals – Development of Rapid Organically Bound Tritium (OBT) Analysis in Marine Products – Kenso Fujiwara	23
1-11 How Does the Dose Rate Change after Decontamination? – Effects of Land Use Type Revealed from Long-Term Monitoring Data – Shigeo Nakama	24
1-12 Radiocesium Behavior in River System – Relationship between Mineral Species and Radiocesium in Riverbed Using Microscopy – Hiroki Hagiwara	25

1-13	Cause of Radioactivity Concentration in Mushrooms – Cesium Selectivity Evaluation of Mushroom Pigment Norbadione A – Hiroya Suno	26
1-14	Estimation of Total Radiocesium Discharged from Fukushima Daiichi NPS to the Coast – Discharge Inventory Decreased to Approximately 1/100000 th Since the Accident – Susumu Yamada	27
1-15	Reconstruction of Atmospheric Release and Dispersion of Radioactive Materials by Computer Simulation – Contribution to the Refinement of Dose Assessment in the Early Stage of the Accident by Improving the Dispersion Calculation Optimization Method – Hiroaki Terada	28
1-16	Initial Air Dose Rate after the Accident at the Fukushima Daiichi NPS – Comparison between Fukushima and Chernobyl – Kazuya Yoshimura	29
1-17	Analyzing Decreasing Trends in Radioactivity and Dose Rate – Changes of Radiocesium Concentration in Soil and Air Dose Rate over Five Years – Satoshi Mikami	30
1-18	Assessment of External Exposure Doses in Daily Life – Development of Assessment Model Based on Local Radiation Surveys – Shogo Takahara	31

2 Research on Nuclear Safety and Emergency Preparedness

Highlight	Implementing Continuous Improvements in Safety and Emergency Preparedness	32
2-1	Measurement of Very Thin Liquid Film Thickness – Technical Development for the Evaluation of Liquid Film Dryout Behavior – Yuki Wada	33
2-2	Reliable Safety Evaluation for Reactivity-Initiated Accidents – Mechanical Property Evaluation of Fuel Cladding under Biaxial Stress Conditions – Takeshi Mihara	34
2-3	Effects of Stress on Oxidation near a Crack Tip – Toward an Understanding of the Mechanism of Environmentally-Assisted Cracking in Stainless Steel – Kuniki Hata	35
2-4	Preparing for Aftershocks After a Major Earthquake – Proposal of Risk Assessment Method Considering Large Aftershocks – Byunghyun Choi	36
2-5	Elucidating HEPA Filter Clogging under Organic Solvent Fire – Development of Severe Accident Assessment Method for Reprocessing Facilities – Takuya Ono	37
2-6	Rapidly and Widely Measuring Radiation from the Sky – Preparedness for Using Aerial Radiation Monitoring during a Nuclear Emergency – Akira Futemma	38

3

Advanced Scientific Research

Highlight

Advanced Science Pioneers the Future 39

3-1

Observing Giant Dipole Vibration in Fission Fragments– Toward Understanding the Fission Process –
Hiroyuki Makii

40

3-2

Improving the Extraction Efficiency by Preventing Aggregation Phenomena of a Complex– Development of a Solvent Extraction Method Using the Strong Hydrophobicity of Fluorine –
Yuki Ueda

41

3-3

Clarifying the Mechanism behind Superconductivity in Uranium Compounds– NMR Research to Reveal the Mechanism of Spin-Triplet Superconductivity –
Yo Tokunaga

42

3-4

Detection of the Singularity of Magnets Using Rotation– Measuring the Angular Momentum Compensation, Key to Speeding Up Magnetic Devices –
Masaki Imai

43

3-5

Closing in on the Longstanding Puzzle of Localized Electrons in an Electron-Conducting Oxide– Using Muons to Unveil the Nature of Localized Electrons in Hydrogen-Doped SrTiO₃ –
Takashi Ito

44

3-6

Revealing Unique Nucleus Shapes by Nuclear Reactions– Cluster Structure and Its Probability –
Kazuki Yoshida

45

4

Nuclear Science and Engineering Research

Highlight

Fundamental Technologies for Nuclear Energy Innovation 46

4-1

Development of Photonuclear Data Library for International Contribution– Accomplishment of a Reliable Database Supporting the Use of Photonuclear Reactions –
Nobuyuki Iwamoto

47

4-2

Development of Nuclear Data for LLFP Transmutation– Models to Predict the Nuclear Cross-Section of Long-Lived Fission Products (LLFPs) –
Futoshi Minato

48

4-3

Accelerated Corrosion of Low-Alloy Steel at the Air/Solution Interface– Clarification of Corrosion Acceleration Mechanism from Structural Analysis of Rust Layer –
Kyohei Otani

49

4-4

Extension of Applicable Range of ESR Dosimetry via Enamel Separation Techniques– External Exposure Dose Estimation of Wild Japanese Macaque in Fukushima Prefecture –
Toshitaka Oka

50

4-5	Real-Time Estimation of Radiation Dose at Flight Altitudes – Development of Warning System for Aviation Exposure to Solar Energetic Particles (SEPs) – Tatsuhiko Sato	51
4-6	Separation of Minor Actinides Using Incinerable Extractants – Recovery of Minor Actinides and Rare Earth Elements in a Concrete Cell – Yasutoshi Ban	52
4-7	Validation of Nuclear Design Accuracy for ADS – Critical Experiment with Plutonium Fuel – Akito Oizumi	53
4-8	Development of Beam Window Materials for ADSs – Post-Irradiation Examination of Beam Window Materials through International Project – Shigeru Saito	54

5 Applied Neutron and Synchrotron Radiation Research and Development

Highlight	Contributions to Developments in Science, Technology, and Academic Research	55
------------------	---	----

5-1	Toward Upgrading High-Intensity Proton Accelerators – A Radio Frequency Quadrupole Linac Using a New Beam Dynamics Design Scheme – Yasuhiro Kondo	56
5-2	Detection of Change in Hydrogen Bond in the Deep Earth – Direct Observation of Symmetrization at High Pressure by Neutron Diffraction – Asami Sano	57
5-3	Mitigation of Damage to the Target Vessel Wall – Enabled High-Power Spallation Neutron Target by Double-Walled Structure – Takashi Naoe	58
5-4	Enabling Material Analysis with Neutron Beams at Manufacturing Sites – Texture Measurement of Steel Materials Using a Compact Neutron Source – Pingguang Xu	59
5-5	Elucidation of Structural Fluctuations of Proteins – Observation of Structure and Dynamics of Protein by Neutron Scattering – Hiroshi Nakagawa	60
5-6	Structural Analysis of Ionic Liquid–Electrode Interface – Nano-Scale Analysis of the Interfacial Structure Using a Quantum Beam – Kazuhisa Tamura	61
5-7	Toward Next-Generation Memory with Low Power Consumption – Observation of Electronic Structure of Alumina Film for Nonvolatile Memory – Masato Kubota	62
5-8	Observation of Electrons in Unconventional Uranium Superconductor – First Observation of the Electronic Structure of UTe_2 – Shin-ichi Fujimori	63

6

HTGR Hydrogen and Heat Application Research

Highlight

Research and Development on HTGR, Hydrogen Production, and Heat Application Technologies 64

-
- 6-1 Whole Core Burnup Characteristic Evaluation Method Using Representative Impurities**
– Cost Reduction for HTGRs Using Inexpensive Graphite Materials –
Shoichiro Okita 65
-
- 6-2 A Threefold Increase in Burnup of HTGR Fuel**
– Development on High-Burnup HTGR Fuel under International Cooperation –
Koei Sasaki 66
-
- 6-3 Toward Harmonization with Renewable Energy**
– HTGR Concept for Accomplishing Hybrid Operation with Renewable Energy –
Hiroyuki Sato 67
-
- 6-4 Toward Commercial Implementation of the IS Process with HTGRs for Hydrogen Production**
– Development of Strength Evaluation Method for Ceramic Structures –
Hiroaki Takegami 68
-
- 6-5 Toward Metallic Sulfuric Acid Decomposers in the IS Process**
– Development of a Corrosion Test Apparatus without Sulfur Dioxide (SO₂) Leakage –
Noriaki Hirota 69
-
- 6-6 Toward Stable and Continuous Hydrogen Production by the IS Process**
– Development of a Pump Shaft Seal Technology for HI Solution Including Highly Concentrated I₂ –
Hiroki Noguchi 70
-
- 6-7 Impact of Exhaust Stack Collapse on the Reactor Building**
– Confirmation of the Integrity of the Reactor Building by 3D Model Collision Analysis –
Masato Ono 71
-

7

Research and Development of Fast Reactors

Highlight

Enhancing the Ability of Research and Development 72

-
- 7-1 Toward Efficient Manufacturing of the Above-Core Structure**
– Routing Study of the Above-Core Structure with a Mock-Up Experiment –
Kazuya Takano 73
-
- 7-2 Reliable Decay Heat Removal by Natural Convection**
– Core Cooling Experiment Using Dipped DHX and Development of Evaluation Method –
Toshiki Ezure 74
-
- 7-3 Development of Fuel Assembly Analysis Method in Fast Reactors**
– Prediction of Thermal Hydraulics in Fuel Assembly with Inner Duct Structure (FAIDUS) –
Norihiro Kikuchi 75
-

7-4	Development of Ultra-High Temperature Tolerant Fuel Claddings – Mechanical Properties of Oxide Dispersion Strengthened Steel Claddings at 1000 °C – Yasuhide Yano	76
------------	--	----

7-5	Exploring an Ignition Mechanism of Hydrogen with Burning Sodium Mist – Visualizing the Ignition Process of Hydrogen Jets Containing Mist Caused by Sodium Leaks in Severe Accidents – Daisuke Doi	77
------------	--	----

8

Research and Development on Fuel Reprocessing, Decommissioning, and Radioactive Waste Management

Highlight	Toward Decommissioning Nuclear Facilities and Managing Radioactive Waste	78
------------------	---	----

8-1	Toward Public Use of the Decommissioning Cost Estimation Code DECOST – Development of a Manual for the DECOST – Nobuo Takahashi	80
------------	--	----

8-2	Radioactive Waste Confirmation Method for Rational Disposal – Study on the Evaluation Methodology of Wastes Generated from Post-Irradiation Examination Facilities – Akina Mitsukai	81
------------	--	----

8-3	Complex Biological Effect of Low-Dose Radiation – Feature Extraction of Multidimensional Data Using Machine Learning – Norie Kanzaki	82
------------	---	----

8-4	Radioactive Liquid Waste Management Technologies – STRAD Project for the Treatment of Radioactive Liquid Waste-Containing Chemicals – Sou Watanabe and Haruka Aihara	83
------------	---	----

8-5	Assessing Underground Fracture Connectivity from the Surface – Development of a Single Borehole Investigation Method – Eiichi Ishii	84
------------	--	----

8-6	Change in Permeability after Backfilling a Research Tunnel – Change in Hydraulic Conductivity in the Simulated Realistic Disposal Environment – Nobukatsu Miyara	85
------------	---	----

8-7	Chemical Signatures Suggesting Recent Fault Activity – Detection of Elemental Changes due to Fault Activity – Masakazu Niwa	86
------------	--	----

8-8	Visualization of Long-Term Variability in Groundwater Flow Conditions – Development of Evaluation Method for Variability of Groundwater Flow Conditions – Hironori Onoe	87
------------	--	----

8-9	Mechanical Modeling of Buffer Materials – Applicability of Elasto-Plastic Constitutive Model under Saltwater Conditions – Yusuke Takayama	88
------------	--	----

8-10	Unveiling the Interaction Mechanism of Fe (II) and Si – Characterization of Ferrous Silicate Co-Precipitates under Reducing Conditions – Paul Clarence M. Francisco	89
-------------	--	----

8-11	Analysis of Radioactive Samples by Plasma Generated in the Microchannel – Determination of Cesium in Highly Radioactive Liquid Waste by Liquid Electrode Plasma Optical Emission Spectrometry – Noriyasu Kodaka	90
-------------	--	----

9

Computational Science and E-Systems Research

Highlight	Computational Science for Nuclear Research and Development	91
------------------	--	----

9-1	CFD Simulation of a Fuel Debris Air-Cooling Experiment – Validation of a Thermal-Hydraulic Model Using the Lattice Boltzmann Method – Naoyuki Onodera	92
------------	--	----

9-2	Using Computer Simulations to Design a Superconducting Neutron Microscope – Simulating All Radiation Types inside the Neutron Microscope and Predicting Its Behavior – Alex Malins	93
------------	---	----

9-3	Understanding the Deformation of Iron from the Movement of Atoms – Analysis of Screw-Dislocation Motion and Slip-Plane Transition by Atomistic Simulations – Tomoaki Suzudo	94
------------	--	----

9-4	Multi-Phase Fluid Simulations Using the World's Largest GPU Supercomputer – Development of Communication-Avoiding Matrix Solvers on GPU – Yasuhiro Idomura	95
------------	---	----

10

Development of Science & Technology for Nuclear Nonproliferation

Highlight	Development of Technology and Human Capacity Building in the Nuclear Nonproliferation and Nuclear Security Fields to Support the Peaceful Use of Nuclear Energy	96
------------------	---	----

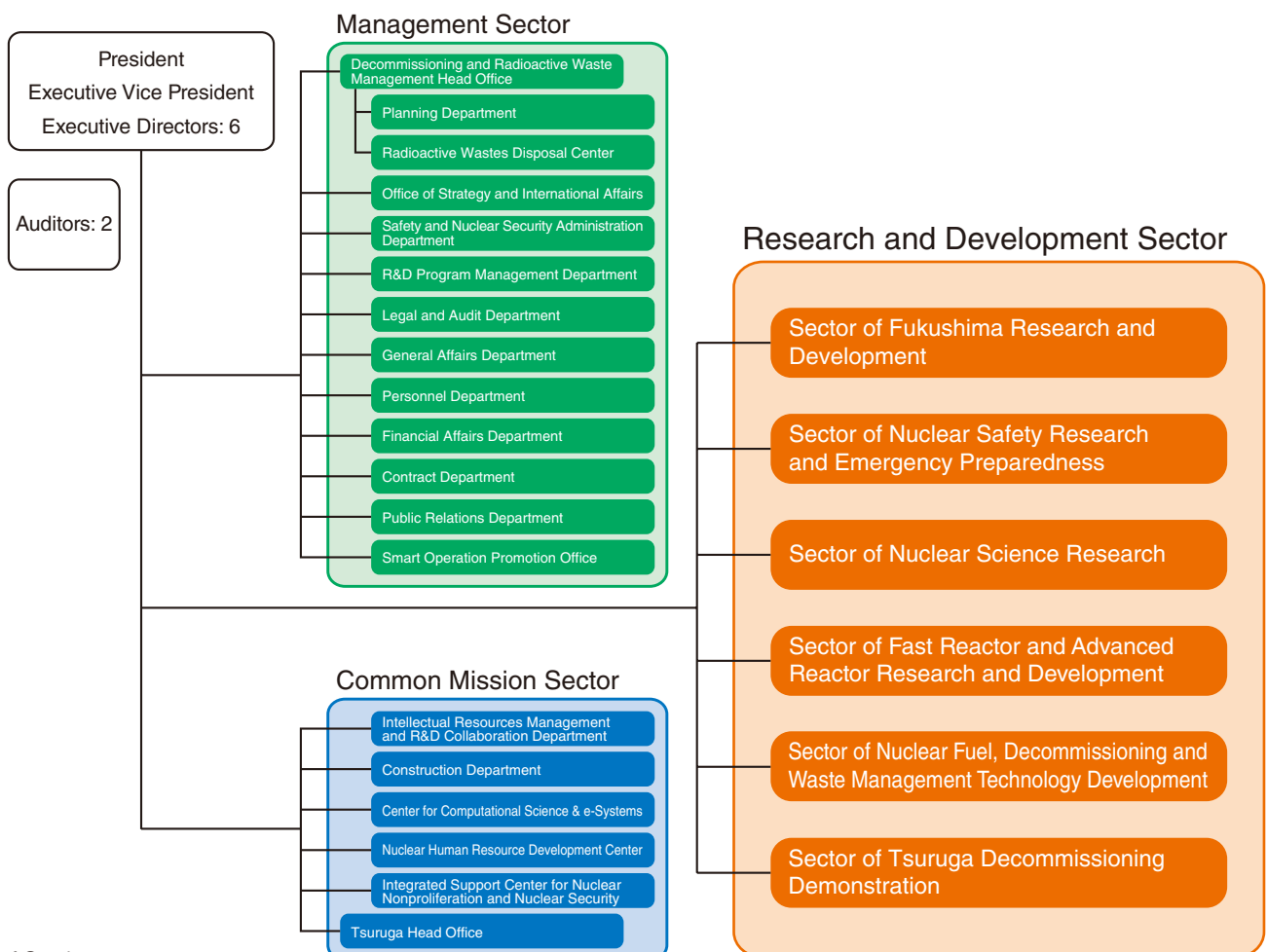
10-1	Nondestructive Assay of Nuclear Materials for Safeguards – Developing Practical Delayed Gamma-ray Spectroscopy Using PUNITA – Tomoki Yamaguchi and Douglas Chase Rodriguez	97
-------------	---	----

About This Publication and the JAEA Organizational Outline

This publication introduces the latest research and development (R&D) endeavors in each field of the Japan Atomic Energy Agency (JAEA), with each chapter presenting the activities from one sector. Each of the R&D sectors performs their activities through one or more R&D centers or institutes, which bases spanning one to several sites. These centers and institutes are located throughout Japan, as shown on the map below. The following brief introduction outlines the research undertaken within each sector.

- The Sector of Fukushima Research and Development** promotes R&D regarding the decommissioning and environmental restoration corresponding to the accident at the Fukushima Daiichi Nuclear Power Station (1F) of Tokyo Electric Power Company Holdings, Inc. (TEPCO). This sector also promotes the development of the R&D infrastructure that is essential to the 1F decommissioning efforts.
- The Nuclear Safety Research Center and Nuclear Emergency Assistance and Training Center in the Sector of Nuclear Safety Research and Emergency Preparedness** perform research into safety measures that support the national nuclear safety bodies that regulate nuclear facilities (such as nuclear power plants) at the Nuclear Science Research Institute. They also perform R&D regarding nuclear emergency monitoring and protective measures at Hitachinaka City, Ibaraki Prefecture.
- The Advanced Science Research Center in the Sector of Nuclear Science Research** explores novel disciplines in advanced atomic energy sciences to develop theories and investigate novel phenomena, materials, and technologies. In particular, seven research themes have been organized under three divisions: advanced actinides science, advanced nuclear materials science, and advanced theoretical physics.
- The Nuclear Science and Engineering Center in the Sector of Nuclear Science Research** carries out fundamental research into various key technologies that are required for nuclear energy use at the Nuclear Science Research Institute.
- The Materials Sciences Research Center and J-PARC Center in the Sector of Nuclear Science Research** are engaged in research using neutrons at the Nuclear Science Research Institute and the Japan Proton Accelerator Research Complex (J-PARC). Research using synchrotron radiation is performed at the Harima SR Radioisotope Laboratory.
- The Reactor Systems Design Department and HTGR Research and Development Center in the Sector of Fast Reactor and Advanced Reactor Research and Development** at the Oarai Research and Development Institute further the development of High-Temperature Gas-cooled Reactor (HTGR) technology, technology for hydrogen production through high-temperature water splitting, and technology for helium gas turbines.

JAEA -Organizational Outline-



As of October, 2020

7. **The Reactor Systems Design Department, Fuel Cycle Design Department, Fast Reactor Cycle System Research and Development Center, and Tsuruga Comprehensive Research and Development Center in the Sector of Fast Reactor and Advanced Reactor Research and Development** aim to establish fast reactor (FR) cycles to address long-term energy security and global environmental issues. This work includes enhancing the safety of the FR system at the Oarai Research and Development Institute, compiling the results on the Prototype Fast Breeder Reactor Monju (MONJU), attaining inspection and repair technologies for the FR system at the Tsuruga Comprehensive Research and Development Center, and manufacturing plutonium fuel and reprocessing spent FR fuel at the Nuclear Fuel Cycle Engineering Laboratories in cooperation with the Sector of Nuclear Fuel, Decommissioning and Waste Management Technology Development.
8. **The Sector of Nuclear Fuel, Decommissioning and Waste Management Technology Development** develops technologies for the safety and rational decommissioning of nuclear power facilities as well as measures for processing and disposing of radioactive waste. It operates at the Aomori Research and Development Center, the Nuclear Fuel Cycle Engineering Laboratories, and the Ningyo-toge Environmental Engineering Center. The sector also performs multidisciplinary R&D that is aimed at improving the reliability of the geological disposal of high-level radioactive waste in Japan. One key field is the establishment of techniques for evaluating the long-term stability of the geological environment, carried out at the Tono Geoscience Center. The main focus at the Horonobe Underground Research Center and the Nuclear Fuel Cycle Engineering Laboratories is on safety assessment and improving technologies for the design of geological disposal facilities; an additional focus at the Nuclear Fuel Cycle Engineering Laboratories is on developing nuclear fuel cycle technology.
9. **The Center for Computational Science & e-Systems** aims to advance simulation technologies and fundamental technologies in computational science as well as the operation and maintenance of computer systems and networks. These activities are mainly conducted at the Nuclear Science Research Institute and the Kashiwa Office.
10. **The Integrated Support Center for Nuclear Nonproliferation and Nuclear Security (ISCN)** plays an active role in strengthening nuclear nonproliferation and nuclear security in both the domestic and international arenas. This is achieved through its many activities, including the development of technologies for IAEA safeguards and nuclear detection and forensics, policy research and analysis, capacity-building support activities targeting Asian countries, operation of CTBT international monitoring facilities located in Japan, and coordination and support for nuclear fuel transportation undertaken by JAEA. These efforts are carried out mainly at Head Office and the Nuclear Science Research Institute.

R&D Institutes/Centers of JAEA



Assistance in Environmental Restoration and Decommissioning

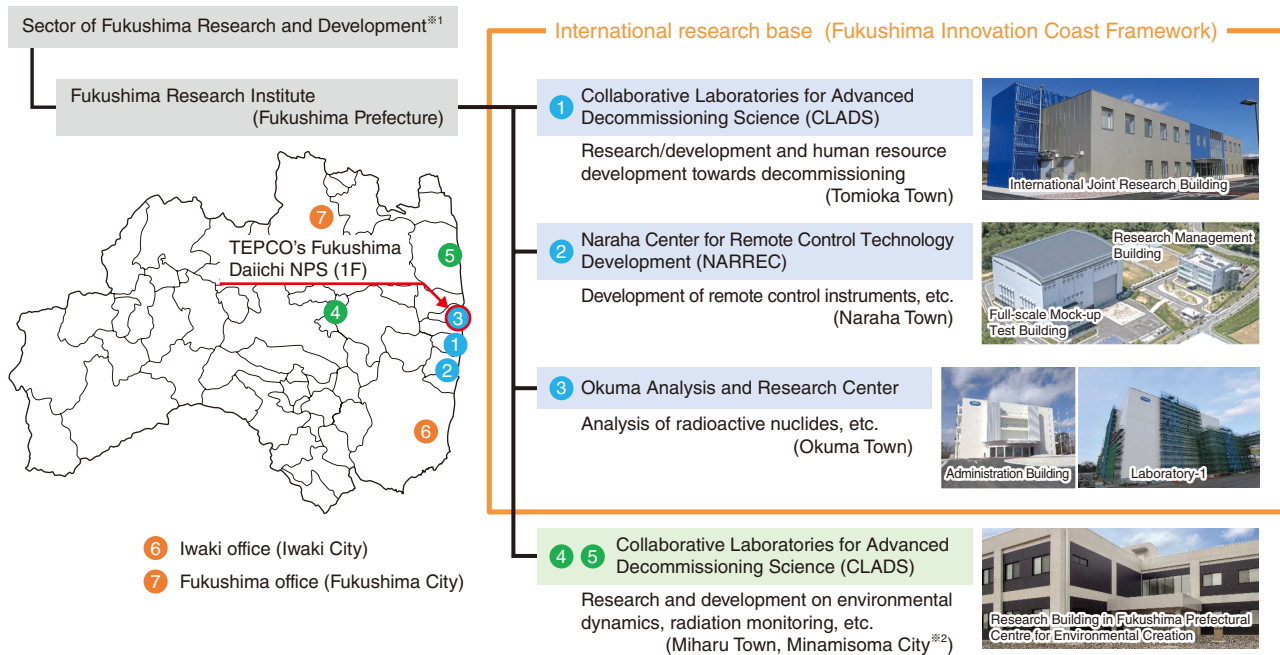


Fig.1-1 Research and development bases and office of Sector of Fukushima Research and Development

※1 In order to engage the R&D for Fukushima revitalization as a whole JAEA, the Sector of Fukushima R&D is cooperating with other Sectors in JAEA.

※2 JAEA is conducting the R&D at the Research Building (Miharu Town) and the Environmental Radiation Monitoring Centre (Minamisoma City) of the Fukushima Prefectural Centre for Environmental Creation.

As Japan's sole comprehensive institute in the field of nuclear energy, Japan Atomic Energy Agency (JAEA) has been engaged in research and development (R&D) of the environmental restoration of Fukushima and the decommissioning of TEPCO's Fukushima Daiichi NPS (1F). The R&D bases of the Sector of Fukushima Research and Development are shown in Fig.1-1.

The International Joint Research Building of Collaborative Laboratories for Advanced Decommissioning Science (CLADS), the Research Management Building and the Full-scale Mock-up Test Building of Naraha Center for Remote Control Technology Development (NARREC), and the Administration Building and Laboratory-1 (currently under construction) of Okuma Analysis and Research Center are all decommissioning-related facilities that play a role in the Fukushima Innovation Coast Framework. In addition, at the Research Building (Miharu Town) and the Environmental Radiation Monitoring Centre (Minamisoma City) of the Fukushima Prefectural Centre for Environmental Creation, both of which were established by Fukushima Prefecture, R&D related to environmental restoration are underway in cooperation with Fukushima Prefecture and the National Institute for Environmental Studies.

As part of research into decommissioning, the leeching behavior of uranium from fuel debris and the elemental distribution in fuel debris were investigated (Topics 1-1 and 1-2, respectively), and remote analysis techniques were developed for in situ analysis (Topic 1-3) to contribute to the removal of fuel debris. Because the radiation dose in the damaged reactor building of 1F is still high, most of the work must be carried out using remote controlled equipment. To verify the operability of this remotely operated equipment, a test field simulating the on-

site environment (Topic 1-4) and a video analysis technique to help the operator of the remotely operated equipment understand the on-site conditions (Topic 1-5) were developed. From the viewpoint of radiation control, estimation of distribution and speciation of cesium, a major source of radiation, in the reactor building are being carried out (Topic 1-6). In addition, to evaluate the safety of radioactive waste storage, the behavior of hydrogen production by water radiolysis in the waste was investigated (Topic 1-7). Collaborative research with international organizations has helped to clarify the progress of the accident and estimate the situation inside the damaged reactor (Topic 1-8).

In environmental restoration research, a number of studies were conducted to elucidate and predict the migration of radionuclides released by the accident (Topics 1-9–1-15). In parallel, a comparative study with the Chernobyl disaster was carried out based on the reassessment of dose rates immediately after the accident (Topic 1-16), which contributed to the retrospective estimation of exposure doses at Fukushima. Furthermore, the off-site distribution of radioactive materials was compiled as a map and made available on the internet (Topic 1-17). The external exposure of residents was assessed (Topic 1-18), and this information is provided to the government for the release of the difficult-to-return zones.

Efforts to promote R&D of environmental restoration and the decommissioning by concentrating expertise are ongoing, as is the active dissemination the findings. JAEA aims to contribute to the reconstruction of Fukushima by building a network among local companies and research and educational institutions to revitalize local industries and develop human resources.

1-1 Evaluation of Uranium Leaching from Fuel Debris in Water

— Leaching Rate Evaluation Considering Effects of Concrete Components, and Comparison with Spent Fuel —

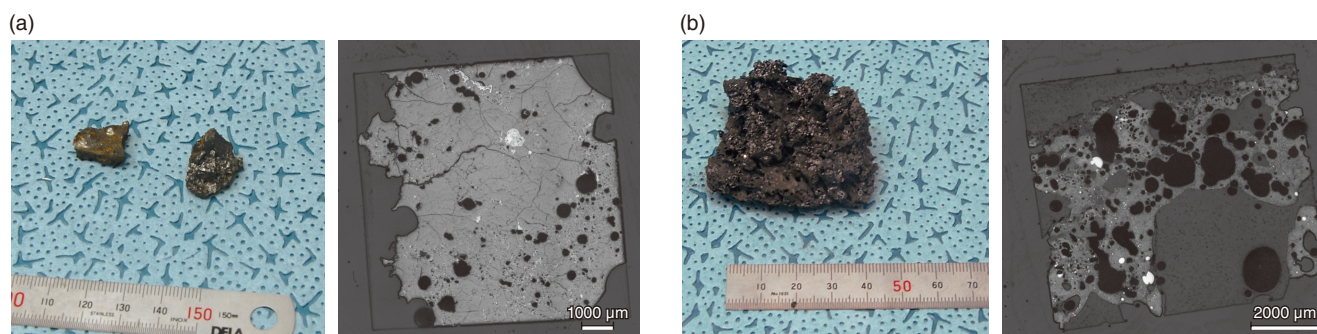


Fig.1-2 Observed appearance (left) and cross section (right) of simulated fuel debris samples from the leaching test

Two types of simulated fuel debris were used. The resulting leaching rates are 2.53 mg/m²/d and 2.86 mg/m²/d with/without concrete components. This is comparable to rates of spent fuels.

(a) Without concrete: A sample containing U, Zr, Fe, rare earths, etc. was heated at 2760 °C for approximately 45 minutes in reducing atmosphere (Ar–H₂). (b) With concrete: A sample containing U, Zr, Fe, rare earth, etc. and additive Si, Ca, Mg as concrete components was heated at 2000 °C for approximately 10 minutes under N₂ atmosphere. In each, the outer appearance is on the left and a cross-sectional optical microscope image is on the right.

Fuel debris at the TEPCO's Fukushima Daiichi NPS (1F) is assumed to be stored in water during transportation and interim storage for cooling after removal from reactors. Therefore, it is important to understand the leaching behavior of fuel debris components into water, especially nuclear materials such as uranium (U), for a safety evaluation of fuel debris transportation and interim storage in water. However, few data on U leaching in water are available; none of these available data come from fuel debris rates. Thus, a leaching test using simulated fuel debris was performed to acquire U leaching rates from fuel debris.

Some samples of the simulated fuel debris are shown in Fig.1-2. Two types of fuel debris have been assumed to be present in 1F: melt of fuels and structural materials, which is generated in reactor pressure vessels, and molten core–concrete interaction (MCCI) products generated in the lower parts of pressure containment vessels. Thus, samples with and without concrete components were prepared.

The simulated fuel debris were immersed in deionized water at approximately 25 °C and irradiated with gamma rays from a ⁶⁰Co source (approximately 80 Gy/h) in air for 100 days. Here, gamma irradiation was used to generate hydrogen peroxide by radiolysis of water, which is expected to affect leaching rates. Furthermore, to limit the production of nitric acid from nitrogen (N₂) in air due to the gamma rays, the volume ratio of the gas phase to the water phase was set to approximately 0.1.

The resulting colloid in the sampled solution was dissolved by adding nitric acid; the U concentration in the solution was then analyzed using inductively coupled plasma mass spectrometry

(ICP-MS). After removing the solution, the container and sample holder were immersed in 0.5 N nitric acid for 24 h for precipitates dissolution; the U concentration in the immersing solution was analyzed. The total amount of U in the solution and precipitate was obtained from these analyses, allowing the leached amount of U to be calculated. The leaching rate was then calculated by dividing the leached amount by the surface area of the pre-test sample and the leaching period. The test was conducted at ATALANTE facility of the French Alternative Energies and Atomic Energy Commission (CEA) with the cooperation of CEA.

The resulting leaching rates of U in the samples with and without concrete components were 2.53 and 2.86 mg/m²/d respectively, and were found to be close. Previous studies have reported U leaching rates of spent fuels in water are 2 mg/m²/d or 83 mg/m²/d according to two typical reports. The U leaching rates of simulated fuel debris obtained in this study therefore do not differ from those of spent fuels.

The leaching rates of fuel debris in 1F thus concluded similar to those of spent fuels regardless of the presence of concrete components. When transportation and storage are applied for 1F fuel debris, the equipment and facilities of spent fuels will be helpful. In addition, the U leaching rates obtained in this study can be utilized as basic data to evaluate behavior for various situations in which fuel debris may come into contact with water, such as transportation, storage, retrieval, and disposal.

(Akira Nakayoshi)

Reference

Nakayoshi, A. et al., Leaching Behavior of Prototypical Corium Samples: A Step to Understand the Interactions between the Fuel Debris and Water at the Fukushima Daiichi Reactors, Nuclear Engineering and Design, vol.360, 2020, p.110522-1–110522-18.

1-2 Distribution of Components in Fuel Debris

— Segregation of Gadolinium and Iron during Solidification Using Simulated Molten Debris —

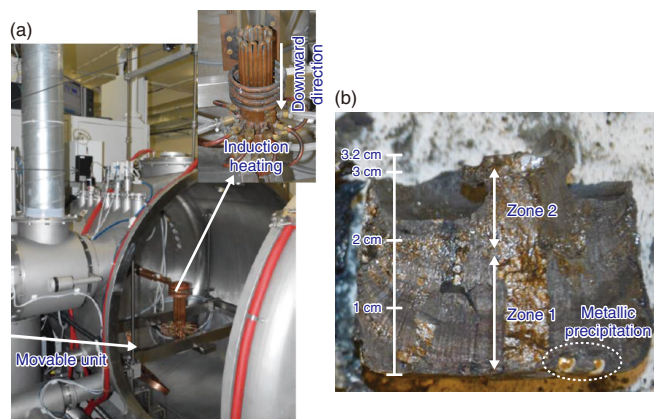


Fig.1-3 (a) View of the cold crucible induction furnace and (b) Cross-sectional image of sample

The liquefaction/solidification test was performed using the cold crucible induction furnace in collaboration with the Research Centre Řež in Czechia. The cross-sectional view of cut solidified sample shows zone 1 (layered structure), zone 2 (no layered structure and owing cavity), and metallic precipitations.

During the severe accident at the TEPCO's Fukushima Daiichi NPS (1F), molten corium consisting of nuclear fuels and structural materials (main component: iron (Fe)) may have formed and solidified at an extremely slow cooling rate. Components in the melt are likely to segregate under slow solidification. Gadolinium oxide (Gd_2O_3), a burnable poison, is present in a limited number of doped uranium dioxide (UO_2) fuel rods owing to the high neutron capture cross-section. From the viewpoint of nuclear criticality safety, it is important to understand the distribution of Gd in the fuel debris. Additionally, an understanding of the distribution of Fe is also important because a significant amount of Fe may be potentially dissolved in the fuel debris and Fe is expected to influence criticality.

To investigate the segregation of Gd and Fe in the fuel debris, a liquefaction/solidification test on simulated core materials (containing UO_2 , ZrO_2 , Gd_2O_3 , FeO , and simulated fission products MoO_3 , Nd_2O_3 , SrO , and RuO_2) approximately 1 kg in weight was performed using a cold crucible induction furnace (Fig.1-3(a)). The melted sample was gradually lowered during the test to achieve slow solidification conditions.

A cross-sectional image of the solidified sample is shown in Fig.1-3(b); here, the bottom region has a layered structure (zone 1) and the upper region has several cavities (zone 2). A schematic of the solidification progress is shown in Fig.1-4. The melt solidified gradually from the bottom-forming layered structure (zone 1). Subsequently, the upper crust was formed. Cavities were also formed during solidification toward the inner region. Additionally, Ru metal was precipitated in the bottom region.

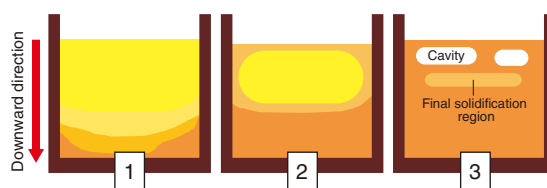


Fig.1-4 Solidification progress of simulated debris

During the test, the melt solidified from the bottom. Subsequently, the upper surface solidified and melt solidified toward the inner region.

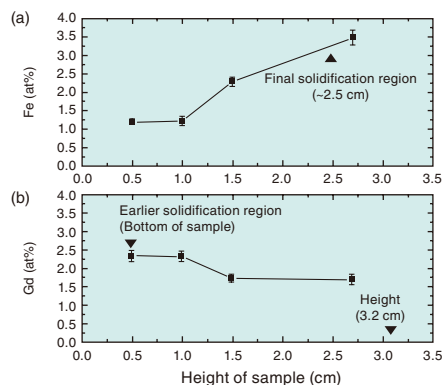


Fig.1-5 (a) Dependence of (a) Fe and (b) Gd concentration on sample heights

(a) The concentration of Fe tended to be higher in the final solidification region; conversely, (b) Gd tended to be higher in the earlier solidification region.

Several pieces were obtained from the central axis of the sample from the top to the bottom regions and subjected to elemental analysis. The resulting concentrations of Fe and Gd in the sample are plotted as a function of sample height in Fig.1-5. The maximum concentration of Fe was 3.5at% at 2.7 cm, close to the estimated final solidification region. This suggests that Fe was segregated in the inner region of the fuel debris, where the melt was solidified later (Fig.1-5(a)). In contrast, the maximum concentration of Gd was 2.4at% at 0.5 cm. This position is close to the bottom of the sample, where the melt was solidified earlier, thus indicating that Gd segregates in the outer surface of the fuel debris. Because the number of Gd-doped fuel rods in a reactor is limited (approximately 1%), slight segregation can affect the recriticality of fuel debris (Fig.1-5(b)).

Although the liquefaction/solidification test of simulated core materials of approximately 1 kg was performed in this study, the mass of the fuel debris in 1F is predicted to be several tons or more. There is thus a large scale gap between the sample studied and 1F debris. Future research will include a larger-scale test (approximately 10 kg) and numerical analysis of segregation to acquire more reliable data on the segregation of components in fuel debris. These data will contribute to the future removal of the fuel debris.

This study was performed joint research between JAEA and Research Centre Řež on "Preliminary tests on molten corium solidification mechanism", and Japan Times has introduced about the article of good cooperative relationship between Japan and Czechia.

(Ayako Sudo)

Reference

Sudo, A. et al., Segregation Behavior of Fe and Gd in Molten Corium during Solidification Progress, Journal of Nuclear Materials, vol.533, 2020, p.152093-1-152093-8.

1-3 50x Increase in Plasma Emission Intensity by Microwave

— Advanced Remote Analysis Technology for Fuel Debris Using Laser-Induced Breakdown Spectroscopy —

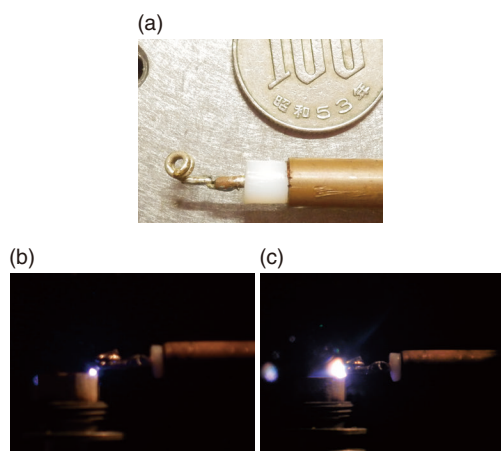


Fig.1-6 Microwave electrode (a) and plasma emission (b) (c)
 (a) A wire approximately 0.6 mm in diameter and 25 mm in length is connected to a core wire of semi-rigid coaxial cable to form a spiral shape. (b) No microwave input. (c) Microwave input. The emission intensity of (c) is clearly stronger.

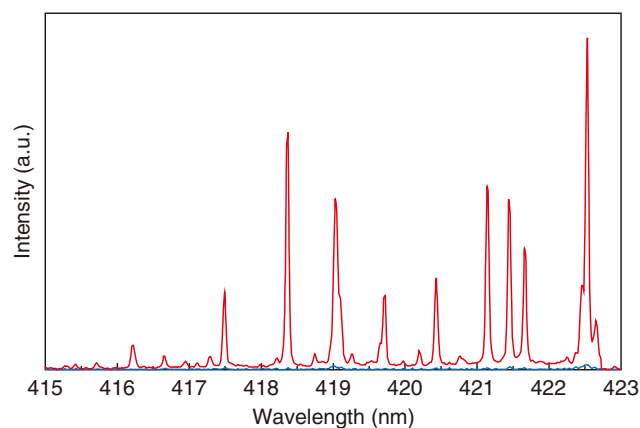


Fig.1-7 Emission spectrum (gadolinium oxide sample)
 Blue line: Laser irradiation only and no microwave; red line: microwaves were input. The intensity was approximately 50 times higher.

The fuel debris generated by the accident at TEPCO's Fukushima Daiichi NPS is highly radioactive, thus making it difficult for people to come in close proximity to it. As collecting fuel debris by a remote controlled operation and transporting it to an analysis facility is time-consuming, an in situ remote analysis of fuel debris would be a safe, efficient alternative. Therefore, laser-induced breakdown spectroscopy (LIBS) was developed to enable in situ analysis in a furnace.

LIBS is an analysis method used to identify the elements contained in a sample by irradiating the surface of the sample with a high-energy laser pulse and analyzing the plasma emission spectra using a spectrometer. An easy-to-operate optical fiber is used to transmit the laser beam into the furnace. A high-resolution spectrometer is required to analyze elements such as lanthanoids in fuel debris, but the emission that passes through such a spectrometer becomes weak and gets buried in noise and thus cannot be detected; it is therefore necessary to enhance the emission itself. Increasing the laser power will increase the emission intensity, but will also damage the optical fiber, so this method cannot be used to increase the emission intensity.

Therefore, a method to increase the plasma emission intensity using microwaves instead of increasing the laser power was developed. The plasma emission can be sustained for a long time by the microwaves, and the total emission increases by time integration. Conventionally, a metallic waveguide was used to transmit microwaves because of its low transmission loss, but

the waveguide cannot be bent freely, and it is difficult to transmit it to a narrow space such as in a furnace. Therefore, for increased compactness and bending freedom, a bendable coaxial cable was used. In addition, a method for bringing the electrode attached to the tip of the cable close to the plasma was devised, without using a resonator to increase the electric field of microwaves in the interaction area with the plasma. As a result, the system was simplified with high flexibility and good operability.

The prototype electrode, as shown in Fig.1-6(a), contained a semi-rigid coaxial cable with an outer diameter of approximately 6 mm and a conductor of approximately 25 mm attached to the core wire at the end and wound into a spiral shape. The enhancement effect can be obtained without winding, but winding was thought to increase stability and compactness by avoiding a fluctuating tip. Photographs of emission at the tip of the electrode are shown in Fig.1-6(b) (c); the emission grew stronger when the microwave was input. An example of the acquired emission spectrum is shown in Fig.1-7. The microwave used has a peak output of 1.3 kW and a duration time of 1 ms. When the microwave is not applied, the plasma emission disappears in approximately 10 μ s; by applying the microwave, emission can be continued for between several 100 μ s and 1 ms. Due to this effect, the total emission light was approximately 50 times greater than that without the microwave. This development presents a step forward in the search for a compact, simple, highly sensitive, and high-resolution system.

(Masaki Oba)

Reference

Oba, M. et al., Development of Microwave-Assisted, Laser-Induced Breakdown Spectroscopy without a Microwave Cavity or Waveguide, Japanese Journal of Applied Physics, vol.59, no.6, 2020, p.062001-1–062001-6.

1-4 Clarifying the Warming Behavior of a Robot Test Pool

— Measurement and Analysis toward Facility Utilization with User Needs —



Fig.1-8 Robot test pool

Underwater robot movements can be observed from side windows and from above. It is also possible to change the water temperature and salinity of the water. To adjust the water temperature, it is necessary to set a reasonable time to adjust 80 tons of water.

The Naraha Center for Remote Control Technology Development (NARREC) is a mockup facility to examine remote devices for the decommissioning of TEPCO's Fukushima Daiichi NPS. NARREC provides various test equipment and has accepted many users since beginning full-scale operation in April 2016. The Robot Test Pool in NARREC is commonly used for testing underwater robots (Fig.1-8).

This pool is composed of cylindrical stainless steel (inner diameter: 4.5 m, water depth: 5 m) with an insulating polystyrene cover. The water temperature can be varied from room temperature to 60 °C by circulating warm water generated by a heater. As the pool contains 80 tons of water when full, it takes approximately 1 day to increase the water temperature from room temperature to 60 °C and approximately 10 days to decrease the water temperature from 60 °C to 20 °C via natural heat dissipation.

Thus, a schedule taking into account the water temperature adjustment time is needed for optimizing the planning and usage of the pool. This includes the clarification of reasonable water temperature adjustment time, taking into consideration the varying heat dissipation behavior of the outer wall, bottom, and water surface of the pool due to the temperature and humidity fluctuations between summer and winter. Therefore, the temperature behavior was investigated and used to develop a model that can be used to evaluate the heat dissipation behavior and resulting temperature change of the water based on the

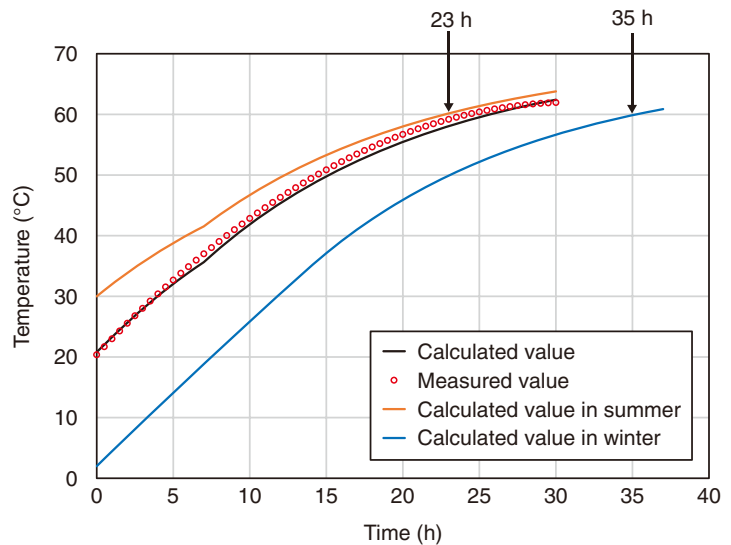


Fig.1-9 Measured and calculated values when the temperature is increased from room temperature to 60 °C

Measured values were taken in June. Calculated values were based on actual measurement conditions and took into account the air temperature, water temperature, and humidity in summer and winter.

atmospheric conditions and pool structure.

A comparison of the measured and calculated values using the developed model in June when the pool was increased from 20 °C to 60 °C is shown in Fig.1-9, as are the calculated values for a similar increase under summer and winter conditions. At the measured value, the room temperature, water temperature, and humidity were 24.7 °C, 20.8 °C, and 50.0%, respectively. For the modeled summer conditions, the room temperature, water temperature, and humidity were assumed as 35.7 °C, 30.0 °C, and 80.0%, respectively. For the modeled winter conditions, the room temperature, water temperature, and humidity were assumed as 5.0 °C, 2.0 °C, and 20.0%, respectively. The results presented here confirm that the developed model satisfactorily reproduced the measured values. Additionally, it would take 23 and 35.5 hours for the water temperature to reach 60 °C in summer and winter, respectively. Further calculations demonstrated that keeping the pool covered can help maintain the water temperature by reducing heat dissipation, and that using the exhaust duct attached to the pool can halve the time required to cool down.

As the developed model allows for the evaluation of the seasonally dependent behavior of the water temperature, it is now possible to estimate the preparation period required for facility use.

(Ryoki Arakawa)

Reference

Arakawa, R. et al., Influence Factors on Temperature Behavior of Robot Test Pool, JAEA-Technology 2019-018, 2020, 157p. (in Japanese).

1-5 3D Reconstruction of Structures from Images

— Development of Image Analysis Method to Support Remote Operation —

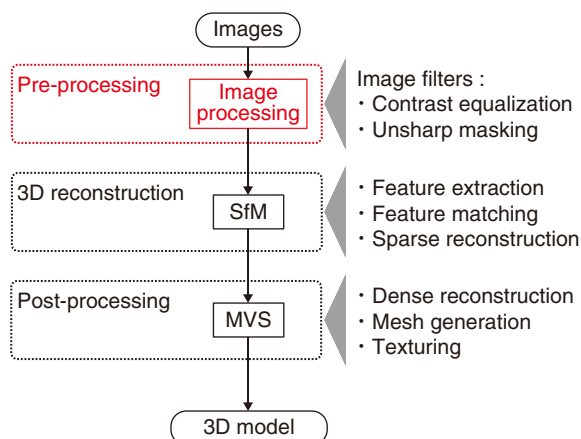


Fig.1-10 Processes required to generate a 3D model from images

A 3D model is generated from images through pre-processing (image processing), 3D reconstruction (SfM), and post-processing (MVS).

As a part of the decommissioning of the TEPCO's Fukushima Daiichi NPS (1F), remotely operated robots have been used for various tasks to reduce the radioactive exposure to workers. In such tasks, it can be difficult to be aware of the robot's working environment, as the operators handling the robots do so by monitoring the images transmitted from cameras mounted on the robots. Due to the operator's resulting lack of spatial awareness, issues such as cable trouble and robot roll-over accidents have occurred. Thus, it is important to provide operators with the necessary information to allow them to perform the tasks safely and efficiently. In this study, a 3D reconstruction method was developed using images obtained by the robot in the working environment to support the remote operation.

To verify the suitability of the 3D reconstruction method in the working environment at the decommissioning site, images obtained by the robot inside the primary containment vessel (PCV) were analyzed. The images were extracted from a video of the survey task available on the TEPCO website. However, the obtained images have low contrast and are blurry, making the extraction of features required for 3D reconstruction difficult. The required image features include feature key points such as the corners and edges of structures. If these image features are insufficiently extracted, the conventional 3D reconstruction method cannot generate an accurate 3D model.

To improve the feature extraction, a pre-processing image processing step was applied using two contrast equalization and unsharp masking image filters. Here, the extracted number of image features was improved by adjusting intensity thresholds and a scaling constant as the parameters of the image filters. Using these pre-processed images, 3D reconstruction was performed by applying Structure from Motion (SfM). SfM

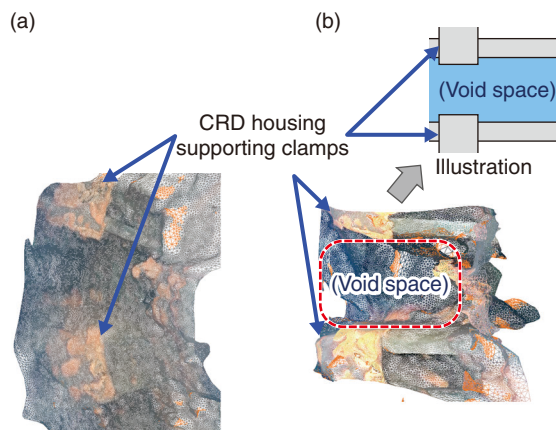


Fig.1-11 Results of 3D reconstruction

Two models show 3D models reconstructed based on (a) original and (b) pre-processed images. This result shows that the 3D model could be reconstructed more accurately since images obtained by the survey task were applied image filters as pre-processing.

computation generally extracts the image features from the images and finds correspondence among the images by a feature-matching calculation. By triangulation, each matched feature is registered as a point in a 3D space; via sparse reconstruction, these points compose a 3D point cloud. However, since the obtained 3D point cloud has a low density, it is still difficult to be aware of all of the surrounding structures. Thus, visibility improvement is required to be aware of the structures in the working environment. To improve visibility, Multi-View Stereo (MVS) was applied as post-processing. The MVS reconstruction produced a dense reconstruction from the 3D point cloud obtained from SfM computation; a mesh surface was then generated based on the dense reconstruction. Moreover, textures were added to the generated mesh surfaces to obtain a final 3D model. A summary of these processes employed to generate a 3D model is shown in the flowchart in Fig.1-10.

To evaluate the correctness of the introduced pre-processing, 3D models based on the pre-processed and original images were compared. As shown in Fig.1-11(a), the 3D model reconstructed from the original images had a few bumps and dips on the surface but was formed a smooth, curved surface. In contrast, the 3D model reconstructed from the pre-processed images had a void space between the supporting clamps of the control rod drive (CRD) housing and was had more surface variations (Fig.1-11(b)). This indicates that applying the developed image pre-processing method helps generate a more-accurate 3D model to support the remote operation for the decommissioning.

Future efforts will include the development of a method for displaying the generated 3D model to the robot operator in real-time for safe decommissioning of the 1F.

(Toshihide Hanari)

Reference

Hanari, T. et al., 3D Environment Reconstruction Based on Images Obtained by Reconnaissance Task in Fukushima Daiichi Nuclear Power Station, E-Journal of Advanced Maintenance, vol.11, no.2, 2019, p.99-105.

1-6 Chemisorption of Cesium on Structural Materials during SA

— Prediction and Verification of Thermodynamic Properties of Cesium Compounds —

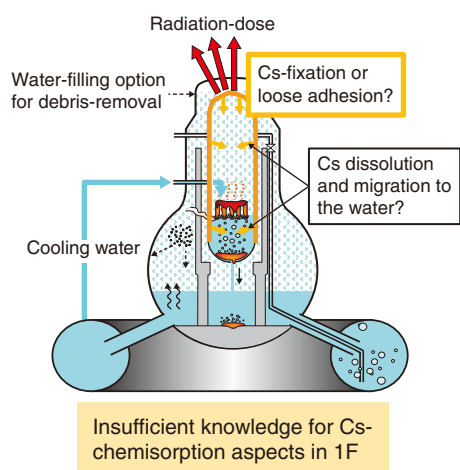


Fig.1-12 Cesium (Cs) transport during SA
Both the chemisorption of Cs to structural materials and the transport of Cs to water are considered as Cs transport behaviors.

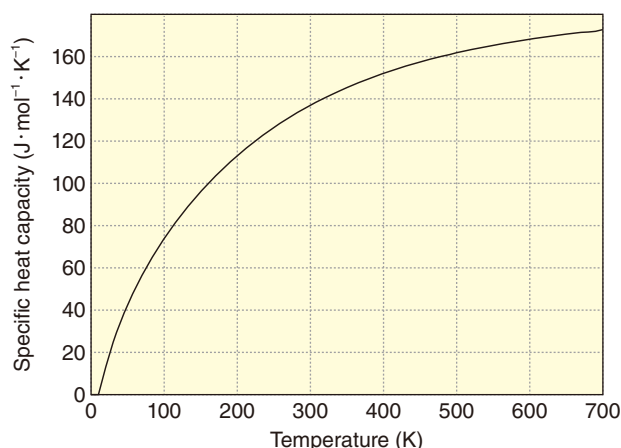


Fig.1-14 Calculated specific heat capacity of CsFeSiO₄
Calculating the specific heat capacity of CsFeSiO₄ made it possible to predict the thermodynamic properties of CsFeSiO₄ at finite temperatures.

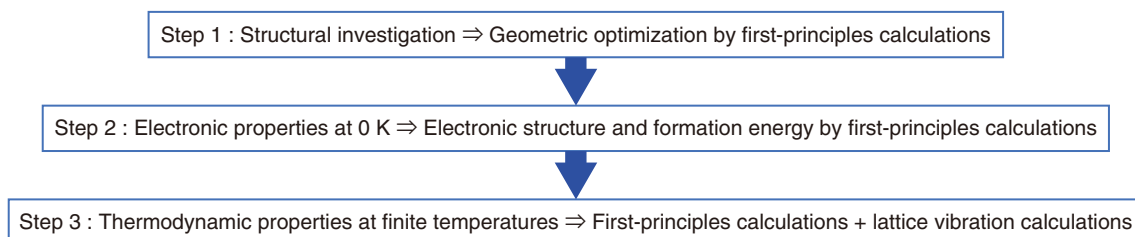


Fig.1-13 Calculation of thermodynamic properties by first-principles calculations and lattice vibration calculations

In a severe accident (SA) such as the TEPCO's Fukushima Daiichi NPS (1F) accident, fission products (FPs) are released into the reactor buildings and environments due to the melting of the core and damage to the reactor vessels. To respond to the accident and to formulate evacuation plans and post-accident decommission processes, it is necessary to understand the release and transport behaviors of FPs and to evaluate the exposure of the public and workers accurately. The release and transport behaviors of FPs depend on the chemical behaviors such as chemical reactions and properties. As shown in Fig.1-12, cesium (Cs) causes chemical reactions with structural materials inside the reactor at high temperatures during an SA; Cs fixed by chemisorption becomes a major radiation source in the reactor. To clarify the behavior of chemisorbed Cs, it is necessary to investigate the chemical species formed during chemisorption.

To investigate these chemical species, a series of Cs chemisorption experiments were performed on stainless steel (SS), which is used as a structural material. The results confirmed that compounds such as CsFeSiO₄, CsFeO₂, and Cs₂Si₄O₉ were formed by reacting with iron (Fe) and silicon (Si) contained in SS during chemisorption. Chemical equilibrium calculations were performed using the thermodynamic data of these compounds to predict the chemical species formed during SAs. However, the thermodynamic data of CsFeSiO₄ required for this prediction have not been reported.

A method to predict thermodynamic properties without measured data was therefore developed based on a combination of first-principles and lattice vibration calculations. This calculation process, summarized in Fig.1-13, involves structural investigations, the calculation of electronic properties at 0 K by first-principles calculations, and the determination of thermodynamic properties at finite temperatures by lattice vibration calculations performed based on these investigations. The validity of this approach was then verified by comparison with reported thermodynamic data such as the standard enthalpy of formation at 298 K, the standard entropy at 298 K, and the temperature dependence of the specific heat capacity for Cs₂Si₂O₅ and Cs₂Si₄O₉. Applications of this approach, furthermore, made it possible to predict the thermodynamic data of CsFeSiO₄. As an example, the calculated specific heat capacity of CsFeSiO₄ is shown in Fig.1-14.

The developed calculation approach proposed here allowed for predicting Cs chemical species chemisorbed on structural materials. Future work will aim to improve the proposed method and include a more in-depth verification of the proposed method with experimental data. Additionally, the proposed method can be used to contribute to assessments on exposures in the 1F reactor.

(Chikashi Suzuki)

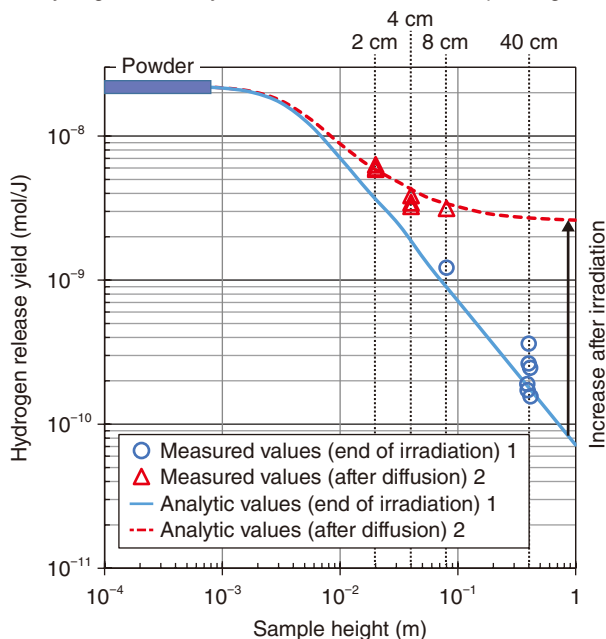
Reference

Miradji, F., Suzuki, C. et al., Cesium Chemisorbed Species onto Stainless Steel Surfaces: An Atomistic Scale Study, Journal of Physics and Chemistry of Solids, vol.136, 2020, p.109168-1-109168-9.

1-7 Hydrogen Release from Geopolymer by Gamma Irradiation

— Reduced Hydrogen Yield of Bulky, Solidified, Water-Saturated Waste —

(a) Comparison of the measured and analytical values of the hydrogen release yield as a function of the sample height



(b) Representation of hydrogen concentration in the model samples at the steady state

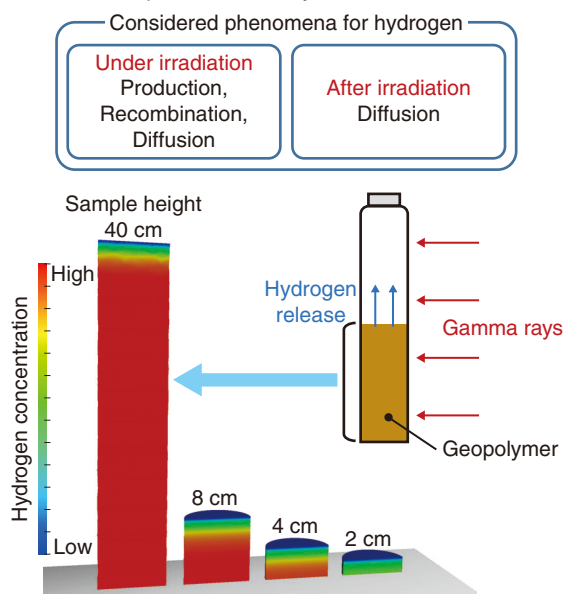


Fig.1-15 Measured and calculated hydrogen release yield as a function of sample height

(a) The measured yield of hydrogen gas released from the cylindrical geopolymer sample irradiated with water at 100% relative humidity was lower than that of the powder. The evaluated value immediately after irradiation is the one of the solid line (1). Since only hydrogen diffusion proceeds after irradiation, the evaluation value approaches the analytical value 2 of the dashed line when all hydrogen diffused to the gas phase. (b) Model representation where a portion of the hydrogen generated under irradiation is consumed by recombination during diffusion to the sample surface.

Geopolymers are inorganic aluminosilicates that form solid ceramic-like materials at ambient temperatures. Geopolymer matrices have been proposed for confining a wide selection of nuclear wastes such as sludge and resins, Mg–Zr alloys, zeolites, Cs and Sr salts, and organic liquids. Geopolymers offer a good solution compared with other binders when a high pH is required, in high-temperature conditions, in case of chemical incompatibility between the waste and available matrices, or when the precipitation of silicate species is needed. However, the release of hydrogen gas (H_2) from wasteforms is a major safety concern for encapsulating nuclear wastes. Hydrogen produced by radiolytic processes is a key factor for geopolymers because of a certain amount of water present in their porous structure.

In this work, the hydrogen release from a geopolymer was measured under ^{60}Co gamma irradiation. The effect of sample size was studied for pure geopolymers, as was the addition of zeolites as an example waste material. The hydrogen release yield, defined as the quantity of hydrogen released into the gas phase per joule of radiation energy, was plotted for powder and 2-, 4-, 8-, and 40-cm long cylindrical samples; the results are shown in Fig.1-15(a). The hydrogen release yield decreased as the sample size increased; the hydrogen released from a 40-cm

long cylinder sample was two orders of magnitude lower than a sample in powder form (1.9×10^{-10} and 2.2×10^{-8} mol/J, respectively).

A simple production, recombination, and diffusion (PRD) model was developed to interpret the results, considering only hydrogen production, potential recombination, and diffusion into the geopolymer matrix. The modeled representation of the experimental samples at steady-state is shown in Fig.1-15(b). Under irradiation, the hydrogen generated by water radiolysis is partially consumed by reactions with other radiolytic products on the diffusion path to the sample surface. The solid blue line in Fig.1-15(a) shows the predicted yield considering the release yield measured immediately after irradiation, reproducing the data. The red dashed line represents the same prediction considering that all of the hydrogen in the sample diffused and was released into the gas phase after irradiation, reproducing the data obtained in these conditions.

Given the diffusion constant of the matrix, the developed model successfully reproduced the evolution of hydrogen release as a function of water saturation level and predicted the evolution at sample sizes of up to 40 cm.

(Isao Yamagishi)

Reference

Cantarel, V., Yamagishi, I. et al., On the Hydrogen Production of Geopolymer Wasteforms under Irradiation, Journal of the American Ceramic Society, vol.102, issue 12, 2019, p.7553–7563.

1-8 Accident Progression Analysis: Units 1-3 at the Fukushima Daiichi NPS

— Insights from International Benchmark Analysis Project —

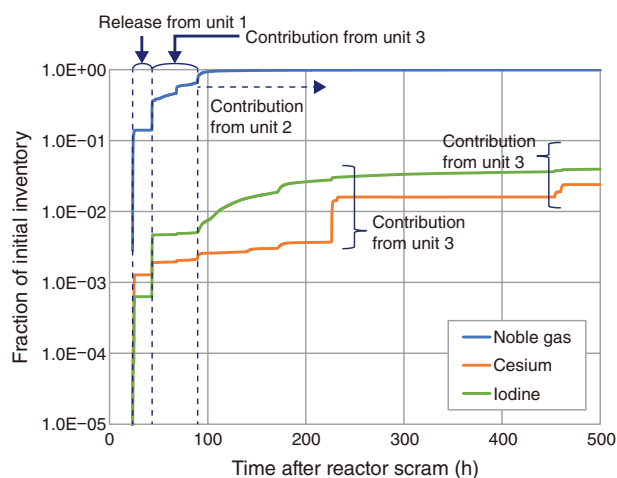


Fig.1-16 Calculated release of major FPs to the environment THALES2/KICHE was used to analyze the chemical reactions of iodine in the liquid phase. A relatively high release fraction of iodine was predicted owing to the consideration of the production of volatile iodine, such as molecular iodine and organic iodine, from chemical reactions with organic species.

The Organization for Economic Co-operation and Development/ Nuclear Energy Agency (OECD/NEA) “Benchmark Study of the Accident at the TEPCO’s Fukushima Daiichi NPS (1F)” (BSAF) project was conducted from 2012 to 2018. One of the objectives of this project is to estimate the status of the reactor pressure vessel (RPV) and containment vessel (CV), the fission product (FP) transfer behavior in the plant, and the source term, which refers to the physical/chemical form and amount of FP released into the environment for the first three weeks, using integral severe accident codes. The participating organizations analyzed the accident progression using common boundary conditions and some assumptions needed for the reproduction of the measured data. Aggregating the analysis results from participants allowed the most plausible accident scenario occurred at 1F to be examined.

JAEA conducted analyses of units 1, 2, and 3 using the THALES2/KICHE code developed at JAEA. The calculated total noble gas, cesium, and iodine released into the environment as a fraction of the total initial inventory in the core at the accident is shown in Fig.1-16. For example, a source term analysis of unit 1 assuming vacuum breaker failure was performed to reproduce the high dose rates observed around a pipe equipped with a vacuum breaker and at the base of the stack. This could arise from the leakage of gas with FPs through the failed vacuum breaker from the drywell (DW) to the wetwell (WW)

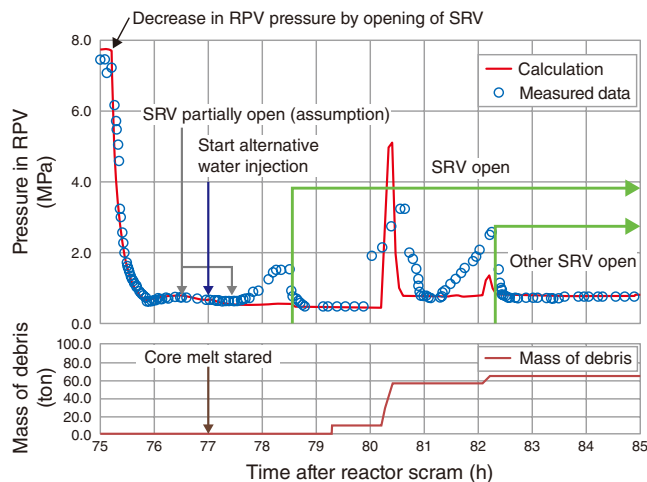


Fig.1-17 Consideration of the cause of observed pressure peaks in RPV of unit 2

The accident progression analysis showed that the three measured pressure peaks after depressurized RPV by safety release valve (SRV) may have been caused by steam and hydrogen generation due to the contact of debris with water in lower plenum.

without scrubbing by water. The analysis of unit 2 focused on the observed three pressure peaks in the RPV 76 hours after the reactor scram, as they seemed to be correlated with the increase in the air dose rate monitored outside 1F. The analysis results over the period of the three peaks are shown in Fig.1-17. Through these long-term analyses based on the measured data, the stability of the code was improved and analytical models for some accident countermeasures were introduced.

In this project, a reasonable consensus for accident progression was reached among participants. For example, regarding unit 1, it was agreed that water injection from outside the CV was performed to cool the core because the equipped cooling systems did not work, however water did not reach the core in the early stage of the accident. Another example of consensus was that the molten fuel was nearly ejected out of the RPV. However, some uncertainties remain, such as the core degradation and relocation model in RPV, the molten core–concrete interaction model, and the remobilization model of FP deposits on the structure’s surfaces for long-term analysis. To overcome these issues and to more fully understand the accident progression, We continues to participate in and manage the successive project of the OECD/NEA study “Analysis of Information from Reactor Buildings and CV of 1F” (ARC-F) as the operating agent.

(Hitoshi Tamaki)

References

- Tamaki, H. et al., Analysis for the Accident at Unit 1 of the Fukushima Daiichi NPS with THALES2/KICHE Code in BSAF2 Project, Proceedings of 18th International Topical Meeting on Nuclear Reactor Thermal Hydraulics (NURETH-18), Portland, U.S.A., 2019, p.72–82, in USB Flash Drive.
- Tamaki, H. et al., Analysis for the Accident at Unit 2 of the Fukushima Daiichi NPS with THALES2/KICHE Code in BSAF2 Project, Proceedings of 18th International Topical Meeting on Nuclear Reactor Thermal Hydraulics (NURETH-18), Portland, U.S.A., 2019, p.100–111, in USB Flash Drive.
- Ishikawa, J., Tamaki, H. et al., Analysis for the Accident at Unit 3 of the Fukushima Daiichi NPS with THALES2/KICHE Code in BSAF2 Project, Proceedings of 18th International Topical Meeting on Nuclear Reactor Thermal Hydraulics (NURETH-18), Portland, U.S.A., 2019, p.536–547, in USB Flash Drive.

1-9 Cause of Cesium Concentration Change in Fish

— Three Transport Pathways from Forests to Fish —

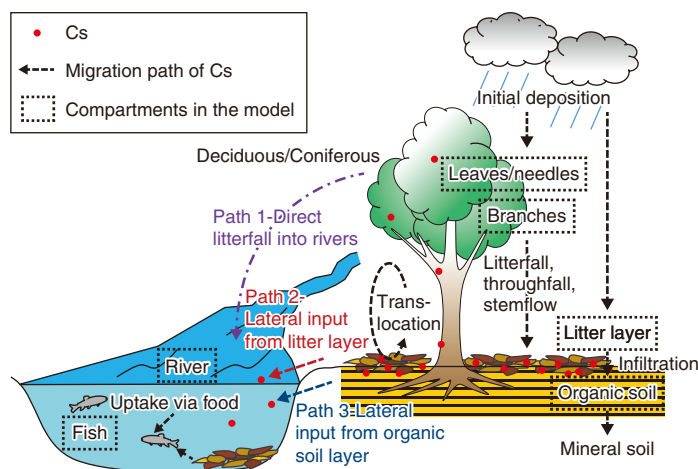


Fig.1-18 Schematic of Cs migration in forest and transport to fish including compartments considered in the simulation model

In the forest, Cs gradually migrates from the tree canopy to the forest floor and from the litter layer to the soil layer. Three transport pathways for Cs to fish living in mountainous streams are possible: direct litterfall into rivers, lateral transfer from the litter layer, and lateral transfer from the soil layer into rivers. The developed model simulates the Cs transfer between forest compartments (e.g., leaves, litter layer, river water) to understand the time evolution of Cs concentration in each compartment.

The Radiocesium (Cs) concentration in freshwater fish caught in Fukushima Prefecture is decreasing with time, allowing shipping restrictions to be lifted. Cs taken up by fish living in mountainous streams is considered to come from forests (Fig.1-18). However, it has been unclear why the Cs concentration is decreasing more rapidly in fish than in the forest and from where in the forest Cs comes into rivers.

In this study, the migration pathways of Cs from the forest to the fish in mountainous streams were analyzed using a developed model coupled with accumulated environmental monitoring data. The model, shown schematically in Fig.1-18, considered leaves/needles, branches, litter layer, organic soil layer, river water, fish, etc., as compartments. At first, the transfer rates of Cs from one compartment to another (e.g., leaves to the litter layer) were determined based on field investigations. The time evolutions of Cs inventories in all compartments were then calculated stepwise. The simulation was then used to clarify that the decrease in the Cs concentration in the fish was linked to the migration of Cs in the forest, including the transport of Cs from the tree canopy to the litter layer and from the litter layer to the underlying organic soil (Fig.1-19). More specifically,

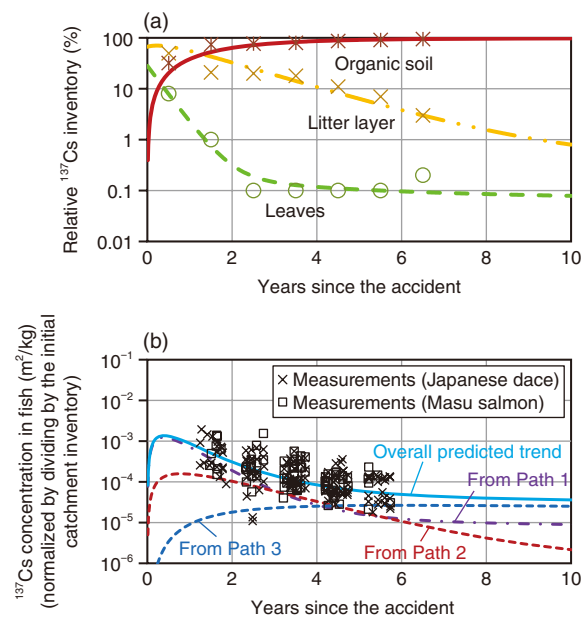


Fig.1-19 Calculated and measured ^{137}Cs concentration in fish

(a) The relative ^{137}Cs inventory in the leaves and litter layer is decreasing while that in organic soil is increasing. (b) As a result, the ^{137}Cs concentration in fish is decreasing, and the contributions from the three pathways are changing with time.

Cs was transferred to fish via a combination of three pathways, as shown in Fig.1-19(b): 1) direct litterfall into the river and its subsequent breakdown, 2) lateral transfer of dissolved Cs derived from the litter layer into the river water, and 3) lateral transfer of dissolved Cs derived from organic soil into river water.

The Cs concentration likely decreased more quickly in fish than in the forest because of the faster decrease of Cs in the leaves/needles and litter layer (Fig.1-19(a)). This resulted in a decreased Cs supply via paths 1 and 2 (Fig.1-19(b)). The contribution from organic soil (i.e., path 3) with a high Cs content will likely increase with time. In the organic soil layer, Cs gradually migrates deep underground and is adsorbed on mineral soil. Thus, understanding the behavior of Cs in organic soil is key for any future predictions of the Cs concentration in freshwater fish living in mountain streams.

The clarification of the mechanism of the changing Cs concentration in mountain stream fish may be useful for lifting shipping restrictions on wild freshwater fish caught in Fukushima Prefecture.

(Hiroshi Kurikami)

Reference

Kurikami, H. et al., Numerical Study of Transport Pathways of ^{137}Cs from Forests to Freshwater Fish Living in Mountain Streams in Fukushima, Japan, Journal of Environmental Radioactivity, vols.208–209, 2019, p.106005-1–106005-11.

1-10 Fast and Easy Analysis of Tritium in Plants and Animals

— Development of Rapid Organically Bound Tritium (OBT) Analysis in Marine Products —

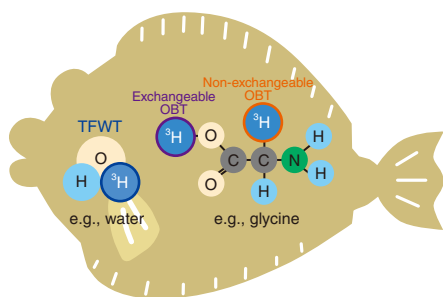


Fig.1-20 Chemical state of tritium in a living body
Tritium exists as tissue free water tritium (TFWT) and organically bound tritium (OBT) in a body.

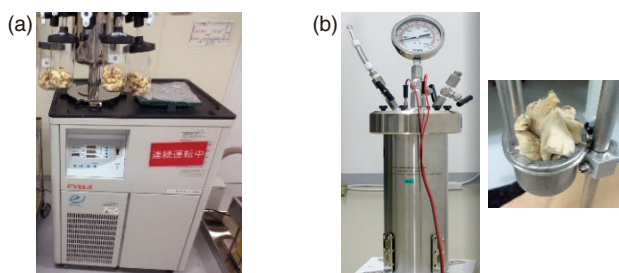


Fig.1-21 (a) Freeze dryer and (b) rapid combustion vessel

(a) The freeze dryer was used to process flounder samples for analysis. (b) The dried flounder samples were then burned in the rapid combustion vessel to decompose organic matter into water, allowing the OBT to be collected.

Table 1-1 Tritium concentration of collected flounder

The concentrations were determined by the conventional and rapid methods with a detection limit of 1 Bq/kg. No tritium was detected.

No.	Method	Collection date	Amount of dry sample (g)	TFWT (Bq/kg-fresh)		OBT (Bq/kg-fresh)	
				Concentration	DL	Concentration	DL
1	Conventional	2015.11.25	120.0	ND	0.84	ND	0.15
2	Conventional	2016.12.22	115.9	ND	0.19	0.04±0.02	0.04
3	Conventional	2016.12.22	115.9	ND	1.02	ND	0.18
4	Rapid	2016.12.22	50.7	ND	0.96	ND	0.16
5	Rapid	2016.12.22	10.8	ND	0.96	ND	0.73
6	Rapid	2018.12.18	11.5	ND	0.90	ND	0.84

DL : lower limit of detection, ND : below the lower limit of detection

Establishing emergency-monitoring methods is an important tool for assessing environmental impacts. The hydrogen isotope tritium (^3H) exists in the environment in water and organic substances as organically bound tritium (OBT) and as tissue-free water tritium (TFWT) (Fig.1-20). To measure the beta particle emission and thus the tritium concentration of a sample, samples need to be converted to tritiated water. TFWT can be removed by a drying process; to recover OBT, processes need to be performed to convert it into TFWT, such as combustion. The Ministry of Education, Culture, Sports Science and Technology's (MEXT's) manual has been established as the standard measurement scheme of tritium in Japan. However, the pretreatment process requires time and technical ability, thus hindering the number of tests possible and decreasing the reliability of the measurements.

Therefore, to increase the reliability and number of possible measurements, a simple pretreatment method was developed with a detection limit of 1 Bq per kilogram of raw flounder using flounder off the coast of Fukushima Prefecture. In this simple, two-step process, a freeze-drying pretreatment process is first used to separate free water in the tissue; combustion is then used to turn organic matter into water. In the freeze-drying process (Fig.1-21(a)), one side of the sample was set to approximately 1 cm like cubes to increase the surface area and shorten the drying time. This allowed the drying process, originally taking

approximately two weeks, to be completed in four days. In the second step, the dried samples were combusted using a rapid combustion vessel (Fig.1-21(b)), which has rarely been used in Japan. This device allows for fast processing when there are few samples. Further, the water recovery, cooling, heating, and degassing processes from the vessel were simplified by focusing on the process of separating excess gas, thus it was confirmed that allowing the gas generated by combustion to be collected simultaneously without separating. These process improvements allowed the process to be shortened from approximately one week to approximately one day. In this system, burning a 10-g sample of dried flounder sample yields 5 ml of combustion water. Due to the lower limit of detection for tritium measured using a liquid scintillation detector and the weight loss due to drying, the obtained lower limit of detection of OBT in biological samples was 1 Bq/kg raw (Table 1-1).

To confirm its reliability, the developed rapid analysis method was used in an annual analysis comparison sponsored by OBT workshop.

At the request of the International Atomic Energy Agency (IAEA), technical guidance was given to IAEA engineers regarding the developed procedure and the installation and operation of the pretreatment equipment.

(Kenso Fujiwara)

Reference

Kuwata, H., Fujiwara, K. et al., Rapid Tritium Analysis for Marine Products in the Coastal Area of Fukushima, Radiation Environment and Medicine, vol.9, no.1, 2020, p.28-34.

1-11 How Does the Dose Rate Change after Decontamination?

— Effects of Land Use Type Revealed from Long-Term Monitoring Data —

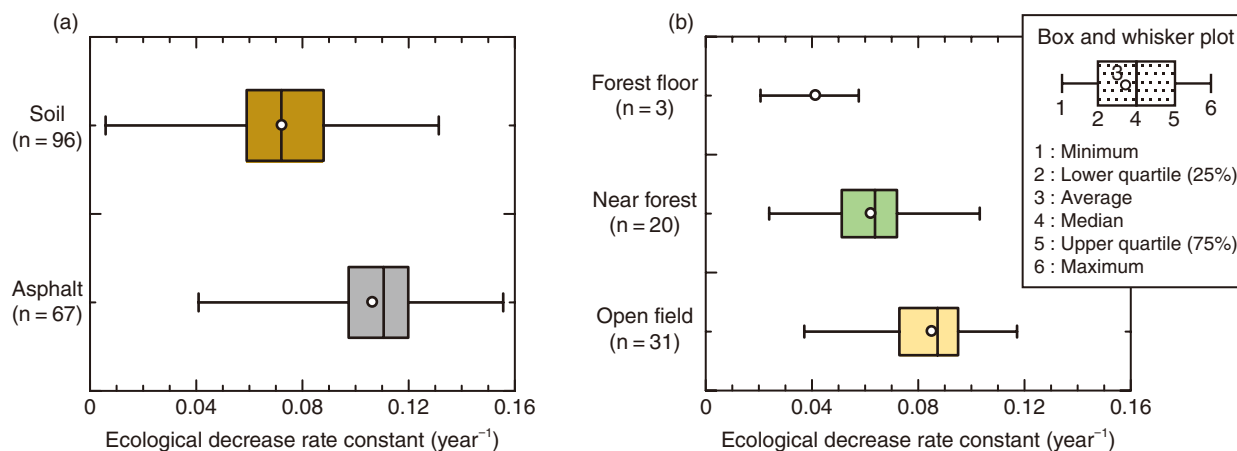


Fig.1-22 Distribution of the estimated ecological decrease rate constant

The air dose rate at all points decreased faster than the attenuation caused by radioactive decay of radioactive cesium. (a) The decrease in the air dose rate was higher on the asphalt pavement than on the soil. (b) The decrease in the air dose rate was lower near the forest than in an open field or on the soil's surface.

The decreasing trend of the ambient dose rate one meter above the ground (i.e., the air dose rate) after decontamination work and the factors affecting this decrease are expected to offer essential information that can be used to estimate and reduce any further public external exposure. The decreasing trends in air dose rates have been qualitatively evaluated across an extensive area around TEPCO's Fukushima Daiichi NPS (1F) using various monitoring methods after the 1F accident. The air dose rate decreased more quickly in residential areas than in paddy fields but more slowly than in forested areas. These results indicated that the land use type affects the change in the air dose rate. However, no quantitative assessment of the impact of human activities has yet been performed. A detailed dataset categorized by the characteristics (e.g. decontaminated, difficult-to-return, or restricted residence zones) is needed for such an assessment. This work therefore aimed to evaluate the effect of land use type on decontamination trends by analyzing the long-term decrease trend of the air dose rate in the decontaminated area in the evacuation zone around the 1F.

Six decontaminated fields in Kawamata Town, Namie Town, Kawauchi Village, Tomioka Town, Shimonogami and Ottozawa in Okuma Town were studied from November 2012 to November 2016. Air dose rates were measured periodically from each of the 163 locations at intervals of one to three months. As the factor of intercomparison, the ecological decrease rate constant was calculated by subtracting the physical decay rate of radioactive cesium (¹³⁴Cs and ¹³⁷Cs; RCs) during the survey period. The estimated ecological decrease rate constant ranged from 0.0058 to 0.16 (year⁻¹), thus indicating that the air dose rate in all areas

studied decreased faster than the physical half-lives of RCs.

To evaluate the effect of surface properties on the variation in the ecological decrease rate constant, the constants of the surface of the soil and the pavement were evaluated separately, as shown in Fig.1-22(a). The ecological decrease rate constant was significantly higher on the asphalt pavement than on the soil surface. This is consistent with the results of prior investigations following the 1F and Chernobyl Nuclear Power Plant accidents. These results suggest that the rapid decrease in air dose rate on the pavement probably resulted from the wash-off of RCs from the surface, indicating that the decrease of air dose rate was higher in the case of pavement wash-off than it was for the vertical penetration of RCs into the soil.

The distribution of the ecological decrease rate constant for the forest floor, areas near the forest, and open fields are shown in Fig.1-22(b). The ecological decrease rate constant increased with the distance from the forest, which included mixed broad-leaved forests and evergreen conifers. Immediately after the 1F accident, RCs were deposited on the canopy. The deposited RCs then gradually moved to the forest floor. Due to the additional source term, the ecological decrease rate constant in the forest is relatively slow. On the other hand, the RCs on the open field penetrated vertically into the soil, the ecological decrease rate constant was relatively fast.

The results of this study will be useful for predicting the long-term future external exposure dose of residents who returned after decontamination.

(Shigeo Nakama)

Reference

Nakama, S. et al., Temporal Decrease in Air Dose Rate in the Sub-Urban Area Affected by the Fukushima Dai-ichi Nuclear Power Plant Accident during Four Years after Decontamination Works, *Journal of Environmental Radioactivity*, vols.208–209, 2019, p.106013-1–106013-8.

1-12 Radiocesium Behavior in River System

— Relationship between Mineral Species and Radiocesium in Riverbed Using Microscopy —

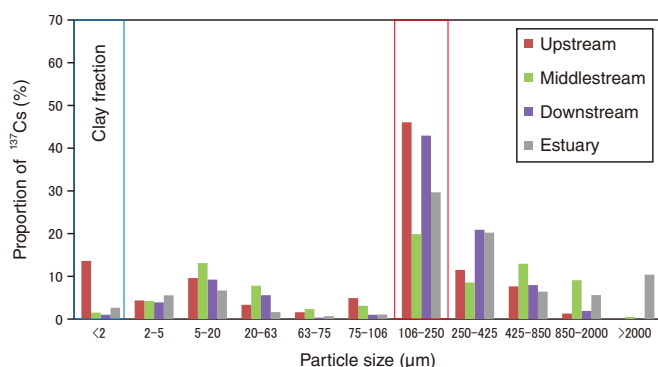


Fig.1-23 Ratio of ^{137}Cs in each size fraction to the total ^{137}Cs in the bulk sediment sampled from the upstream reservoir to the estuary

Fine sand (106–250 μm : red box in figure) contained the highest ^{137}Cs quantities. Unlike in previous studies, coarse fractions contained high levels of ^{137}Cs .

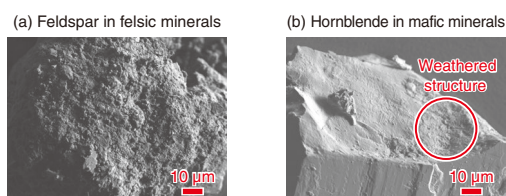
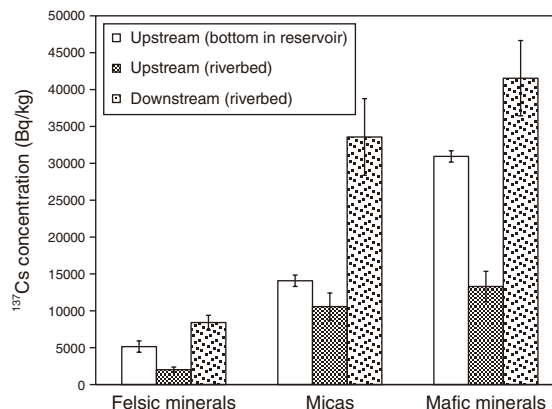


Fig.1-25 Morphological characteristic of the representative minerals hand-picked from the fine sand fraction using SEM
The surface of (a) feldspar in felsic minerals and (b) hornblende in mafic minerals were likely to be weathered.

Most of the radiocesium (^{137}Cs) emitted from the TEPCO's Fukushima Daiichi NPS accident was deposited into the river system, where it was transported by soil particles and redistributed in the downstream area. Identifying the dominant mineral species that have adsorbed ^{137}Cs is necessary to predict the elution from a mineral to river water and sedimentation behavior of ^{137}Cs . In this study, the relationship between the dominant mineral species that adsorb ^{137}Cs and the behavior of ^{137}Cs moving downstream from the upstream reservoir within the Tomioka river basin is clarified.

Some sediment samples were collected in the riverbed from the upstream to the downstream. The collected sediments were divided into 11 fractions by their size (i.e., according to their Wentworth grain size) via sedimentation and centrifugation. The radioactivity of ^{137}Cs in each fraction was determined using a germanium semiconductor detector. The contribution of ^{137}Cs in each size fraction to the total ^{137}Cs concentration in the bulk sediment was then calculated using the weight frequency of each fraction. The results indicate that the fine sand fraction (106–250 μm) in the riverbed sediments contained the largest ^{137}Cs quantities (Fig.1-23) due to the higher weight proportion of fine sand to other fractions. Thus, mineral species in the coarse-



(a) Felsic minerals (b) Micas (c) Mafic minerals

Fig.1-24 ^{137}Cs concentrations in each mineral and separated mineral obtained from the fine sand fraction at the riverbed and reservoir

The fine sand was separated into (a) felsic minerals, (b) micas, and (c) mafic minerals. Although previous studies have indicated that ^{137}Cs is poorly sorbed onto mafic and felsic minerals, ^{137}Cs was sorbed these minerals.

grain fraction except clay minerals strongly adsorbed ^{137}Cs .

The mineral species were then separated using morphological observations from the size-fractionated sediments to identify which mineral species strongly adsorb ^{137}Cs . Using a microscope and X-ray diffractometer, the mineral species were separated and identified as mafic minerals (hornblende, augite, and magnetite), as mica (vermiculite), as felsic minerals (quartz and feldspars) (Figs.1-24(a)–(c)). Micas, which have been reported to have adsorbed ^{137}Cs , and mafic minerals were demonstrated to have an equivalent ability to adsorb ^{137}Cs . The felsic minerals, which have been reported as poor adsorbers of ^{137}Cs , also contained ^{137}Cs . Scanning electron microscopy (SEM) demonstrated that the surface of the feldspars and hornblende has many fine particles and a flaky structure due to weathering (Fig.1-25), which may promote the sorption of ^{137}Cs . This study may contribute to clarifying the sorption and desorption mechanisms of ^{137}Cs on minerals for evaluating the transport of ^{137}Cs .

This work was performed in collaboration with Niigata University, entitled “Mineralogical study on behavior of radiocesium in environment”.

(Hiroki Hagiwara)

Reference

Hagiwara, H. et al., Mineral Composition Characteristics of Radiocesium Sorbed and Transported Sediments within the Tomioka River Basin in Fukushima Prefecture, *Journal of Environmental Radioactivity*, vol.211, 2020, p.106042-1–106042-10.

1-13 Cause of Radioactivity Concentration in Mushrooms

— Cesium Selectivity Evaluation of Mushroom Pigment Norbadione A —

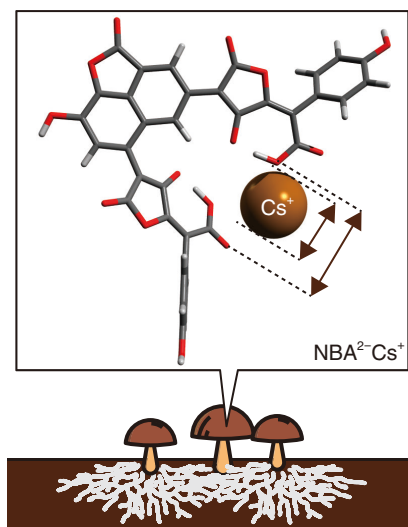


Fig.1-26 Radioactive cesium concentration mechanism in mushrooms

The brown pigment norbadione A, a scissor-like molecule, binds cesium ions. The binding becomes more stable when the scissor spacing matches the cesium ion diameter.

Radiocesium (Cs) released by the accident at the TEPCO's Fukushima Daiichi Nuclear Power Station has been reported to be partly retained in fungi, lichens, and trees in forests, and particularly concentrated in mushrooms. The concentration of Cs in mushrooms was noticed after the Chernobyl nuclear plant accident, with high concentrations observed around the pigments contained in the mushroom cups. One representative mushroom pigment molecule is norbadione A (NBA; $C_{35}H_{18}O_{15}$), which is the predominant pigment of the Bay Boletus in Europe and the Pisolithus arrhizus in Japan's pine forests. Norbadione A is known to bind with Cs (see Fig.1-26), and has been investigated experimentally and via molecular dynamics simulations to clarify its selective binding mechanism. Here, the selective binding mechanism was attributed to the scissor-like molecular structure of norbadione A.

In this study, state-of-the-art quantum chemical computational techniques were used to calculate the structure of norbadione A, the free energy of formation of the binding between norbadione A and Cs, and the binding free energy between norbadione A and Cs, which characterizes the binding strength in

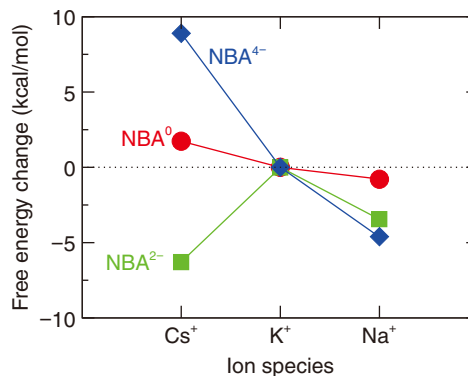


Fig.1-27 Free energy change for alkali-metal ion exchange of norbadione A in water

The change in free energy $\Delta G_{\text{aq}}^{\text{exc}}$ associated with replacing potassium bound with norbadione A to with cesium and or sodium. Three forms are considered: NBA⁰ with no dissociated hydrogen ions (H⁺), NBA²⁻ with two dissociated H⁺, and NBA⁴⁻ with four dissociated H⁺. A negative $\Delta G_{\text{aq}}^{\text{exc}}$ indicates a transformation to a more stable form.

a living body (i.e., in water). As potassium is generally abundant in living bodies and binds with norbadione A, the possibility of cesium concentration can be evaluated by calculating the free energy change associated with replacing a potassium ion with a Cs ion. The results demonstrated that NBA²⁻, norbadione A with two dissociated hydrogen ions, binds more stably with a Cs ion than with potassium or sodium ions (Fig.1-27). This indicates that cesium is selectively bound with norbadione A. For most other biomolecules, potassium binding is more stable than Cs binding, whereas Cs binding is more stable than potassium binding for norbadione A. This anomaly is likely owing to the scissor-like molecular structure of norbadione A; the scissor spacing matches the cesium ion diameter, as shown in Fig.1-26. Several mushroom pigments are known to have scissor-like molecular structures such as norbadione A and badione A; their characteristic scissor-like structures may be one reason for the high concentration of Cs in mushrooms.

This research was conducted using the supercomputer SGI ICE X in the JAEA.

(Hiroya Suno)

Reference

Suno, H. et al., Quantum Chemical Calculations for the Norbadione A Complexes with Cs⁺, K⁺, and Na⁺ in Gas and Aqueous Phases, Chemical Physics Letters, vol.730, 2019, p.26-31.

1-14 Estimation of Total Radiocesium Discharged from Fukushima Daiichi NPS to the Coast

— Discharge Inventory Decreased to Approximately 1/100000th Since the Accident —

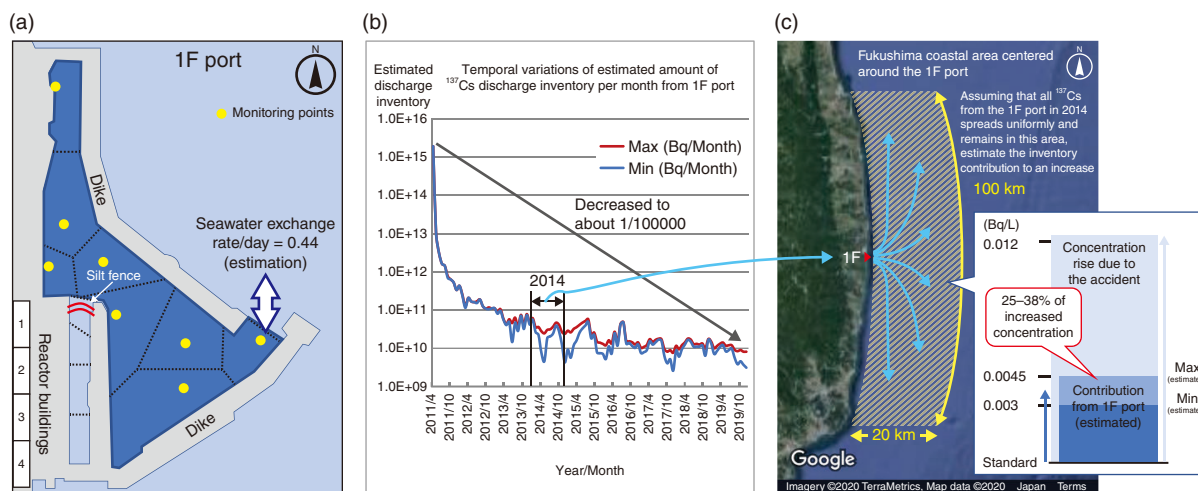


Fig.1-28 (a) Schematic of the Fukushima Daiichi NPS (1F) port, (b) temporal variations of estimated ^{137}Cs discharge per month from the 1F port and (c) 20 km (east–west) and 100 km (north–south) coastal area around the 1F port

(a) The concentration of ^{137}Cs in seawater has been monitored (yellow dots) inside the 1F port since 2013 and the concentration data have been published nearly every day. The black dotted lines represent the borders of the Voronoi cells obtained by using Voronoi tessellation for a set of the monitoring points. (b) The estimated monthly discharge decreased to approximately 1/100000th of that in the early stage of the accident. (c) Assuming that all ^{137}Cs from the 1F port in 2014 spread uniformly and remains in the coastal area, the inventory discharge is estimated to contribute an increase of 0.003 to 0.0045 Bq/L. Since the observed concentration in the sea area was increased by 0.012 Bq/L due to the accident, the contribution of the ^{137}Cs from the 1F port to the concentration rise is approximately 25% to 38%.

Radionuclides (notably, ^{137}Cs) were released into the environment by the accident at the TEPCO's Fukushima Daiichi NPS (1F). Some rose into the atmosphere and fell on the ground and sea, whereas others were discharged directly into the ocean as contaminated water. Just after the accident, radionuclide concentration of seawater increased near the 1F port due to the direct discharge. However, since the direct discharge was suppressed by the Japanese government and TEPCO, the observed concentrations then decreased rapidly; current concentrations are very low. This work therefore scientifically estimated the amount of ^{137}Cs released from the initial stage of the accident to the present and evaluate the impact on the environment.

As most radionuclides released into the ocean were assumed to be from the 1F port, the amount of ^{137}Cs in the port was focused on. Since the concentration is monitored daily at the eight points shown in Fig.1-28(a), the 1F port was divided into eight areas using the Voronoi tessellation method. The amount of ^{137}Cs in each area was calculated by multiplying the volume of seawater by the observed concentration of ^{137}Cs in each area. When the observed concentration is below the detectable limit, the true concentration is between zero and the detectable limit;

therefore, the total amount of ^{137}Cs inside the 1F port (shown in Fig.1-28(a)) was estimated with the interval from zero to the detectable limit. Thus, the daily discharge inventory was estimated by multiplying the estimated total amount in the port and 0.44, which is the seawater exchange rate between the inside and outside of the port. This rate was estimated from the concentration decrease observed in the early stages of the accident. The monthly discharge inventory of ^{137}Cs from the port from April 2011 to March 2020 is shown in Fig.1-28(b). The results indicate that by 2018 the discharge inventory had decreased to approximately 1/100000th of that in the initial stages of the accident.

Assuming that all ^{137}Cs discharged from the port in 2014 spread uniformly and remained in the coastal area surrounding 1F (Fig.1-28(c)), its contribution to the concentration rise was evaluated to be approximately 25% to 38%. However, this is likely to be an overestimate, as ^{137}Cs is spread further than this area. This indicates a greater contribution of other sources (such as run-off from rivers) to the increase in the coastal concentration, and a lesser contribution of the 1F port.

(Susumu Yamada)

Reference

Machida, M., Yamada, S. et al., Seven-Year Temporal Variation of Cesium-137 Discharge Inventory from the Port of Fukushima Dai-ichi Nuclear Power Plant: Continuous Monthly Estimation of Cesium-137 Discharge in the Period from April 2011 to June 2018, Transactions of the Atomic Energy Society of Japan, vol.18, issue 4, 2019, p.226–236 (in Japanese).

1-15 Reconstruction of Atmospheric Release and Dispersion of Radioactive Materials by Computer Simulation

— Contribution to the Refinement of Dose Assessment in the Early Stage of the Accident by Improving the Dispersion Calculation Optimization Method —

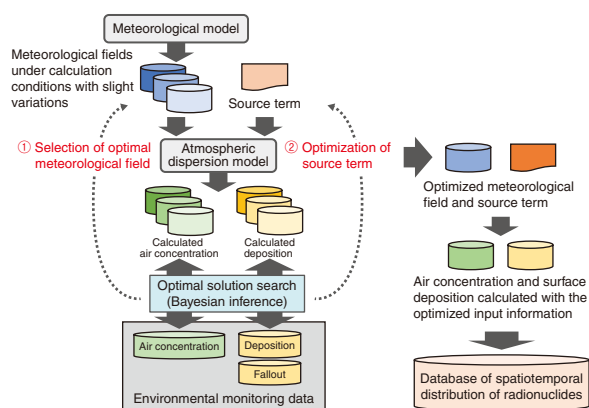


Fig.1-29 Optimization method of atmospheric dispersion calculation

The developed method combines the ensemble meteorological calculation, which creates a lot of slightly different meteorological fields, and the Bayesian inference, which statistically searches the optimum solution. This method makes it possible not only to optimize the source term but also to improve the reproducibility of the meteorological field.

To evaluate the radiological dose to the public resulting from the accident at the TEPCO's Fukushima Daiichi NPS (1F), especially in the early stage when the measured data are limited, it is necessary to reconstruct the spatiotemporal distribution of radioactive materials in the environment by atmospheric dispersion simulations. In such simulations, the atmospheric transport and surface deposition of radioactive materials are calculated using calculated meteorological fields (wind, precipitation, etc.) and the source term of the radioactive materials. In the previous studies, the reproducibility of meteorological simulations using a data assimilation method was not sufficient due to the lack of measured data, being a cause of uncertainty in the calculated radioactive plume. Thus, when estimating the source term from the comparison of dispersion calculations and environmental monitoring data, it was necessary to correct dispersion calculations and select monitoring data with a subjective evaluation based on expert knowledge and experiences.

In this study, we succeeded in optimizing source term using a statistical method, Bayesian inference, by improving the reproducibility of the meteorological simulation by feeding back the comparison results of dispersion calculation results and environmental monitoring data (Fig.1-29). First, many meteorological fields were created by many meteorological calculations with slightly different initial conditions. Based on Bayesian inference using the dispersion calculation results using various meteorological fields and the ^{137}Cs air concentration measurements such as hourly data by analysis of suspended particulate matter (SPM) at many monitoring stations, the

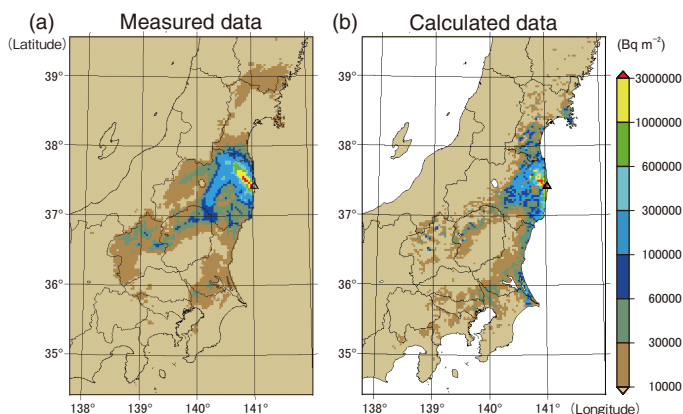


Fig.1-30 Surface deposition distribution of ^{137}Cs

The reproducibility of the ^{137}Cs surface deposition on April 1, 2011 was evaluated by comparing the calculated data (b) with the data measured by an airborne survey (a). A large amount of deposition was reproduced to the northwest of the 1F (Δ), the central part of Fukushima Prefecture, and the Kanto region.

optimum meteorological field (i.e., that best reproduces the radioactive plume movement) was selected (① in Fig.1-29). Next, the source term estimated by the previous study was optimized using Bayesian inference, which uses the dispersion calculation results with the optimum meteorological field and various environmental monitoring data such as air concentration, surface deposition map and daily fallout (② in Fig.1-29).

This optimized dispersion calculation was validated using environmental monitoring data of ^{137}Cs . Comparing the air concentration with the SPM data indicated that the percentage of calculated values within 1/10 to 10 times the observed values improved to 47.3% from 35.9% in the previous study. The simulation successfully reproduced the distribution of the surface deposition observed by airborne survey (Fig.1-30) and the calculated ^{137}Cs deposition amount on land was 2.1×10^{15} Bq, closer to the observed 2.4×10^{15} Bq than the results by the previous study of 3.7×10^{15} Bq.

A database of the spatiotemporal distribution of major radionuclides (^{131}I , ^{134}Cs , ^{137}Cs , ^{132}Te) in the environment was then constructed using the optimized source term and dispersion calculation. This database was used for a comprehensive dose assessment along with the behavioral pattern of evacuees and contributed to the refinement of the dose estimate in a Japanese dose assessment project.

This research includes the results of the FY2018 research on the health effects of radiation, supported by the Ministry of the Environment of Japan (MOE).

(Hiroaki Terada)

Reference

Terada, H. et al., Refinement of Source Term and Atmospheric Dispersion Simulations of Radionuclides during the Fukushima Daiichi Nuclear Power Station Accident, Journal of Environmental Radioactivity, vol.213, 2020, p.106104-1–106104-13.

1-16 Initial Air Dose Rate after the Accident at the Fukushima Daiichi NPS

— Comparison between Fukushima and Chernobyl —

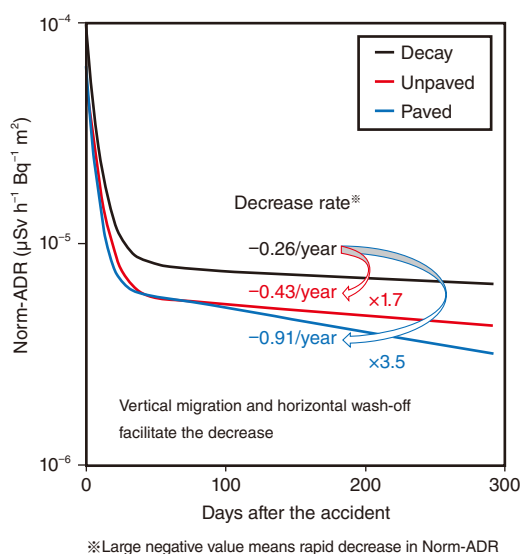


Fig.1-31 Decrease in Norm-ADR of monitoring data (“Unpaved” and “Paved”) and “Decay”

The faster decrease in the Norm-ADR of observed data than of the radionuclide decay indicates that the decrease was facilitated by vertical penetration and horizontal wash-off of radionuclides. The different decrease rate between the paved and unpaved regions demonstrates the difference in the radionuclide’s migration based on land use.

The air dose rate (ADR) is an important quantity that is used to estimate the public exposure. However, the decrease in ADR and the factors contributing to this decrease during the initial period after the TEPCO’s Fukushima Daiichi NPS accident have not been studied. In this work, collected ADR data from Fukushima Prefecture in 2011 with fine temporal resolution were analyzed to evaluate the time dependency of the ADR.

To analyze the data across various monitoring sites with different deposition levels, the ADR was normalized by dividing it by the initial deposition amount of ^{137}Cs . The normalized data (norm-ADR) were categorized into two data sets: unpaved areas ($\geq 50\%$ covered by grassland and bush) and paved areas ($\geq 50\%$ covered by paved surfaces and buildings). The resulting time dependencies of the norm-ADR of the unpaved and paved areas, in addition to the decrease due to radionuclide decay, are shown in Fig.1-31. All situations of the norm-ADR decreased rapidly immediately after the accident, followed by a slower decrease. The rapid decrease during the initial period was mainly due to the decay of ^{131}I and ^{132}I (with half-lives of 8 days and 2.3 hours, respectively). The norm-ADR of the observed data decreased faster than the decay of radionuclides after the initial period, and the norm-ADR decreased faster in paved regions than in unpaved regions (paved and unpaved in Fig.1-31,

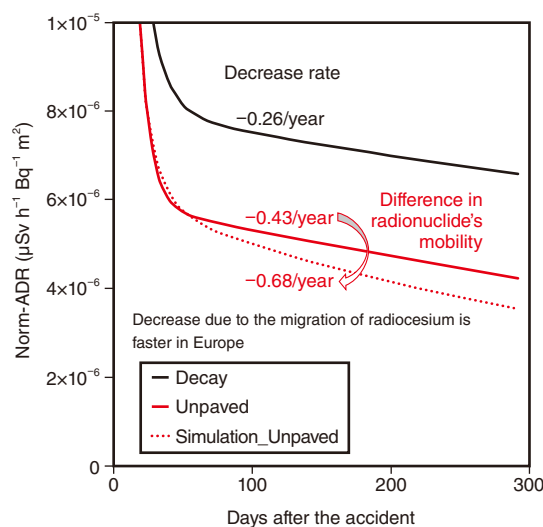


Fig.1-32 Decrease in Norm-ADR of observed data “Unpaved” and simulated result “Simulation_Unpaved”

To compare the decrease trend between Fukushima and Chernobyl, Norm-ADR was calculated from the radionuclide’s composition in Fukushima and decreased with the rate observed in Europe (Simulation_Unpaved). The slower decrease in “Unpaved” suggests less mobility of radionuclides in Fukushima than in the Chernobyl area.

respectively). These results indicate that the decrease in the ADR is facilitated by radionuclide migration in the environment (e.g., vertical penetration and horizontal wash-off), and that this effect depends on the surface. Since urban areas are largely covered by impermeable components such as roads, their ADR was inferred to decrease more rapidly than other unpaved areas such as agricultural fields and forest, reducing the exposure of local residents.

The decrease in the ADR due to the migration of radionuclides has been studied extensively in Europe after the Chernobyl Nuclear Power Plant accident. To compare the decrease rate between Fukushima and Europe, the decrease in the norm-ADR was simulated based on the decrease rate observed in Europe and using the radionuclide’s composition in Fukushima. The results, summarized in Fig.1-32, demonstrated a faster decrease in the Norm-ADR simulated unpaved surface using data from the Chernobyl area (Simulation_Unpaved) than the unpaved regions of Fukushima. This results suggest that the radiocesium migration associated with the decrease in the ADR was less in Fukushima than in the Chernobyl area.

These results will help to retrospectively estimate the ADR and exposure of local residents.

(Kazuya Yoshimura)

Reference

Yoshimura, K. et al., Initial Decrease in the Ambient Dose Equivalent Rate after the Fukushima Accident and Its Difference from Chernobyl, Scientific Reports, vol.10, 2020, p.3859-1–3859-9.

1-17 Analyzing Decreasing Trends in Radioactivity and Dose Rate

— Changes of Radiocesium Concentration in Soil and Air Dose Rate over Five Years —

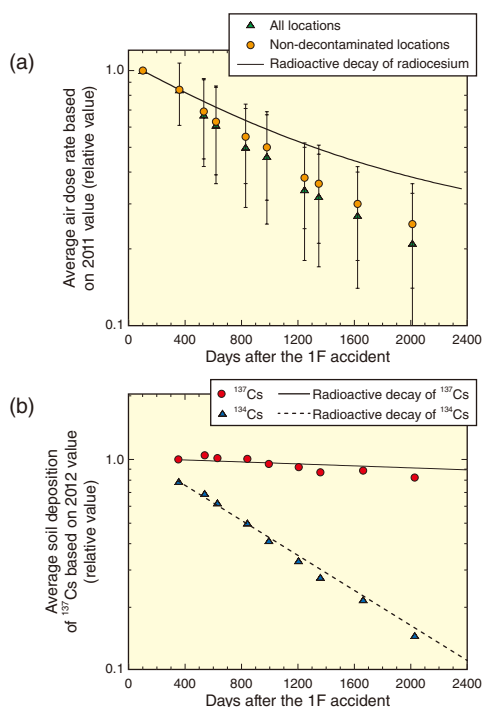


Fig.1-33 Temporal changes of air dose rate and radiocesium soil deposition based on the fixed-points survey (relative value)

(a) Air dose rate without the contribution of natural radiation; (b) ^{134}Cs and ^{137}Cs soil deposition at non-decontaminated locations.

After the accident at the TEPCO's Fukushima Daiichi NPS (1F), the government announced a policy to create radiation and radioactive materials distribution maps based on land monitoring. In June 2011, maps of the air dose rate distribution were completed and disseminated based on measurements taken from approximately 2200 locations (fixed-point survey) in Fukushima Prefecture mainly within an 80 km-radius area from the 1F using survey meters at non-paved and undisturbed areas in cooperation with universities, research institutes, etc. From 2012 to 2016, the fixed-point survey continued and was expanded by increasing the number of measurement locations to approximately 6500, mainly within the 80-km area surrounding the 1F. The average air dose rate from the fixed-point survey decreased annually, as shown in Fig.1-33(a). Maps of the air dose rate distribution generated from the observed data confirm that areas with relatively high dose rates are shrinking (see Fig.1-34). Furthermore, the rate of decrease of the dose rate was greater than the rate due to the radioactive decay of radiocesium considering both ^{134}Cs and ^{137}Cs . If the air dose rate decreases according to the radioactive decay, in 2016 it will be approximately 37% of the value in June 2011. However, the air dose rate decreased further, to approximately 24% of the original value at non-decontaminated locations. In addition, the average air dose rate at all locations, including the decontaminated locations, decreased to approximately 19% of the original value; thus, the average air dose rate has been reduced to about half of the expected value in the case of only radioactive decay. This is due in part to human activities including decontamination work.

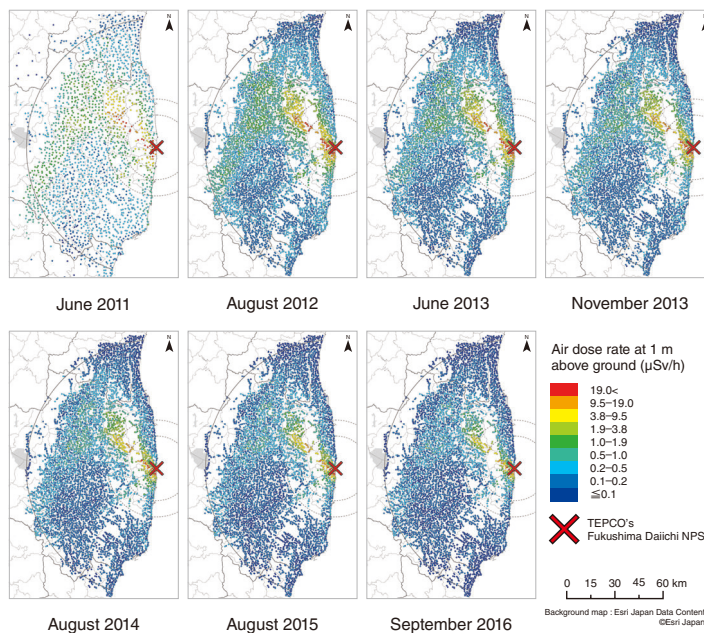


Fig.1-34 Air dose rate distribution maps based on the fixed-point survey since 2011 (including contribution of natural radiation)

The areas with relatively high dose rates indicated by red, yellow and green, have been shrinking gradually.

The amount of radioactive material deposited on the soil (soil deposition) in open spaces with little artificial disturbance was measured in situ using portable germanium semiconductor detectors each year since 2012 across approximately 380 locations within an 80-km area surrounding the 1F to analyze the temporal changes. As shown in Fig.1-33(b), the average soil deposition of ^{134}Cs and ^{137}Cs measured at the non-decontaminated locations decreased following the trend of the corresponding radioactive decay.

This seemed to contradict the lower air dose rate found at the non-decontaminated locations than the radioactive decay of radiocesium. The excess reduction of the air dose rate over the radioactive decay was 0.65 ($= 0.24/0.37$). When the slight migration of radiocesium in the depth direction during this period is taken into consideration, the analysis results show that the air dose rate decreased by approximately 0.7 times due to the radiation shielding effect of soil. Thus, the air dose rate decreases faster than the soil deposition decrease rate because the gamma rays are blocked by the penetration of radiocesium in the soil in the depth direction, not by the horizontal migration of the radiocesium.

This research is part of the results by consignment project conducted on “Aggregation of radioactive material distribution data associated with TEPCO Fukushima Daiichi Nuclear Power Station accident in FY2016”, supported by the Nuclear Regulation Authority (NRA), Japan.

(Satoshi Mikami)

Reference

Mikami, S. et al., The Deposition Densities of Radiocesium and the Air Dose Rates in Undisturbed Fields around the Fukushima Dai-ichi Nuclear Power Plant; Their Temporal Changes for Five Years after the Accident, *Journal of Environmental Radioactivity*, vol.210, 2019, p.105941-1–105941-12.

1-18 Assessment of External Exposure Doses in Daily Life

— Development of Assessment Model Based on Local Radiation Surveys —

Table 1-2 Time spent in various locations and dose reduction factor

Time spent various locations per day (h)		Indoor worker (N = 273)	Outdoor worker (N = 324)
Inside	Wooden house	17.2±1.5	15.8±2.1
	Concrete building	6.1±0.6	0.9±0.7
Outside		0.7±0.5	7.3±2.7

Dose reduction factor	
Wooden house	0.28±0.02 (2011–2014) 0.36±0.07 (after 2015)
Concrete building	0.14–0.18*

* The details of the DRF for concrete buildings can be found in the footnotes.

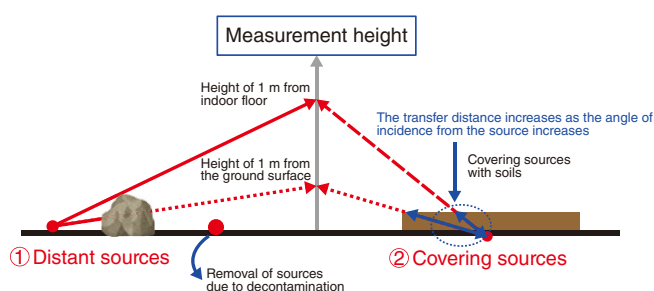


Fig.1-35 Distribution of radiation sources after decontamination
If decontamination is performed, the contributions from ① distant sources and ② covering sources increase.

External exposure from radionuclides deposited on the ground surface has been the dominant exposure pathway for humans in the area affected by the accident at TEPCO's Fukushima Daiichi NPS. To assess the doses from this pathway, it is necessary to clarify (i) exposure rates and (ii) the time spent in various locations in daily life.

In this study, locations were classified into three types: inside a wooden house, inside a concrete building, and outside. Under this classification, the time spent by residents in these locations in the city of Fukushima was studied. In addition, to evaluate the dose reduction factor (DRF), the ambient dose equivalent rate was measured inside and outside the houses. Furthermore, a personal dosimeter was distributed to the survey participants, and individual doses were measured.

From these measurements and surveys, the time spent in each classified location and the DRF for Japanese wooden houses were clarified; a summary of the results is shown in Table 1-2. The DRF is defined as the ratio of the ambient dose equivalent rate measured inside to that measured outside a house. All indoor and outdoor measurements were performed 1 m above the floor and above the ground surface, respectively.

The ambient dose equivalent rates measured indoors and outdoors decreased by decontamination. Further, the DRFs increased after 2015, when decontamination in Fukushima was generally completed, due to the increased contribution of distant or covered radiation sources. As described in Fig.1-35, radiation from these sources is shielded by obstacles on the ground or ground covering (e.g., soil). The shielding effect decreases as

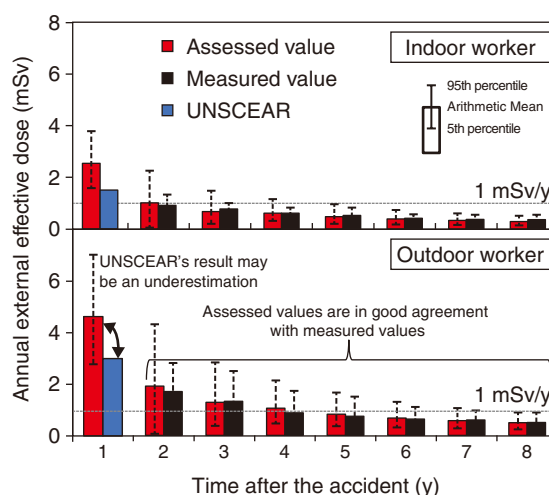


Fig.1-36 Comparison of assessed values with measured values and with UNSCEAR's assessment

The assessed values were in good agreement with measured values, thus verifying the developed model.

the angle of incidence from the source increases. Therefore, when decontamination is performed, the decrease of dose rate measured 1 m above the indoor floor is less than that measured 1 m above the ground surface. Thus, the DRF increased after decontamination.

Doses to the public were assessed using the results shown in Table 1-2 as the product of the ambient dose equivalent rate and the time spent in each location. The dose rate for each location was calculated by multiplying the observation results of the ambient dose equivalent rate measured outside by the DRF.

The results of the developed dose assessment model are presented and compared with the measured data and the results of United Nations Scientific Committee on the Effects of Atomic Radiation (UNSCEAR)'s project in Fig.1-36. As the assessment results are in good agreement with the measured values in Fukushima, the developed model was validated. In comparing the developed model to the results provided by UNSCEAR, their result may be an underestimation, as the UNSCEAR assessment used a value of 0.15 as a DRF for wooden houses in the first year after the accident. Finally, in comparison with the national long-term dose target of 1 mSv/y, no participants exceeded this dose in Fukushima eight years after the accident, based on the results of the measured values and developed model.

(Shogo Takahara)

* Furuta, T., Takahashi, F., Study of Radiation Dose Reduction of Buildings of Different Sizes and Materials, *Journal of Nuclear Science and Technology*, vol.52, issue 6, 2015, p.897–904.

Reference

Takahara, S. et al., Assessment Model of Radiation Doses from External Exposure to the Public after the Fukushima Daiichi Nuclear Power Plant Accident, *Health Physics*, vol.118, issue 6, 2020, p.664–677.

Implementing Continuous Improvements in Safety and Emergency Preparedness

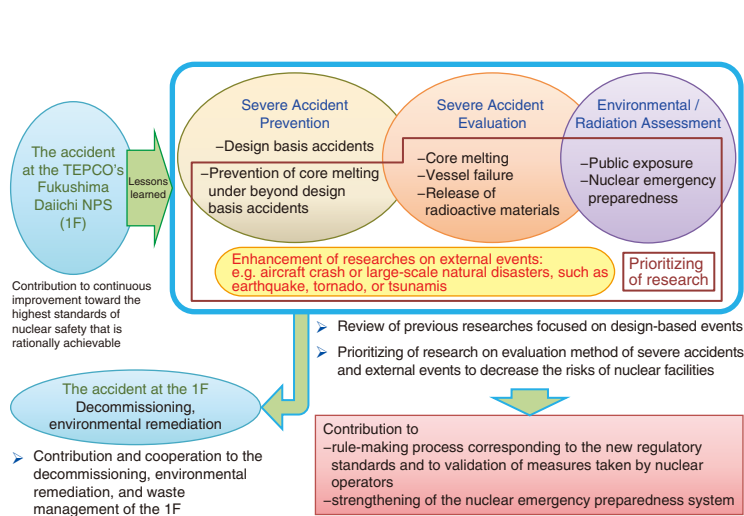


Fig.2-1 Directions of activities at the Sector of Nuclear Safety Research and Emergency Preparedness

In accordance with the lessons learned from the accident at 1F, we have promoted studies on severe-accident prevention efforts, nuclear-emergency-preparedness, and environmental-impact assessments have been performed, as have safety assessments for design-basis events.

The Sector of Nuclear Safety Research and Emergency Preparedness aims to perform advanced safety research from a long-term viewpoint to provide a technical basis for nuclear safety assessments through calculations, experiments, and measurement techniques, as well as technical support for nuclear regulatory authorities. These efforts contribute to the development of safety criteria and/or guidance, and supports to update safety regulations with continuous improvement of safety.

Our previous research focused on design basis events before the accident at the TEPCO's Fukushima Daiichi NPS (1F) was carefully reviewed in accordance with the lessons learned from the accident, as shown in Fig.2-1. To reduce the risks associated with operating nuclear facilities and its uncertainties, a variety of research activities, such as the prevention and mitigation during the progression of severe accidents, the assessment of external events, preparation for and in response to emergency situations, and nuclear criticality safety assessment of fuel debris related to the 1F accident, have been expanded and prioritized.

Large-scale facilities have thus been constructed thanks to external funding. For example, the high pressure thermal-hydraulic loop (HIDRA) shown in Fig.2-2 was constructed under contract with the Nuclear Regulation Authority, and has since been used to develop further sophisticated evaluation techniques for the core heat transfer. The Nuclear Safety Research Reactor (NSRR) shown in Fig.2-3, has been used to investigate the fuel failure limit, and the effect of fuel failure on the nuclear reactor during reactivity-initiated accidents (RIAs), which is a design-basis accident used to evaluate the safety of a nuclear reactor. To improve the safety of light-water reactors, we are also playing a role of the operating agent at the OECD/NEA project of "Analysis of Information from Reactor Buildings and

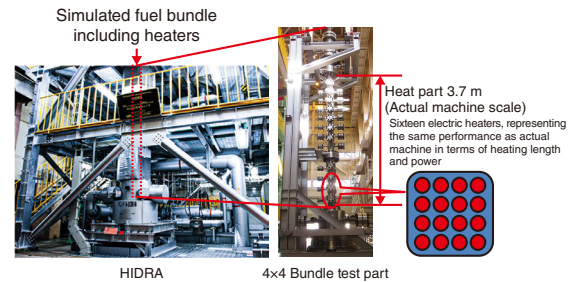


Fig.2-2 High pressure thermal-hydraulic loop (HIDRA)

The HIDRA experiments provide data on reactor core cooling performance under severe thermal hydraulic conditions beyond the design basis.

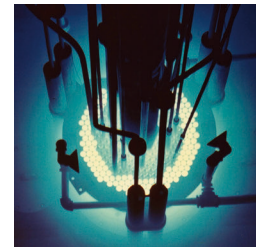


Fig.2-3 Nuclear safety research reactor (NSRR)

The experiment which simulates a rapid power increase during a reactivity-initiated accident can be safely performed.

Containment Vessels of Fukushima Daiichi NPS (ARC-F)". In addition, several studies on material degradation, structural integrity of components important for safety, and ultra-trace analysis of nuclear materials for nuclear safeguards, among others, have been performed.

To investigate emergency preparedness, the effectiveness of radiation protection countermeasures of shelters has been evaluated, as has the performance level required for nuclear emergency response materials/equipment. Moreover, techniques to integrate monitoring data obtained by different methods and to investigate radioactivity distributions in coastal regions around 1F are under development. Domestic nuclear power plants are now monitored for background activity in preparation for nuclear emergencies.

This chapter presents the results of recent research on the following topics: Measurement technique for evaluating reactor core cooling performance under severe thermal-hydraulic condition (Topic 2-1), Mechanical properties of fuel cladding under RIA conditions (Topic 2-2), Environmentally assisted cracking of stainless steel under BWR primary coolant condition (Topic 2-3), Risk evaluation considering large aftershock (Topic 2-4), Clogging behavior of a HEPA filter during the solvent fire at a reprocessing facility (Topic 2-5), and Emergency monitoring technique using aircraft (Topic 2-6).

Moreover, three topics related to the analysis of accident sequences in units 1 to 3 in 1F (Topic 1-8), the temporal change of radioactivity distribution for five years after the 1F accident (Topic 1-17), and the estimation of exposure dose for residents after 1F accident (Topic 1-18) are described in Chapter 1.

2-1 Measurement of Very Thin Liquid Film Thickness

— Technical Development for the Evaluation of Liquid Film Dryout Behavior —

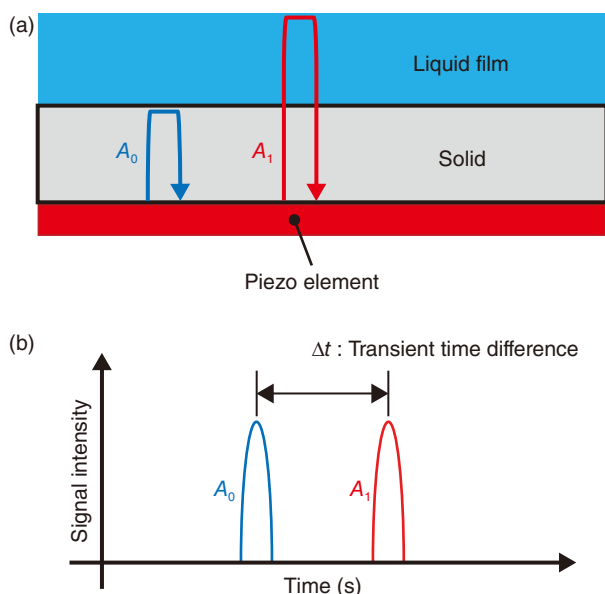


Fig.2-4 Conceptual design of liquid film thickness measurement technique using ultrasound

(a) An emitted signal from a piezo element is reflected from the solid-liquid interface (A_0) and the liquid film surface (A_1) and received by the piezo element. (b) The liquid film thickness can be calculated by measuring a transient time difference between the signals and sound speeds in the media.

In a light water reactor (LWR), if the core power suddenly rises, evaporation from the liquid film covering the fuel cladding increases rapidly, causing the liquid film to be depleted and the cladding surface to be exposed. This phenomenon, known as dryout, causes an increase in the surface temperature of the fuel cladding. In most cases, dryout is temporary, and eventually the cladding surface is covered with the liquid film again due to a decrease of core power. This behavior, known as rewetting, is an important phenomenon from the viewpoint of ensuring the fuel integrity.

Prior researchers have monitored the liquid film thickness by measuring the cladding surface temperature or have investigated the behavior of the liquid film during dryout and rewetting. The liquid film thickness at dryout and rewetting is considered to be 0.1 mm or less for actual LWR condition. There was no technique to measure such thin liquid film under high pressure and high temperature condition. Therefore, in this study, we aim to develop a non-intrusive and high-precision thin liquid film measurement technique using ultrasound.

For this purpose, the first goal was set to measure the thickness of a liquid film less than 0.1 mm in thickness with high accuracy. In the liquid film thickness measurement using ultrasound, as shown in Fig.2-4(a), ultrasound waves are emitted from a piezo element mounted outside of the solid wall toward the liquid film existing on the opposite side of the mounting surface. The liquid film thickness can be calculated based on the sound speed and the transient time difference between the waveforms reflected

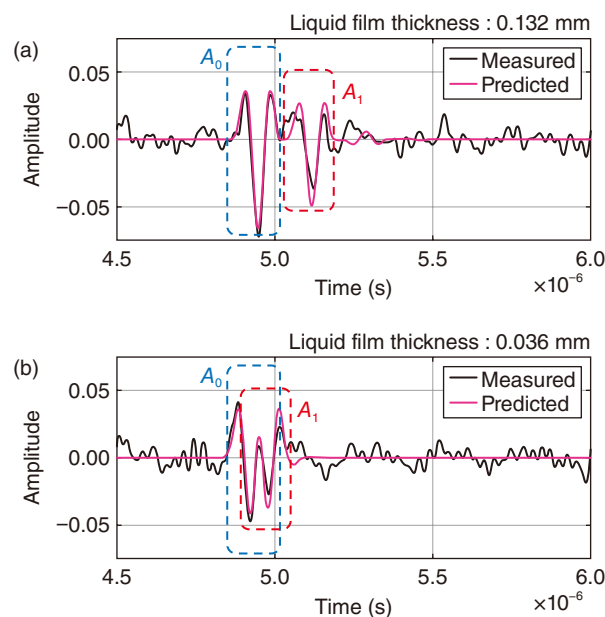


Fig.2-5 Received signals using the developed device to measure the liquid film thickness

Resulting waveforms of liquid film thickness measurement of (a) 0.132 and (b) 0.036 mm, where the solid black and magenta lines indicate the measured and predicted signal, respectively. The predicted signal is in good agreement with the measured signal, thus confirming that the proposed technique can accurately measure liquid films less than 0.1 mm in thickness.

from the solid-liquid interface and the liquid film surface (A_0 and A_1 , respectively), as shown in Fig.2-4(b).

For the accuracy even for measuring very thin liquid films, high frequency and high damping ratio are required for the carrier signal, which was the biggest development factor in this study. We have developed a device that generates ultrasound waves at a frequency approximately 10 times that of device applied in conventional study with a high damping ratio so that the emitted waveform is near a single pulse waveform. The resulting waveforms detected when measuring the film thickness, shown in Fig.2-5, shows two distinct waveforms, indicated by the dashed red and blue lines. These waveforms correspond to the reflected waveforms indicated in Fig.2-4. Here, a clearer separation of the two waveforms allows for a more accurate measurement; for very thin liquid films, the two waveforms may partially overlap, as shown in Fig.2-5(b). To address this issue, we have developed a liquid film thickness evaluation method using the predicted signal that matches the measured signal by ultrasound propagation analysis. The signal predicted by the proposed method is confirmed to match the measured signal, as shown in Fig.2-5.

Currently, this technique is available only at atmospheric pressure and room temperature. Efforts to make the necessary technical developments enabling liquid film measurement under actual LWR conditions are ongoing.

(Yuki Wada)

Reference

Wada, Y. et al., Ultrasound Measurement of Upward Liquid Film Flow in Vertical Pipe, Proceedings of 18th International Topical Meeting on Nuclear Reactor Thermal Hydraulics (NURETH-18), Portland, U.S.A., 2019, p.4518-4531, in USB Flash Drive.

2-2 Reliable Safety Evaluation for Reactivity-Initiated Accidents

— Mechanical Property Evaluation of Fuel Cladding under Biaxial Stress Conditions —

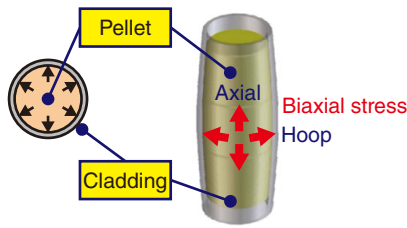


Fig.2-6 Anticipated stress state of nuclear fuel cladding during reactivity-initiated accidents (RIAs)

Pellet–cladding mechanical interaction (PCMI) during RIA induces a biaxial stress state, including tensile forces in both the axial and hoop directions of the fuel cladding.

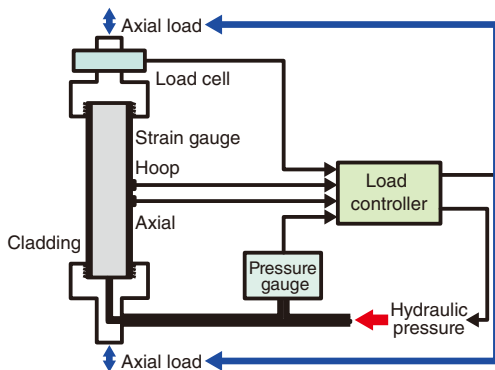


Fig.2-7 Biaxial tensile testing machine

Internal pressure and axial tension are simultaneously applied to a cladding specimen. A dedicated load controller provides a fully controlled stress ratio (axial/hoop) during testing.

Reactivity-initiated accidents (RIAs) must be addressed during the safety design evaluation of light-water reactor facilities. In an RIA, a control rod ejection or drop triggers a fast rise in reactor power. Fuel pellets are then heated and thermally expanded, resulting in pellet–cladding mechanical interaction (PCMI), during which pellets rapidly push against the cladding (see Fig.2-6). This may lead to mechanical failure of the cladding. Since the safety of this event is based on the number of failed fuel rods, the reliability depends on the accuracy of the fuel failure limit adopted. Although the failure limit has been thought to be affected by the biaxial stress state, i.e., the simultaneous tensile forces in both the axial and hoop directions in the cladding, little systematic data acquired under mechanical conditions relevant to PCMI have been made available.

A biaxial tensile testing machine enabling precise control of the “stress ratio” (i.e., the ratio of axial stress to hoop stress) originally developed by Kuwabara et al.* was therefore modified and applied to a cladding specimen, as shown in Fig.2-7. The modification involved the design of a new jig to hold the tube specimen and a control program. Implementation allowed for data of Zircaloy-4 cladding deformation behavior to successfully be obtained for stress ratios from 0.5 to 1, which includes RIA conditions. The resulting relationship between the stress ratio and extended plastic deformation level is shown in Fig.2-8.

Plastic strain (measure of cladding deformation whose accumulated plastic work is equivalent to that in the case of a uniaxial tensile condition at a given plastic strain)

● 0.002 ▼ 0.01 ◆ 0.02

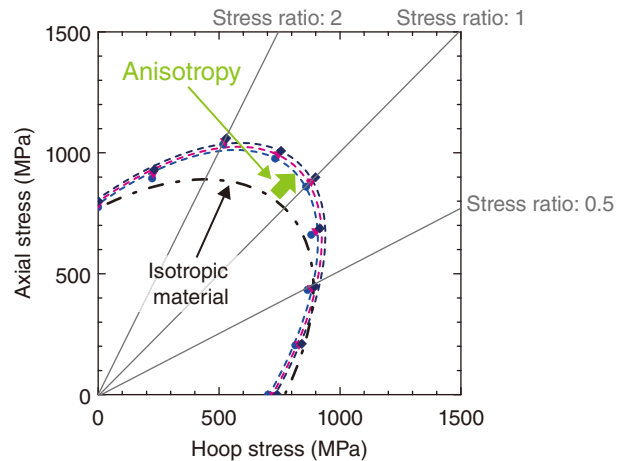


Fig.2-8 Deformation anisotropy of Zircaloy-4 cladding

Each colored point represents a given biaxial stress state and each curve represents an equivalent plastic deformation level. The extension of the ellipse toward the upper-right indicates a deviation from isotropic hardening behavior with deformation; i.e., enhanced hardening at a stress ratio of approximately 1.

Here, when compared with that of an isotropic material, the resulting ellipse extended to the upper-right with deformation (i.e., behaved anisotropically). Microscopic observation of the specimen by scanning electron microscopy revealed that this anisotropic behavior is a result of the combined effect of the intrinsic anisotropy of the Zr crystal with its hexagonal close-packed structure and the biased crystal orientations introduced in the fabrication process of the polycrystalline cladding. This study provided novel deformation anisotropy data of the PWR-type cladding, which led to a proposed mechanical property model describing plastic hardening behavior under biaxial stress conditions.

This developed model was then applied to computer simulations of PCMI failure performed by JAEA; the knowledge obtained by these simulations has been reflected in the new PCMI failure threshold which we have proposed recently to improve the reliability and rationality of safety regulations.

The study was conducted in FY2015, sponsored by the Nuclear Regulation Authority (NRA), Japan.

(Takeshi Mihara)

* Kuwabara, T. et al., Yield Locus and Work Hardening Behavior of a Thin-Walled Steel Tube Subjected to Combined Tension-Internal Pressure, Journal de Physique IV, vol.105, 2003, p.347–354.

Reference

Mihara, T. et al., Deformation Behavior of Recrystallized and Stress-Relieved Zircaloy-4 Fuel Cladding under Biaxial Stress Conditions, Journal of Nuclear Science and Technology, vol.55, issue 2, 2018, p.151–159.

2-3 Effects of Stress on Oxidation near a Crack Tip

— Toward an Understanding of the Mechanism of Environmentally-Assisted Cracking in Stainless Steel —

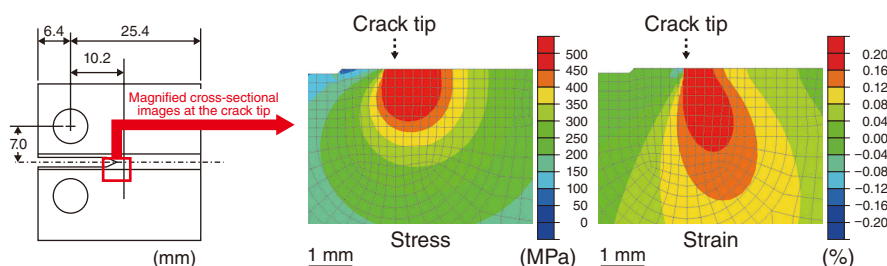


Fig.2-9 Configuration of a CT specimen and contour figures of stress and strain near a crack tip in a 7-kN loaded CT specimen ($K = 30 \text{ MPa(m)}^{1/2}$) immersed in a simulated BWR coolant condition
The FEA results show a lower half of the crack tip in the specimen.

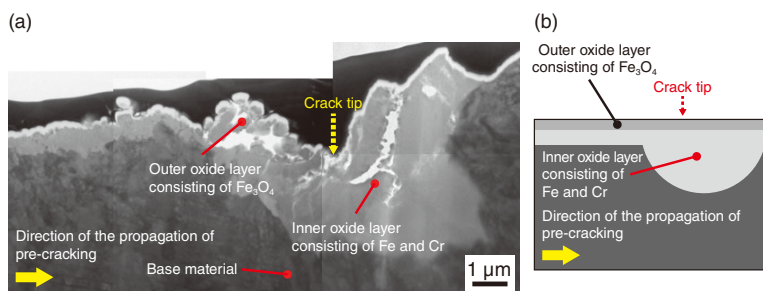


Fig.2-10 A cross-sectional image obtained by TEM (a) and a schematic illustration (b) near a crack tip for a 7-kN loaded CT specimen ($K = 30 \text{ MPa(m)}^{1/2}$) immersed in a simulated BWR coolant condition for 224 hours

An oxide inner layer was observed around the crack tip, where the strain and tensile stress were concentrated.

Environmentally-assisted cracking (EAC) is known as a significant degradation issue for stainless steels used in primary coolant loops and core internals subjected to high-temperature and high-pressure water ($\sim 300 \text{ }^\circ\text{C}$) in light-water reactors. This cracking is induced in susceptible materials by welding, tensile residual stress, and a corrosive environment. The detailed mechanism of crack propagation has not yet been clarified. Tensile stress, which is known as a parameter that enhances crack propagation, may promote local plastic strain near a crack tip (see the red region of the finite element analysis (FEA) shown in the right figure of Fig.2-9). The effect of plastic strain on EAC is not understood well. Efforts were therefore made to focus on the role of local strain induced by tensile stress during oxidation around crack tips and the propagation of EAC. To do so, an immersion test was performed under a simulated boiling water reactor (BWR) coolant condition at $290 \text{ }^\circ\text{C}$ and 9 MPa ($10 \text{ } \mu\text{S/m}$ in conductivity) using compact tension (CT) specimens made of a 316L stainless steel to produce oxide layers inside cracks. During the immersion test, a 7-kN constant load was applied to the specimens to cause stress concentration at a crack tip in the specimens. Here, the stress intensity factor, K , (a parameter that represents the driving force for crack growth) at the crack tip of a fatigue pre-crack was set to $30 \text{ MPa(m)}^{1/2}$. Detailed observations of oxide layers near crack tips were performed using a transmission electron microscope (TEM) after the immersion test.

As shown in Fig.2-10, an outer oxide layer consisting of

magnetite (Fe_3O_4) and an inner oxide layer containing iron (Fe) and chromium (Cr) were observed inside the cracks in the immersed specimens. The characteristically thick inner layer was produced near the crack tip in loaded specimens (see Fig.2-10(a)). The thick oxide layer near the crack tip indicates that oxygen diffuses from the bulk water into the crack. However, the gap size of the crack during this immersion test was estimated to be less than $1 \text{ } \mu\text{m}$ by FEA. This narrow gap would inhibit the diffusion of oxygen dissolved in water to the crack tip, thus suppressing the oxide growth at the crack tip. The inner oxide layer observed in this study ($0.3 \text{ } \mu\text{m}$ after a 50-hour immersion) was much thicker than that observed in a previous study using unloaded specimens with a similarly narrow gap ($0.09 \text{ } \mu\text{m}$ after a 1000-hour immersion). Considering the strain near the crack tip simulated by FEA in Fig.2-9, dislocations, which are induced by the tensile stress, were concluded to provide diffusion paths for oxygen atoms.

Future work will consist of crack growth rate tests to investigate effects of the thick oxide layer near crack tips induced by tensile stress on crack propagation. These experimental results and new findings will allow for a better understanding of the mechanism of EAC to confirm the conservativeness of the current integrity assessment method for EAC.

A part of this study was conducted in FY2013 and FY2014, sponsored by the Nuclear Regulation Authority (NRA), Japan.

(Kuniki Hata)

Reference

Kasahara, S., Hata, K. et al., Influence of Applied Load on Oxidation in the Vicinity of Crack Tips of Stainless Steel under High Temperature Water, *Zairyo-to-Kankyo*, vol.68, issue 9, 2019, p.240–247 (in Japanese).

2-4 Preparing for Aftershocks after a Major Earthquake

— Proposal of Risk Assessment Method Considering Large Aftershocks —

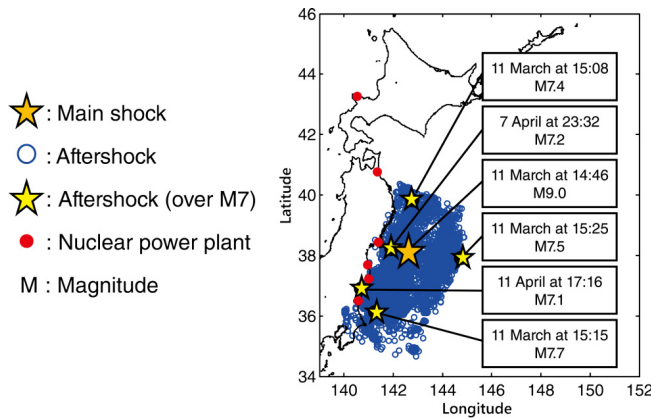


Fig.2-11 Aftershock distribution caused by the 2011 Tohoku earthquake

After the 2011 Tohoku earthquake, several large-scale aftershocks of M7 and above were reported, many of which caused significant damage. A risk assessment method that can appropriately consider the effects of large aftershocks is thus required.

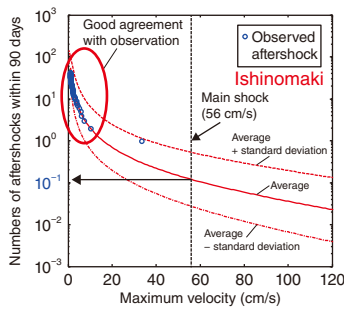


Fig.2-12 Aftershock hazard evaluation of the 2011 Tohoku earthquake (at Ishinomaki, within 90 days of the main shock)

The predicted numbers of aftershocks was in good agreement with the observed data. The results indicate that an average 0.1 of aftershock numbers are exceeded the seismic intensity (maximum velocity) of the main shock (56 cm/s) within 90 days after the main shock.

During conventional seismic probabilistic risk assessments (seismic PRAs) of nuclear facilities, only the impact of main shocks are considered; evaluation methods considering aftershocks have not yet been established. In the aftermath of the 2011 Tohoku earthquake, which logged the largest recorded magnitude (M) in Japan, M9, several large-scale aftershocks of M7 and above were reported, many of which caused significant damage (see Fig.2-11). This presented an opportunity to reconsider the effects of aftershocks during seismic PRAs. This research therefore was focused on the development of a seismic hazard assessment method that evaluates the possibility of a nuclear power plant being affected by large earthquake motions; further, aftershock hazard evaluation methods that consider the impacts of large aftershocks were investigated.

One of the issues associated with seismic hazard evaluation methods considering large aftershocks is the difficulty in predicting the timing, scale, and probability of aftershocks. To address this, aftershock records of large main shocks exceeding M7, including the M9-class Tohoku earthquake, were analyzed and used to develop a semi-empirical aftershock model. Based on the analysis of the aftershock records, the scope of application of the conventional aftershock occurrence model was expanded to aftershocks of large main shocks of the M9 class. This includes the relationship between the main shock and aftershock scales and the relationship between the aftershock scale and numbers of aftershocks. Aftershock hazard evaluation methods,

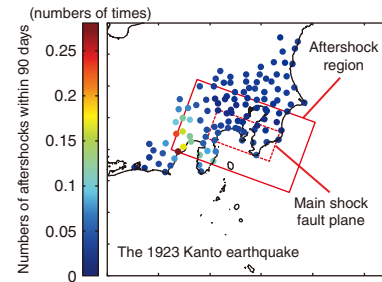


Fig.2-13 Example aftershock hazard map

The proposed method maps the numbers of aftershocks that exceeds the maximum velocity of the main shock. An aftershock hazard map could be used for regional disaster prevention measures, such as wide-area evacuation plans.

which could be used to calculate the relationship between the intensity (maximum velocity) and numbers of aftershocks, were then proposed by combining the aftershock occurrence model and distance attenuation formula of the conventional seismic hazard evaluation method. As an example, the aftershock hazard following the 2011 Tohoku earthquake was evaluated and compared with observed data, as shown in Fig.2-12.

To apply this evaluation method to the seismic PRA of a nuclear facility, a typical aftershock scenario can be considered for a nuclear power plant, and aftershock hazard evaluation can be performed in advance. Further, an aftershock hazard map based on the predicted probability of an aftershock exceeding the seismic intensity of the main shock was proposed. This map, an example of which is shown in Fig.2-13, could be used in the development of wide-area evacuation plans.

Domestic nuclear facilities in Japan are required to implement disaster prevention and mitigation measures in preparation for a predicted Nankai Trough earthquake, which is expected to cause large aftershocks over a wide area. Therefore, it is essential to establish a seismic PRA method that appropriately considers the effects of large aftershocks.

Accordingly, aftershock hazard evaluation methods are under development and efforts to improve the more realistic seismic PRA method, which accounts for the effects of the main shock and aftershocks, are ongoing.

(Byunghyun Choi)

Reference

Choi, B. et al., Engineering Applications Using Probabilistic Aftershock Hazard Analyses: Aftershock Hazard Map and Load Combination of Aftershocks and Tsunamis, Geosciences, vol.8, issue 1, 2018, p.1-1-1-22.

2-5 Elucidating HEPA Filter Clogging under Organic Solvent Fire

— Development of Severe Accident Assessment Method for Reprocessing Facilities —

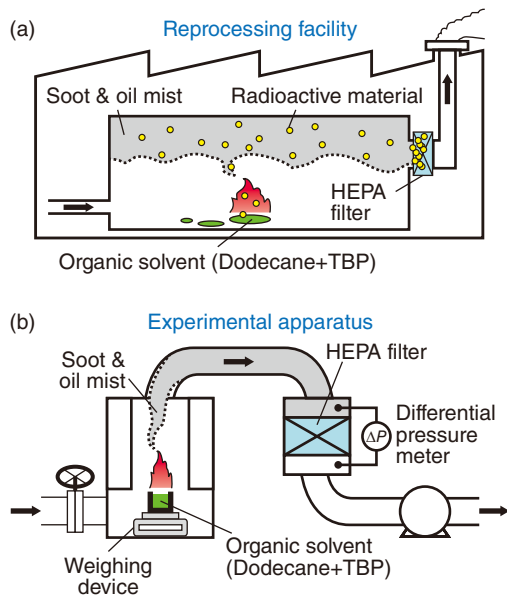


Fig.2-14 Schematics of an organic solvent fire (a) and the designed experimental apparatus (b)

An organic solvent fire in a reprocessing facility was simulated, during which soot and oil mist from combustion clog the HEPA filter, causing an increase in the differential pressure of the filter.

Reprocessing facilities are equipped with high-efficiency particulate air (HEPA) filters that trap particulate radioactive material within the facility. A lot of organic solvent consisting of tributyl phosphate (TBP) and dodecane are used to recover useful elements from spent nuclear fuel. As the solvent mixture is combustible, the fire risk in the facility must be considered. Furthermore, severe accidents must be considered when assessing the safety of the facility.

This study therefore aimed to estimate how long a HEPA filter can remain intact under an organic solvent fire, as a damaged filter can increase the leakage of radioactive material from the reprocessing facility, as shown in Fig.2-14(a).

In a fire, the HEPA filter can become clogged with soot and oil mist from burning combustible substances. If the differential pressure (ΔP) of the filter exceeds its limit, the filter may be damaged. We have used a small experimental apparatus (Fig.2-14(b)) to burn various combustible substances and measure the change of ΔP of the filter. As a result, we found that the ΔP rises sharply at the late stage of combustion of the mixed solvent. This finding is important because it suggests that the filter can become damaged more quickly than expected in conventional evaluations.

To clarify the mechanism behind the sharp increase in the ΔP , the relationship between the increase in the ΔP and the change of

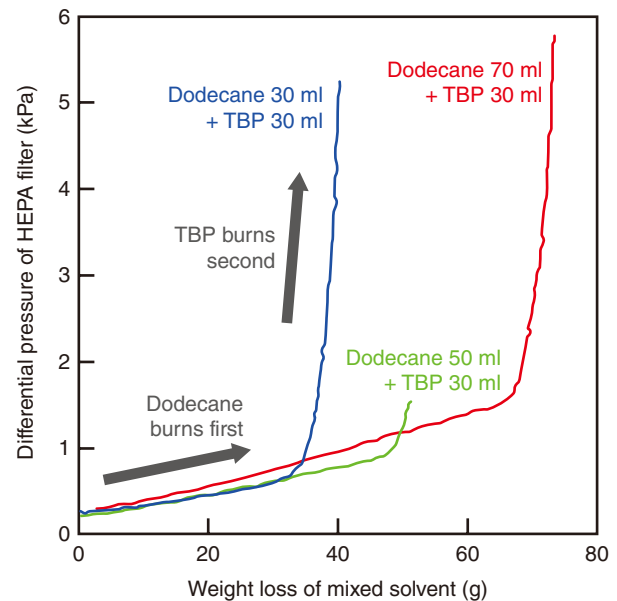


Fig.2-15 Change in differential pressure (ΔP) of HEPA filter
Dodecane burns preferentially when a mixture of dodecane and TBP is burned. TBP then burns after the dodecane burns out; this combustion of TBP causes a sharp rise in the ΔP .

solvent composition during combustion. We prepared three types of mixed solvents using 30 ml of TBP and either 30, 50, or 70 ml of dodecane. These mixed solvents were then burned while the resulting change in the ΔP of the HEPA filter was measured. The amount of soot and oil mist released, the weight loss of the mixed solvent, and changes in the solvent composition with combustion were also measured and analyzed.

As a result, the ΔP of the HEPA filter gradually increased in the early stages of combustion before sharply increasing in the late stage, as shown in Fig.2-15. During combustion, dodecane, which is relatively combustible, burns first; TBP then burns second. Solvents containing less dodecane saw a sharp increase in the ΔP earlier during combustion; further, the increase consistently occurred near the point at which dodecane was expected to burn out. Additionally, the amount of oil mist released increased at this point. Since TBP is relatively inflammable, an unburned oil mist containing TBP was likely released at this later stage of combustion, thus clogging the filter and causing the sharp rise in the ΔP .

This study was performed under the research entrusted in FY2016, sponsored by the Nuclear Regulation Authority (NRA), Japan.

(Takuya Ono)

Reference

Ono, T. et al., Rapid Clogging of High-Efficiency Particulate Air Filters during In-Cell Solvent Fires at Reprocessing Facilities, Nuclear Technology, vol.206, issue 1, 2020, p.40-47.

2-6 Rapidly and Widely Measuring Radiation from the Sky

— Preparedness for Using Aerial Radiation Monitoring during a Nuclear Emergency —

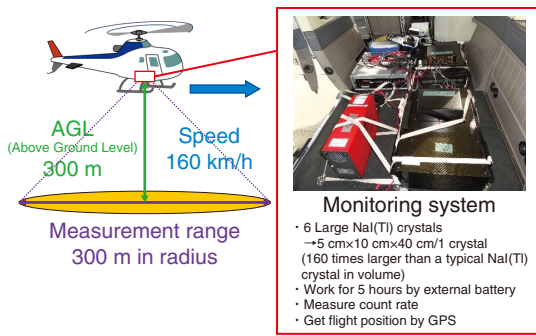


Fig.2-16 Overview of ARM
ARM is performed at 300-m AGL and 160 km/h with the monitoring system on board.

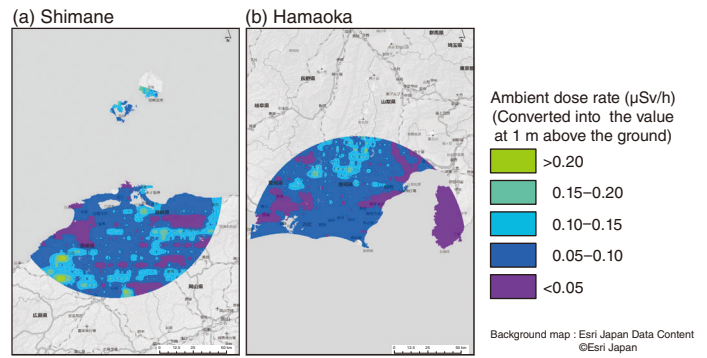


Fig.2-17 Example results of ARM
The natural background dose rate around the (a) Shimane and (b) Hamaoka Nuclear Power Stations.

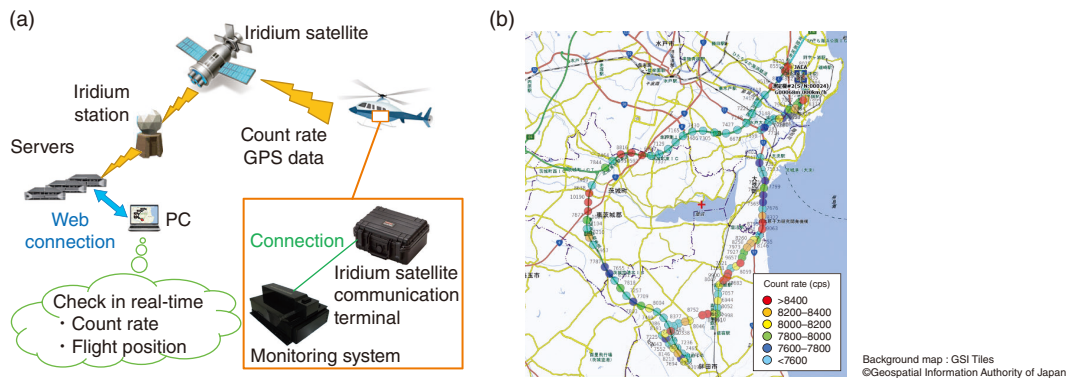


Fig.2-18 Real-time ARM Data Communication System
(a) System schematic. This system enables the real-time sharing of ARM data on the ground via satellite communications.
(b) Communicated car position and count rate, displayed as dots and numbers, respectively, during the test performed in the Ibaraki Prefecture. Dot color varies according to the level of count rate.

During a nuclear emergency, aerial radiation monitoring (ARM) via aircrafts such as manned helicopters could be utilized to aid decision-making in public protective actions and to evaluate the residual environmental radiological effect. ARM allows for rapid and widespread measurements (Fig.2-16), including in remote or relatively inaccessible regions, such as forests, mountains, or areas with a relatively high dose rate. In fact, ARM had been performed to map the ground deposition of radioactive nuclides in the months immediately following the accident at TEPCO’s Fukushima Daiichi Nuclear Power Station. In the more than nine years since this incident, ARM has been further developed and is now fully prepared to use following in the event of a nuclear emergency.

Firstly, all considerations to ensure safe deployment of ARM have been performed, as has the measuring of the natural background radiation level surrounding the nuclear power stations in Japan. In 2018, ARM was conducted to acquire these data within an 80-km radius surrounding the Shimane and Hamaoka Nuclear Power Stations; the resulting maps of the natural background dose rate are shown in Fig.2-17. Since much of the area surrounding the Shimane Nuclear Power Station is within the controlled airspace of airports and government agencies, it is necessary to get flight permission from air traffic authorities beforehand. In the Hamaoka area, it is vital

to have a detailed understanding of the location of densely packed aerial cableways to prevent collisions, particularly in precipitous mountain areas. This data collection process and development of background radiation maps will allow for the prompt performance of ARM and evaluation of environmental radiological effects during a nuclear emergency.

Secondly, the Real-time ARM Data Communication System (Fig.2-18(a)) was developed to provide ARM results swiftly during a nuclear emergency. This system allows ARM data to be shared on the ground via satellite, thus enabling real-time monitoring (from a PC) of the helicopter’s location and measured radiation levels. To test the data communication capabilities, a test was run from a car driven in Ibaraki Prefecture; the results, shown in Fig.2-18(b), demonstrated that the count rate and position of the car were correctly displayed without interruption. A similar test via helicopter is now being planned, as is the introduction of a program that automatically calculates the ambient dose rate from ARM data to further aid decision-making in public protective actions during a nuclear emergency.

This study was conducted as part of the contract research in FY2018, sponsored by the Nuclear Regulation Authority (NRA), Japan.

(Akira Futemma)

Reference

Futemma, A. et al., Background Radiation Monitoring Using Manned Helicopter for Application of Technique of Nuclear Emergency Response in the Fiscal Year 2018 (Contract Research), JAEA-Technology 2019-017, 2019, 95p. (in Japanese).

Advanced Science Pioneers the Future

To discover new principles and phenomena, the Advanced Science Research Center is conducting frontier research related to atomic energy sciences. Toward the International COE by using the advantage of JAEA.

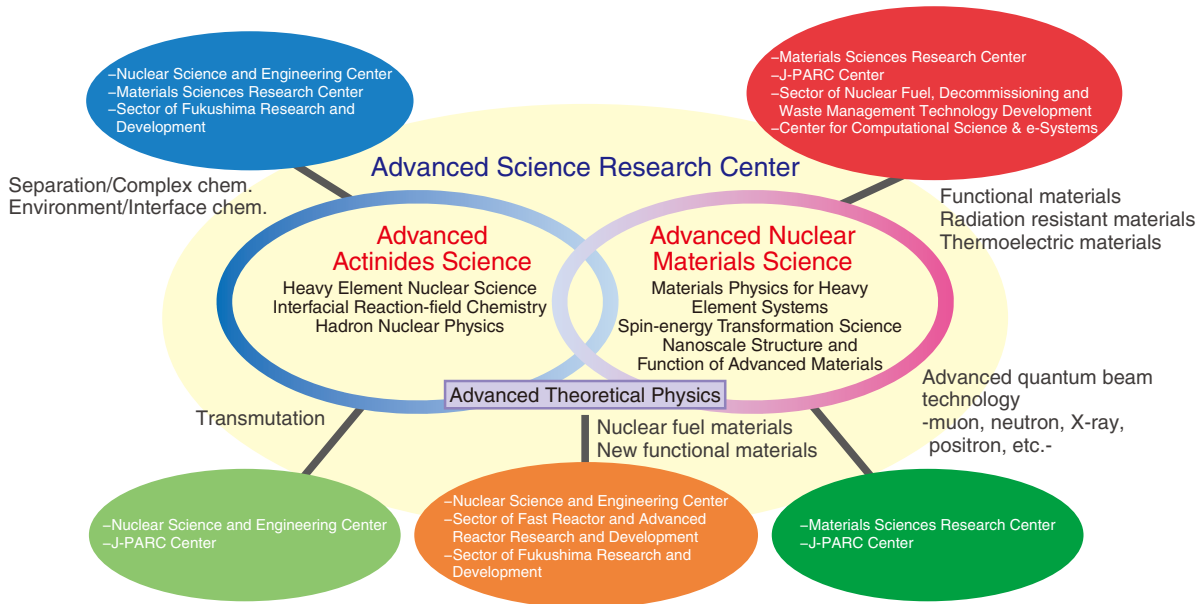


Fig.3-1 The role of advanced nuclear scientific research

This work aims to perform high-impact scientific and technical studies related to state-of-the-art nuclear and materials science.

The greater part of nuclear-energy-related technology is grounded on basic sciences. Apart from seeking solutions to today's energy problems, future research must respond to the new stage of nuclear energy developments that are expected in the next few decades.

The Advanced Science Research Center (ASRC) explores the unlimited possibility of nuclear energy from the perspective of basic science. During this process, we aim to establish new research fields and further develop the existing science and technology.

We started our mid-term plan in FY2015, focusing on two main areas: advanced actinides science and advanced nuclear materials science.

The former aims to conceptualize nuclear and heavy-element-based actinide science in a new way, whereas the latter aims to investigate and develop new materials for nuclear energy purposes. In FY2019, a theoretical physics group connecting these areas was established, which aimed to develop and enhance new research ideas across the various fields of sciences of the existing research areas. Through interactions between the two areas and in collaboration with research institutes within and outside of the Japan Atomic Energy Agency new fields of nuclear-energy science are being cultivated (Fig.3-1).

Numerous achievements were made in FY2019, many of which are highlighted in this chapter.

Through the advanced actinides science program, the high-energy prompt fission γ -ray spectrum in the fission of ^{235}U induced by a thermal neutron was measured and dipole vibration was found in fission fragments; this is discussed in Topic 3-1. This measurement will help the further understanding of the fission mechanism since the origin of such high-energy γ -rays

reflects the manner in which fission fragments are produced.

In the field of chemical research, a solvent extraction method based on the strong hydrophobicity of fluorine atoms was developed. This method drastically improves the extraction efficiency by preventing aggregation phenomena in a complex, and is discussed in Topic 3-2.

Substantial results were also achieved in the field of advanced nuclear materials science. During analysis of the uranium compound UTe_2 , a signal of a new type of superconductivity, i.e., spin-triplet superconductivity, was detected from the nuclear magnetic resonance using a single crystal (Topic 3-3).

In ferrimagnetic systems, the temperature of an angular momentum compensation (AMC) between the total angular momentum and spin angular momentum in $\text{Ho}_3\text{Fe}_5\text{O}_{12}$ was measured, as detailed in Topic 3-4. This phenomenon is attracting attention as a candidate for high-speed magnetic memories.

The localized electrons in electron-doped SrTiO_3 may provide new functionalities because itinerant and localized electrons generally show completely different transport and magnetic properties. Muons (μ^+) were used to irradiate a SrTiO_3 single crystal and trace a localized electron by the μ^+ spin rotation using the $\mu^+\text{SR}$, method (Topic 3-5).

In nuclear theory, an alpha-cluster structure was investigated in-nuclei through nuclear reaction theory in a proton knockout reaction, representing the first example of a quantitative reproduction of the α -knockout experiment with reaction theory. As discussed in Topic 3-6, this demonstrates that this method can quantitatively investigate cluster states.

The ARSC aims to develop a broad knowledge base of nuclear sciences and demonstrate this basis via basic nuclear research.

3-1 Observing Giant Dipole Vibration in Fission Fragments — Toward Understanding the Fission Process —

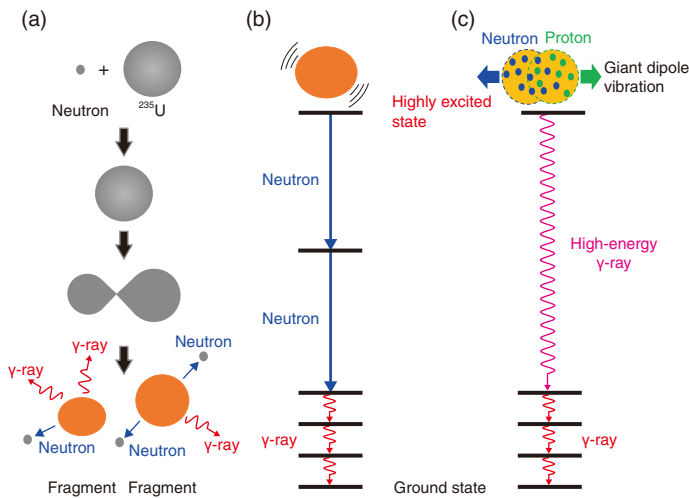


Fig.3-2 Formation (a) and deexcitation (b) (c) processes of a fission fragment

In general, γ -rays are emitted after neutron emissions (b); however, this work details a process (c) in which high-energy γ -rays are emitted without neutron emissions.

Neutron-induced fission of uranium-235 (^{235}U) produces energy for nuclear power generation. During nuclear fission, two fission fragments are produced, and neutrons and γ -rays are emitted from the fragments. Neutrons are used to sustain a chain reaction by inducing further fission, and γ -rays are absorbed by the surrounding materials and contribute about 3% of the heat released in a nuclear reactor. Therefore, data on the multiplicity and the energy spectrum of the emitted neutrons and γ -rays can help to improve the safety of the nuclear reactor.

The emission of neutrons and γ -rays from the fission fragments is summarized in Fig.3-2. At the instance of fission, the fission fragments are highly excited. In general, neutrons are dominantly emitted and release a large amount of excitation energy; once neutron emission is no longer energetically possible, γ -ray emission occurs (i.e., Fig.3-2(b)). In this simple picture, the maximum energy of γ -rays does not exceed the energy required for neutron emission (about 7 MeV). In fact, measured γ -ray spectra are limited below the γ -ray energy of 7 MeV for neutron-induced fission of ^{235}U . By contrast, this work aimed to extend the known γ -ray spectrum to higher energies. To do so, we developed a new detection system with a sensitivity 100000 times higher than that of previous studies. As a result, γ -rays with energies of up to 20 MeV were successfully measured, as shown in Fig.3-3. The observed γ -ray yield in the region above 12 MeV is higher

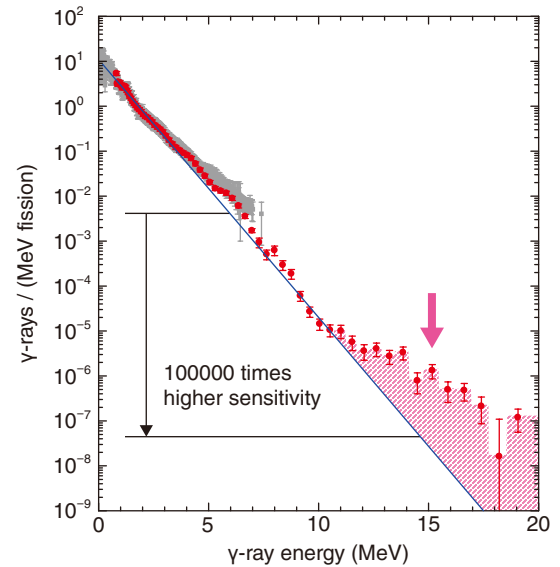


Fig.3-3 γ -ray energy spectrum

The red circles and gray squares show the present and previous results, respectively. The solid line is the spectrum expected from the general deexcitation process; the component with a peak at approximately 15 MeV is highlighted.

than that in the spectrum expected from the general deexcitation process. This indicates the presence of a mechanism in which a large amount of excitation energy is released by γ -rays without emission of neutrons.

These results were then further analyzed using a theoretical model; high-energy γ -ray emission was found to be caused by the giant dipole vibration. In this vibration process, well-known to appear in the high-energy γ -ray absorption process, the protons in the nucleus move in one direction while the neutrons move in the opposite direction. Here, the vibration appeared at the instance of fission, i.e., when the nucleus divided into two. The unique appearance of this vibrational behavior was thus captured by observing high-energy γ -rays emitted during fission. These measurements of high-energy γ -rays are expected to help further the understanding of the fission mechanism, since the origin of such high-energy γ -rays reflects how fission fragments are produced in the fission process.

This study was conducted on “Measurement of high-energy prompt gamma-rays in fission for surveillance detector to monitor criticality of fuel debris”, supported by the Ministry of Education, Culture, Sports, Science and Technology (MEXT), Japan.

(Hiroyuki Makii)

Reference

Makii, H. et al., Effects of the Nuclear Structure of Fission Fragments on the High-Energy Prompt Fission γ -ray Spectrum in $^{235}\text{U}(n_{th}, f)$, Physical Review C, vol.100, issue 4, 2019, p.044610-1–044610-7.

3-2 Improving the Extraction Efficiency by Preventing Aggregation Phenomena of a Complex — Development of a Solvent Extraction Method Using the Strong Hydrophobicity of Fluorine —

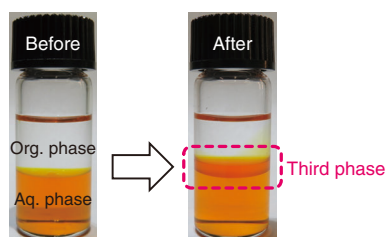


Fig.3-4 Snapshot of the third phase formation
After extraction, a third phase is formed, which is insoluble in both organic and aqueous phases.

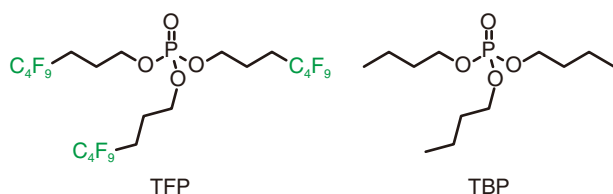


Fig.3-5 Chemical structures of tri(4,4,5,5,6,6,7,7,7-nonafluoroheptyl) phosphate (TFP) and tributyl phosphate (TBP)
TFP has good solubility in a fluorosolvent due to its C₄F₉ group.

The efficient separation of various radionuclides is vital in reducing the amount and toxicity of radioactive waste. The separation of metal ions such as radionuclides is carried out by a hydrometallurgical process mainly based on solvent extraction, which is a separation technique used to concentrate and separate a certain target component by using distribution of a solute between two immiscible solutions. Solvent extraction has been widely adopted as a practical process in the reprocessing of spent nuclear fuel and in refining valuable metals. Further, the extraction of Zr(IV) as a fission product from aqueous HNO₃ solutions has been investigated extensively because the presence of Zr in the tributyl phosphate (TBP)-based reprocessing of spent nuclear fuel is problematic. Zr species are likely to form a third phase during the extraction of Zr by TBP from HNO₃ aqueous solutions, as shown in Fig.3-4.

Formation of this third phase in the reprocessing of spent fuel is undesirable, as it could cause safety and criticality concerns due to the high metal concentrations. However, few applicable extraction methods or extractants have been proposed that do not suffer from these problems. A Zr-loaded organic phase from liquid-liquid extraction with TBP was recently reported to demonstrate hierarchical aggregation behaviors of Zr(NO₃)₄(TBP)₂ coordination complexes, which self-assemble into primary clusters that coalesce further to form superclusters. This supercluster formation portends the formation of third phase.

This work therefore aimed to develop a fluoroalkylated phosphate (TFP) for Zr(IV) extraction to increase the extraction

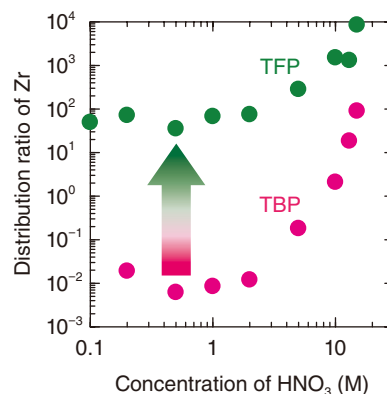


Fig.3-6 Effect of HNO₃ concentration on the distribution ratio (extraction efficiency) of Zr by TFP and TBP
TFP had a much higher Zr(IV) extraction performance than TBP despite the TFP concentration in the fluorosolvent phase being one-tenth of that of TBP. Moreover, no third phase formed even in the high concentration-TBP system.

performance and prevent third-phase formation. The structure of the developed TFP compound is shown alongside the structure of TBP in Fig.3-5. Fluorinated solvents such as perfluorinated alkanes have unique chemical properties, including low toxicity, non-flammability, and immiscibility with both water and organic solutions. The high hydrophobicity of a fluorosolvent reduces the formation of a third phase and interfacial crud.

To compare the extraction capabilities of the developed TFP compound and TBP and analyze the extraction dependency on the concentration of HNO₃, Zr(IV) was then extracted from an HNO₃ solution by 0.05 M TFP and 0.5 M TBP; the results are compared in Fig.3-6. Despite its concentration being one-tenth of that of TBP, the 0.05 M TFP had a much higher Zr(IV) extraction performance. Moreover, no third phase formed, even as the concentration of TFP was increased. To verify the reason for the superior Zr(IV) extraction performance of TFP, the compositions of each phase before and after water, HNO₃, and Zr(IV) extraction were determined using both TFP and TBP. The concentrations of water and HNO₃ molecules in the fluorosolvent phase lowered during Zr(IV) extraction, indicating that, unlike with TBP, water and HNO₃ molecules do not preferentially interact with TFP. The superior performance of TFP makes it suitable as an alternative extractant to TBP in the Zr(IV) extraction system and to other conventional organic extraction systems.

(Yuki Ueda)

Reference

Ueda, Y. et al., Extraction Performance of a Fluorinated Phosphate for Zr(IV) from HNO₃ Solution: Comparison with Tri-*n*-Butyl Phosphate, Solvent Extraction and Ion Exchange, vol.37, issue 5, 2019, p.347-359.

3–3 Clarifying the Mechanism behind Superconductivity in Uranium Compounds — NMR Research to Reveal the Mechanism of Spin-Triplet Superconductivity —

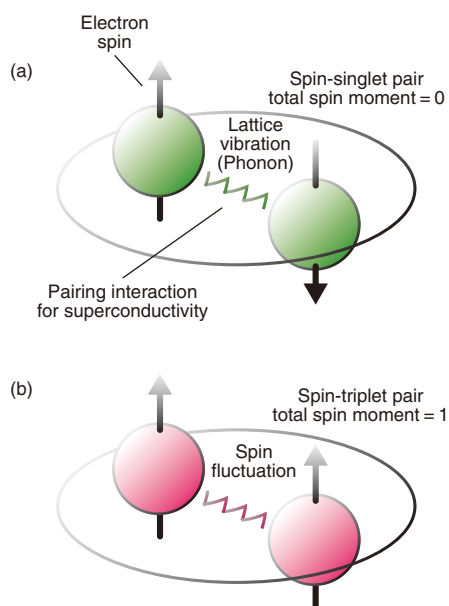


Fig.3-7 Two types of superconducting electron pairs

In general, superconducting pairs adopt a spin-singlet state, in which the spins of the pairs are all antiparallel (a). However, in some uranium compounds, superconducting pairs adopt a spin-triplet state, in which the spins of the pairs are all parallel (b).

Uranium, known for its usage as a nuclear fuel, has recently attracted a great deal of attention in the field of basic research on superconductivity. After the first discovery of superconductivity in mercury by Kamerlingh Onnes in 1911, many new superconductors have been discovered, including copper oxide and iron-based superconductors. From these discoveries, it has become clear that the mechanism behind superconductivity is far more diverse than originally thought. Since 2000, a variety of unconventional superconducting phenomena have been found in compounds containing uranium. Investigating one such phenomenon has allowed for the detailing of the spin-triplet superconductivity present in uranium compounds.

The essence of superconductivity is that two electrons form a pair (i.e., a superconducting pair), with making collective motion in materials. As shown in Fig.3-7(a), in conventional, spin-singlet superconductors, the spins of superconducting pairs are all antiparallel and thus the total spin moment is equal to zero. On the other hand, in a spin-triplet superconducting state, the spins are parallel and the total spin moment is equal to one (Fig.3-7(b)). As a result, ferromagnetism and superconductivity, which has generally been considered as mutually exclusive phenomena, can coexist in the microscopic state in the spin-triplet superconductors. Furthermore, while a field will typically destroy superconductivity, field-induced superconductivity has been observed with spin-triplet pairs. In 2018, a new spin-triplet superconductor, UTe_2 was discovered. Since then, a variety of unconventional superconducting phenomena has been found in UTe_2 . To reveal the origin of these phenomena, intensive

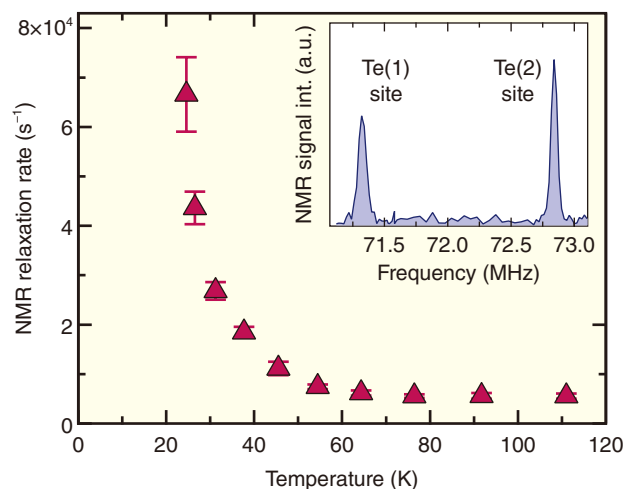


Fig.3-8 Temperature dependence of the NMR relaxation rate and the NMR spectrum

Under an applied magnetic field, the development of magnetic fluctuations in the material leads to the increase of the NMR relaxation rate ($1/T_2$) at low temperatures. Two NMR peaks corresponding to the two inequivalent Te sites in a crystal were observed, as shown in the inset figure.

studies are now being undertaken by researchers in Japan, in the United States, across the European Union, and in other countries.

In an effort to study the electronic states of UTe_2 from a microscopic viewpoint, nuclear magnetic resonance (NMR) experiments using a single crystal were conducted. The observed NMR spectrum is shown in the inset of Fig.3-8; here, two NMR peaks are present, arising from the two inequivalent Te sites in a unit cell. Both peaks are very sharp, confirming the high quality of the single crystal. Using the observed NMR signal, the temperature dependence of the NMR relaxation rate, $1/T_2$, was measured and is displayed in Fig.3-8. The relaxation rate of $1/T_2$ is a physical quantity reflecting the strength of the magnetic fluctuations created by electron spins at the observed nuclear position. The measurements revealed the development of strong magnetic fluctuations along a specific axial direction of the crystal at low temperatures, where superconductivity appears. This implies that the magnetic fluctuations may create the attractive force of the spin-triplet pairing, as has been theorized since the 1980s. Recently, UTe_2 has been suggested to have potential applications in next-generation quantum computing devices.

This study was conducted on “Understanding of the Superconducting Mechanism and Search for a Novel Superconducting State in Uranium Heavy-Fermion Compounds”, supported by the Japan Society for the Promotion of Science (JSPS) KAKENHI Grant-in-Aid for Scientific Research (S) (No.15H05745).

(Yo Tokunaga)

Reference

Tokunaga, Y. et al., ^{125}Te -NMR Study on a Single Crystal of Heavy Fermion Superconductor UTe_2 , Journal of the Physical Society of Japan, vol.88, no.7, 2019, p.073701-1–073701-4.

3-4 Detection of the Singularity of Magnets Using Rotation

— Measuring the Angular Momentum Compensation, Key to Speeding Up Magnetic Devices —

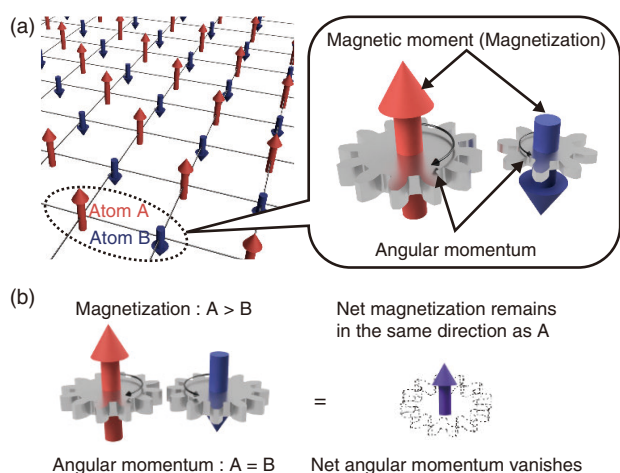


Fig.3-9 Schematic of a ferrimagnet

(a) Electric magnetic moments of atoms A and B are aligned in antiparallel. The magnetic moment of A is larger than that of B. (b) Net angular momentum vanishes at the angular momentum compensation temperature, but magnetization still remains.

The origin of magnetism in magnets is electron angular momentum. The electron has a spin angular momentum that corresponds to the rotation and an orbital angular momentum that corresponds to the orbital motion centered on the nucleus. These angular momenta cause a microscopic magnet, i.e., a magnetic moment. Magnetization appears due to the alignment of the magnetic moments within magnetic materials.

A ferrimagnet contains multiple types of magnetic atoms whose magnetic moments align in opposite directions, as shown in Fig.3-9(a). Here, the magnetic moment of A is larger than the magnetic moment of B, and as a whole, the north pole of the magnet is the same direction of the magnetic moment of A.

Some ferrimagnets have compensation temperatures, at which the magnetic moments or angular momenta of A and B compensate each other. At the magnetization compensation temperature T_M , the net magnetization vanishes. At the angular momentum compensation temperature T_A , the angular momenta of A and B compensate each other, but the net magnetization remains, as shown in Fig.3-9(b). However, conventional magnetization measurements have not been able to measure the angular momentum compensation temperature.

The Barnett effect was therefore used to determine the T_A of the ferrimagnet $\text{Ho}_3\text{Fe}_5\text{O}_{12}$; when a matter rotates, the angular momentum aligns in the rotational axis, thus magnetizing the matter. The measured temperature dependence of the magnetization induced by mechanical rotation is shown

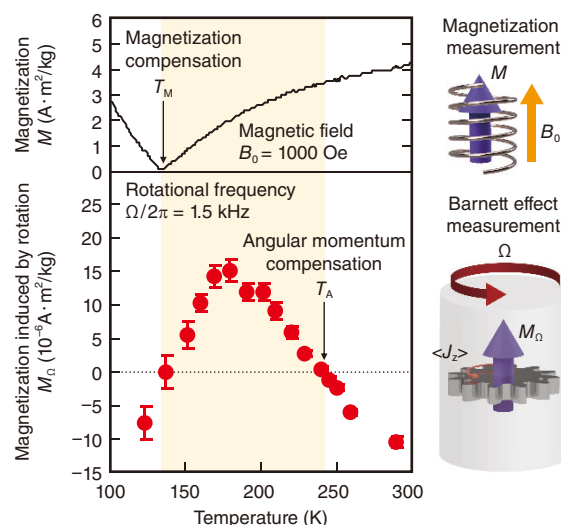


Fig.3-10 Magnetization and Barnett effect measurements

Usual magnetization measurements can only measure the magnetization compensation temperature. The Barnett effect determines the angular momentum compensation temperature as the temperature where the magnetization induced by rotation becomes zero.

in Fig.3-10. The magnetization induced by rotation reaches zero at T_A , as the Barnett effect does not work due to the net-zero angular momentum. Furthermore, T_A was shifted to room temperature (293 K) by partial substitution of holmium (Ho) with dysprosium (Dy) in $\text{Ho}_3\text{Fe}_5\text{O}_{12}$.

Magnetic memories store data in the magnetization direction and rewrite each bit by reversing the direction. For a normal magnet, the magnetization reverses with precession due to the angular momentum; precession prevents a smooth reversal of magnetization. On the other hand, the magnetization reverses at a high speed at T_A , where the angular momentum disappears. Thus, T_A has been attracting attention as a candidate for high-speed magnetic memories.

The developed technique to determine T_A using the Barnett effect is expected to accelerate the search for materials applicable in high-speed magnetic devices.

This work was supported by JST ERATO Grant Number JPMJSK1402, and by the Japan Society for the Promotion of Science (JSPS) KAKENHI Grant-in-Aid for Scientific Research on Innovative Areas (Research in a proposed research area) (No.26103005), Grant-in-Aid for Scientific Research (A) (No.26247063), Grants-in-Aid for Scientific Research (B) (No.16H04023, No.17H02927), and by Grants-in-Aid for Scientific Research (C) (No.15K05153, No.16K06805).

(Masaki Imai)

References

- Imai, M. et al., Observation of Gyromagnetic Reversal, Applied Physics Letters, vol.113, issue 5, 2018, p.052402-1–052402-3.
 Imai, M. et al., Angular Momentum Compensation Manipulation to Room Temperature of the Ferrimagnet $\text{Ho}_{3-x}\text{Dy}_x\text{Fe}_5\text{O}_{12}$ Detected by the Barnett Effect, Applied Physics Letters, vol.114, issue 16, 2019, p.162402-1–162402-4.

3-5 Closing in on the Longstanding Puzzle of Localized Electrons in an Electron-Conducting Oxide — Using Muons to Unveil the Nature of Localized Electrons in Hydrogen-Doped SrTiO₃ —

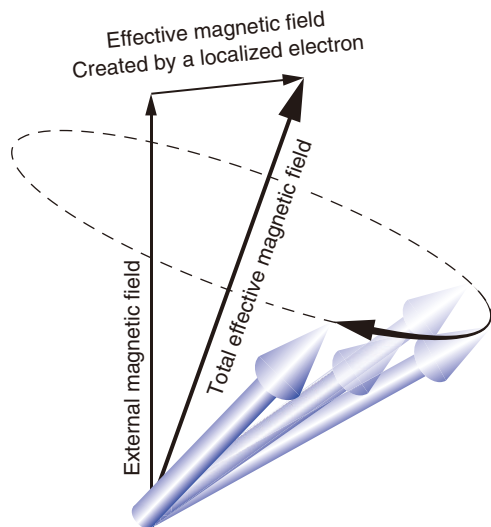


Fig.3-11 μ^+ spin precession under an external magnetic field
The μ^+ spin (3D arrow) precesses about the axis of the total effective magnetic field (B_{tot}) that is felt by μ^+ at a frequency proportional to the magnitude of B_{tot} . When an unpaired electron is localized near μ^+ , the precession frequency shifts from the value for bare μ^+ due to an additional effective magnetic field created by the localized electron.

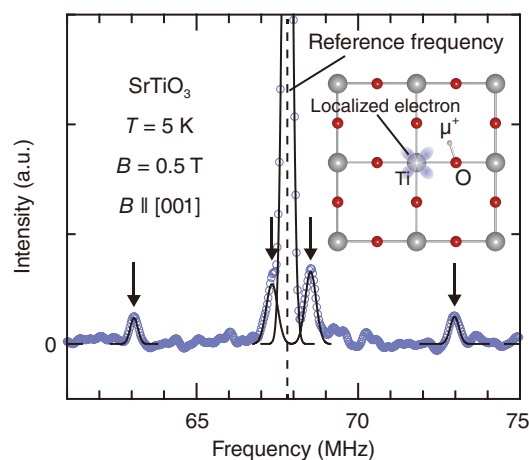


Fig.3-12 μ^+ SR frequency spectrum of SrTiO₃
The shifts from the reference frequency for bare μ^+ indicate that an unpaired electron is localized around an interstitial μ^+ . The inset shows the position of the localized electron, which was determined from the frequency shifts.

In recent decades, much attention has been focused on the development of electronics based on metal oxides, known as oxide electronics, as this approach may allow for functionality and performance improvements of electronic devices beyond the limit of existing silicon-based technologies. Strontium titanate (SrTiO₃), a dielectric material commonly used in capacitors, holds the key to establishing the oxide electronics. Although an insulator in its pure form, SrTiO₃ changes into an excellent electron conductor when doped with impurities such as Nb, La, and H, or when O atoms are removed from the lattice. The excess electrons injected into the conduction band by these treatments show exceptionally high mobility in transition metal oxides, which is useful in many state-of-the-art applications.

The existence of conduction electrons with itinerant characteristics has been established; further, some traces of localized electrons have also been detected in electron-doped SrTiO₃ by several experimental techniques. The existence of localized electrons could provide new functionalities to this important material, as itinerant and localized electrons generally show completely different transport and magnetic properties. However, the exact nature of the localized electrons is still far from being fully understood.

To solve the longstanding puzzle of the localized electrons in electron-doped SrTiO₃, radioactive positively charged muons

(μ^+) were used in our experiment. Muons implanted into SrTiO₃ chemically mimic hydrogen impurities in the dilute doping limit and serve as an electron donor. The muons also act as an atomic-scale magnetic probe to investigate the nature of excess electrons, which are brought into the lattice with them, as shown in Fig.3-11. This μ^+ -based approach provides a higher sensitivity in signal detection than similar techniques using real hydrogen.

A single-crystalline wafer of SrTiO₃ was irradiated with a μ^+ beam delivered from an accelerator; the nature of excess electrons was then investigated by the μ^+ spin rotation (μ^+ SR) method. A clear signature of electron localization on a Ti atom adjacent to an interstitial μ^+ was successfully observed at cryogenic temperatures, as detailed in Fig.3-12. Furthermore, the binding energy of the localized electron was unexpectedly low, thus suggesting that the localized electron can be interchanged with itinerant electrons even at moderate temperatures. These findings from the pseudoisotope experiment imply that the localized electron in hydrogen-doped SrTiO₃ is a temporarily immobilized electron that is weakly bound at a special Ti site adjacent to an ionized dopant. The insights from this study shed new light on the dual behavior of excess electrons in electron-doped SrTiO₃.

(Takashi Ito)

Reference

Ito, T. U. et al., Polaronic Nature of a Muonium-Related Paramagnetic Center in SrTiO₃, Applied Physics Letters, vol.115, issue 19, 2019, p.192103-1–192103-4.

3-6 Revealing Unique Nucleus Shapes by Nuclear Reactions

— Cluster Structure and Its Probability —

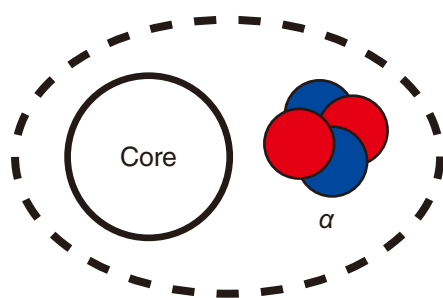


Fig.3-13 Cluster structure

A schematic of the cluster structure. An α particle consisting of two protons (●) and two neutrons (●) and a core nucleus is spatially separated and represents two cluster structures. A cluster structure is expected if the core nucleus is very stable or the system has excitation energy close to the energy to separate the system into an α and a core nucleus.

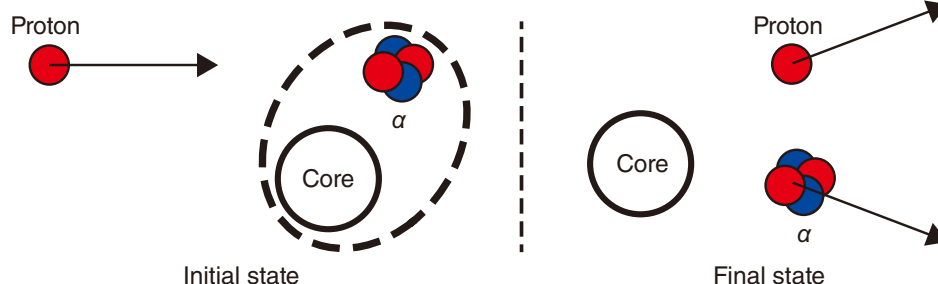


Fig.3-14 The proton (●) induced an α -knockout reaction from a target nucleus

Nuclei, which consist of only two types of particles, protons and neutrons (called nucleons), are known to exhibit a wide variety of aspects, in contrast with their simple composition. One of the most interesting nuclear structures is the cluster structure.

In this structure, nucleons are divided into two or more clusters and the nucleus forms an unusual shape instead of a simple sphere. In particular, the α -cluster structure, in which the nucleus is divided into an α -particle and a core nucleus and shown in Fig.3-13, has been commonly observed, as the α -particle is very stable and strongly bound. The cluster states are mainly expected to exist in light nuclei with the same number of protons and neutrons as α -particles (e.g., ^8Be , ^{12}C , ^{16}O , ^{20}Ne , ^{24}Mg), and both experimental and theoretical studies are ongoing.

To investigate the cluster structure and its probability, the proton-induced knockout reaction was studied. In this reaction, shown in Fig.3-14 a proton is bombarded into a target nucleus and an α -particle is knocked out. The knockout reaction is a method of knocking out an α -particle from the nucleus by bombarding it with protons with relatively high incident energy (i.e., several hundred MeV). One advantage of this method is that the reaction probability (i.e., reaction cross section) and the α -cluster state probability have a one-to-one correspondence, since the transition of the bound state to the scattering state of the α -particle is in a one-step process at such

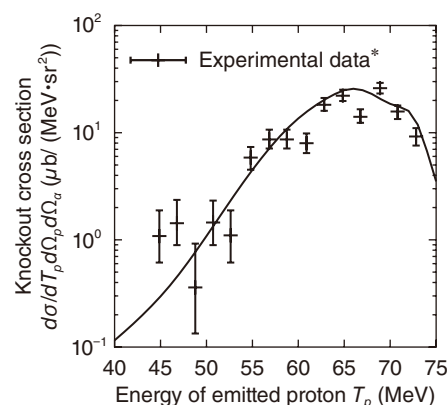


Fig.3-15 $^{20}\text{Ne}(p,p\alpha)^{16}\text{O}$ reaction cross section

A comparison between the experimental data (Carey, T. A. et al.)^{*} and the theoretical calculation of the reaction assuming 26% of the $\alpha + ^{16}\text{O}$ cluster state in the ^{20}Ne ground state (solid line).

high incident energy.

Since both α and ^{16}O nuclei have a double-closed-shell nature (i.e., a nuclear magic number), ^{20}Ne is a promising nucleus for $\alpha + ^{16}\text{O}$ cluster structure. The α -knockout experiment from ^{20}Ne was performed in 1984; according to the results of the analysis at that time, about 60% of the $\alpha - ^{16}\text{O}$ cluster component probability was expected in the ^{20}Ne ground state. However, this number was about 2–3 times greater than the predictions of structural theory, and has yet to be adequately addressed.

Using a structural theory based on nucleon degrees of freedom and reaction theory calculations with the latest interactions between scattering particles, this work demonstrated that the proposed theoretical calculation method of the knockout reaction cross section reproduces experimental data without any inconsistencies, as detailed in Fig.3-15. This work therefore represents the first quantitative reproduction of the α -knockout experiment with the reaction theory, and provides an important result showing that this method can quantitatively investigate cluster states.

(Kazuki Yoshida)

^{*} Carey, T. A. et al., Alpha-Particle Spectroscopic Strengths Using the $(p, p\alpha)$ Reaction at 101.5 MeV, Physical Review C, vol.29, issue 4, 1984, p.1273–1288.

Reference

Yoshida, K. et al., Quantitative Description of the $^{20}\text{Ne}(p, p\alpha)^{16}\text{O}$ Reaction as a Means of Probing the Surface α Amplitude, Physical Review C, vol.100, issue 4, 2019, p.044601-1–044601-6.

Fundamental Technologies for Nuclear Energy Innovation

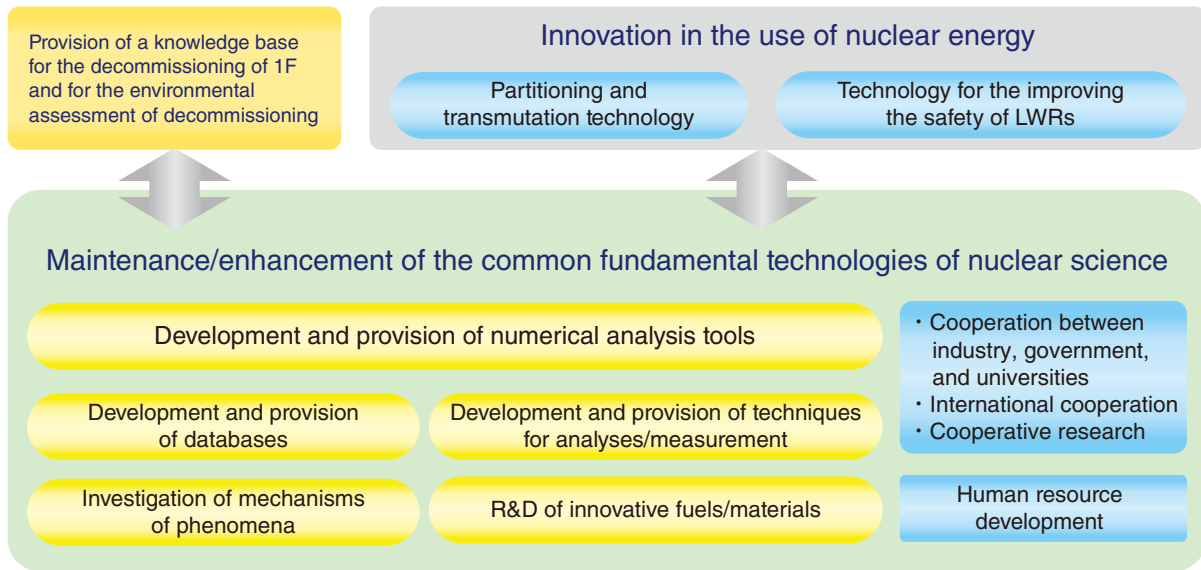


Fig.4-1 Overview of nuclear science and engineering research

The Nuclear Science and Engineering Center maintains and enhances fundamental technologies for the use of nuclear energy and radiation. The Center also aims to provide a knowledge base for the decommissioning of the TEPCO's Fukushima Daiichi NPS (1F), and contribute to the safety improvements of light water reactors (LWRs) and the development of partitioning and transmutation technology for reducing the impact of radioactive wastes.

Common fundamental technologies and knowledge platforms, such as databases, numerical analysis tools, analytical technologies, and knowledge of phenomena mechanisms, are necessary to support the use of nuclear energy and radiation. As illustrated in Fig.4-1, the Nuclear Science and Engineering Center (NSEC) aims to maintain such fundamental technologies and knowledge of nuclear science state-of-the-art and provides these technologies and knowledge for industry, universities, and governmental agencies; the NSEC has also contributed to the safety improvements of LWRs and the development of partitioning and transmutation technology for reducing the impact of radioactive wastes. Recent results of the ongoing research and development (R&D) activities at NSEC are introduced in this chapter.

In one such project, JAEA assisted in the development of a photonuclear data library hosted by IAEA by providing the data for 147 out of 219 nuclides now maintained in the library. This improved-reliability database is expected to contribute to reducing the amount of radioactive wastes associated with decommissioning electron accelerator facilities (Topic 4-1).

A nuclear reaction model that evaluates nuclear data with high accuracy was also proposed. This model may be applied to nuclear transmutation investigations into the reduction of long-lived fission products (LLFP) in nuclear wastes (Topic 4-2).

To ensure the long-term integrity of the reactor pressure vessel (RPV) at the TEPCO's Fukushima Daiichi NPS (1F), the corrosion rate of steels at the air/solution interface was investigated, as this simulates the interface between cooling water and the atmosphere on the RPV inner wall. The investigation demonstrated that the corrosion rate at the air-solution interface is more than four times faster than the corrosion rate in an environment that is in constant contact with cooling water (Topic 4-3).

Prior investigations have detailed a detection limit of electron spin resonance (ESR) dosimetry of 100–200 mGy using teeth enamel; external exposure below 100 mGy is difficult to detect. Here, using pure enamel separated from dentine by centrifugation,

the detection limit was improved to less than 40 mGy. To verify and demonstrate the applicability of this methodology, the teeth of wild Japanese macaques captured at Namie-town in Fukushima Prefecture were subjected to external dose estimation, some of which show estimated exposure doses below 100 mGy (Topic 4-4).

When a large solar flare occurs, the radiation dose due to solar energetic particles (SEP) may increase, especially at flight altitudes, thus presenting a potential hazard to aircrews and passengers. A physics-based model for estimating SEP dosages anywhere in the atmosphere was therefore developed under the collaboration between several institutes in Japan. The SEP dose calculated by this system will be used as mandatory information for aviation operation management by the International Civil Aviation Organization (ICAO) (Topic 4-5).

As a part of the development of partitioning and transmutation technology, we have proposed a novel separation process called SELECT, which uses extractants comprising carbon, hydrogen, oxygen, and nitrogen. The proposed separation process allowed for the successful separation of uranium and plutonium from a dissolution solution of spent nuclear fuel; furthermore, minor actinides and rare earth elements were successfully recovered from the residual solution (Topic 4-6).

A critical experiment with plutonium fuel was conducted to validate the nuclear cross-section of lead (Pb), which acts as a moderator in an accelerator-driven system (ADS), using a critical assembly in the United States. The validity of lead nuclear data in fast-neutron system was verified by this US–Japan collaboration experiment (Topic 4-7).

To develop a material irradiation database for the design of ADSs, specimens irradiated at the proton accelerator in Switzerland underwent post-irradiation examination as the international project. Since the specimen has a special shape, the deformation behavior after irradiation varied from the standard specimen; a new correction formula is required (Topic 4-8).

4-1 Development of Photonuclear Data Library for International Contribution — Accomplishment of a Reliable Database Supporting the Use of Photonuclear Reactions —

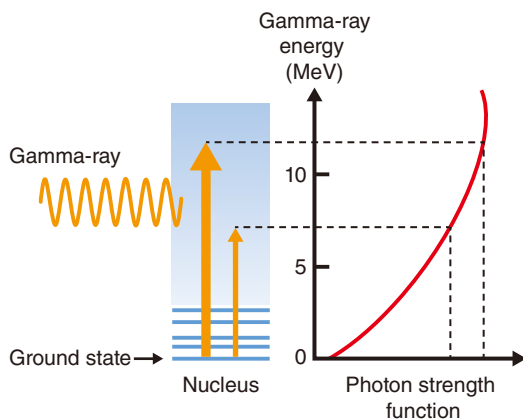


Fig.4-2 Relationship between the gamma-ray absorption of a nucleus and the photon strength function

A nucleus is excited from the ground state when it absorbs high-energy gamma-rays; the photon strength function provides the degree of absorption. In this figure, high-energy gamma-rays are more easily absorbed than low-energy ones, indicating that the cross section at the high gamma-ray energy is larger.

Photonuclear reactions are the phenomenon that occur when a nucleus is irradiated with high-energy gamma-rays. Photonuclear database is one of the fundamental libraries for scientific researches as well as practical applications. Nevertheless, large discrepancies are present between the cross sections measured at different facilities by groups which led photonuclear researches from the 1960s to the 1980s. These discrepancies make uncertainty in, for example, the amount of radioactive waste present in the decommissioning of electron accelerator facilities. As a result, the radioactive wastes increase due to taking larger margin in waste disposal. Therefore, the International Atomic Energy Agency (IAEA) began a coordinated research project to develop an improved-reliability photonuclear data library in 2016; researchers from 15 countries participated.

From extensive application viewpoints, photonuclear data are required to cover wide gamma-ray energy and nuclide ranges. As these requirements cannot be satisfied by experiments only, a nuclear reaction model is vital. Thus, the nuclear reaction model code CCONE developed by JAEA was used to help develop this database; four up-to-date photon strength function models were installed in it (Fig.4-2). By applying these photon strength functions to cross section calculations, the photon strength function model showing the best performance was selected, based on the comparison of calculated cross sections with measured data for many nuclides and wide energy ranges.

The evaluation of 140 nuclides from chlorine (atomic number

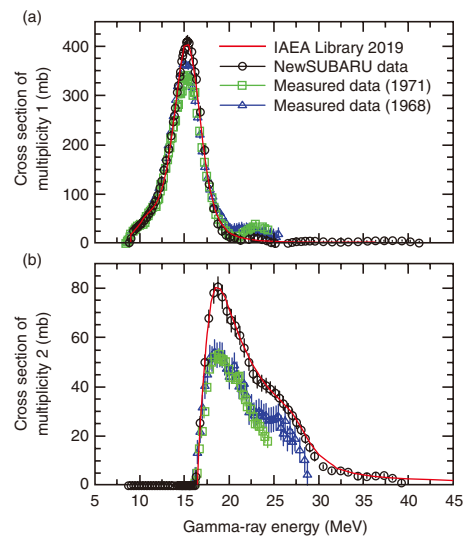


Fig.4-3 Cross sections of ^{139}La with different neutron multiplicities

Neutron multiplicity represents the number of neutrons emitted by a nuclear reaction. Here, data from the developed photonuclear data library and measured data are compared for neutron multiplicities (a) 1 and (b) 2; the developed dataset accurately reproduces the latest measured data (measured at the NewSUBARU radiation facility).

$Z = 17$) to plutonium ($Z = 94$) was then performed in the gamma-ray energy range of 1 to 200 MeV. Photonuclear data such as photo-absorption, photo-neutron, and fission cross sections were derived. In particular, the photo-neutron cross sections were carefully improved in the giant dipole resonance region (10 to 20 MeV), where the cross sections are large. This improvement leads to the increase of practicality to many fields.

To demonstrate the updates made to the library, a comparison of the evaluated photo-neutron cross sections for Lanthanum-139 (^{139}La) for multiplicities 1 and 2 is shown in Fig.4-3. The calculated data are in good agreement with those submitted by the collaborating experimental groups; further, the amount of neutrons emitted by photonuclear reactions was shown to be larger than previously considered.

The developed photonuclear data library includes the nuclear data of 219 nuclides from deuterium (^2H) to ^{241}Pu , of which the nuclear data for 140 new and 7 existing nuclides were provided by JAEA. This is remarkable contribution to the database development.

The resulting improved and more reliable photonuclear database is expected to contribute to a reduction in the radioactive waste associated with decommissioning electron accelerator facilities, and to the optimization of gamma-ray irradiation used in radiation therapy for human subjects.

(Nobuyuki Iwamoto)

Reference

Kawano, T., Iwamoto, N. et al., IAEA Photonuclear Data Library 2019, Nuclear Data Sheets, vol.163, 2020, p.109–162.

4-2 Development of Nuclear Data for LLFP Transmutation

— Models to Predict the Nuclear Cross-Section of Long-Lived Fission Products (LLFPs) —

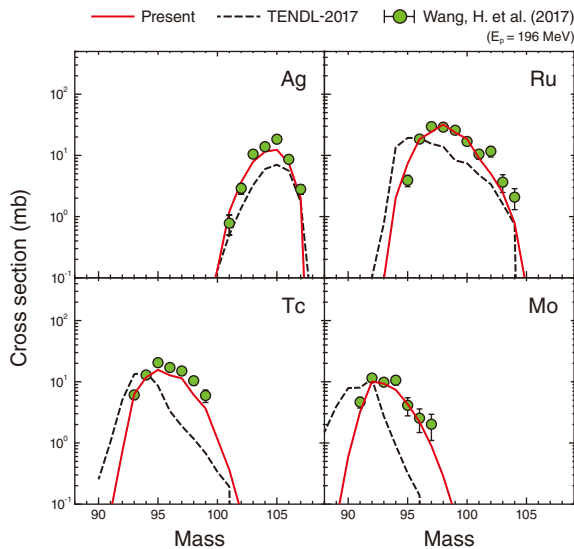


Fig.4-4 Nuclear cross-section of isotopes produced via the $p + {}^{107}\text{Pd}$ reaction

Calculated and experimental cross-section data of the Ag, Ru, Tc, and Mo isotopes resulting from irradiating a ${}^{107}\text{Pd}$ beam into a proton target. The present evaluation method better reproduced the experimental data (Wang, H. et al. (2017))^{*} than the existing nuclear data (TENDL-2017).

Nuclear reactors generate radioactive wastes, a part of which can retain high radioactivity for generations. In Japan, a deep geological repository has been mapped out to avoid passing the management of high-level wastes (HLWs) on to future generations. Another method to reduce the noxiousness of HLWs may be by transmuting the long-lived fission products (LLFPs) in HLW into short-lived or stable isotopes.

One proposed method of inducing transmutation involves irradiating a proton or neutron beam produced by an accelerator or reactor into LLFP. To draw the most efficient blueprint of the transmutation system, numerical simulation is necessary, which requires detailed nuclear data as input such as proton and neutron cross-sections of LLFP. However, due to the difficulty in measuring the cross-sections of LLFP samples experimentally, the available nuclear data is limited. Thus, evaluating the transmutation system with high accuracy has not yet been possible.

To evaluate cross-sections when experimental data is limited, a nuclear model is required. To this end, an evaluation method that can produce nuclear data with higher accuracy than conventional models was developed by adopting (1) resonance capture cross-sectional data of low-energy neutrons based on the nuclear statistical properties, (2) gamma-ray emission probabilities derived from up-to-date nuclear models, and (3) nuclear-level densities computed from a new nuclear model considering nuclear deformation. Finally, we developed a new

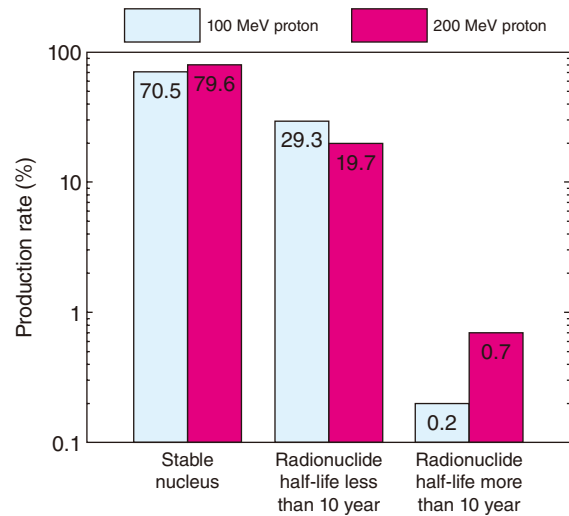


Fig.4-5 Resulting isotopes from simulated transmutation

Ratio of nuclides produced by irradiating a proton beam (100 and 200 MeV) into ${}^{107}\text{Pd}$. The majority of ${}^{107}\text{Pd}$ was changed into stable or short-lived isotopes with half-lives of less than 10 years.

evaluated data file with the evaluation method.

Fig.4-4 shows nuclear cross-section of isotopes produced via proton and ${}^{107}\text{Pd}$. The present evaluation method gives superior capabilities in reproducing experimental data (Wang, H. et al. (2017))^{*} than the existing nuclear data (TENDL-2017). The evaluated data was then applied to simulate transmutation; the irradiation of a proton into ${}^{107}\text{Pd}$ (half-life: 6.5 million years) is shown as an example in Fig.4-5. Here, the majority of ${}^{107}\text{Pd}$ was transformed into stable or short-lived isotopes with half-lives of less than 10 years.

The developed evaluated data is expected to contribute nuclear research into employing transmutation as a method for reducing and resource recycling of LLFPs. Similarly, the new evaluation method, developed using up-to-date nuclear models, may also be applicable to non-LLFP nuclides. In future, we plan to provide database important for development of neutron source using accelerator and radiation dose evaluation of medical proton accelerator facility with the evaluation method.

This work was funded by the IMPACT Program of Council for Science, Technology and Innovation (Cabinet Office, Government of Japan), “Reduction and Re-source Recycling of High-level Radioactive Wastes through Nuclear Transmutation”.

(Futoshi Minato)

^{*} Wang, H. et al., Spallation Reaction Study for the Long-Lived Fission Product ${}^{107}\text{Pd}$, Progress of Theoretical and Experimental Physics, vol.2017, issue 2, 2017, p.021D01-1–021D01-10.

Reference

Kunieda, S., Minato, F. et al., JENDL/ImPACT-2018: A New Nuclear Data Library for Innovative Studies on Transmutation of Long-Lived Fission Products, Journal of Nuclear Science and Technology, vol.56, issue 12, 2019, p.1073–1091.

4-3 Accelerated Corrosion of Low-Alloy Steel at the Air/Solution Interface

— Clarification of Corrosion test Acceleration Mechanism from Structural Analysis of Rust Layer —

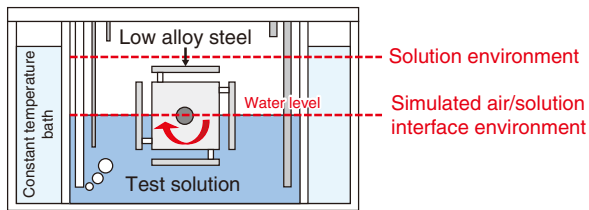


Fig.4-6 Simulated air/solution interface and corrosion environment

The water level is adjusted to maintain a solution environment and simulate the air/solution interface.

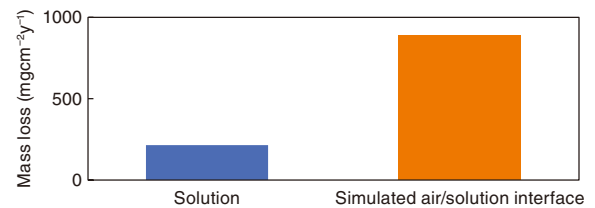


Fig.4-7 Corrosion acceleration at the simulated air/solution interface

The corrosion rate is more than four times higher at the simulated air/solution interface than in the solution environment.

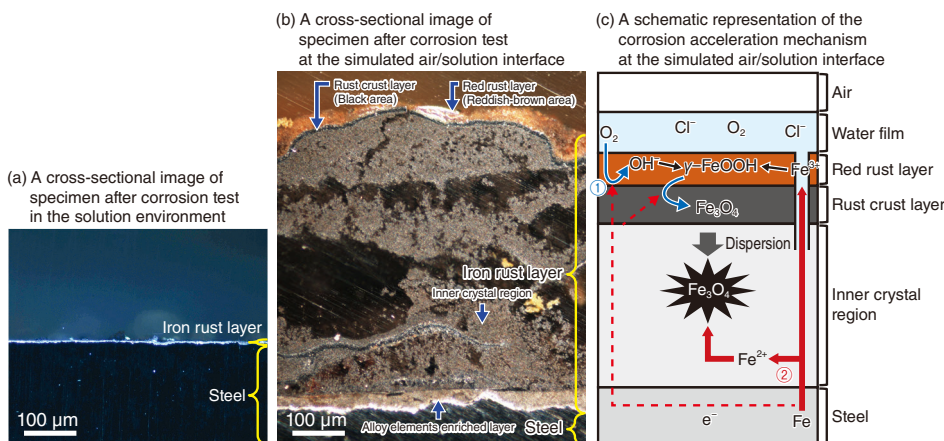


Fig.4-8 Cross-sectional images of specimens after corrosion tests (a) in the solution environment and (b) at the simulated air/solution interface; and (c) a schematic representation of the corrosion acceleration mechanism at the simulated air/solution interface

The corrosion of low-alloy steel is accelerated due to the formation of a complicated rust layer at the simulated air/solution interface, because the rust as this layer contributes to the acceleration of the oxygen reduction reaction at the interface.

Units 1–3 of the TEPCO's Fukushima Daiichi NPS (1F) have been injected with cooling water; internal investigations of the reactor have confirmed that low-alloy steels (steels containing $\leq 10\%$ of alloying elements) are exposed to an air/solution interface. Previous studies have shown that the corrosion rate of carbon steel at the air/solution interface is increased by the formation of a liquid film on the carbon steel, as the film accelerates the oxygen reduction reaction. However, the corrosion rate of low-alloy steels used in the 1F reactor pressure vessel (RPV) at the air/solution interface have not yet been clarified.

Therefore, corrosion tests of low-alloy steel were performed in a solution environment and at a simulated air/solution interface using the test apparatus shown in Fig.4-6. The results indicated that the corrosion rate of low-alloy steel at the air/solution interface was more than four times faster than that in the solution environment (see Fig.4-7).

Cross-sectional observations of the rust layer were then performed to clarify the mechanism behind this acceleration; the resulting images are shown in Figs.4-8(a) and (b). Although a red rust layer was formed in the solution environment, it was peeled off during the process of pulling up from the solution, leaving only a thin layer of iron rust. On the other hand, cross-sectional analysis indicated that the rust layer formed at the simulated air/solution environment had a red rust layer consisting of γ -FeOOH, a rust crust layer consisting of Fe_3O_4 ,

an inner crystal region composed of crystalline Fe_3O_4 , and an alloy-elements-enriched layer at the rust-steel interface. Only the inner crystal region became thicker during the growth of the iron rust layer.

A schematic of the accelerated corrosion mechanism of the low-alloy steel at the simulated air/solution interface is shown in Fig.4-8(c). Here, the oxygen reduction reaction (①: $1/2\text{O}_2 + \text{H}_2\text{O} + \text{e}^- \rightarrow 2\text{OH}^-$), which controls corrosion, occurs in the rust crust layer near the liquid film that is in contact with the air. The electrical connection between the crust layer and steel was confirmed through the inner crystal region; this suggests that electrons generated by the iron dissolution reaction (②: $\text{Fe} \rightarrow \text{Fe}^{2+} + 2\text{e}^-$) are supplied to the crust layer. The oxygen reduction reaction thus likely occurs in the crust layer despite the thickening of the inner crystal region. Meanwhile, no crust layer was formed in the solution environment, due to the low supply of oxygen via diffusion. Therefore, a slower corrosion rate is expected in the solution environment, because the accelerated corrosion, contributed to by the rust crust layer, does not occur.

This study shows that the formation of the crust layer causes the accelerated corrosion of low-alloy steel at the air/solution interface. Future work will aim to clarify the effects of oxygen concentration and seawater composition on the corrosion rate and mechanism, which will contribute to ensuring the long-term integrity of the 1F RPV.

(Kyohei Otani)

Reference

Otani, K. et al., Analysis for the Mechanism of Accelerated Corrosion on Low Alloy Steel in Air-Solution Alternating Condition, *Zairyo-to-Kankyo*, vol.68, issue 8, 2019, p.205–211 (in Japanese).

4-4 Extension of Applicable Range of ESR Dosimetry via Enamel Separation Techniques

— External Exposure Dose Estimation of Wild Japanese Macaque in Fukushima Prefecture —

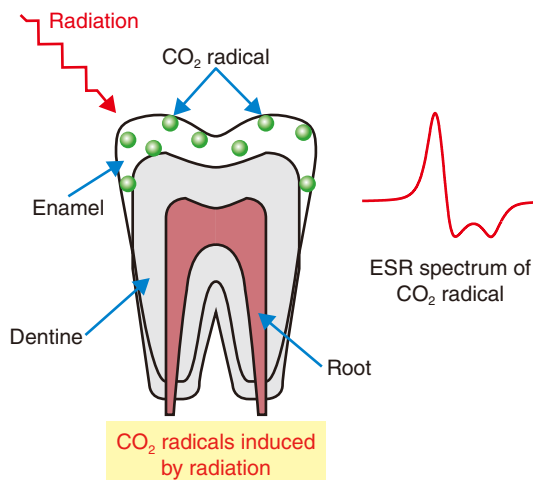


Fig.4-9 CO₂ radicals induced by radiation

The intensity of the CO₂ radicals present in tooth enamel can be measured by ESR spectrometry.

The release of radioactive materials from the TEPCO's Fukushima Daiichi NPS (1F) to the environment has resulted in long-term low-dose (below 100 mGy) exposure to humans and animals. To understand the biological effects and ensure radiation safety for individuals, the precise estimation of exposure dose is important.

Electron spin resonance (ESR) dosimetry is a powerful tool for exposure dose estimation. During ESR dosimetry, the CO₂ radical, which is induced in tooth enamel by radiation and retained with a lifetime of more than 10⁷ years, is measured, as shown in Fig.4-9. The relationship between exposure dose and CO₂ radical intensity, i.e., the dose–response curve, enables the estimation of the external exposure dose of individuals. This technique has been commonly applied to estimate high-dose exposure (from a few hundred mGy to a few Gy) in humans, for example, after exposure by an atomic bomb, the nuclear plant accident in Chernobyl, or working in the nuclear industry workers. ESR dosimetry using human teeth has been reported to have a detection limit of 100–200 mGy. However, to apply ESR dosimetry for the dose estimation due to the 1F accident, this limit must be improved. This work therefore aimed to improve the detection limit to detect the exposure dose below 100 mGy using enamel separation technique by centrifugation; the developed methodology was then applied to detect the exposure dose of wild Japanese macaque from Fukushima Prefecture.

Organic materials in dentine are known to interfere when using ESR to measure the CO₂ radical; it has been necessary to remove dentine and prepare dentine-free enamel samples. However, because of the small size of macaque teeth, it is difficult to grind away with a dental bur. Here, dentine was removed based on

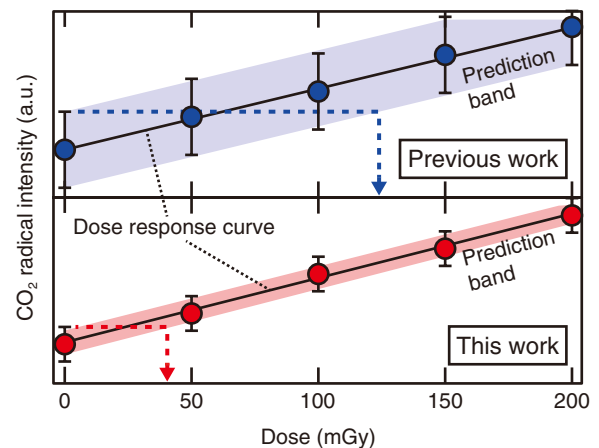


Fig.4-10 Dose–response curve for tooth enamel

The purple and red bands represent the 90% prediction bands of each curve. Dotted arrows show the detection limit. The methodology proposed here was demonstrated to more precisely estimate a lower exposure dose than prior methods.

the difference in the density between enamel and dentine. To do so, the molar teeth of Japanese macaque were crushed into grains using a cryo-press; the enamel (density of 2.0–2.1 g/cm³) was separated from dentine (density of 2.8–3.0 g/cm³) by centrifugation. By this developed methodology, we can obtain “pure” enamel than the prior one.

To obtain the dose–response curve, enamel samples were irradiated by a ⁶⁰Co gamma ray up to 200 mGy (50, 100, 150, and 200 mGy) by cumulative irradiation. Before the first irradiation and after each irradiation, samples were measured by ESR to obtain a precise dose–response curve (see Fig.4-10). From this dose–response curve, the detection limit was estimated to be < 40 mGy. Seven wild Japanese macaques captured in Namie in the Fukushima Prefecture, about 15 km away from 1F, were then subjected to external dose estimation. Three of them had an estimated exposure dose between 45–81 mGy, which cannot be measured by prior methods.

The improved detection limit will enable the examination of the relationship between external radiation doses (≥ 40 mGy) and the resulting biological effects on wild Japanese macaques, as well as on Japanese field mice and raccoons in Fukushima Prefecture; future aims include assessing the exposure radiation dose for children in Fukushima Prefecture.

This study was conducted on “Dose assessment of external radiation exposure in Fukushima children using deciduous teeth”, supported by the Japan Society for the Promotion of Science (JSPS) KAKENHI Grant-in-Aid for Scientific Research (C) (No.18K09906).

(Toshitaka Oka)

Reference

Oka, T. et al., External Exposure Dose Estimation by Electron Spin Resonance Technique for Wild Japanese Macaque Captured in Fukushima Prefecture, Radiation Measurements, vol.134, 2020, p.106315-1–106315-4.

4-5 Real-Time Estimation of Radiation Dose at Flight Altitudes

— Development of Warning System for Aviation Exposure to Solar Energetic Particles (SEPs) —

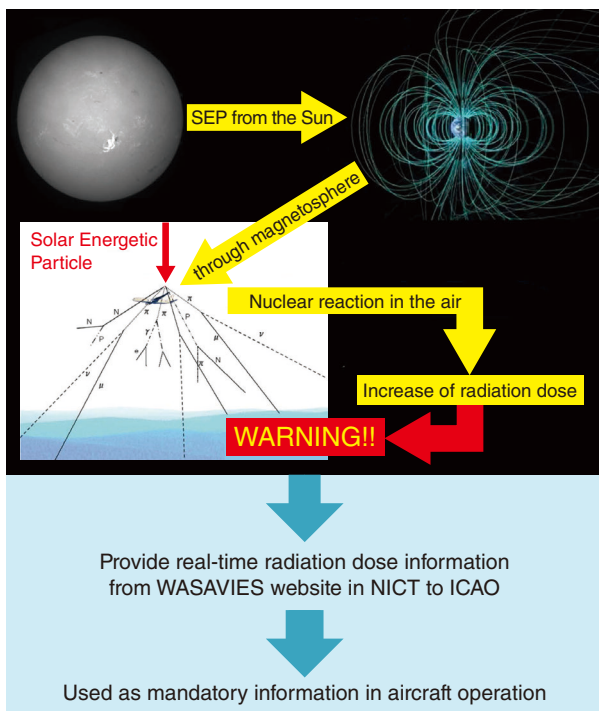


Fig.4-11 Information flow in WASAVIES

WASAVIES consists of the combination of three SEP transport simulation models from the Sun to the ground level of the Earth. When the calculated radiation doses at flight altitude exceed a certain threshold level, a warning is issued to airline companies through the ICAO.

When a large solar flare occurs, the radiation doses due to solar energetic particle (SEP) may increase, especially at flight altitudes, and can thus be a potential hazard to aircrews and passengers. Therefore, the development of a system for nowcasting and/or forecasting radiation doses due to SEP exposure is an important challenge in space weather research. Collaboration with other research fields such as nuclear physics and radiological protection is key for such a development.

A physics-based model was thus developed for SEP dose estimation anywhere in the atmosphere; this model, designated as the Warning System for Aviation Exposure to Solar Energetic Particles (WASAVIES) and summarized in Fig.4-11, was developed via collaboration between several institutes in Japan. WASAVIES is based on the combination of three SEP transport simulation models from the Sun to the ground level of the Earth. When the calculated radiation doses at flight altitude exceed a certain threshold, a warning is issued to airline companies through the International Civil Aviation Organization (ICAO). JAEA was responsible for developing the SEP transport simulation model in the atmosphere based on PHITS and integrating the models to develop the automatic analysis program.

The performance of WASAVIES was examined by analyzing the four major solar particle events of the 21st century; the accuracy of the nowcast data obtained by the model has

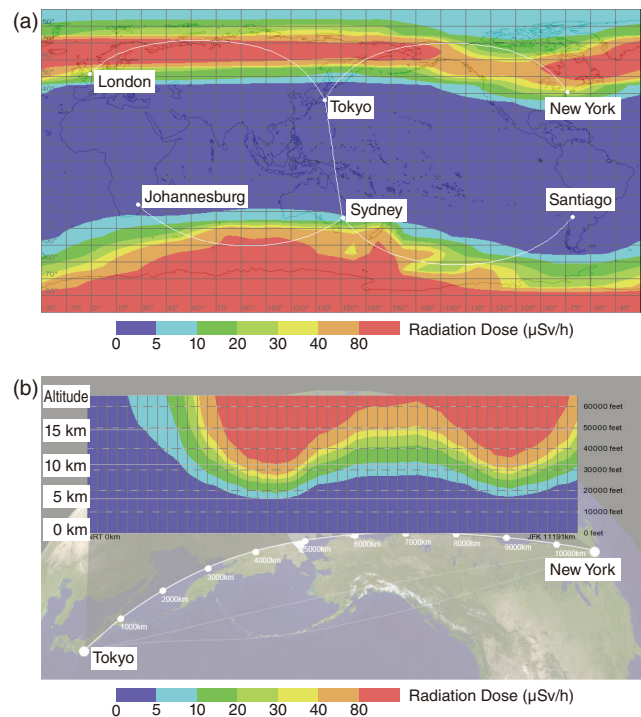


Fig.4-12 Example of radiation doses calculated by WASAVIES
Panels (a) and (b) show the worldwide dose rate map at 12 km and route-dose rate map between Tokyo and New York, respectively, during the peak of the solar particle event occurring on Jan. 20th, 2005.

been validated by the reproducibility of ground and satellite observations. The WASAVIES-calculated worldwide dose rate map at 12 km and route-dose rate map between Tokyo and New York during the peak of the solar particle event occurring on Jan. 20th, 2005 are shown in Figs.4-12(a) and (b) respectively. The complicated latitude, longitude, and altitude dependences of the dose rates, such as the southern asymmetry, can be seen in these figures, owing to the sophisticated physics models implemented in WASAVIES.

A web-interface of WASAVIES was also developed and opened via the public server of the National Institute of Information and Communications Technology (NICT, <https://wasavies.nict.go.jp/>) on Nov. 7th, 2019. The radiation dose during solar flares calculated via WASAVIES will be used as mandatory information for aviation operation management by ICAO. This study demonstrates a successful example of interdisciplinary research achieved through collaboration among researchers in various fields, such as space weather, solar physics, upper atmosphere, nuclear physics, and radiation protection.

This study was partly supported by the Japan Society for the Promotion of Science (JSPS) KAKENHI Grant-in-Aid for Scientific Research on Innovative Areas (Research in a proposed research area)(No.15H05813).

(Tatsuhiko Sato)

Reference

Sato, T. et al., Real Time and Automatic Analysis Program for WASAVIES: Warning System for Aviation Exposure to Solar Energetic Particles, Space Weather, vol.16, issue 7, 2018, p.924-936.

4-6 Separation of Minor Actinides Using Incinerable Extractants

— Recovery of Minor Actinides and Rare Earth Elements in a Concrete Cell —

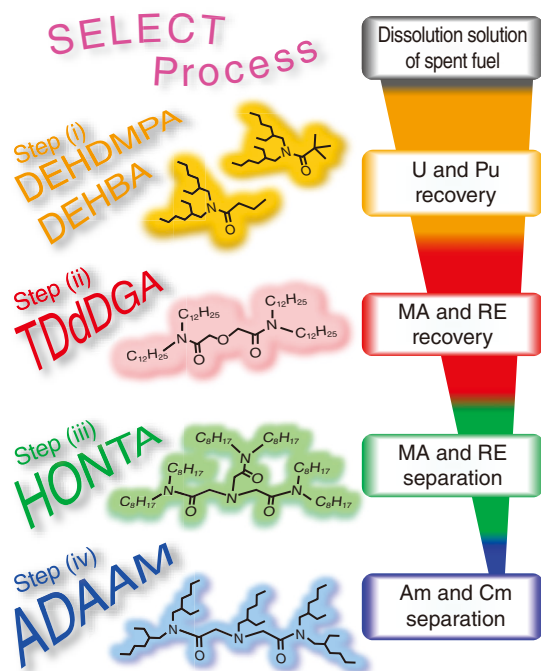


Fig.4-13 Schematic of SELECT process and extractants used
Extractants decomposed into gases by incineration are employed to reduce the volume of secondary waste.

To reduce the radiotoxicity and volume of high-level radioactive waste, separation and transmutation technologies by which some radioactive isotopes are transmuted using an accelerator-driven system after separation from a dissolution solution of spent nuclear fuel or high-level liquid waste have been under development. The separation of americium (Am) and curium (Cm), designated here as minor actinides (MAs), is necessary to achieve this goal, as MAs consist of isotopes with high radioactive toxicity or a high heat-generation rate.

Many of the solvent separation processes developed to date use extractants consisting of phosphorus and sulfur; however, such extractants are difficult to decompose into gases by incineration, and thus can increase secondary waste. To overcome this challenge, a separation process using extractants comprising carbon, hydrogen, oxygen, and nitrogen was developed; this process, entitled SELECT (Solvent Extraction from Liquid waste using Extractants of CHON-type for Transmutation), is summarized schematically in Fig.4-13, including the extractants used in each step. Since the dissolution solution of spent nuclear fuels and high-level radioactive liquid waste consist of various elements, single-step separation is difficult. The SELECT process, therefore, consists of four steps.

In Step (i), uranium (U) and plutonium (Pu) are recovered

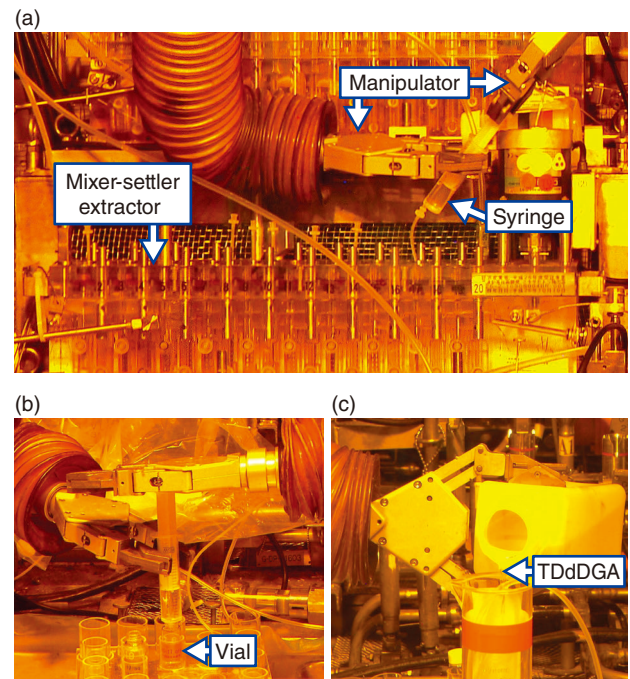


Fig.4-14 Recovery of MA and RE performed in a concrete cell
(a) Sampling from mixer-settler extractors using a syringe, (b) transferring a sample in to a vial, and (c) adding the extractant TDdDGA.

from the dissolution solution of spent nuclear fuel; they can be reused as nuclear material. The MAs and rare earth elements (REs) are then recovered from other fission products in Step (ii), and thereafter MA and RE are separated from each other in Step (iii). Finally, Am and Cm are then separated in Step (iv).

The successful demonstration of Step (i) has been performed via continuous counter-current experiments, in which monoamides such as DEHBA and DEHDMPA were used as extractants. A continuous counter-current experiment was thus designed and carried out to validate Step (ii) using a high-level liquid waste obtained from the demonstration of Step (i) (Fig.4-14). Although TODGA has been commonly employed as an extractant to recover MA and RE from high-level liquid waste, TDdDGA was used here, due to its demonstrated higher extraction capacity. Due to the high radioactivity of the experimental solution, the experimental apparatuses were installed in a concrete cell and were operated by manipulators.

The resulting recoveries of the MAs and REs were >98% and 86.9–99.9%, respectively, thus demonstrating the validity of Step (ii). For further development of SELECT process, studies on Step (iii) and Step (iv) using HONTA and ADAAM as extractants, respectively, are ongoing.

(Yasutoshi Ban)

Reference

Ban, Y. et al., Extraction of Trivalent Rare Earths and Minor Actinides from Nitric Acid with *N,N,N',N'*-Tetradodecyldiglycolamide (TDdDGA) by Using Mixer-Settler Extractors in a Hot Cell, *Solvent Extraction and Ion Exchange*, vol.37, issue 1, 2019, p.27–37.

4-7 Validation of Nuclear Design Accuracy for ADS

— Critical Experiment with Plutonium Fuel —



Fig.4-15 Critical Assembly 'COMET', in the United States National Criticality Experiments Research Center (NCERC)
(<https://www.nssc.gov/pages/facilities/NCERC.html>).

A fast-neutron system dedicated to transmutation (i.e., an accelerator-driven system: ADS) has been investigated to reduce the environmental burden of high-level radioactive waste (HLW). An ADS is capable of converting partitioned long-lived nuclides with strong radiotoxicity into stable or short-lived nuclides by fission reactions with neutrons. The top candidate for a coolant used in the ADS is lead bismuth, which is chemically stable and highly safe. However, Japan nuclear facilities do not have experience with the use of lead bismuth as a nuclear reactor coolant, and the characteristics of the nuclear reaction (i.e., the probability of reaction, or nuclear cross-section) of lead have not been sufficiently verified. Hence, experimental work was performed to validate the nuclear cross-section of lead in fast-neutron cores using a critical assembly (Fig.4-15) in the United States.

In an ADS, fast neutrons generated by the spallation reaction of a lead-bismuth target are gradually moderated by a nuclear reaction with a lead-bismuth coolant, leading to fission after absorption to long-lived nuclides. Fast neutrons generated by the fission are also used for the next fission reaction through a similar moderation process (fission chain reaction). Thus, to correctly predict the neutron-mediated fission chain reaction in an ADS, it is important to accurately evaluate the nuclear cross-section of lead that affects the neutron moderation in the coolant. Because moderation of fast neutrons exhibits different tendencies for different types of fuel, verification in several kinds of fuel is effective and reliable.

To verify the nuclear cross-section of lead, the effect of removing (voiding) the lead from an experimental core on a fission chain reaction was measured. The influence is known as the “lead-void-reactivity worth”. By voiding lead, neutrons are less moderated, maintain their high speeds, and are thus more likely to cause further fission in a core with a particular fuel or to escape from one core into another. This different tendency

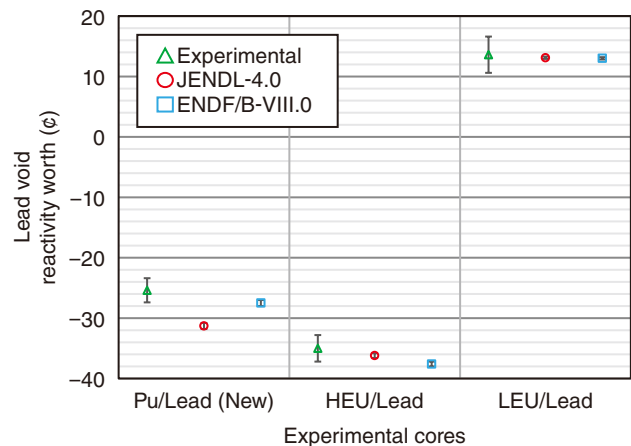


Fig.4-16 Comparison of experimental and calculated reactivity worth

The experimental data is indicated as \triangle . The analytical results using the evaluated nuclear-data library developed by JAEA (JENDL-4.0) and the United States (ENDF/B- VIII.0) are indicated as \circ and \square , respectively. The accuracy of each nuclear data library was validated by this experimental series.

among fuel characteristics results in an accurately measurable value, i.e., the criticality (reactivity) of the core, and allows for the verification of the nuclear cross-section of lead. Two experimental cores with different uranium (U) isotope ratios, including a highly-enriched uranium (HEU)/lead-experimental core rich in ^{235}U and a low-enriched uranium (LEU)/lead-experimental core rich in ^{238}U , have been constructed. Recently, a measurement was conducted using a plutonium (Pu) /lead-experimental core in a similar way as the experiments using U.

In Pu fuel, neutrons moderated by lead generally have a higher probability of fission than unmoderated fast neutrons. Therefore, removing the lead from the Pu/lead experimental core decreased the amount of moderated neutrons escaping from the core; the fission chain reaction then became less likely to occur. This resulted in a negative lead-void-reactivity worth, as shown in Fig.4-16. These measurements were compared with the calculated values using nuclear cross-section data developed in Japan (JENDL-4.0) and the United States (ENDF/B-VIII.0). The results calculated using ENDF/B-VIII.0 well reproduced the experimental data, whereas using JENDL-4.0 caused an overestimation by almost 6 cents in absolute value. Further analysis of the gap between the calculations using JENDL-4.0 and ENDF/B-VIII.0 indicated that the fundamental cause was due to the difference in the nuclear data of the Pu isotope ^{239}Pu , and not that of lead.

By this study, experimental data using Pu were added to a series of experiments for reliable validation of the nuclear cross-sections of lead. Cooperation between the research groups in Japan and the United States will continue to further advance R&D into transmutation technology by expanding experimental data validating nuclear cross-sections.

This research was conducted as part of a collaboration with the Los Alamos National Laboratory in the United States.

(Akito Oizumi)

Reference

Fukushima, M., Oizumi, A. et al., Systematic Measurements and Analyses for Lead Void Reactivity Worth in a Plutonium Core and Two Uranium Cores with Different Enrichments, Nuclear Science and Engineering, vol.194, issue 2, 2020, p.138–153.

4-8 Development of Beam Window Materials for ADSs

— Post-Irradiation Examination of Beam Window Materials through International Project —

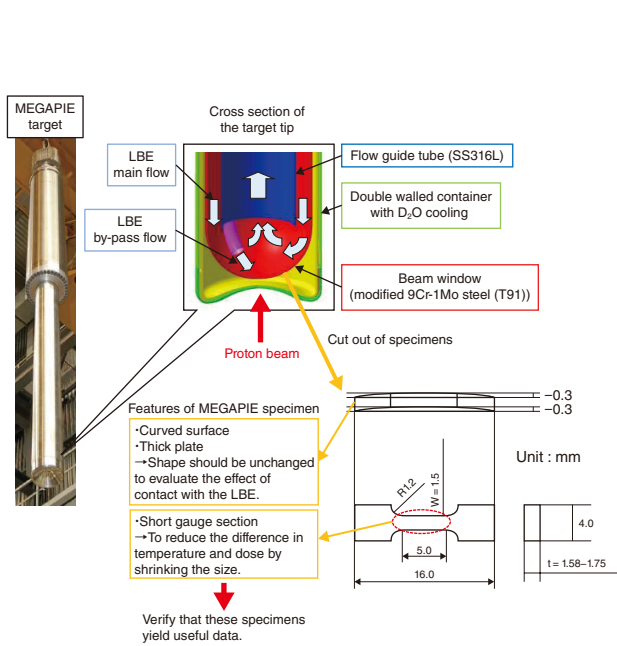


Fig.4-17 Overview of MEGAPIE (MEGAWatt Pilot Experiment) Irradiation

The MEGAPIE target was irradiated with protons under LBE flow. The specimens, made of modified 9Cr-1Mo steel (T91), were cut from the beam window (BW) section of the target. Post-irradiation examination (PIE) was carried out by participating countries.

A beam window (BW) of an ADS is required to transmuted long-lived radioactive nuclides contained in spent fuel using proton accelerators and is corroded by high-temperature lead-bismuth eutectic (LBE) alloys. The BW is located in a severe environment and can be seriously damaged by the irradiation of impinging protons and spallation neutrons. It is therefore necessary to understand the possible irradiation damage to the BW material. However, the number of facilities worldwide where experimental irradiation of BW materials under such a severe environment is limited. Thus, an international project entitled the Megawatt Pilot Experiment, i.e., MEGAPIE, was launched with an aim of constructing an irradiation database of candidate materials for ADSs.

As shown in Fig.4-17, the particle accelerator at Paul Scherrer Institute in Switzerland was used to irradiate the LBE flow protons. Post-irradiation examinations (PIEs), in which the specimens made of modified 9Cr-1Mo steel (T91) were cut from the beam window of the target to examine the changes of their mechanical properties, were shared by the participating countries. However, the shapes of the specimens in the PIEs were very different from those of standard specimens, i.e., the specimens were as twice thick as the standard ones, and specimens' surfaces were curved. To verify whether useful data could be obtained from these differently shaped specimens, the effects of the shape on the tensile properties were studied systematically using non-irradiated specimens. Although prior researchers have investigated the impact of shape on tensile

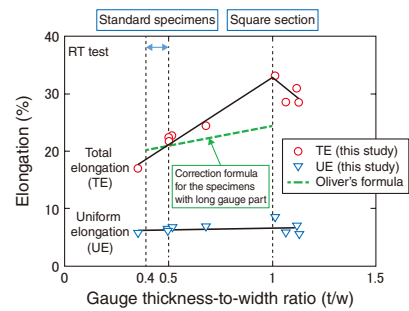


Fig.4-18 Relationship between the elongation of non-irradiated specimens and the gauge thickness-to-width ratio (t/w)

Here, the total elongation increased with increasing t/w ; in uniform elongation, the t/w has no effect on the elongation. The correction formula for standard specimens thus cannot represent the data obtained for MEGAPIE specimens.

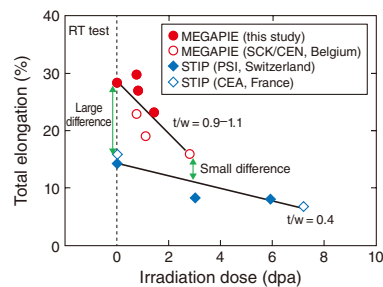


Fig.4-19 Relationship between the total elongation of irradiated specimens and irradiation dose

A difference in total elongation due to different t/w decreases with the increase in irradiation dose. This is caused by the deformation behavior changes due to the irradiation defects introduced into the material.

properties, the gauge the specimens in question have all been sufficiently long ($l/w > 5.5$, here, l is the lengths of the gauge sections); here, however, the gauge parts of the specimens obtained from MEGAPIE ($l/w = 3.33$) were rather short.

The results indicated that the strength and uniform elongation of the specially shaped specimens were similar to those of the standard specimens, but the total elongation was 1.5 to 2.0 times higher. Further, examination of the effects of the gauge thickness/width ratio (t/w) on the tensile properties indicated that the total elongation increased with increasing gauge thickness until $t/w = 1$, as shown in Fig.4-18. Known correction formulas for standard specimens (long gauge) could not be applied to these specially shaped MEGAPIE specimens. Regarding irradiated specimens, the reduction rate of the total elongation with increasing irradiation dose was higher than that of the standard specimens, as shown in Fig.4-19. Therefore, a correction formula considering both the difference in shape and the decrease of elongation due to irradiation was proposed.

When studying accelerator-irradiated materials such as those used in ADSs, specially shaped specimens are unavoidable; the proposed correction formula will thus be useful for future design of ADS materials and the PIE of irradiated materials.

In addition, no specific effects due to contact with the LBE was observed in this irradiation. Future work will consist of irradiation tests under higher temperatures for further investigation of ADS design.

(Shigeru Saito)

Reference

Saito, S. et al., Experimental Validation of Tensile Properties Measured with Thick Samples Taken from MEGAPIE Target, Journal of Nuclear Materials, vol.534, 2020, p.152146-1-152146-16.

Contributions to Developments in Science, Technology, and Academic Research

In accordance with the Science and Technology Basic Plan formulated by the Government of Japan, we have aimed to contribute to the advancement of science and technology and the promotion of industry in Japan through the production of innovative results using neutron and synchrotron radiation. This has included using the high-intensity proton accelerator at the Japan Proton Accelerator Research Complex (J-PARC) and the JAEA synchrotron radiation beamlines at the Super Photon ring-8 GeV (SPring-8), as well as upgrading neutron facilities and devices and pursuing world-leading research in fields such as nuclear energy and materials sciences that utilize neutron and synchrotron radiation.

(1) Research and development at J-PARC

J-PARC comprises a series of three proton accelerators, including a linear accelerator (linac), a 3-GeV rapid cycling synchrotron (RCS), and a 50-GeV synchrotron, and three experimental facilities. These facilities include the Materials and Life Science Experimental Facility (MLF) for a wide range of research fields using neutron and/or muon beams (Fig.5-1), the Hadron Experimental Facility for nuclear and particle physics experiments using K-mesons and other particles, and the Neutrino Experimental Facility for T2K particle physics experiments using neutrinos. These experimental facilities are open to users from across the globe.

Successive tests and component improvements have been conducted on the accelerators to realize stable operation with a 1-MW beam; as a result, a stable and continuous operation at 1 MW for 10.5 hours has been achieved. At the MLF, the user program for seven scheduled run cycles (153 days) was successfully accomplished with an availability of over 90%.

The first stage of a radio-frequency quadrupole linac (RFQ) was developed under an upgraded program. This RFQ is an unprecedented RFQ that incorporates an optimal beam-dynamics design for accelerating large-current beams, thus allowing for a more stable operation of the accelerator (Topic 5-1).

A new beam feedback system was introduced to the RCS to improve the quality of the extracted beam after acceleration and further reduce beam loss.

At MLF, 21 neutron spectrometers and 2 muon instruments were constructed, and a wide range of experiments related to materials and life science have been conducted. On the surface of the Earth, hydrogen atoms in minerals generally take an asymmetric position between two oxygen atoms. Using the neutron diffractometer “PLANET” (Beam Line No.11), the symmetrization of hydrogen bonding in a mineral in the deep Earth was found at the high pressure of 18.1 GPa, which corresponds to the pressure at approximately 520 km deep into the Earth’s mantle (Topic 5-2).

As the high-intensity proton beam injects to the neutron target, cavitation damage degrades the structural integrity of the mercury target vessel. By adopting double-walled structure

and narrowing the channel for the mercury target vessel, the cavitation damage during high power operation of MLF was reduced drastically, thus confirming the cavitation reduction effect by decreasing the width of channel and increasing the flow velocity (Topic 5-3). This double-walled structure was adopted in the actual target vessel, and post irradiation examination data shows the designed structure can drastically reduce the cavitation damage.

(2) Research and development at the Materials Sciences Research Center (MSRC)

MSRC aims to create innovative results and seed research in a wide range of scientific, technological, and academic fields by developing and improving neutron and synchrotron radiation instruments for advanced structural and functional analysis in Tokai (JRR-3 and J-PARC) and in Harima (SPring-8).

In FY2019, a novel and precise texture measurement technique using the accelerator-driven compact neutron source was successfully developed in strong collaboration with the Institute of Physical and Chemical Research (RIKEN) (Topic 5-4). The developed technique is expected to contribute to the development of innovative materials and products at various manufacturing sites, as it does not require large neutron experimental facilities.

An identified structural change of protein was investigated using inelastic neutron scattering techniques and computer simulations (Topic 5-5). This change was used to clarify the mechanism of function of proteins. This achievement confirmed the importance of studying protein dynamics by the inelastic neutron scattering technique and showed that this technique is a powerful tool for investigating the function of proteins. This research was done in collaboration with University of Tokyo, Tokyo Institute of Technology, Japan Synchrotron Radiation Research Institute, Comprehensive Research Organization for Science and Society, and JAEA. Ionic liquids have recently been investigated as promising candidates as non-inflammable electrolyte in rechargeable batteries. Their practical use would allow for a rechargeable battery that is safer than current products. Here, the unknown structure of the electric double layer in the vicinity of the electrolyte–electrode interface was detected using neutron reflectivity measurements (Topic 5-6).

The mechanism behind the working memory of amorphous aluminum oxide, which is a candidate for next-generation nonvolatile memory to prevent deterioration by rewriting, was studied in cooperation with the National Institute for Materials Science and the National Institute of Advanced Industrial Science and Technology (Topic 5-7). These results contributed to the development of next-generation nonvolatile memory with low electricity consumption.

A new superconductor, UTe_2 , was discovered at the end of 2018. The first successful observation of the electronic state of UTe_2 was achieved (Topic 5-8). Future work will aim to continue contributing to the universal understanding of various material properties, such as magnetism and electronic conductivity of uranium compounds.



Fig.5-1 J-PARC’s first experimental hall at MLF

5-1 Toward Upgrading High-Intensity Proton Accelerators — A Radio Frequency Quadrupole Linac Using a New Beam Dynamics Design Scheme —

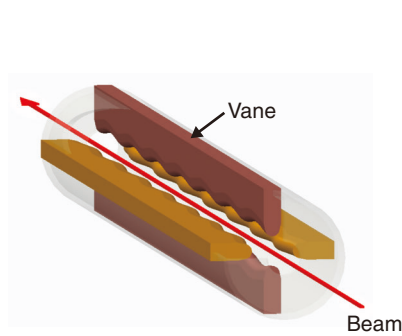


Fig.5-2 Schematic view of the RFQ
Acceleration and focusing are done by the electric field generated by four vanes.

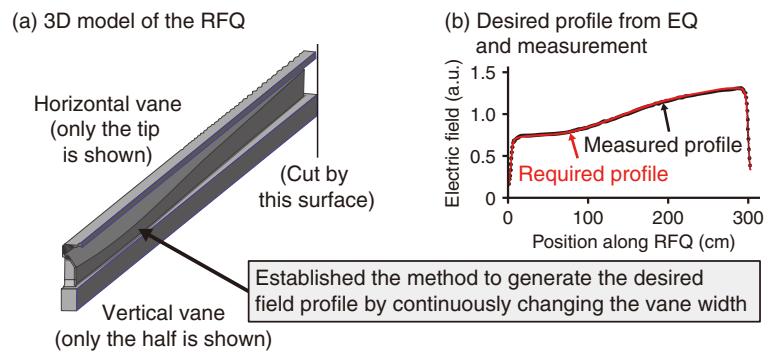


Fig.5-3 3D design method to obtain the desired field from the equipartitioning
To obtain the desired field profile, the shape of the RFQ was designed using a 3D model (a). The measured field was agreed well to the desired one as shown in (b).

(a) Under testing at the RFQ test stand

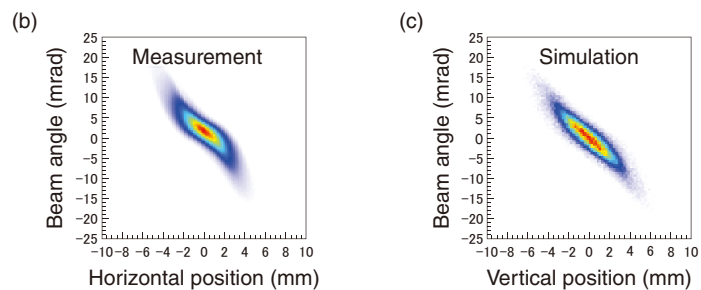


Fig.5-4 Beam test of the new RFQ

The beam test of the new RFQ was conducted at the test stand (a). The right figures indicate the spread of the beam. The simulation (c) and the measurement (b) are agreed within the uncertainty of the injection beam to the RFQ.

The radio frequency quadrupole linac (RFQ) is the frontend accelerator of the J-PARC accelerator complex. It is a critical accelerator which determines the beam quality. We realized a new dynamics RFQ implemented a beam dynamics scheme optimized for the high-intensity beam.

To accelerate low-energy particles effectively, the RFQ uses the electric field generated by the four vanes surrounding the beam, as shown in Fig.5-2. To satisfy the requirement of J-PARC, a 60-mA beam should be accelerated. At this high current, the repulsive force between each particle in the beam (space-charge force) is very strong; how to overcome this force is a large issue.

We focused on the equipartitioning (EQ) scheme which is the de facto standard for the linacs except for the RFQ. This scheme is suitable for accelerating high-intensity beams because it properly treats the space-charge force and balances the focusing and accelerating forces. However, in the RFQ, both the focusing and accelerating force should be generated by the shape of the vane-tips, different from the ordinary linacs, in which both the forces can be adjusted independently. Consequently, a more-complex electric field profile than the ordinary RFQ is required if the ideal EQ is adopted. To avoid this difficulty, we

partially applied the EQ to only the most important part for the beam dynamics. This makes the field profile flat. This RFQ is providing the beam every day for the user operation of J-PARC.

Toward the improvement of the performance of the RFQ, we progressed the development based on the experiences of the current RFQ. We performed more detailed beam simulation, and newly developed a method to obtain the required electric field from the equipartitioning with full use of the three-dimensional electromagnetic design tool, as shown in Fig.5-3. With these efforts, we succeeded in developing the world first fully equipartitioned RFQ used for user operation which requires high reliability. As shown in Fig.5-4, the beam test was conducted and the required beam performance was achieved. From this result, we proved that the required performance for J-PARC can be realized with the compact RFQ whose length is 15% shorter by optimizing the beam dynamics.

Since this beam dynamics design scheme contributes to the cost reduction, it is expected not only to be used for the large-scale facilities like J-PARC but also to meet the increasing demands for wider applications such as compact neutron sources.

(Yasuhiro Kondo)

Reference

Kondo, Y. et al., Development of a Radio Frequency Quadrupole Linac Implemented with the Equipartitioning Beam Dynamics Scheme, *Physical Review Accelerators and Beams*, vol.22, issue 12, 2019, p.120101-1–120101-8.

5-2 Detection of Change in Hydrogen Bond in the Deep Earth — Direct Observation of Symmetrization at High Pressure by Neutron Diffraction —

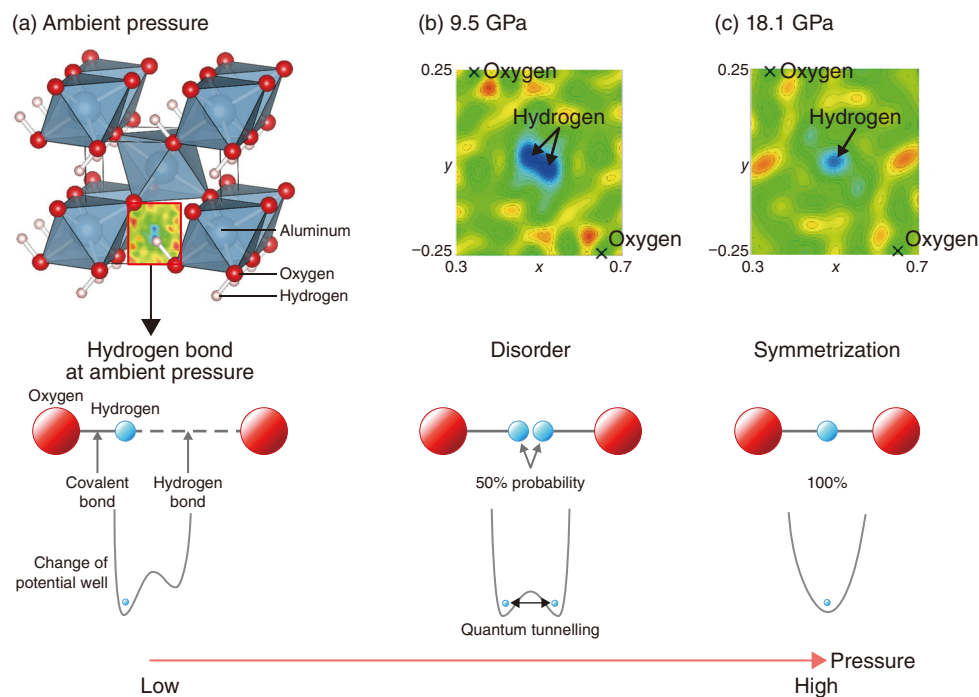


Fig.5-5 Crystal structure of δ -AlOOH at ambient pressure and change in the nuclear density map of δ -AlOOH at high pressure (a) At ambient pressure, hydrogen atoms make covalent bonds and hydrogen bonds between the AlO_6 octahedral chain. Applying pressure led to a (c) symmetrization via (b) a disordered state.

Hydrogen exists not only on the Earth's surface as liquid water but also as hydrous minerals in the deep mantle, which contain hydroxyl ions and/or water molecules in their structure. Since pressure and temperature increase as the depth increases in the Earth's mantle, understanding the behavior of hydrogen bonds in minerals under such extreme conditions is necessary to understand the physical properties of the mantle.

On the surface of the Earth, hydrogen atoms generally take an asymmetric position between two oxygen atoms in minerals, forming a short covalent bond on one side and a long and relatively weak hydrogen bond on the other side. However, it was theoretically predicted in 1970's that in high pressure ice, hydrogen is located at the center between two oxygen atoms in the so-called symmetrization of the hydrogen bond. Considerable effort has been expended to investigate pressure-induced hydrogen bond symmetrization, but most of the studies have been based on indirect methods such as X-rays and spectroscopy.

To investigate the effect of hydrogen bond symmetrization on physical properties of minerals, neutron diffraction experiments were conducted on δ -AlOOH (Fig.5-5(a)) using the high-pressure neutron diffractometer PLANET in the MLF at J-PARC. This hydrous phase is a potential candidate for the carrier of hydrogen into the deep mantle because of its wide stability field at high pressures and temperatures.

As a result, a decrease in the length of the hydrogen bond with the oxygen atom was observed at high pressure. Additionally, the strengthening of the hydrogen bond and weakening of the covalent bond were observed, as reflected by the decrease and increase in each distance, respectively. The hydrogen atom finally became equidistant between the two oxygen atoms at 18.1 GPa, which corresponds to the pressure at an approximate

depth into the mantle of 520 km (Fig.5-5(c)). This result indicates that the hydrogen bond as an electrostatic interaction that is seen at the surface of the Earth disappears at the high pressure deep within the mantle. Instead, the hydrogen bonds covalently at high pressure with the oxygen atoms on either side. A disordered state was also observed below the symmetrization pressure, in which the hydrogen atom occupies two equivalent sites by quantum tunneling with 50% probability, as a precursor to the symmetrization (Fig.5-5(b)).

Previous studies have reported interesting changes to the physical properties in δ -AlOOH, such as a stiffening behavior along the directions where hydrogen bonds lie and an increase in the bulk modulus and sound velocities at high pressure. Furthermore, the conditions of these reported changes agree well with the detected pressures of the disorder and symmetrization. Using neutron diffraction, which allowed for the direct observation of hydrogen position, this work therefore revealed that a small change in the atomic position of hydrogen via the symmetrization can change the bulk physical properties of the mineral.

This work indicated that under high pressure conditions in the deep Earth, hydrogen bonds change in appearance and become more like covalent bonds due to the change in the distance between the oxygen atoms, increasing the elastic wave velocity. This detailed symmetrization of hydrogen bonds under high pressure must be considered when interpreting seismic wave velocity data based on the physical properties of hydrous minerals.

This study was supported by the Japan Society for the Promotion of Science (JSPS) KAKENHI Grant-in-Aid for Young Scientists (B) (No.22740349), and by Grants-in-Aid for Scientific Research on Innovative Areas (Research in a proposed research area) (No.20103001, No.15H05826).

(Asami Sano)

Reference

Sano-Furukawa, A. et al., Direct Observation of Symmetrization of Hydrogen Bond in δ -AlOOH under Mantle Conditions Using Neutron Diffraction, Scientific Reports, vol.8, 2018, p.15520-1–15520-9.

5-3 Mitigation of Damage to the Target Vessel Wall

— Enabled High-Power Spallation Neutron Target by Double-Walled Structure —

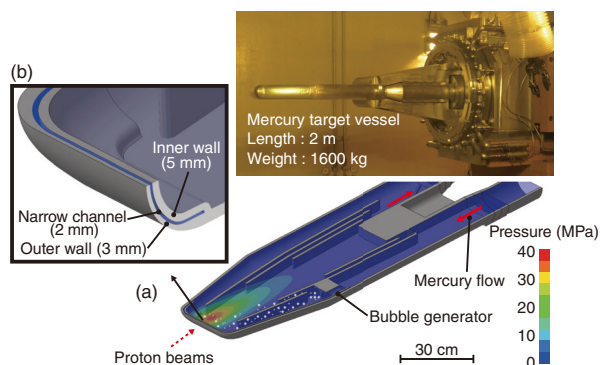


Fig.5-6 Photograph and cross sectional-image of the double-walled mercury target vessel

A maximum initial pressure of approximately 40 MPa was generated due to the 1-MW proton beam injection. A double-walled structure with a narrow channel was applied to the front part of the vessel at high-pressure region.

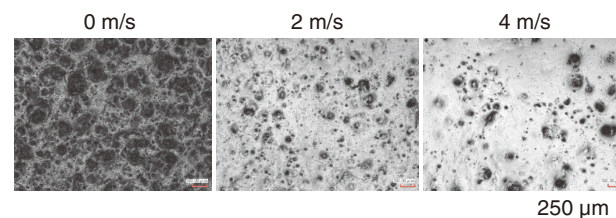


Fig.5-7 Macroscopic images of the damaged surface for the gap width of 2 mm in various mercury flow velocities obtained by a laser scanning microscope

The experimental impact force due to the cavitation was reduced by increasing the flow velocity, since the pressure distribution around the wall varies with the flow velocity.

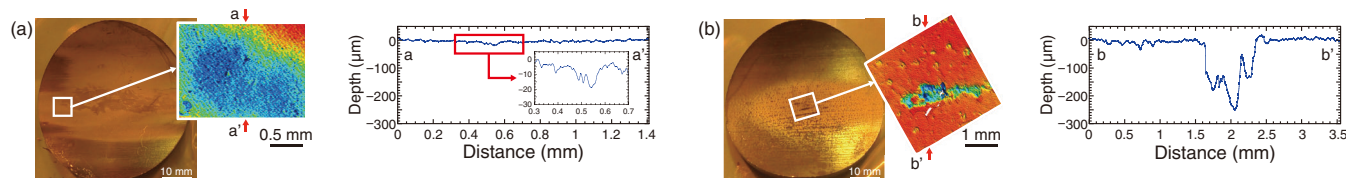


Fig.5-8 Erosion damage formed on the inner wall of the mercury target vessel

The shape of the damaged surface was replicated using a silicone piece of rubber for a detailed 3D damage observation because of the high radiation dose. The damage on the outer wall (a) of the narrow channel was drastically reduced when compared with the inner wall (b).

At J-PARC, neutrons are produced for materials and life science research by injecting high-intensity proton beams into mercury. More high-power proton beam injection is required to increase the resolution of the neutron measurement. When the high-intensity proton beam hits the mercury in the stainless steel vessel (i.e. the target vessel), half of the proton beam energy is used for neutron production, whereas half is lost as waste heat. For a 1-MW proton beam injection (representing the goal at J-PARC), the local mercury pressure increases by approximately 40 MPa due to the instantaneous thermal expansion. The mercury pressure thus drops below the saturated vapor pressure during the propagation of the pressure wave, causing cavitation (depressurized boiling) (Fig.5-6(a)). The cavitation bubble collapses when the pressure recovers above the saturated vapor pressure, thus causing damage to the vessel wall. Since the resulting damage to the vessel wall increases with operating time and proton beam power and degrades the structural integrity of the target vessel, mitigating this damage to the vessel wall is necessary to achieve long-term high-power operation of the high-intensity proton beam.

In this work, gas microbubbles were injected into the mercury to absorb the thermal expansion of the mercury and thus mitigate the pressure waves that produce cavitation. The results showed that the pressure of the mercury was reduced by approximately

one-third and the resulting damage to the vessel wall was drastically reduced. Furthermore, to achieve a high-power stable operation, an inner wall with a narrow mercury channel was adopted to contribute to the outer wall protection. In this adopted double-walled structure, shown in Fig.5-6(b). Based on the results of cavitation damage experiment, a gap width of the narrow channel of the mercury target vessel of 2 mm was selected, with a mercury flow velocity of approximately 4 m/s (Fig.5-7).

Photographs and detailed analyses of the resulting damage of the outer and inner walls of the mercury target vessel operated for 4200 hours at an average proton beam power of 430 kW are shown in Fig.5-8. The damage on the surface of the outer wall that faced the narrow channel was less than 20 μm in depth, whereas a maximum cavitation damage of approximately 260 μm in depth was formed on the inner wall. These results thus demonstrated that adopting the designed double-walled structure can drastically reduce the cavitation damage.

Future efforts to continue working toward stable operation at the world's highest pulsed-neutron facility will include quantitative assessment of the damage caused by cavitation to the double-walled mercury target vessel while increasing the proton beam power.

(Takashi Naoe)

Reference

Naoe, T. et al., Mitigation of Cavitation Damage in J-PARC Mercury Target Vessel, JPS Conference Proceedings, vol.28, 2020, p.081004-1–081004-6.

5-4 Enabling Material Analysis with Neutron Beams at Manufacturing Sites — Texture Measurement of Steel Materials Using a Compact Neutron Source —

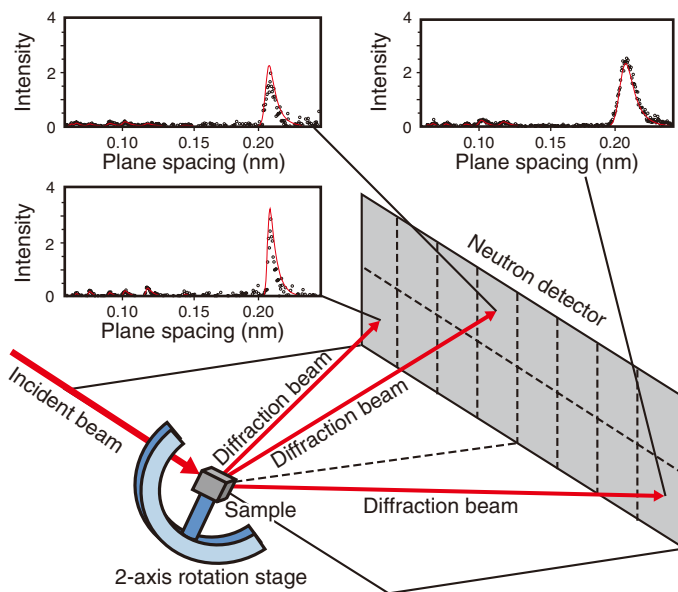


Fig.5-9 Schematic illustration of the developed texture measurement technique using the RIKEN accelerator-driven compact neutron source (RANS)

The incident neutron beam generated from RANS was diffracted by the sample on the 2-axis rotation stage. These diffracted neutron beams were position-sensitively collected by 16 region-divided panels of a neutron detector. The diffraction patterns from all sample orientations were measured through necessary 2-axis sample rotations.

Steel materials are composed of a huge number of single-crystalline grains that are usually of various crystallographic orientations. Most material processes such as rolling or heating may result in the formation of some preferred crystallographic orientation(s) in these crystal grains (i.e. a texture), which strongly affects the material's mechanical properties, including strength and ductility. As the development of steel materials with high strength and ductility is essential to realize light-weight designs of motors and other transportation systems, a reliable method to evaluate and control the textures of steel materials is required. Crystal diffraction using high-penetrating neutrons is well-known as the most effective method to obtain a polycrystalline bulk sample of steel averaged over a large volume. However, facilities capable of providing the necessary neutron source for such a measurement have been limited to a handful of large science experimental facilities with either a nuclear research reactor or a large proton accelerator. In this work, a precise texture measurement technique suitable for various manufacturing sites was developed by collaboration between the Institute of Physical and Chemical Research (RIKEN) in Japan, with their accelerator-driven compact neutron source technique, and JAEA, with their well-established texture measurement technique using high-flux neutron diffraction.

The highly effective detection of weak diffraction neutron beams is particularly important during the neutron diffraction texture measurement using the RIKEN accelerator-driven compact neutron source (RANS). Here, an optimized distribution setup of rubber shielding plates around the RANS diffractometer had reduced background noise and enabled clear recognition of multiple diffraction peaks. A 2-axis rotation method was

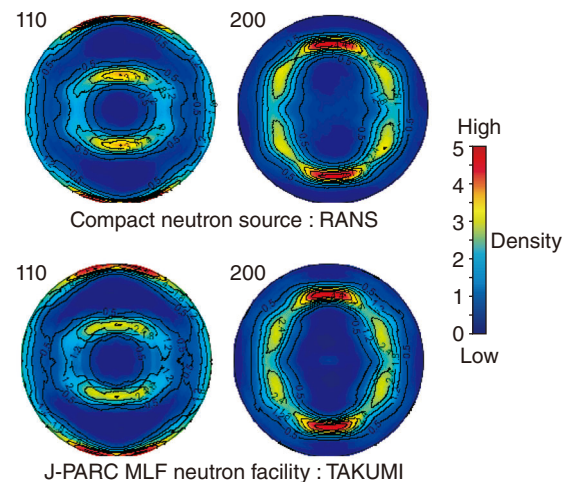


Fig.5-10 Contour plots of the distribution of crystallographic orientations (Pole figures)

The resulting pole figures of a typical steel material measured on RANS were consistent with those obtained from the engineering material diffractometer TAKUMI at the MLF at J-PARC. The numbers 110 and 200 represent the diffraction plane indices of the neutron diffraction patterns.

employed to scan all sample orientations referring to the incident neutron beam easily. The active region of the neutron detector was divided to simultaneously collect the diffraction patterns from 16 directions (Fig.5-9). This allowed for a reduction in the required number of sample rotations, thus shortening the total measurement time. Finally, the texture analysis conditions were optimized to effectively refine the weak neutron diffraction patterns. As a result, the first texture measurement of a typical steel material with a single-phase ferrite structure was successfully achieved using a compact neutron source. The pole figures obtained using the proposed method on the RANS showed good agreement with those obtained using the engineering material diffractometer TAKUMI at the MLF at J-PARC, as shown in Fig.5-10, suggesting that the high precision level of crystallographic texture obtained in 0.5 h using the neutron facility, which operates at three orders of magnitude stronger, can be realized using a compact neutron source in 5.0 hours.

The developed neutron diffraction texture measurement can be implemented at ordinary laboratories and manufacturing sites, and through the complementary collaboration with high-flux large neutron facilities, this texture technique is thus expected to further contribute to the development of innovative materials and products.

This study was part of the cooperative project with RIKEN on “Development of on-site residual stress measurement technique of bulk metals using hybrid neutron diffraction”, supported by the Japan Society for the Promotion of Science (JSPS) KAKENHI Grant-in-Aid for Scientific Research (B) (No.17H03161).

(Pingguang Xu)

Reference

Xu, P. G. et al., In-House Texture Measurement Using a Compact Neutron Source, *Journal of Applied Crystallography*, vol.53, part 2, 2020, p.444–454.

5-5 Elucidation of Structural Fluctuations of Proteins

— Observation of Structure and Dynamics of Protein by Neutron Scattering —

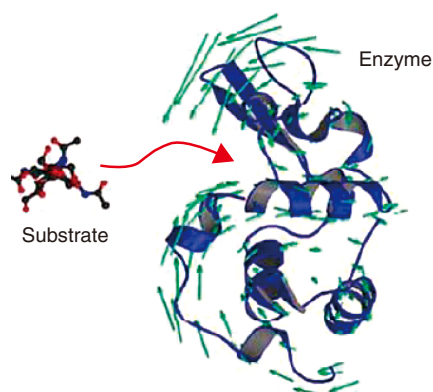


Fig.5-11 Protein dynamics during functional expression

Enzyme proteins change their structure to react with a substrate. These structural fluctuations, shown with green arrows, can be seen by inelastic neutron scattering experiments.

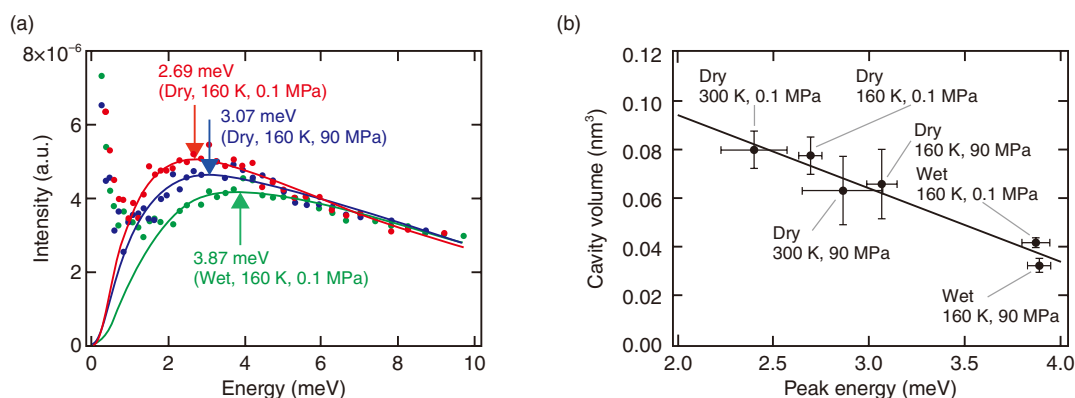


Fig.5-12 (a) Boson peak of a protein (nuclease), and (b) relationship between boson peak position and cavity volume in various environments

(a) Boson peak positions, indicated by arrows, are changed by hydration, temperature, and pressure. (b) The peak position is correlated with the cavity volume inside a protein.

Proteins play a central role in all enzymatic reactions from intracellular reactions to chemical reactions catalyzed by enzymes in detergents. Researchers have considered that knowledge of the three-dimensional structure and specific complementing counterpart (substrate), like a lock and its key, is necessary for understanding the function of a protein. However, proteins have a soft structure that fluctuates in response to the surrounding environment; such structural fluctuations are necessary for binding to the substrate molecule (Fig.5-11).

Inelastic neutron scattering enables the quantitative and accurate measurement of structural fluctuations in the THz region (1 THz = 4.1 meV), which is important for the expression of protein functions. The boson peak, which is observed in this energy region, has been demonstrated to be directly related to the structural fluctuation of the protein molecule. Elucidating the relationship between the boson peak of proteins and their three-dimensional structure is vital from the viewpoint of structural science to derive a universal principle for predicting biological reactions from the structural fluctuations of proteins.

In this study, the effect of hydration, temperature, and pressure on a boson peak of the protein (nuclease) were studied by inelastic neutron scattering. The results, as shown in Fig.5-12(a), indicated that hydration, cooling, and pressing each caused the peak position

to shift to a higher energy. To investigate the relationship between the peak shift and the protein structure, a molecular dynamics simulation was used to calculate the cavity volume inside the protein. A correlation was found between the peak position and cavity volume (Fig.5-12(b)). Therefore, the fluctuations of the protein structure are related to the atomic packing of the protein structure. Using this correlation between the volumetric properties and structural fluctuations of a protein, measuring the dynamics will help clarify the three-dimensional structure of the protein, even for proteins with unknown structures.

In this study, characteristics of protein dynamics, which are associated with the structure, were elucidated using inelastic neutron scattering and molecular dynamics simulations. This achievement confirms the importance of studying protein dynamics by neutron scattering. Inelastic neutron scattering is expected to become an increasingly effective tool for such studies.

This study was partly supported by the Japan Society for the Promotion of Science (JSPS) KAKENHI Grant-in-Aid for Challenging Research (Exploratory) (No.18K18828), “Molecular selective phonon spectroscopy at amorphous interface by inelastic neutron scattering”.

(Hiroshi Nakagawa)

Reference

Nakagawa, H. et al., Universality and Structural Implications of the Boson Peak in Proteins, Biophysical Journal, vol.117, issue 2, 2019, p.229–238.

5-6 Structural Analysis of Ionic Liquid–Electrode Interface — Nano-Scale Analysis of the Interfacial Structure Using a Quantum Beam —

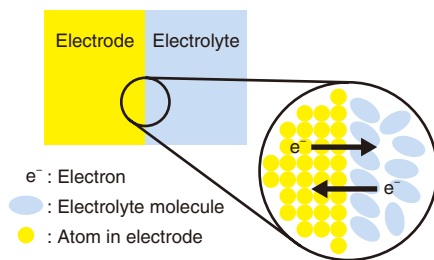


Fig.5-13 The electrolyte–electrode interface inside a battery
Batteries use electrochemical reactions, which occur at interfaces between electrolytes and electrodes.

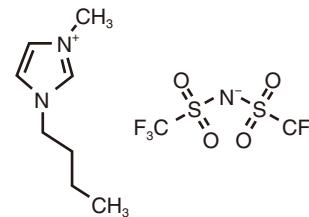


Fig.5-14 Ionic liquid: 1-butyl-3-methylimidazolium bis(trifluoromethylsulfonyl)amide
Ionic liquids consist of pairs of cations (left) and anions (right).

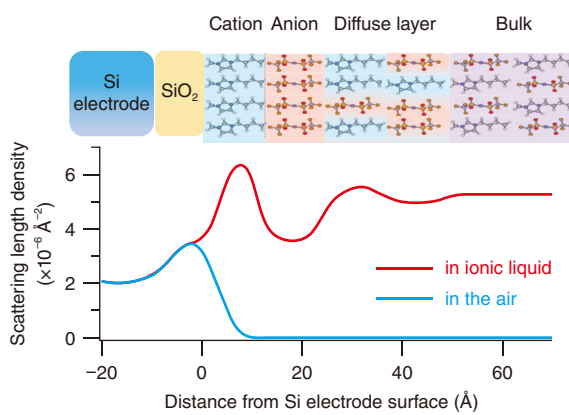


Fig.5-15 Detailed structure of the interface explored using neutron reflectivity

Ionic liquid molecules create a layered structure on the negatively charged Si electrode surface. It was experimentally revealed that the first layer was a layer of cation molecules (peak shown at 0 Å is derived from a native oxide layer on the Si surface). The precise deuteration technique developed in this research allowed the analysis of the interfacial structure with nano-scale precision.

The interface between a solid and a liquid, known as the solid–liquid interface, is a place where a variety of chemical reactions occur and is thus strongly connected to daily life. For example, batteries use electrochemical reactions, which occur at the electrode–electrolyte interface, as shown in Fig.5-13. Chemical reactions, which occur at interfaces, are thought to be affected by the atomic order of the solid surface and the order of the liquid molecule to be adsorbed on the solid surface. For a deeper understanding of chemical reactions, therefore, it is necessary to clarify the reaction rate as well as the nano-scale structure of the reaction interface.

Ionic liquids have gained attraction as a “brand-new” electrolyte to study electrochemical reactions in ionic liquids. A typical molecular structure of an ionic liquid is shown in Fig.5-14; an ionic liquid is a salt that is in a liquid state at room temperature. Unlike water or organic solvents, ionic liquids have high electric conductivity and are nonvolatile. However, the reactivity of electrochemical reactions in water is different than in ionic liquids. This is likely due to the order of ionic liquid molecules adsorbed on the electrode. However, the order of the molecules is not easily calculated. Therefore, the structure of the ionic liquid–electrode interface was experimentally analyzed using quantum beams (including X-ray and neutron) at SPring-8 and J-PARC.

As neutrons can interact with light elements such as hydrogen, carbon, and oxygen, structural analysis using neutrons is suitable for the analysis of the order of ionic liquid molecules. Further, selective structural analysis is possible by substituting hydrogen (H) with deuterium (D) at the site of interest on the molecules. A highly effective and precise deuteration technique was therefore developed and used to study the order of ionic liquid molecules adsorbed on the surface of a Si electrode on the nano-scale. The resulting neutron reflectivity as performed at the MLF at J-PARC SHARAKU is summarized in Fig.5-15. The analysis revealed that ionic liquid molecules create a layered structure near the negatively charged Si electrode surface and that cation molecules constitute the first layer. Future work will aim to further clarify the dependence of the electrode potential on the interfacial structure and the relationship between the interfacial structure and the molecular structure of ionic liquids.

This study was conducted on “Study of the electrical double layer structure formed in ionic liquids using quantum beam scattering techniques”, supported by the Japan Society for the Promotion of Science (JSPS) KAKENHI Grant-in-Aid for Scientific Research (C) (No.15K05402).

(Kazuhiisa Tamura)

Reference

Akutsu-Suyama, K., Tamura, K. et al., Controlled Deuterium Labelling of Imidazolium Ionic Liquids to Probe the Fine Structure of the Electrical Double Layer Using Neutron Reflectometry, *Physical Chemistry Chemical Physics*, vol.21, issue 32, 2019, p.17512–17516.

5-7 Toward Next-Generation Memory with Low Power Consumption — Observation of Electronic Structure of Alumina Film for Nonvolatile Memory —

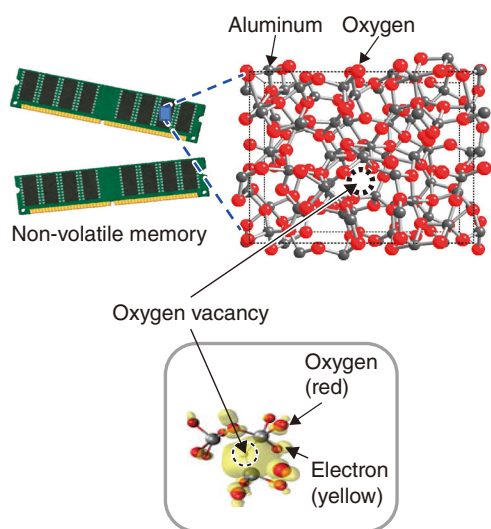


Fig.5-16 Schematic of the structure of amorphous alumina

In amorphous alumina, oxygen and aluminum atoms are not regularly arranged. Electrons related to memory are demonstrated to be mainly distributed around oxygen sites.

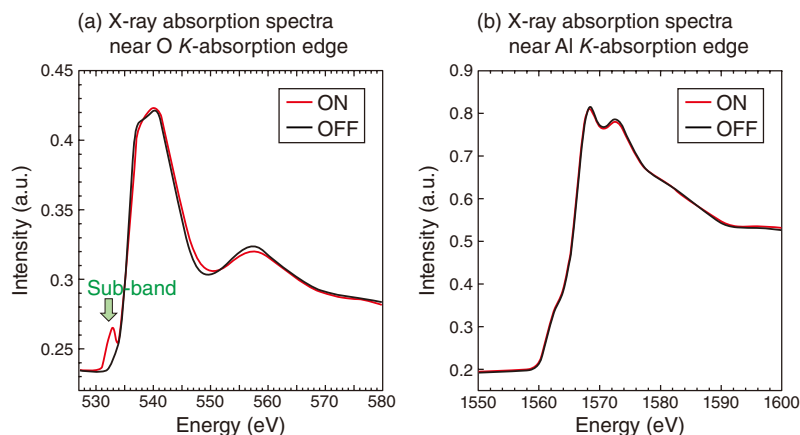


Fig.5-17 X-ray absorption spectra for ON/OFF memory states

X-ray absorption spectroscopy (XAS) was performed on amorphous alumina film. Absorption spectra for (a) oxygen and (b) aluminum sites. In (a), a change of electronic states (appearance of sub-band) was detected.

The conventional main memory of a computer requires a successive electric power supply to retain digital data, thus causing high electricity consumption. To solve this problem, resistive random access memory (ReRAM), which employs a resistance switching induced by voltage, is a promising candidate for the next generation of memory. Many transition metal oxides have been studied as candidates for ReRAM materials. However, the resistive switching associated with ReRAM in transition metal oxides is concomitant with changes in the valence number. As in any chemical reaction, this process is accompanied by minor reactions and byproducts, which reduce the endurance of the ReRAM device and have thus hindered the widespread usage of transition metal oxides in universal memory systems.

In this work, the ReRAM effect in amorphous alumina with vacancy-type oxygen defects (AlO_x), as shown in Fig.5-16, was investigated. In an amorphous material, atoms are not regularly arranged, unlike in a crystal. Based on first-principle calculations, a charge–discharge model of oxygen vacancy in AlO_x was proposed. The electronic structure of the valence band was studied in a high-resistance state (HRS) and a low-

resistance state (LRS) in the AlO_x . To detect differences in the electronic structures between the LRS and HRS in an element-selective manner, X-ray absorption spectroscopy was performed.

The results demonstrated the changes in electronic structures between the LRS and the HRS of the AlO_x film. The subpeak for the charging of electrons into oxygen vacancies was observed in the X-ray absorption spectra near the *K*-absorption edge of the oxygen (Fig.5-17(a)). This subpeak likely corresponds to the mid-gap found via the first-principles calculation. The energy spectra of the LRS and HRS near the *K*-absorption edge of the aluminum were nearly identical (Fig.5-17(b)). This suggests the absence of any byproducts. These results are supportive of the proposed charge–discharge oxygen vacancy model.

These results demonstrate that amorphous alumina is a good candidate for the next generation of nonvolatile memory. As Earth's surface is rich in oxygen and aluminum and AlO_x film can be produced with a low environmental impact, this work opens the door to a lowered electrical consumption in a modern computer-dependent society.

(Masato Kubota)

Reference

Kubota, M. et al., Direct Observation of Electronic Structure Change by Resistance Random Access Memory Effect in Amorphous Alumina, AIP Advances, vol.9, issue 9, 2019, p.095050-1–095050-4.

5-8 Observation of Electrons in Unconventional Uranium Superconductor — First Observation of the Electronic Structure of UTe_2 —

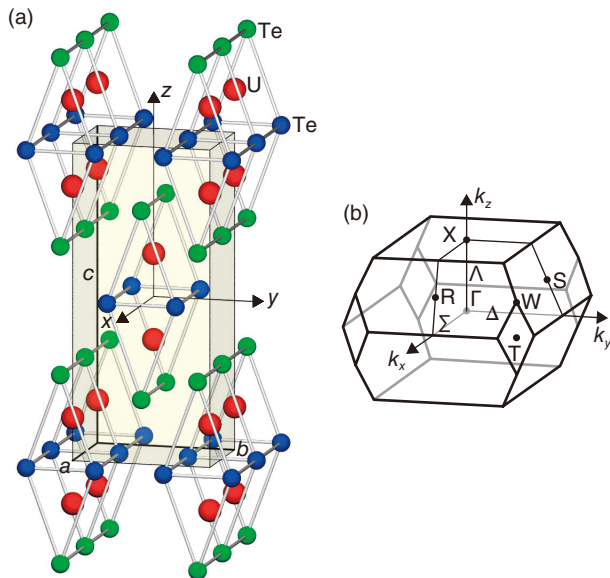


Fig.5-18 Crystal structure and Brillouin zone of UTe_2
(a) Crystal structure of UTe_2 (b) Brillouin zone of UTe_2 , which represents the minimum unit in momentum space.

Actinide compounds, including uranium compounds, have complex properties, such as diverse magnetism and superconductivity, and deserve a unique position in strongly correlated electron systems. In late 2018, UTe_2 (Fig.5-18) was discovered to exhibit a novel superconductivity, thus attracting worldwide attention. To understand this novel mechanism of superconductivity, the electronic structure of the compound must first be clarified.

The JAEA beamline, SPring-8 BL23SU, can safely handle radioactive materials such as uranium compounds and is the only facility worldwide with access to the soft X-ray regime required for actinide research. Soft X-ray angle-resolved photoemission spectroscopy is an experimental technique used to directly observe the electronic structure of materials by measuring the kinetic energy and angular distribution of the emitted photoelectrons. We have revealed the electronic structure of many uranium compounds. Based on that experience, we rapidly carried out the research on UTe_2 and clarified the electronic state of UTe_2 for the first time worldwide.

The observed band structure of UTe_2 , obtained by soft X-ray angle-resolved photoelectron spectroscopy, is shown in Fig.5-19(a). Here, the highest intensity corresponds to the band

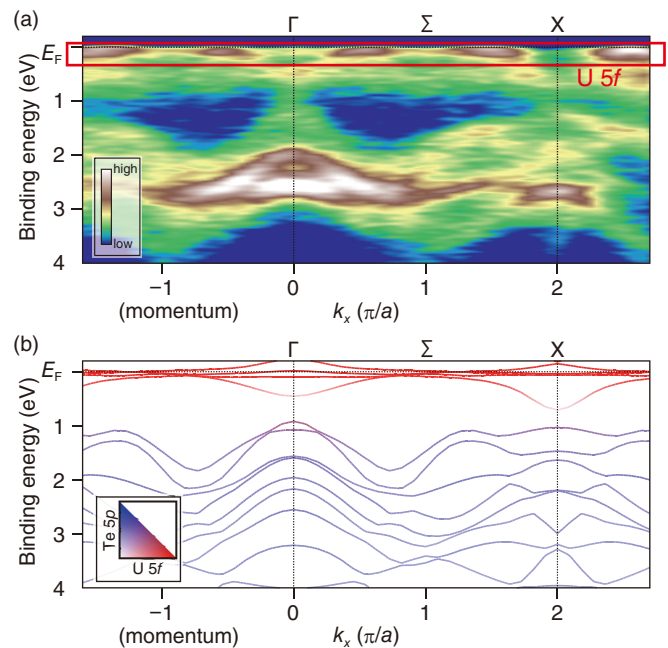


Fig.5-19 Observed and calculated band structure of UTe_2
(a) Band structure of UTe_2 obtained by angle-resolved photoelectron spectroscopy. The color of the spectral image indicates the photoelectron intensity; a stronger intensity corresponds to a band structure. (b) Calculated band structure in the same energy and wavenumber region as in the experiment. The red and blue bands indicate the contributions from the electronic orbitals of U and Te, respectively.

structure. The band structure of the U $5f$ electrons, which is directly related to superconductivity, was successfully observed. The theoretically calculated band structure, shown in Fig.5-19(b), clarifies the overall band structure. A strong contribution by the U $5f$ states was observed in the vicinity of the Fermi level, which determines the superconducting properties of this compound. These results indicate that the U $5f$ states in UTe_2 have an itinerant nature with an electron correlation effect. This result provides fundamental information for understanding the electronic structure of UTe_2 as well as a model for describing the superconductivity in this compound.

This study was conducted on “Elucidation of the three-dimensional electronic structure of heavy-fermion superconductors”, supported by the Japan Society for the Promotion of Science (JSPS) KAKENHI Grant-in-Aid for Scientific Research (C) (No.18K03553), and on “Elucidation of the electronic structure of strongly correlated uranium compounds by three-dimensional ARPES”, by Grant-in-Aid for Scientific Research on Innovative Areas (Research in a proposed research area) (No.16H01084).

(Shin-ichi Fujimori)

Reference

Fujimori, S. et al., Electronic Structure of UTe_2 Studied by Photoelectron Spectroscopy, Journal of the Physical Society of Japan, vol.88, no.10, 2019, p.103701-1–103701-5.

Research and Development on HTGR, Hydrogen Production, and Heat Application Technologies

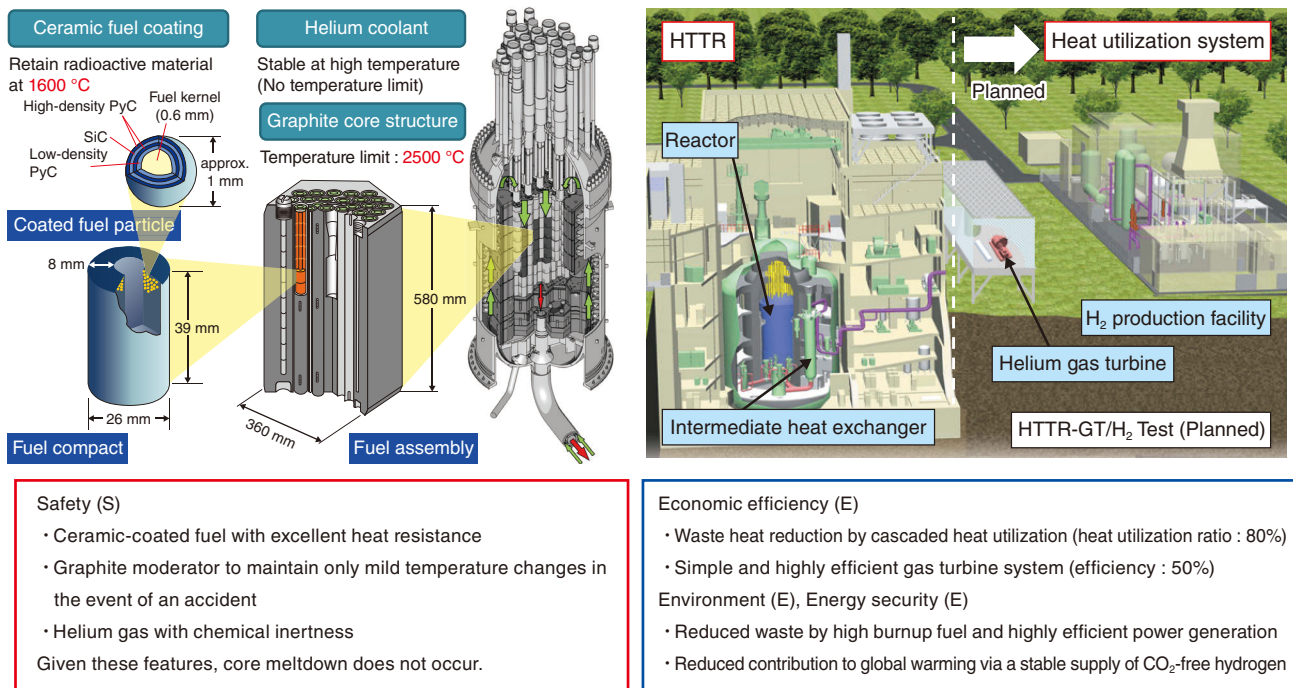


Fig.6-1 Features of HTGR and plan of HTTR-GT/H₂ test

The HTGR is a helium gas-cooled and graphite-moderated thermal-neutron reactor with excellent inherent safety features. The HTGR meets various heat application requirements, including producing hydrogen and generating power. The HTGR also meets the 3E+S policy targets in Japan's Strategic Energy Plan. JAEA's final target is the successful demonstration of coupling a nuclear reactor and heat application systems by connecting a gas turbine and hydrogen production facilities to Japan's first HTGR, HTTR.

Japan's energy supply-demand structure is fragile because of its excessive dependence on imported fossil resources. To remedy this situation while reducing greenhouse gas emissions that cause global warming, Japan is advancing the use of safe nuclear energy.

High Temperature Gas-cooled Reactor (HTGR) is a nuclear reactor with various industrial uses, including high-efficiency power generation by a helium gas turbine and hydrogen production, as shown in Fig.6-1. "Chapter 3. Promotion of technology development, 2. Technical challenges to be addressed" of the 5th Strategic Energy Plan, decided by the Cabinet in July 2018, mentions that "Under international cooperation while looking at overseas market trends, GOJ also facilitates R&D of nuclear technologies that serves the safety improvement of nuclear use, such as HTGRs which are expected to be utilized in various industries including hydrogen production and which has an inherent safety".

JAEA has Japan's only HTGR, the High Temperature Engineering Test Reactor (HTTR) in Oarai, Ibaraki-ken. The HTTR, constructed by domestic technologies, is the only HTGR worldwide that can extract heat from the reactor at 950 °C. The HTTR attained a reactor outlet temperature of 950 °C in 2004 and continuously and stably operated for 50 days in 2010, thus demonstrating a stable supply of high-temperature nuclear heat. The inherent safety features of the HTGR were confirmed in a loss-of-forced-cooling test without inserting the control rod. In these tests, the reactor intrinsically shut down and maintained a stable state.

Recently, the industrial, academic, and governmental council which was established following a recommendation from the WG of R&D on HTGR technologies, the Nuclear Science and Technology Commission, under the Ministry of

Education, Culture, Sports, Science and Technology (MEXT) has been developing strategies for commercializing HTGRs and deploying Japanese HTGR technologies overseas. This has involved the establishment of a cooperation policy and domestic organization structure for an experimental and commercial reactor in Poland. Development structure for HTGR through international cooperation is under establishing. We aim to expand overseas the most advanced HTGR technology in the world, cultivated through the design, safety review, construction, operation, maintenance, and safety evaluation of HTTR, and to return the demonstrated results by overseas projects to Japan.

Recent developments in the development of HTGR technology have included the study of graphite material aiming to cost reduction, the development of a high burnup fuel through international cooperation, and a conceptual study on a system to complement intermittent renewable energy (Topics 6-1-6-3, respectively). In research on the thermochemical iodine-sulfur (I-S) process, which is an innovative hydrogen production technology using the heat of HTGR, JAEA has developed a strength evaluation method for ceramic components, a corrosion test apparatus for corrosion-resistant metallic materials, and a shaft seal system for a liquid hydrogen iodide transfer pump (Topics 6-4-6-6, respectively). An evaluation method for the collapse impact of a stack to the HTTR using 3D realistic collision analysis was developed (Topic 6-7).

On June 3rd, 2020, JAEA obtained permission by the Nuclear Regulation Authority to modify the reactor installation of the HTTR in conformity to the New Regulatory Requirements without large-scale modifications nor added reinforcements against earthquakes due to the inherent safety features of the HTGR. The HTTR is now in the final preparation stage toward restarting.

6-1 Whole Core Burnup Characteristic Evaluation Method Using Representative Impurities — Cost Reduction for HTGRs Using Inexpensive Graphite Materials —

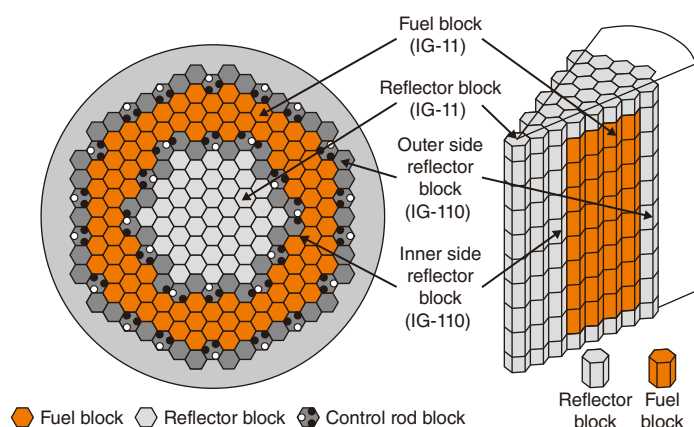


Fig.6-2 Horizontal cross-sectional view (left) and bird's-eye view (right) of the GTHTR300 core

The GTHTR300 (600 MW thermal power, 730 days cycle length, 8 m high (8×1 m layers), and 5.5 m outer diameter of the fuel region) is a commercial HTGR designed by JAEA. Burnup characteristics of this core were investigated using inexpensive graphite materials.

In HTGRs, impurities such as boron and iron present in graphite can negatively impact the criticality. The HTTR was designed with IG-110 high-purity graphite blocks in the fuel region to reduce the influence of these impurities on the criticality. In contrast, the high-temperature gas turbine power-generation system, the Gas Turbine High-Temperature Reactor 300 (GTHTR300) was initially designed using only IG-11 graphite blocks, which have a lower purity than IG-110, for economic efficiency, although it was later redesigned to employ IG-110 over concerns regarding the criticality (Fig.6-2). However, as commercial reactors require high economic efficiency, the GTHTR300 would be a more attractive proposition if the core could be established using only inexpensive IG-11 graphite blocks. To do this, it is necessary to show that sufficient criticality can be achieved using the inexpensive IG-11 graphite blocks. This work therefore investigated the burnup of impurities in the graphite. Due to their large absorption cross-section, impurities with a strong poisonous effect should be burned up quickly. Thus, if it is confirmed that these impurities burnup in the early stages of the cycle, it can be confirmed that the criticality is not affected and that there is only a negligible effect on the cycle length.

However, to perform such a calculation, it is necessary to simulate a burnup of the entire core, which deals with the burnup of all the impurities in graphite. The number of nuclides that can be treated by the burnup chain model of the entire core calculation is limited to the important ones for the evaluation

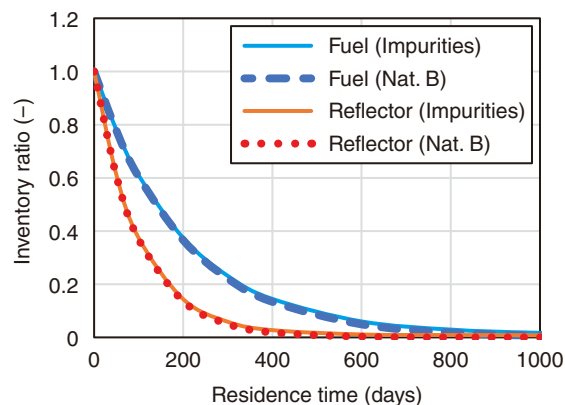


Fig.6-3 Burnup characteristics of impurities in the fuel and reflector blocks

The dashed lines show the burnup characteristics when the impurities are represented by natural boron (Nat. B); the solid lines represent the burnup characteristics when the impurities are burned directly. The dashed lines show good agreement with the solid lines, indicating that this is an acceptable substitution. Here, the boron equivalent represents the impurity value converted to natural boron weight considering the reaction between the impurity nuclides and neutrons. The vertical axis is normalized based on the boron equivalent on day zero in the reactor.

of the core characteristics, and it is not realistic to treat the burnup of all nuclides in the entire core calculation because the post-implementation data is too complex to maintain. For this reason, a radionuclide decay production calculation code ORIGEN was first used to evaluate the burnup characteristics of impurities for the GTHTR300 design. The calculation results indicated that the burnup of these impurities can be simulated by the burnup of natural boron as a representative impurity, as shown in Fig.6-3. The impurities in IG-11 were thus converted to boron equivalents and the burnup calculation of the entire core was performed using the burnup calculation code using the Monte Carlo method (MVP-BURN). This analysis indicated that using the IG-11 graphite blocks causes an increase in the cycle length by approximately 10% when compared with the conventional GTHTR300 design, which does not consider the burnup of impurities. In the conventional design, impurities are assumed to remain even at the End of Cycle (EOC), thus accounting for this increase.

These results indicate that the impurities found in graphite burnup before the EOC, and these impurities do not interfere with the criticality at the EOC, even when the lower-cost IG-11 graphite blocks are used in the design.

Future efforts will focus on further economic improvements to the HTGR design such as revising the shuffling pattern of the fuel block to improve burnup.

(Shoichiro Okita)

Reference

Fukaya, Y. et al., Burn-Up Characteristics and Criticality Effect of Impurities in the Graphite Structure of a Commercial-Scale Prismatic HTGR, Nuclear Engineering and Design, vol.326, 2018, p.108–113.

6-2 A Threefold Increase in Burnup of HTGR Fuel

— Development on High-Burnup HTGR Fuel under International Cooperation —

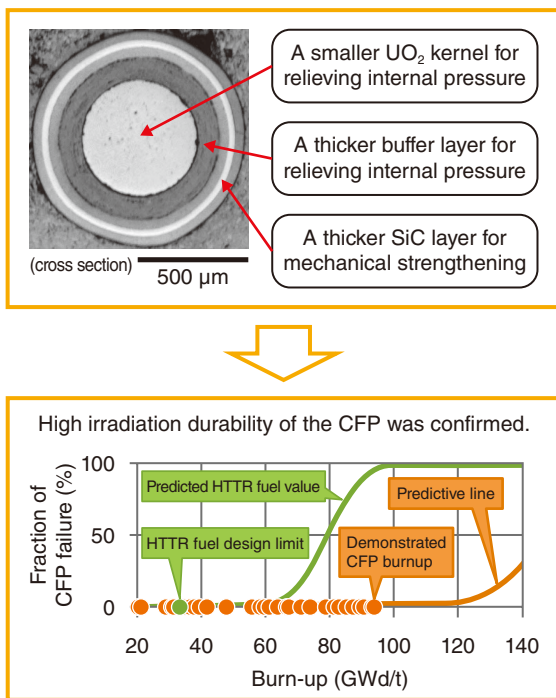


Fig.6-4 Features of the high-burnup CFP design and its neutron irradiation test result

The newly-designed high-burnup coated fuel particle (CFP) employs a smaller UO_2 kernel and thicker carbon-buffer and SiC layers than those of the conventional CFP for the HTTR.

High temperature gas-cooled reactor (HTGR) has attracted attention as one of small modular reactors. To reduce the costs associated with achieving the economic goals of HTGR, its fuel performance should be improved to increase safely the amount of energy extracted from uranium fission. The conventional fuel used for the High Temperature Engineering Test Reactor (HTTR), the 30-MWt helium-cooled HTGR in Japan, is designed to burn up to 33 GWd/t in maximum.

A coated fuel particle (CFP) contains an UO_2 kernel wrapped in four successive and thin ceramics, including, from the innermost to the outermost layer, a low-dense pyrolytic carbon (PyC) as a buffer, a high-dense PyC, a silicon carbide (SiC) and a high-dense PyC. These so-called “coating layers” confine the fission product (FP) released from the UO_2 kernel burned during operation. The coating layers could be failed by excess high pressure inside the CFP due to the gaseous FPs and carbon monoxide generated by uranium fission when the burnup exceeds the design limit of the CFP.

In this study, therefore, a CFP was developed corresponding to a burnup extension. To improve retention of gas components, the newly-designed particle, shown in Fig.6-4, features a smaller diameter of the fuel kernel and thicker layers for the buffer and the SiC coatings. The new CFP was manufactured using existing mass production technology by Japanese HTGR fuel maker, Nuclear Fuel Industries, Ltd. In this process, CFPs approximately 1 mm in diameter are poured into a molding die together with a base material consisting of graphite powders and phenol resin binder, and then calcinated and solidified to form a cylindrical fuel compact. Since the development of the

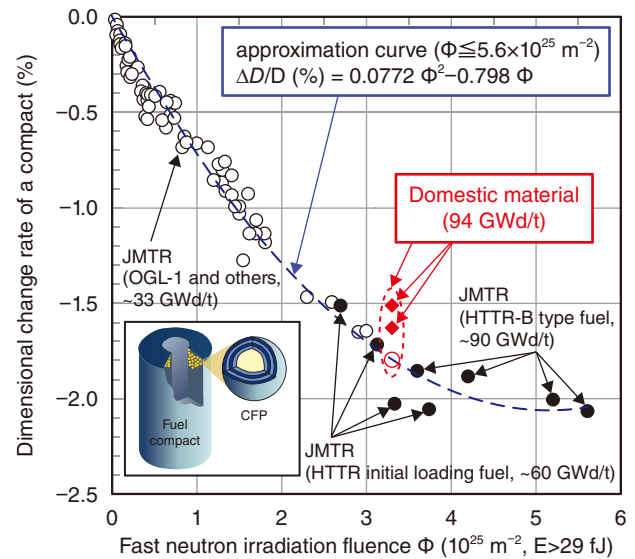


Fig.6-5 Experimental relationship between the dimensional change rate of the fuel compact as a function of the fast neutron fluence

Neutron irradiation test with the fuel compact burnt up to 94 GWd/t results that the dimensional change rate of the fuel compact with new domestic base material is comparable to that of the conventional using imported material.

HTTR, procurement of this base material has relied on imports. For practical use of Japanese HTGR fuel, it is necessary to develop new domestic base materials having similar properties under neutron irradiation to the conventional. In this study, the fuel compact using newly-developed domestic was fabricated and confirmed its integrity. And then, a neutron irradiation test was performed in the WWR-K irradiation reactor in the Institute of Nuclear Physics in Kazakhstan under international cooperation. As the result, it was indicated that the dimensional change rate of the fuel compact made of domestic base material was comparable to that made of the conventional imported material (Fig.6-5). The dimensional change of the fuel compact due to neutron irradiation significantly affects the heat removal performance of the fuel rod, which limit the burnup and lifetime of the fuel.

Thus, both integrity of the new CFP for higher burnup than that of the HTTR and applicability of the new domestic base material for the fuel compact were successfully demonstrated at a 100 GWd/t burnup range of the practical HTGR. Furthermore, these results show the capabilities of the HTGR fuel design by JAEA and the mass production technology by Nuclear Fuel Industries, Ltd. are among the world’s leaders.

Future work will focus on advanced technologies upgrading performance and economy of the HTGR fuel, such as, by increasing the packing fraction of CFPs in a fuel compact to extend fuel lifetime and by coating an additional zirconium carbide layer as an oxygen getter material to prevent from failure of the CFP due to its internal gas pressure.

(Koei Sasaki)

Reference

Ueta, S., Sasaki, K. et al., Research and Development on High Burnup HTGR Fuels in JAEA, Mechanical Engineering Journal, vol.7, issue 3, 2020, p.19-00571-1–19-00571-12.

6-3 Toward Harmonization with Renewable Energy

— HTGR Concept for Accomplishing Hybrid Operation with Renewable Energy —

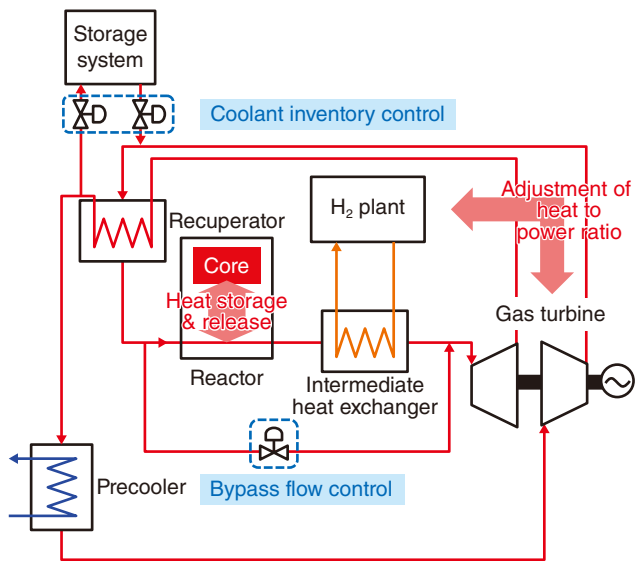


Fig.6-6 HTGR concept accomplishing economical hybrid operation with variable renewable electricity sources

Long time-scale variations can be compensated by adjusting the heat-to-power ratio using the coolant inventory and bypass flow controls at constant reactor power. Short time-scale variations can be compensated by varying the gas turbine power generation rate at the rated reactor power using the coolant inventory control with the help of massive core heat storage.

Wide-scale penetration of variable renewable electricity technologies, such as solar and wind energy, is expected in the near future to significantly reduce CO₂ emissions and move toward a more sustainable electricity production. Due to the inherent stochasticity of many renewable sources, hydropower and fossil-based power plants have been required to balance the gaps between the supply and demand in the electric grid. However, using fossil fuel-based power plants are not a preferable option because these generators release massive amounts of CO₂ into the atmosphere. Existing nuclear power plants are typically run in baseload mode to avoid any impact of power variation on components or power generation efficiency, which would lead to a decreased economic efficiency.

The development of an HTGR capable of offering economic CO₂-free grid stability that has not been provided by other power generation technologies will promote its deployment in a carbon-constrained world. As a result of comprehensive review of unique HTGR characteristics, it was determined that a gas turbine can be used to compensate for seasonal and daily variations in renewable energy technologies without sacrificing power generation efficiency by controlling the coolant inventory because helium obeys the ideal gas law. In addition, the heat-to-power ratio in an HTGR can be adjusted at constant reactor power by varying the flow rate of a bypass line to a reactor and an intermediate heat exchanger due to the hydrogen and electricity cogeneration capability (Fig.6-6). Furthermore, the

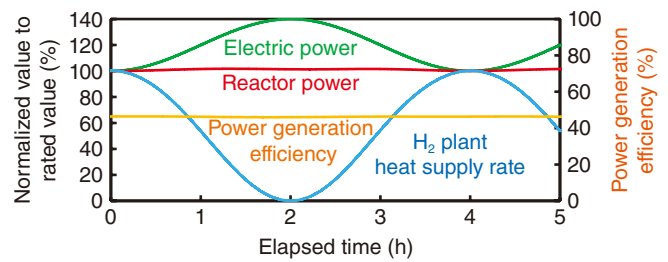


Fig.6-7 Dynamic behavior of the HTGR plant during load-following operation in a long time-scale variation of renewable power generations

Variations in renewable electricity generation can be compensated by an HTGR at constant reactor power and power generation efficiency.

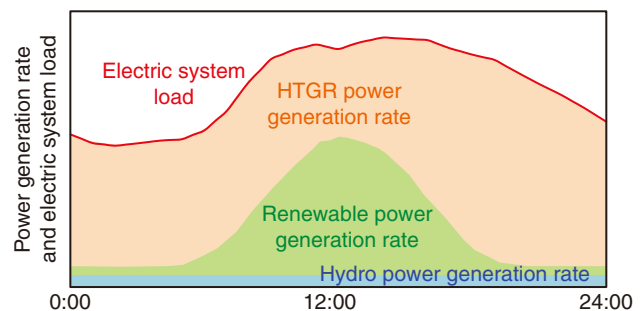


Fig.6-8 Example hybrid operation using HTGRs and renewable electricity sources

The hybridization capability of an HTGR with renewable electricity generation can contribute to the realization of a zero-emission electricity generation system.

HTGR can change the power output on the order of seconds or minutes at a constant reactor power by using the inventory control with the aid of the large thermal capacity of the graphite reactor core. In summary, the electricity generation rate of an HTGR can be varied in accordance with various types of load variations induced by the use of intermittent renewable energy sources.

To demonstrate the efficacy of the operational strategies suggested above, numerical simulations were performed for load-following operations in long and short time-scale variations. The plant dynamics of the GTHTR300C, a commercial HTGR hydrogen and electricity cogeneration system designed by JAEA, were thus evaluated using a system analysis code based on RELAP5. Several improvements were made to the code to extend its applicability to HTGR cogeneration plants. The simulation results demonstrated that power generation rate of the GTHTR300C can be adjusted to correspond to the demand in a load-following scenario at constant reactor power and power generation efficiency without significant equipment modifications (Fig.6-7).

Overall, HTGRs were demonstrated to be capable of operating in a hybrid mode with variable renewable power generation and can thus contribute to the realization of a zero-emission power generation system (Fig.6-8).

(Hiroyuki Sato)

Reference

Sato, H. et al., Study of an HTGR and Renewable Energy Hybrid System for Grid Stability, Nuclear Engineering and Design, vol.343, 2019, p.178–186.

6-4 Toward Commercial Implementation of the IS Process with HTGRs for Hydrogen Production — Development of Strength Evaluation Method for Ceramic Structures —

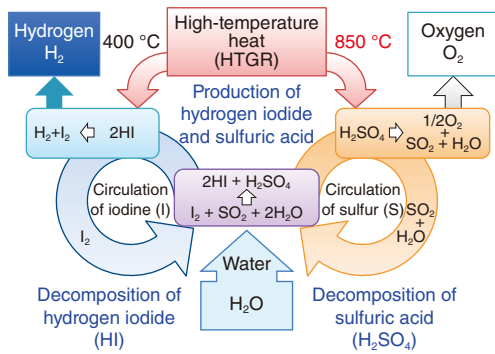


Fig.6-9 Schematic of IS process for the thermochemical production of hydrogen

The IS process produces hydrogen from water using high-temperature heat from the HTGR and three chemical reactions. Combining the IS process with the HTGR as a heat source makes it possible to produce hydrogen without CO₂ emissions.

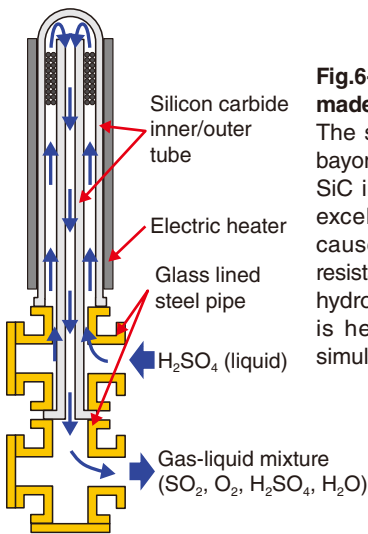


Fig.6-10 Sulfuric acid decomposer made of silicon carbide (SiC)

The sulfuric acid decomposer is a bayonet-type reactor consisting of a SiC inner and outer tube. SiC has excellent resistance to corrosion caused by sulfuric acid and heat resistance. In the current continuous-hydrogen production test, the SiC is heated by electric heaters to simulate helium gas heating.

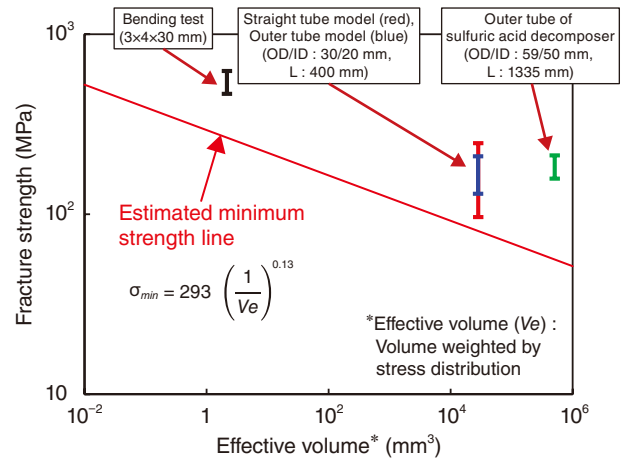


Fig.6-11 Estimated minimum strength equation and experimental validation using SiC structure

The fracture strength of the straight tube model, the outer tube model, and the outer tube of the sulfuric acid decomposer with different volumes failed at higher stresses than the minimum strength estimated from the minimum strength equation.

Hydrogen and oxygen can be produced through a chemical reaction between iodine (I) and sulfur (S) in the thermochemical water-splitting iodine-sulfur (IS) process, as shown in Fig.6-9. As the IS process uses highly corrosive chemicals such as hydrogen iodide and sulfuric acid at high temperatures, the materials used for the process must be corrosion resistant and heat resistant.

During the IS process, the sulfuric acid decomposer decomposes extremely corrosive sulfuric acid at temperatures up to 850 °C. Due to its corrosion and heat resistance, existing metal materials cannot be used for the decomposer. A sulfuric acid decomposer made of silicon carbide (SiC), which is a ceramic material with excellent heat and corrosion resistance, was thus proposed for the sulfuric acid boiling/evaporation part of the decomposer, as shown in Fig.6-10; the performance and reliability of this proposed decomposer have been confirmed by continuous hydrogen production tests.

Because the heat source of a commercial IS plant is high-pressure helium gas from an HTGR, the SiC sulfuric acid decomposer must be approved by the High Pressure Gas Safety Act. However, because the average strength of ceramic materials decreases with increasing volume, it is not possible to evaluate the strength of a full-scale structure from the strength of a small bend test specimen according to the JIS standard.

A strength evaluation method that can be applied to a full-size

ceramic apparatus was therefore developed. The objective of the strength evaluation method was to determine the minimum strength of the structure so that it can be designed considering the strength variation of ceramic materials. The minimum strength estimation equation was developed by combining the relationship between crack size and fracture strength (fracture mechanics) and the relationship between crack distribution and fracture strength (fracture probability); the resulting minimum strength equation is shown in Fig.6-11. Destructive testing of SiC specimens of various sizes up to the actual size of the decomposer was then performed by applying water pressure to obtain the strength distribution equation and validate the calculated minimum strength equation.

The results, as shown in Fig.6-11, demonstrated that all of the fracture strengths were above the minimum strength derived from the estimation equation. Thus, it was confirmed that the developed strength estimation equation could be used to evaluate the minimum strength for full-scale SiC structures. This result paves the way for the evaluation of the strength of the SiC structure in the sulfuric acid decomposer.

Future work will include establishing the design method of the SiC structure by adding a safety factor and enhancing its reliability of through the use of newly developed corrosion-resistant metals.

(Hiroaki Takegami)

Reference

Takegami, H. et al., Development of Strength Evaluation Method of Ceramic Reactor for Iodine-Sulfur Process and Hydrogen Production Test in Japan Atomic Energy Agency, Nuclear Engineering and Design, vol.360, 2020, p.110498-1-110498-6.

6-5 Toward Metallic Sulfuric Acid Decomposers in the IS Process

— Development of a Corrosion Test Apparatus without Sulfur Dioxide (SO₂) Leakage —

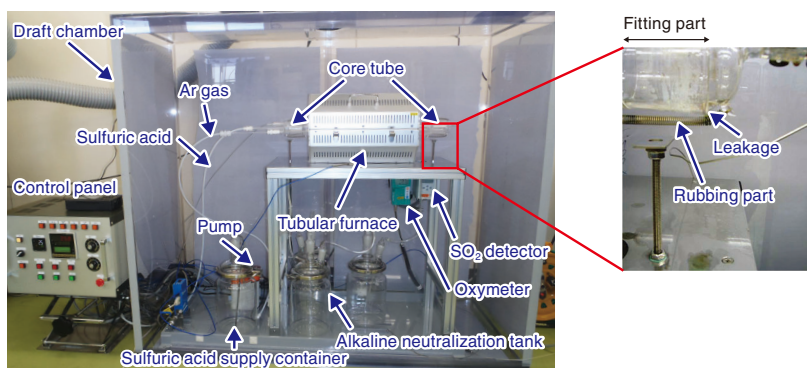
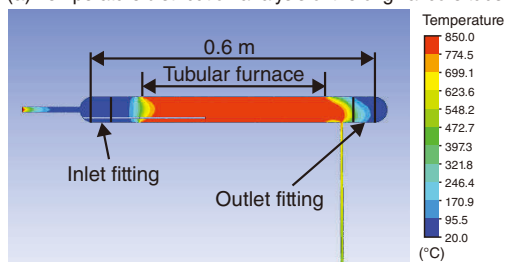


Fig.6-12 Designed corrosion test apparatus and location of SO₂ leak

As a safety measure, this device automatically shuts down if abnormal heating (≥ 900 °C) or SO₂ leakage occurs. In the original device, SO₂ leaked from the fitting part on the outlet side and the device automatically stopped.

(a) Temperature distribution analysis of the original core tube



(b) Temperature distribution analysis of the improved core tube

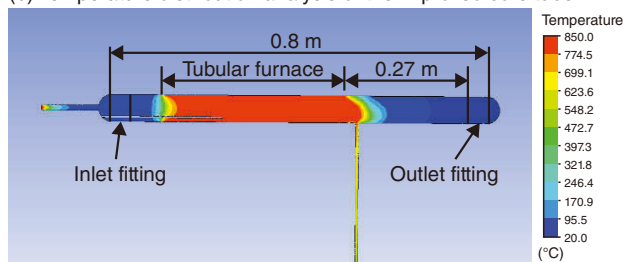


Fig.6-13 Effect of reducing the temperature of the fitting on the outlet side by optimizing the dimensions of the furnace tube

(a) In the unmodified core tube (0.6 m), the temperature at the outlet fitting exceeded the usable temperature (515 °C) of the fluorine grease. (b) In the improved core tube (0.8 m), the temperature can be reduced to room temperature by moving the outlet fitting away from the tubular furnace.

The IS process, a thermochemical hydrogen production method that is a potential heat-application technology of HTGRs, treats highly corrosive hydrogen iodide (HI), iodine (I₂), sulfuric acid (H₂SO₄), and sulfur dioxide (SO₂) at high temperatures. Any material involved in the process must have excellent heat resistance and corrosion resistance. In particular, the temperature inside the pressure vessel that decomposes sulfuric acid (i.e., the sulfuric acid decomposer) reaches the maximum temperature in the IS process of 850 °C. Ceramics such as SiC have thus been considered for use as sulfuric acid decomposers. However, since SiC is expensive and making the sulfuric acid decomposer larger is difficult. As a result, it is also difficult to reduce the manufacturing cost because SiC must be jointed together. Heat-resistant and corrosion-resistant metallic materials that can replace SiC as the sulfuric acid decomposer are under development.

To commercialize said heat-resistant and corrosion-resistant metallic materials, the corrosion resistance of the developed material must be demonstrated in a sulfuric acid decomposition environment. A corrosion test apparatus was thus developed and demonstrated to provide excellent heat resistance and avoid corrosion for a long time (Fig.6-12). The apparatus consists of a control panel, a sulfuric acid supply container, a pump, a quartz glass core tube, a tubular furnace, and an alkali neutralization tank for neutralizing gasified SO₂ by sulfuric acid. With the exception of the control panel, the supplies were stored in the draft chamber. By using argon as the carrier gas, gasified SO₂ could be spread throughout the metal test piece installed in the core tube. For safety, several measurement devices were also installed to monitor the sulfuric acid solution, the amount of

SO₂ gas, the temperature distribution in the tubular furnace, and the oxygen concentration after sulfuric acid decomposition. If the temperature reaches 900 °C or SO₂ leaks into the draft chamber, the system is automatically shut down. Since the sample is installed in the core tube for each test, both sides of the core tube have a fitted structure. In a trial run, liquid sulfuric acid flowed into the core tube; after a while, SO₂ leaked from the fitting on the outlet side, triggering the automatic stop of the apparatus. This leakage was caused by the temperature rise of the rubbing part at the outlet of the core tube, which weakened the adhesive force of the fluorine grease applied to this part. Additionally, liquid sulfuric acid had pooled near the outlet-side fitting, which also contributed to the leakage of SO₂ gas. To address this problem, thermo-fluid calculations were performed to optimize the dimensions of the core tube. The calculation results indicated that increasing the distance between the tubular furnace and the outlet-side fitting would reduce the temperature of the outlet fitting to room temperature; using the determined dimensions, a core tube that could be safely stored in the draft chamber was designed (Fig.6-13).

In fact, SO₂ leakage does not occur in the improved core tube for a long period because the number of steps inside the core tube is minimized to eliminate liquid pools, and the core tube is lengthened to avoid temperature rise. Corrosion tests on various metallic materials using the designed apparatus are ongoing. Future work will include the development of a heat-resistant and corrosion-resistant metallic material for use as a sulfuric acid decomposer.

(Noriaki Hirota)

Reference

Hirota, N. et al., Development of New Corrosion Test Equipment Simulating Sulfuric Acid Decomposition Gas Environment in a Thermochemical Hydrogen Production Process, *Zairyo-to-Kankyo*, vol.68, issue 6, 2019, p.137-142 (in Japanese).

6-6 Toward Stable and Continuous Hydrogen Production by the IS Process

— Development of a Pump Shaft Seal Technology for HI Solution Including Highly Concentrated I₂ —

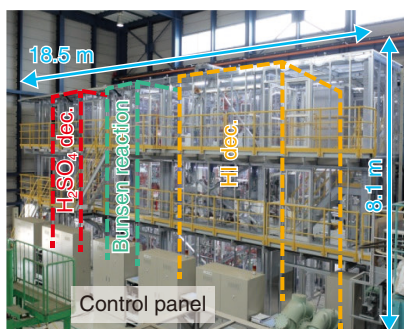


Fig.6-14 External view of hydrogen production test facility

This facility is being used for the demonstration of hydrogen production via the IS process toward the practical application of the IS process.

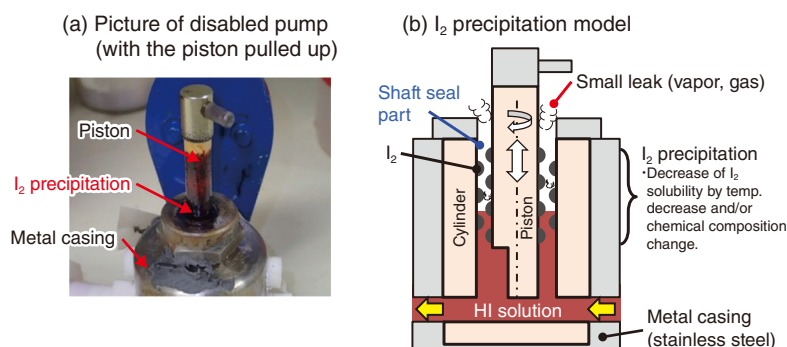


Fig.6-15 Pump malfunction during a hydrogen production test

(a) Solid I₂ was observed on the piston surface of the disabled pump. (b) This malfunction was likely caused by an increasing sliding friction resistance due to a buildup of precipitated I₂ in the narrow gap between the piston and the cylinder owing to the decreased I₂ solubility.

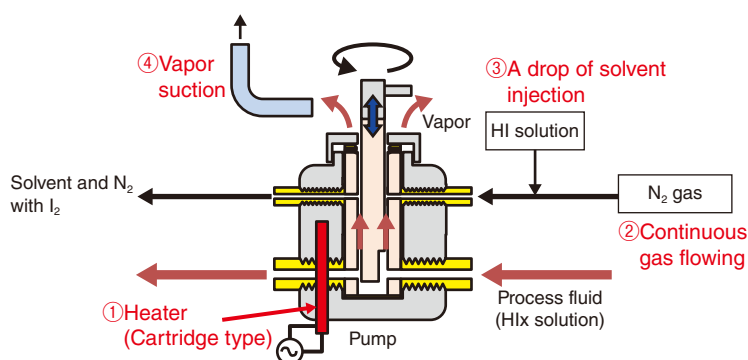


Fig.6-16 Development of shaft seal technology

A shaft seal technology was developed to prevent I₂ precipitation by introducing four elemental technologies; ① a heater for preventing I₂ precipitation, ② an inert gas flow to purge HI and I₂ from the narrow gap, ③ the injection of a small amount of solvent to dissolve I₂, and ④ a vapor suction nozzle to stop the leakage of HI and I₂ vapor.

The thermochemical water-splitting IS process offers a potential heat-application technologies of HTGRs. Due to the high required reaction temperature of 900 °C and highly corrosive fluids involved, such as sulfuric acid, iodine (I₂) and hydrogen iodide (HI), all components must be made of industrial materials with high corrosion and heat resistance. A hydrogen production test facility has been constructed in 2013 (Fig.6-14); since then, a series of continuous hydrogen production tests have been performed to verify the integrity of all IS process components and control methods of the closed IS process.

For example, an 8-hour hydrogen production test was performed with a hydrogen production rate of 10 L/h in 2016. However, a pump containing a solution of HI with a high concentration of I₂ was stopped during operation. Solid I₂ was observed on the piston surface of the disabled pump, as shown in Fig.6-15(a). The pump malfunction was likely caused by leakage of process fluid containing I₂ near its solubility limit into the narrow gap between the piston and cylinder, where I₂ was then precipitated due to a decrease in temperature and/or a change in chemical composition. The precipitated I₂ caused an increase in the slide friction, causing the pump to eventually stop (Fig.6-15(b)).

To prevent I₂ precipitation in the narrow gap, a shaft seal

technology was developed by injecting gas and liquid into the narrow gap to flush out solid I₂ (Fig.6-16). This developed shaft seal included four components: ① a heater for preventing I₂ precipitation due to the decrease in temperature, ② an inert gas flow to purge the process fluid and solvent from the gap, ③ the injection of a small amount of solvent (HI solution) to dissolve I₂ that had precipitated in the gap, and ④ vapor suction to remove the leakage from the top side of the pump. The pump equipped with the developed shaft seal technology was then verified under conditions similar to those when the pump stopped functioning. The modified pump worked continuously and stably for 24 h, thus confirming the effectiveness of the developed shaft seal technology. This technology has been applied to the pumps used in the hydrogen production test facility, where hydrogen production was then conducted successfully for 31 hours with a hydrogen production rate of approximately 20 L/h.

The introduction of a composition adjustment method of Bunsen solution to the facility based on findings from continuous operation is underway. Future work will involve operational data collection and analysis of component reliability for the practical application of the IS process.

(Hiroki Noguchi)

Reference

Noguchi, H. et al., R&D Status of Hydrogen Production Test Using IS Process Test Facility Made of Industrial Structural Material in JAEA, International Journal of Hydrogen Energy, vol.44, issue 25, 2019, p.12583–12592.

6-7 Impact of Exhaust Stack Collapse on the Reactor Building

— Confirmation of the Integrity of the Reactor Building by 3D Model Collision Analysis —

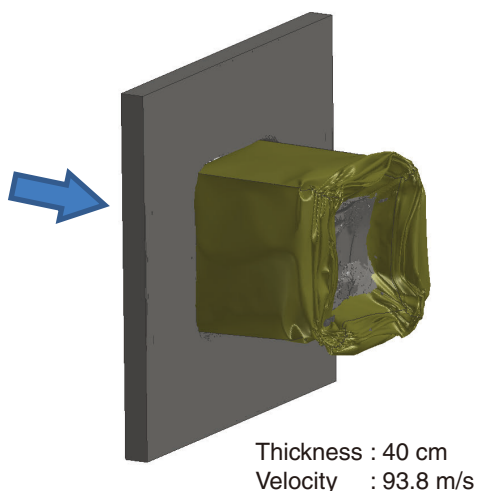


Fig.6-17 Obtaining physical properties of reinforced concrete by collision analysis

A flying object with speed of 93.8 m/s can penetrate the 40 cm thickness reinforced concrete. The physical properties of concrete in this analysis were equal to or greater than those calculated in the empirical formula.

After the accident at the TEPCO's Fukushima Daiichi NPS due to the Great East Japan Earthquake, the safety of the reactor in the event of a tornado has become important as part of measures against natural disasters. The integrity evaluation of the reactor building has been limited to evaluating whether a simple flying object caused by a tornado could penetrate the wall. However, complicated structures such as exhaust stacks surround the reactor building. This study therefore constructed a 3D model of an exhaust stack using a commercial program that is used in the collision analysis of cars and aircrafts. The collision behavior when the exhaust stack crashes into the reactor building was also investigated.

When conducting collision analysis, it is necessary to set the physical properties of reinforced concrete of the reactor building. Since the physical properties of reinforced concrete are difficult to obtain owing to the use of reinforcing steel, they were retrieved by referring to the empirical formula obtained from experiments by the Nuclear Regulation Authority. A collision analysis between flying objects and reinforced concrete plate was then performed, as shown in Fig.6-17. The flying objects studied included a container 2.4 m in length, 2.6 m wide, and 6.0 m in depth, and a steel plate 4.0 mm thick and weighing 2300 kg. The physical properties of reinforced concrete were then estimated using these collision analyses. As a result, if the compressive fracture strain and tensile fracture strain were set to 0.03 and 0.087, respectively, the result of the empirical

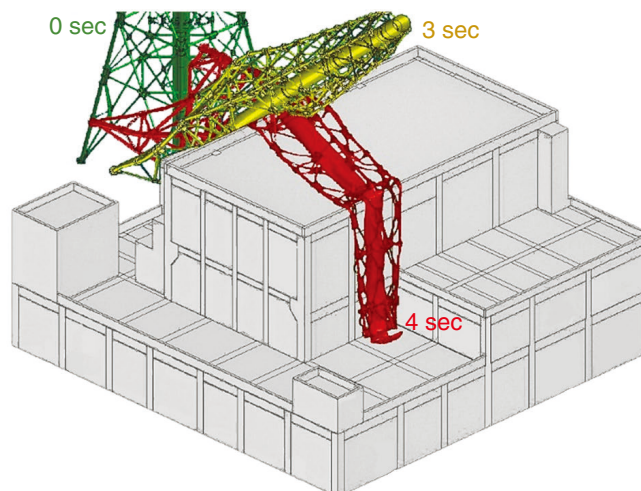


Fig.6-18 Collision between stack and reactor building

Simulation showed behavior of stack from before to after collision. Three seconds after the wind begins to blow, the stack tilts and collides with reactor building after four seconds. The reactor building is not deformed and no significant effect on reactor building nor interior facilities.

formula could be reproduced. Additionally, the analysis results were confirmed to have a similar conservativeness as the empirical formula.

To simulate the collapse of the exhaust stack, three of the stack's steel legs on the opposite side of the reactor building were not fixed. The exhaust stack was assumed to have collapsed due to a strong wind with a wind speed of approximately 100 m/s. The resulting collision behavior when the stack falls toward the roof of the reactor building is shown in Fig.6-18. The exhaust stack started tilting 3 seconds after the wind blew; it then collided with the reactor building at 4 seconds from the start of the wind blow. The results showed that the exhaust stack was significantly damaged after the collision, but the reactor building was not deformed and therefore the internal facilities were not affected. This is because the exhaust stack is more easily deformed than is the reactor building. The kinetic energy of the exhaust stack, rather than being converted into the strain energy of the reactor building, was mostly converted into its own strain energy.

In conclusion, collision simulations between the exhaust stack and the HTTR reactor building were performed by developing a 3D model representing the complicated shape of the exhaust stack. As a result, the integrity of the reactor building in the event of a tornado was confirmed.

(Masato Ono)

Reference

Ono, M. et al., Evaluation of Impact with High Temperature Engineering Test Reactor Using Realistic Model of Stack and Reactor Building, Transactions of the Atomic Energy Society of Japan, vol.19, issue 2, 2020, p.110-120 (in Japanese).

Enhancing the Ability of Research and Development

The fast reactor cycle (fast reactor and associated fuel cycle) is expected to supply enough energy to fulfill global electricity demands in a sustainable and environmentally friendly fashion. Fast-reactor technology allows the utilization of most of the available uranium resources, making it possible to continue operation for as long as a thousand years. By transmuting minor actinides, it significantly reduces the heat generation and radiotoxicity of vitrified radioactive waste that is to be disposed of geologically.

The “Fast Reactor Strategic Roadmap” put forth by the Japanese Government in December 2018 specified research target areas for the following ten years in fast reactor development in Japan. JAEA was requested to maintain fundamental research and development capabilities that meet the needs of the private sector, which will be proposing various innovative reactor concepts under the Nuclear Energy × Innovation Promotion (NEXIP) initiative, and to continue efforts toward the international standardization of safety and structural codes and standards, of which it has led development. Based on the research and development plan JAEA formulated commensurate with the Roadmap, JAEA’s Sector of Fast Reactor and Advanced Reactor Research and Development is developing numerical analysis tools and evaluation methods that fit with new reactor design concepts, the enhanced reduction of radioactive waste, and fuel cycle technologies such as fuel fabrication and reprocessing. Codes and standards for safety and structural design are being developed to best materialize the innovative characters of new reactors. The proposed codes and standards structure is summarized in Fig.7-1, where the safety standards and structural codes are seamlessly connected through risk-informed technologies and the System Based Code concept

to allocate margins in a way that balances safety, economics, and sustainability most appropriately. JAEA is developing technologies to be equipped in the structure, and engages in standardization activities in international and overseas organizations as well as in Japan.

Some of the recent achievements in fast reactor developments at JAEA are described in this chapter. Efforts toward the commercialization of fast reactors, including recent developments in the feasibility of manufacturing the upper core structures of tank-type reactors using only domestic technologies, which were a result of a 3D-CAD-based design study conducted in collaboration with France, are reported in Topic 7-1. In Topics 7-2 and 7-3, the subject of thermal-hydraulic analysis is delved into. High-precision experimental data demonstrating the feasibility of the decay heat removal system for sodium cooled fast reactors is presented in Topic 7-2, whereas the feasibility of the fuel assembly with an internal duct to enhance the safety of sodium cooled fast reactors is detailed via a newly extended sub-channel analysis code is discussed in Topic 7-3. Moving to safety analysis developments in sodium-cooled fast reactors, the JAEA-developed oxide-dispersed strengthened steel used in the fuel cladding of sodium-cooled fast reactors was verified to have remarkable ultra-high temperature characteristics at 1000 °C, representing a significant improvement over conventional austenitic steels and thus offering improved core safety (Topic 7-4). Finally, the ignition of hydrogen gas was visualized in combustion tests using high-definition and high-speed shooting methods to clarify the fact that ignition of sodium mixed hydrogen jet is the ignition of hydrogen that occurs locally around ignited sodium mist, as discussed in Topic 7-5.

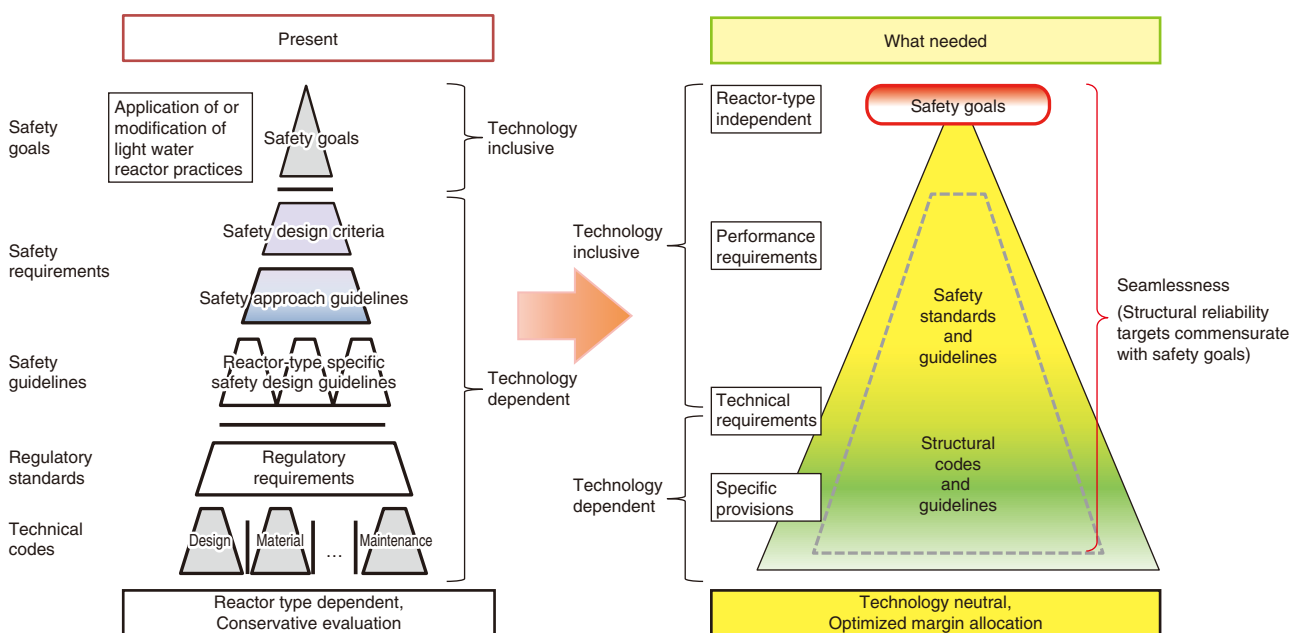


Fig.7-1 Structure of the codes and standards for nuclear innovation

7-1 Toward Efficient Manufacturing of the Above-Core Structure — Routing Study of the Above-Core Structure with a Mock-Up Experiment —

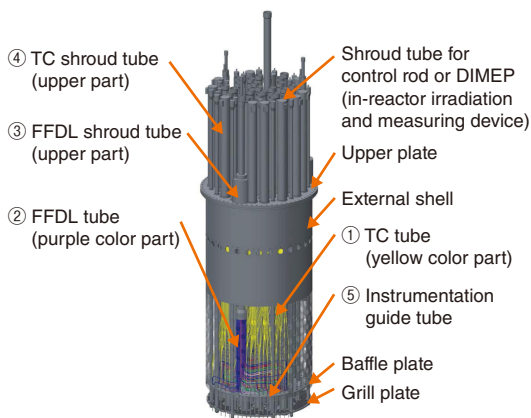


Fig.7-2 Major components of the above-core structure (ACS) and arrangement of the instrumentation tubes in the 3D-CAD study
The performed routing study included 702 TC and FFDL tubes to identify a feasible arrangement and assembling procedure into the ACS to be installed in ASTRID600.



Fig.7-3 Mock-up experiment
Based on the 3D-CAD study, a one-third partial full-scale mock-up was created.

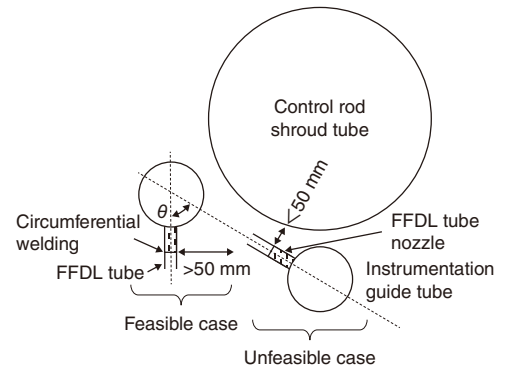


Fig.7-4 Weldability schematic of the FFDL tube nozzle
The FFDL tube nozzle should be arranged within the appropriate range to ensure the necessary space for circumferential welding.

In a sodium-cooled fast reactor (SFR), several tubes are installed above each fuel subassembly to monitor the core. The above-core structure (ACS) is a structure designed to support the control rod drive mechanisms and instrumentation systems, such as thermocouples (TCs) and the failed fuel detection and location (FFDL) system, each with their various tubing and materials, in an SFR. The complexity of the integration of said systems has been identified as an issue in ACS development. This work therefore aimed to perform a routing study for TC and FFDL tubing using 3D modeling and a mock-up design of the ACS to clarify the integration process. This work was done as part of an SFR collaboration program between France and Japan.

The resulting arrangement of the tubes from the 3D-CAD study, designed for feasibility in assembly and for worker access, is shown in Fig.7-2. Here, the TC tubes (① in Fig.7-2) and FFDL tubes (② in Fig.7-2) were first divided into a few parts in the axial direction in consideration of the assembling process. To secure a work space, the assembling work of the instrumentation tubes has to be progressed from the center toward the outside of the ACS; the 702 instrumentation tubes and shroud tubes (③ and ④ in Fig.7-2, respectively) were thus designed.

The designed arrangement was then built in a mock-up at one-third partial full-scale based on the 3D-CAD study, as pictured in Fig.7-3. Although the TC and FFDL tubes did not contact each other in the 3D-CAD study, some contacts were found in the mock-up experiment. These contacts were attributed to

manufacturing dimensional tolerances caused by the necessary bending of the long, straight tubes into the required complex shapes. Re-evaluation of the 3D-CAD study including the implementation of the manufacturing dimensional tolerances is a promising solution.

The welding torches used in the mock-up experiment need at least 50 mm around the welding line of the tube. However, in some areas, the distance between the FFDL tube nozzle and the instrumentation guide tube (⑤ in Fig.7-2) was less than 50 mm, depending on the horizontal orientation of the guide tube. Welding between the FFDL tube nozzle and the FFDL tube was therefore impossible at these points. To address this issue, future work will involve evaluating the appropriate range of the FFDL tube nozzle orientation to ensure the necessary space for welding, as shown in Fig.7-4. The arrangement of the tubes should then be re-evaluated based on this range.

The performed CAD study and partial-full-scale mock-up will aid in the development of fabrication and manufacturing efforts for the design of the ACS.

This study is part of the results conducted on “Technology development program of fast reactor international cooperation, and others”, supported by the Agency for Natural Resources and Energy (ANRE), the Ministry of Economy, Trade and Industry (METI), Japan.

(Kazuya Takano)

Reference

Takano, K. et al., Routing Study of Above Core Structure with Mock-Up Experiment for ASTRID, Proceedings of 2019 International Congress on Advances in Nuclear Power Plants (ICAPP 2019), Juan-Les-Pins, France, 2019, 8p.

7-2 Reliable Decay Heat Removal by Natural Convection

— Core Cooling Experiment Using Dipped DHX and Development of Evaluation Method —

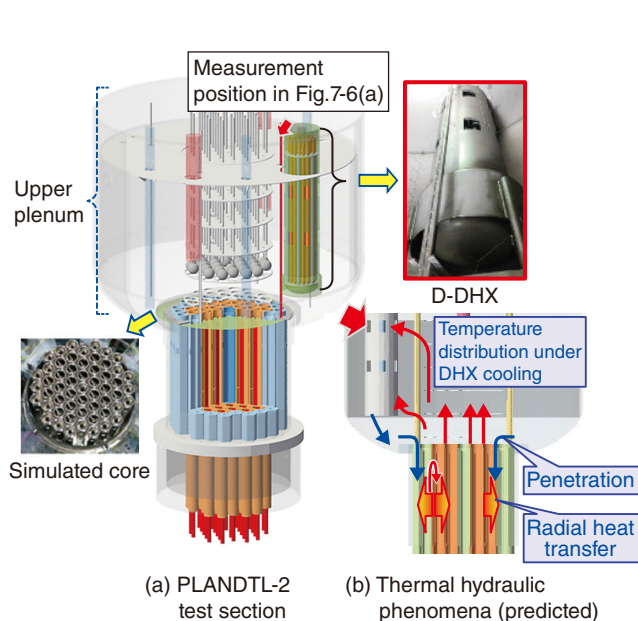


Fig.7-5 Schematic and imaging of the test section of PLANDTL-2 and target phenomena in natural circulation decay heat removal with D-DHX

The PLANDTL-2 test section (a) models major components of a SFR with 1/5th scale to simulate core cooling behavior (b) by a dipped-type direct heat exchanger (D-DHX).

Decay heat removal systems (DHRSs) that take advantage of thermal properties of liquid sodium (Na) have been studied to enhance the safety of SFRs. A DHRS using a heat exchanger dipped in the upper plenum of the reactor vessel (i.e., a dipped-type direct heat exchanger, D-DHX), shown in Fig.7-5(a) is a prime candidate. This system can work in case of the loss of external power supply to the plant, because high-temperature Na from the core is cooled through the D-DHX returns to the core by natural convection. During the operation of the D-DHX, the low-temperature Na from the D-DHX penetrates the fuel assembly (FA) and the gap between FAs. To clarify the core coolability using the D-DHX, it is important to investigate the thermal interaction between the low-temperature Na and the high-temperature Na. From this perspective, a series of Na experiments using Na experimental apparatus PLANDTL-2 were performed under D-DHX operation to clarify the core coolability and to validate numerical analysis methods.

An overview of the test section of PLANDTL-2 is shown in Fig.7-5; here, major components of SFRs, such as an upper plenum, a simulated core, and a D-DHX were installed at approximately a 1/5th scale. The core was modeled by hexagonal wrapper tube channels consisting of 30 electric heating channels and 25 non-heating channels. More than 550 points of thermocouples were installed inside the test section

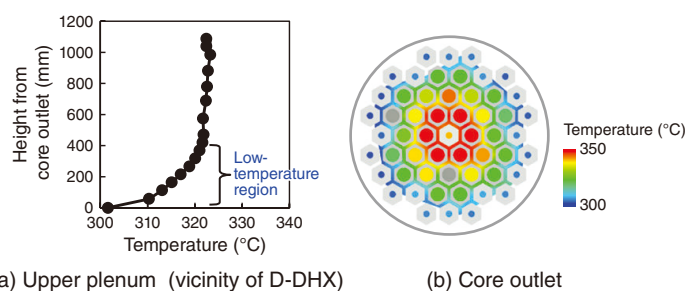


Fig.7-6 Example temperature distribution in PLANDTL-2

In (a), a low-temperature region is formed in the bottom of the upper plenum; core cooling behavior in its outer region is observed in (b).

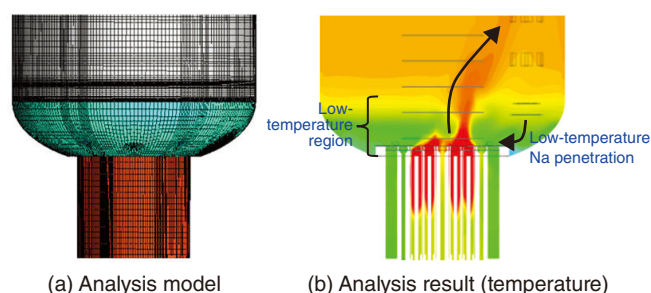


Fig.7-7 Example numerical simulation of PLANDTL-2

In the numerical result (b) using the CFD analysis model (a), typical phenomena were observed, such as the formation of the low-temperature region and penetration into the core.

to obtain a detailed temperature profile across the reactor vessel; a resulting representative measured profile temperature distribution is shown in Fig.7-6. Here, a low-temperature region was formed in the bottom of the upper plenum by the Na from the D-DHX (Fig.7-6(a)). The low-temperature Na penetrated the inside of the channels and the gaps between them from the outer region of the core (Fig.7-6(b)). The results indicate that the core was stably cooled by the D-DHX operation and the safety-enhanced SFR was feasible.

Measured data in PLANDTL-2 were also used to validate the evaluation method based on numerical analyses using computational fluid dynamics (CFD). As shown in Fig.7-7, it is expected that prediction of thermal hydraulic phenomena inside the reactor vessel becomes possible through the validation using the data obtained in PLANDTL-2. This will allow for the replacement of large-scale SFR tests with numerical analyses, thus reducing the development costs in future.

This study is part of the results conducted on “Technology development program of fast breeder reactor international cooperation, and others”, supported by the Agency of Natural Resources and Energy (ANRE), the Ministry of Economy, Trade and Industry (METI), Japan.

(Toshiki Ezure)

Reference

Ezure, T. et al., Study on Multi-Dimensional Core Cooling Behavior of Sodium-Cooled Fast Reactors under DRACS Operating Conditions, Proceedings of 18th International Topical Meeting on Nuclear Reactor Thermal Hydraulics (NURETH-18), Portland, U.S.A., 2019, p.3355–3363, in USB Flash Drive.

7-3 Development of Fuel Assembly Analysis Method in Fast Reactors

— Prediction of Thermal Hydraulics in Fuel Assembly with Inner Duct Structure (FAIDUS) —

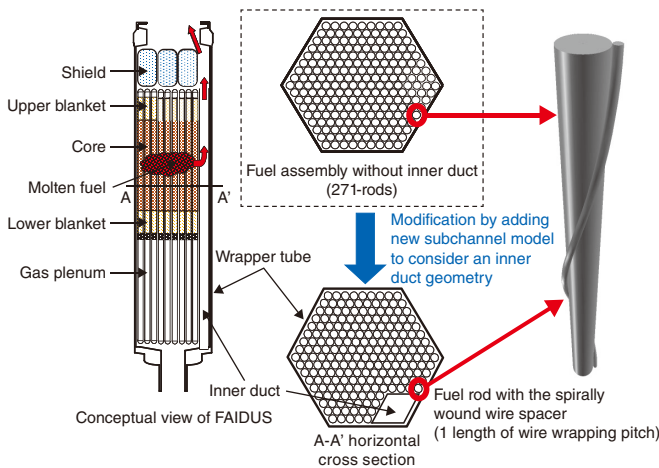


Fig.7-8 Fuel assembly with inner duct structure (FAIDUS) schematic
 In a core-disruptive accident, re-criticality is avoided by discharging molten fuel outside of the core region through the inner duct.

Table 7-1 Major specifications and boundary conditions of fuel assembly

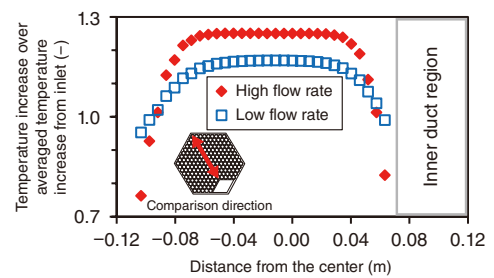
High and low flow rates at rated and decay heat removal operations, respectively, were set, referring to tentative specifications of large-scale advanced-SFR design.

Item	High flow rate	Low flow rate
Number of fuel rods	255	
Heated length (m)	1	
Coolant temperature at inlet (°C)	395	
Power of fuel assembly (MW)	8.3	0.25
Mass flow rate (kg/s)	34.2	1.03

In the design study of a SFR, the use of a specific fuel assembly (FA) with an inner duct structure called FAIDUS, in which the inner duct of the rhombic cross-section is installed at the corner of the hexagonal wrapper tube, as shown in Fig.7-8, has been investigated to enhance safety of SFR against a core disruptive accident. In FA as well as FAIDUS, fuel rods with a spirally wound wire spacer are installed in the wrapper tube to maintain the sodium flow area. A subchannel analysis code, ASFRE, was thus developed as a FA design tool to perform parametric analyses of thermal hydraulics. In ASFRE, the control volume is a flow region (subchannel) surrounded by fuel rods or a wrapper tube. Prior research has used experimental data to validate ASFRE for FAs without an inner duct. However, it is necessary to estimate the temperature distribution with the inner duct because of the resulting asymmetrical layout of fuel rods in FAIDUS.

This work therefore aimed to further develop ASFRE by adding a new subchannel model to consider the inner duct geometry; thermal hydraulics analyses in FAIDUS were then performed at two representative flow rate conditions as listed in Table 7-1. The resulting horizontal distribution of the temperature of sodium at the top of the heated section is shown

(a) Temperature distribution along the traverse line from inner duct



(b) Temperature distribution in the peripheral region

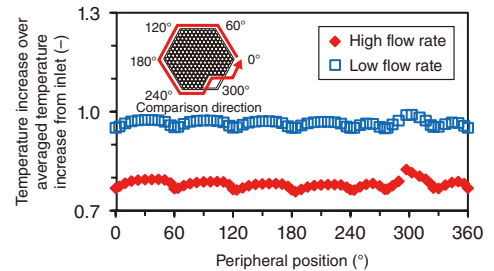


Fig.7-9 Numerical results of thermal hydraulics in FAIDUS at the top of the heated section

The local temperature increase near the corner of the inner duct (300°) at the high and low flow rate conditions were due to the high-temperature flow of sodium from inside to the region near the inner duct by horizontal flow due to a spirally wound wire spacer.

in Fig.7-9(a). At the representative low flow rate, a smaller temperature difference was indicated between the center and peripheral regions than at the representative high flow rate because the flow rate ratio in the center region increased due to the buoyancy effect in the FA. Further, the existence of the inner duct caused an asymmetric distribution at both flow rate conditions. The temperature distribution along the peripheral region on the wall of the FA is shown in Fig.7-9(b). Here, a periodic pattern at every 60° was shown, in accordance with the contact condition of the wire spacer on the wrapper tube wall, except at the corner of the inner duct, where a different contact condition was present for FAIDUS. Thus, ASFRE was deemed as valid for usage in evaluating the temperature distribution in FAIDUS.

Since experimental data of the thermal hydraulics in FAIDUS have not yet been obtained, future work will involve thermal hydraulic evaluation of ASFRE for FAs including FAIDUS through code-to-code comparisons with the detailed CFD analysis to confirm the accuracy of the evaluation results presented here.

(Norihiro Kikuchi)

Reference

Kikuchi, N. et al., Subchannel Analysis of Thermal-Hydraulics in a Fuel Assembly with Inner Duct Structure of a Sodium-Cooled Fast Reactor, Journal of Nuclear Engineering and Radiation Science, vol.5, issue 2, 2019, p.021001-1–021001-12.

7-4 Development of Ultra-High Temperature Tolerant Fuel Claddings

— Mechanical Properties of Oxide Dispersion Strengthened Steel Claddings at 1000 °C —

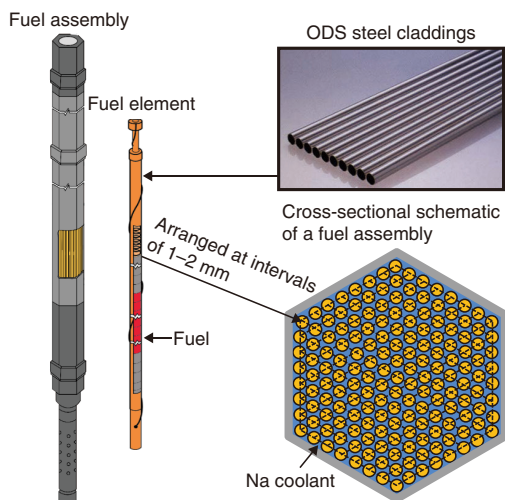


Fig.7-10 Fuel assembly and fuel element of a fast reactor

Fuel claddings requires excellent resistance to deformation and fracture to trap radioactive materials in the fuel element and to play the important safety function of maintaining a flow path for cooling.

A fuel element is manufactured by filling a nuclear fuel with fuel cladding and sealing both ends with end plugs. The fuel claddings trap not only nuclear fuel, which produces high-density energy by nuclear fission in the nuclear reactor, but radioactive materials produced by this nuclear fission, as well. They also have the important safety function of maintaining the coolant flow path to cool the exoergic nuclear fuels (as shown in Fig.7-10).

Oxide dispersion strengthened (ODS) steels have been under development as a fuel cladding for SFRs by JAEA. It has been clarified that ODS steel has the highest creep strength level near the maximum operating temperature (about 700 °C) in the world and to be effective for the high burnup fuel claddings of SFRs. To further clarify the safety of ODS steel and ensure the prevention of severe accidents and of the release of radioactive materials to the environment, it is necessary to evaluate its tolerance for deformation and destruction at ultra-high temperatures exceeding 700 °C.

Creep rupture tests of ODS steel claddings were therefore performed at 1000 °C, the results of which are as shown in Fig.7-11, where they are compared with those of heat-resistant austenitic steel (AH-4)* developed by a Japanese steel company for use up to temperatures ≥ 1000 °C. The creep rupture strength of ODS steel was much higher than that of AH-4 even at 1000 °C, even though the strength of ferritic steels is known to be lower than that of austenitic steels at high temperatures. These data demonstrated the superior creep rupture strength of ODS steel at 1000 °C. Further, the change in outer diameter of the ODS steel was much smaller (less than a few percent), thus

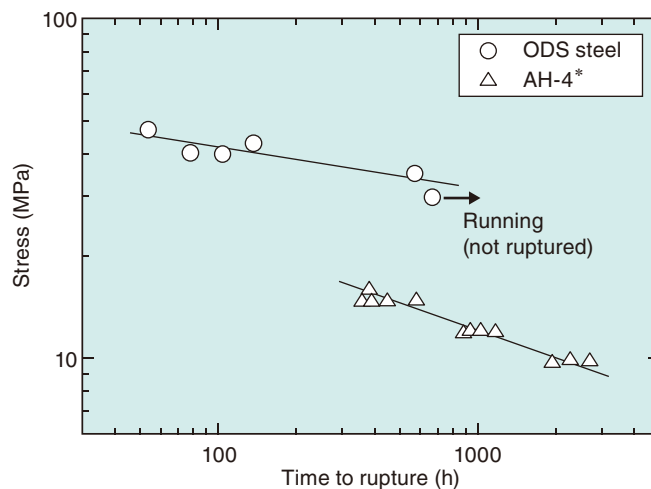


Fig.7-11 Creep rupture tests of ODS steel at 1000 °C

Creep rupture strength of JAEA's ODS claddings for SFRs was much higher than those of heat-resistant austenitic steel (AH-4)*, which was developed for use up to temperatures above 1000 °C.

indicating that its resistance to deformation was much higher than that of austenitic steels. These results thus demonstrate the strong tolerance of ODS steel to ultra-high temperature rupture and deformation. In addition, temperature-transient-to-burst tests, which has been used for evaluating the strength of claddings in transient events such as loss-of-flow (temperature is increased in a short time from several hundred to around 1000 °C), were also carried out. As the result, the validity of the design analysis method suggests that the life fraction rule could be used for rupture life prediction of ODS steel claddings in transient and accident events with a certain accuracy.

In the future, it will acquire data on the mechanical properties of ODS steels under various conditions required for design and analysis, including at temperature range ≥ 1000 °C, to contribute to the continual safety improvement of SFRs. Therefore, JAEA will continue research and development of ODS steels to carry out technological feasibility assessments.

This study is part of the results conducted on “R&D of ODS ferritic steel fuel cladding for maintaining fuel integrity at the high temperature accident condition” entrusted to Hokkaido University, supported by the Ministry of Education, Culture, Sports, Science and Technology (MEXT), Japan. JAEA was subcontracted by Hokkaido University to carry out the research.

(Yasuhide Yano)

* Yamamoto, S. et al., Heat-Resistant Austenitic Stainless Steel, Nippon Steel & Sumitomo Metal Technical Report, no.106, 2014, p.96–102.

Reference

Yano, Y. et al., Ultra-High Temperature Creep Rupture and Transient Burst Strength of ODS Steel Claddings, Journal of Nuclear Materials, vol.516, 2019, p.347–353.

7-5 Exploring an Ignition Mechanism of Hydrogen with Burning Sodium Mist

— Visualizing the Ignition Process of Hydrogen Jets Containing Mist Caused by Sodium Leaks in Severe Accidents —

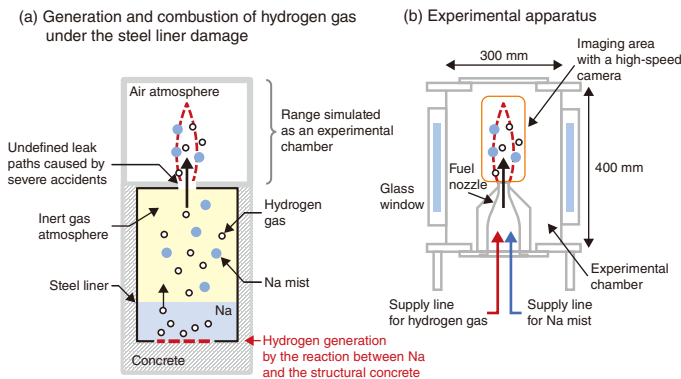


Fig.7-12 (a) Hydrogen generation when a steel liner is damaged and (b) the designed experimental apparatus

(a) Hydrogen is generated by the reaction between leaked Na and structural concrete if the liner is damaged during a severe accident. This hydrogen burns in a room filled with air. (b) The flame was observed through a quartz glass window.

Sodium (Na) used in sodium-cooled fast reactors (SFRs) burns in oxygen and can react with water to generate hydrogen gas. To prevent leaked Na from reacting with water in structural concrete, a steel liner is built inside a room where Na components or Na pipes are installed. In the event of severe accidents, however, a Na-concrete reaction caused by a damage to the liner would generate hydrogen gas and Na mist (fine droplets). When this hydrogen gas and Na mist are emitted into the room filled with air, hydrogen is considered to burn like a burner besides sodium combustion as shown in Fig.7-12(a). This combustion of hydrogen jets containing Na mist is a phenomenon specific to SFRs and is a different combustion mode from hydrogen deflagration due to hydrogen accumulated in the room. The ignition mechanism of hydrogen with a burning Na mist must be clarified to gain a better understanding of ignition risks of SFRs during severe accidents.

Therefore, a combustion experiment was performed to visualize the ignition process of hydrogen jets by high-speed and high-sensitivity imaging. A Na mist (about 15 g/m^3) was produced from Na vapor heated at $750 \text{ }^\circ\text{C}$ in an inert gas atmosphere and was mixed with 10% hydrogen ($260 \text{ }^\circ\text{C}$, diluted with an inert gas). The hydrogen gas and Na mist were then emitted into an experimental chamber containing 21% oxygen, which was designed to simulate a room filled with air (Fig.7-12(b)). Additionally, as a comparative experiment, only Na mist was emitted without hydrogen gas; here, the burning Na mist produced a conical flame, caused by combustion of invisible small mist, and many sparks scattered intermittently outside the conical flame, as shown in the monochrome image

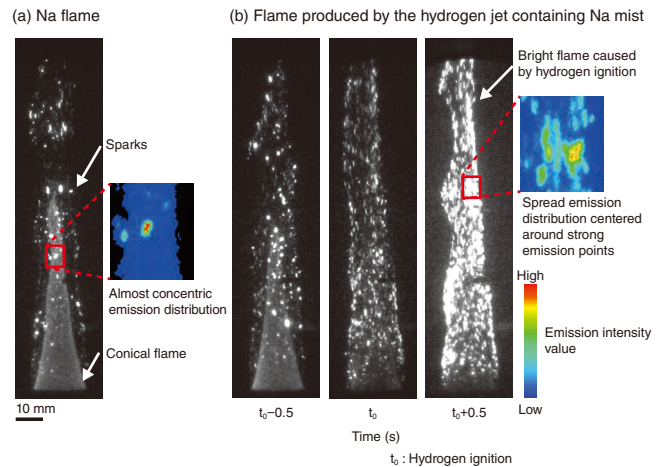


Fig.7-13 Observed flames: (a) Na and (b) hydrogen containing Na mist

(a) The Na flame was produced by a Na mist emitted upward. (b) A hydrogen jet containing a Na mist gradually changed into a new bright flame after the Na flame was produced. The ignition mechanism of hydrogen was clarified based on these observations.

of Fig.7-13(a). With the inclusion of hydrogen, the Na flame was also formed; however, within 1 s, a new bright flame was produced that gradually covered the conical Na flame, as visible in Fig.7-13(b). Because this bright flame only appeared when the Na mist and hydrogen coexisted, the flame can be attributed to the ignition of hydrogen.

To focus on the change in brightness of flame from the time (t_0) when this change started compared to the brightness of only Na flame, the spatial distribution of emission intensity was analyzed using a coloring method that maps the intensity values into assigned colors, shown in the small colored maps of Fig.7-13. In the sparks of the Na flame, the emission distribution was nearly concentric and localized around a strong emission point generated by the burning of each Na mist particle (Fig.7-13(a)). Once the hydrogen was ignited, the distribution spread across a larger area and contained the sparks (Fig.7-13(b)). This difference in emission distribution indicates that during the ignition of the hydrogen jet containing the Na mist, hydrogen was locally ignited around the burning Na mist particles. Future work will investigate the ignition conditions of hydrogen under various oxygen concentrations.

This study is part of the results conducted on “Development of Estimation Technology for Availability of Measure for Failure of Containment Vessel in Sodium Cooled Fast Reactor” entrusted to University of Fukui, supported by the Ministry of Education, Culture, Sports, Science and Technology (MEXT), Japan. JAEA was subcontracted by University of Fukui to carry out the research.

(Daisuke Doi)

Reference

Doi, D. et al., Visualizing an Ignition Process of Hydrogen Jets Containing Sodium Mist by High-Speed Imaging, Journal of Nuclear Science and Technology, vol.56, issue 6, 2019, p.521–532.

Toward Decommissioning Nuclear Facilities and Managing Radioactive Waste

To maintain and develop its research and development (R&D) capabilities by strengthening the safety of its nuclear facilities and ensure steady implementation of back-end measures, JAEA issues the “Medium- and Long-Term Management Plan of our Facilities” (issued on April 1, 2017, amended on April 1, 2020) as a comprehensive plan detailing the following three points:

- the selection and consolidation of facilities,
- safety measures, and
- the management of back-end issues.

In the plan, 89 nuclear facilities were chosen to be decommissioned.

Among the large facilities, JAEA submitted an application for permission to proceed with the decommissioning of MONJU and the Tokai Reprocessing Plant (TRP) to the Nuclear Regulation Authority (NRA), which led to the NRA granting permission for the decommissioning of MONJU on March 28, 2018, and for that of TRP on June 13, 2018. The application to the NRA for permission of the decommissioning of the Uranium Enrichment Demonstration Plant is ongoing.

The implementation of back-end measures requires long-term prospects and policies, including those regarding the processing and disposal of radioactive waste; the decommissioning of TRP has been expected to take approximately 70 years to complete.

JAEA therefore published a long-term prospect and policy for back-end measures, the “Back-end Roadmap”, on December 26, 2018.

To ensure safe and appropriate nuclear facility decommissioning and radioactive waste management, it is necessary to introduce new technologies and knowledge and to promote the development of technologies for advanced safety and cost reduction. Technologies for the safe and effective dismantling of nuclear facilities, the minimization and stabilization of radioactive wastes, and the disposal of radioactive wastes are under development (Fig.8-1). The proposed disposal project applies to low-level radioactive wastes from research facilities of universities, private organizations, and JAEA facilities.

Specifically, this year saw a making of the calculation cord manual for the dismantling cost of nuclear facilities (Topic 8-1), an investigation of the evaluation method of the radioactivity concentration in radioactive waste (Topic 8-2), an evaluation of the influence of a low dose of radiation on the human body using machine learning (Topic 8-3), and the development of a safe disposal technology of radioactive liquid waste containing various chemical substances (Topic 8-4).

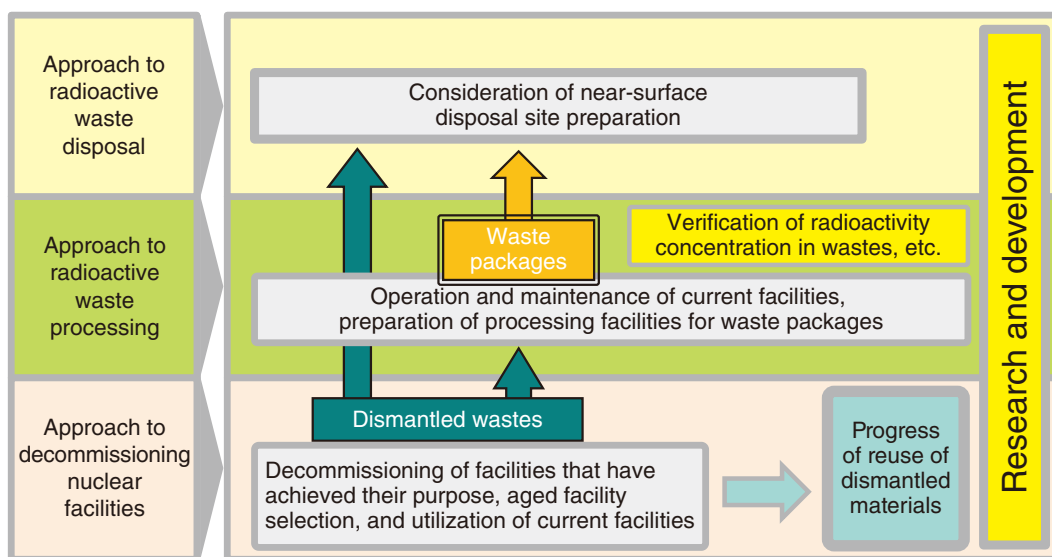


Fig.8-1 Outline of low-level radioactive waste management

R&D of the decommissioning of nuclear facilities and processing of radioactive wastes, including waste treatment and waste characterization, has been promoted.

R&D to Improve Technology and Reliability of Geological Disposal in Japan

Geological disposal is internationally recognized as the most appropriate method for the long-term isolation of high-level radioactive waste (HLW), which is produced during the generation of nuclear power, from human environments. This critical issue must be approached sensibly by the present generation and will remain crucial regardless of any revision of the national nuclear energy policy.

In Japan, fuel spent in nuclear reactors is reprocessed to extract

the reusable uranium and plutonium for power generation. The liquids separated from the spent fuel during chemical reprocessing are solidified into a stable glass form. Under the Japanese disposal concept, vitrified waste is then encapsulated in a thick steel overpack, surrounded by highly compacted bentonite, and placed in a stable geological environment at a depth of more than 300 m below the surface (Fig.8-2).

R&D in relevant fields such as geoscience, repository

engineering, and safety assessments are ongoing, as summarized in Fig.8-3, and are vital to improving their sound technical basis and be reflected in the implementation and regulatory activities.

At the Horonobe Underground Research Center, R&D of three important issues targeting sedimentary rock (e.g., near-field performance study) are being conducted using underground facilities (Topics 8-5 and 8-6).

To evaluate the long-term stability of geological environments in Japan, studies on topics such as tectonics, volcanic and faulting activities, and dating techniques are ongoing at the Toki Geochronology Research Laboratory (TGR) at the Tono Geoscience Center (Topic 8-7). Further, the R&D activities completed in FY2019 as part of the project at the Mizunami Underground Research Laboratory (URL) targeting crystalline rock will enhance their efforts in backfilling the galleries (Topic 8-8).

To further expand the knowledge regarding geological disposal, extensive studies to assess the performance of the disposal system, engineered barrier systems, and long-term chemistry and migration of radionuclides at Tokai are being studied (Topics 8-9 and 8-10). These studies exploit the data regarding geological environments that were obtained through

geoscientific research at both mentioned URLs.

Results of the R&D activities have been summarized as a web-based report (CoolRep), which has been made available on JAEA's public website (CoolRep: <https://kms1.jaea.go.jp/CoolRep/english.html>).

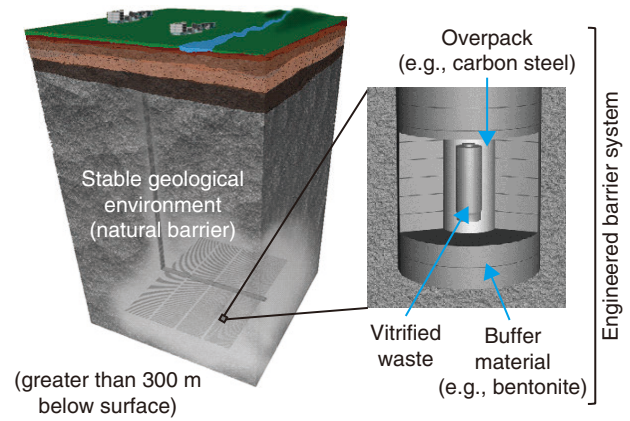


Fig.8-2 Schematic view of the basic concept for the geological disposal of high-level radioactive waste in Japan

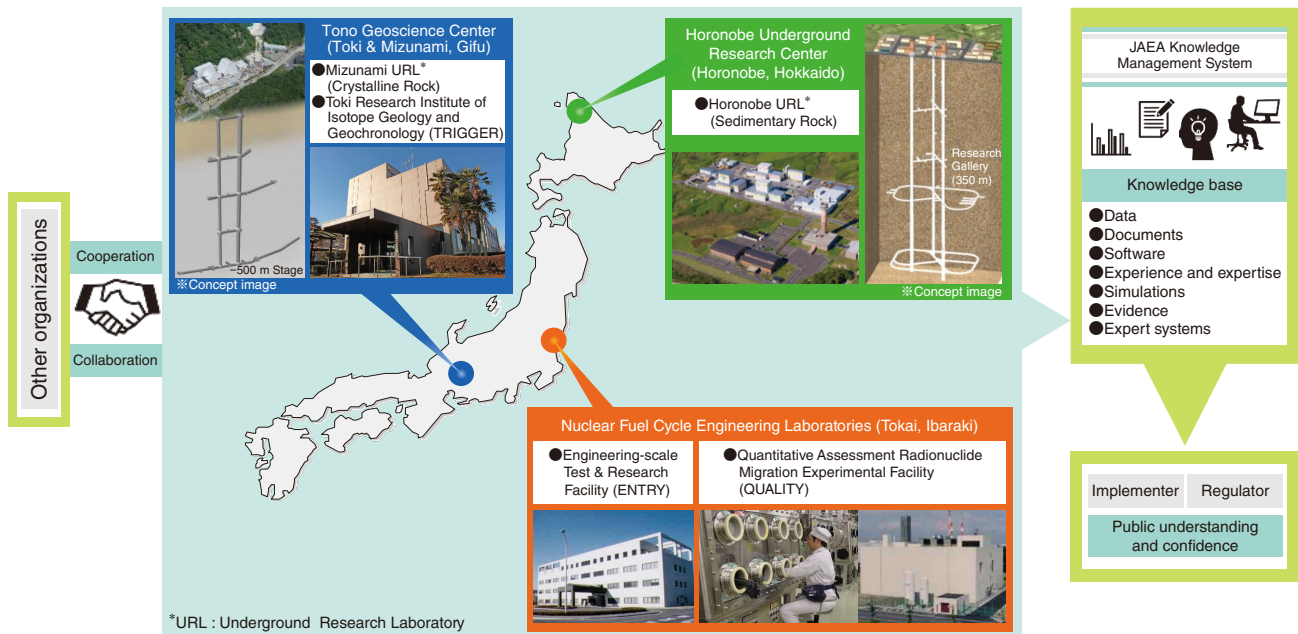


Fig.8-3 Structure of JAEA R&D activities

Improvement of Reprocessing Technologies and Decommissioning of Tokai Reprocessing Plant

The vitrification of HLW is promoting with a primary focus on safety and on the risk reduction of the radioactive material stored. JAEA has also developed advanced vitrification techniques. Further, an advanced technique for analyzing the components of HLW for vitrification was developed. In this technique, radioactive samples including HLW are analyzed inside a shielded cell or glovebox. An analytical apparatus applied in such an environment must be small enough to be installed in a narrow space, be remotely operated, and be

easily maintainable. To meet these requirements, the developed analytical method uses optical emission spectrometry based on the plasma generated into bubbles in microchannels with a hundred-micrometer width (Topic 8-11). This remote-analysis technique developed for radioactive samples is expected to be useful analytical method in a variety of applications, such as for process control measures in cement solidification facilities, for liquid waste generated by decontamination, and for vitrification.

8-1 Toward Public Use of the Decommissioning Cost Estimation Code DECOST — Development of a Manual for the DECOST —

Table 8-1 Input datasheet example for estimating the dismantling cost using DECOST

The information required for estimating the dismantling cost includes the unit cost per worker, building information related to the dismantling of the facility, special equipment information for individually evaluating the work required, and waste-related information for calculating the total amount of work. In the manual, methods to obtain this information are explained and a summary datasheet is provided. Here, the necessary information acquired from the Japan Power Demonstration Reactor (JPDR) is summarized. JPDR was the first reactor in Japan to carry out nuclear power generation and was the first facility to demonstrate that we could dismantle and demolish a nuclear reactor.

Input information		Data		Input information		Data		Input information		Data		
Type of facility		Reactor		Accelerator shielding (Metal)		0 t		Concrete_CL		524 t		
Consumption tax		3 %		Accelerator shielding (Concrete) by wire saw		0 t		Concrete_NR		19295 t		
Unit cost	Worker	XXXX	¥/man-day	Special equip.	Accelerator shielding (Concrete) by batch removal		0 t		Miscellaneous solid_L0		0 t	
	Manager of radiation management	XXXX	¥/man-day		Remote dismantling (Cell)		0 ¥ ; 0 n		Miscellaneous solid_L1		0 t	
	Manager of work management	XXXX	¥/man-day		Metal_L0		0 t		Miscellaneous solid_L2		2.4 t	
Building info.	Decontamination systems	0 n		Waste related info.	Metal_L1		44 t		Miscellaneous solid_L3		7.9 t	
	Floor area of cell	0 m ²			Metal_L2		118 t		Miscellaneous solid_CL		0 t	
	Floor area of controlled area	23800 m ²			Metal_L3		78 t		Miscellaneous solid_NR		0 t	
	Floor area of building (steel slate)	0 m ²			Metal_CL		865 t		Casks		XXXX ¥ ; 19 n	
	Safe-storage period	0 year			Metal_NR		1324 t		1m ³ steel containers		XXXX ¥ ; 0 n	
Special equip.	Lining weight	23 t		Concrete_L0		0 t		Drum (epoxy coatings)		XXXX ¥ ; 1125 n		
	Centrifuge weight	0 t		Concrete_L1		60 t		Drum (galvanized containers)		XXXX ¥ ; 0 n		
	Large sized GB weight	0 t		Concrete_L2		83 t		Drum (concrete linings)		XXXX ¥ ; 0 n		
	Small sized GB weight	0 t		Concrete_L3		1477 t		Flexible container		XXXX ¥ ; 1147 n		

To decommission a nuclear facility after serve its expected purpose, all equipment must be dismantled and all contamination by nuclear materials must be removed; the costs of such an operation must be estimated when developing a decommissioning plan. Therefore, in 2007, an estimation code was developed, the Simplified Decommissioning Cost Estimation Code for Nuclear Facilities (DECOST); this code can be applied to a wide variety of nuclear facilities and has been used in JAEA. This method allows you to easily estimate decommissioning costs based on the characteristics and similarities of facilities, dismantling methods, etc. Since 2017, all nuclear licensees in Japan are obliged to develop and publish a decommissioning plan of all their nuclear facilities before they go live, i.e., an initial decommissioning plan, by the law for the regulation of nuclear source material, nuclear fuel material, and reactors amended. The initial decommissioning plan must also include the estimated costs required for decommissioning. JAEA thus created and published a manual, in which how to use the cost estimation formulas and the required information for DECOST were summarized, for all nuclear licensees to estimate the dismantling costs of their various types of nuclear facilities with reference to DECOST. However, DECOST is still in the preparatory stage for public release from JAEA's website.

When using DECOST, the type of facility to be evaluated is first selected, where the cost items based on the facility type and the corresponding formulas are selected. Next, the user inputs the data required for the cost calculation, which includes the unit cost of workers, the building information of the facility, and the waste related information (hereinafter, input information) to calculate the cost of dismantling each item. In the manual, an overview of DECOST is provided, i.e., the dismantling costs estimation methods, and how to acquire and enter the input information. Nuclear facilities include facilities

for various purposes such as nuclear reactors for testing and research, uranium-handling facilities, MOX handling facilities, and reprocessing facilities. Therefore, nuclear facilities are classified into 10 types in DECOST and each type has its own set of formulas, which are prepared by the same basic concept.

For this reason, the characteristics of each type of facility are described in the manual; further, each type of facility is associated with a JAEA facility for reference and to make it easier for the DECOST users to determine which of the 10 facility types the target facility falls under. Additionally, a table was created that allows users to easily select the required set of formulas to estimate the cost of dismantling the facility by simply selecting the type of facility.

The user must prepare up to 42 input information when estimating the dismantling cost using DECOST. Input information includes, for example, the total floor area of the controlled area and the amount of dismantled waste, classified by disposal type (e.g., radioactive or non-radioactive) and by materials (e.g., concrete or metal). Alongside the required datasheet for preparation of the input information, the manual provides a datasheet including data of the successfully dismantled facility JPDR as an input example so that it can be used as a reference for recording input information (see Table 8-1).

This manual was published in 2018 so that nuclear licensees other than JAEA can use it to create an initial decommissioning plan. Since then, four nuclear licensees have stated that they used the manual. When JAEA announced the initial decommissioning plan in January 2019, DECOST had been used to estimate the dismantling costs of nearly all JAEA-owned nuclear facilities. Future improvements to DECOST will include updating with the latest data on facility dismantling, here recently.

(Nobuo Takahashi)

Reference

Takahashi, N. et al., The User Manual of the Simplified Decommissioning Cost Estimation Code for Nuclear Facilities (DECOST), JAEA-Testing 2018-002, 2018, 45p. (in Japanese).

8-2 Radioactive Waste Confirmation Method for Rational Disposal

— Study on the Evaluation Methodology of Wastes Generated from Post-Irradiation Examination Facilities —

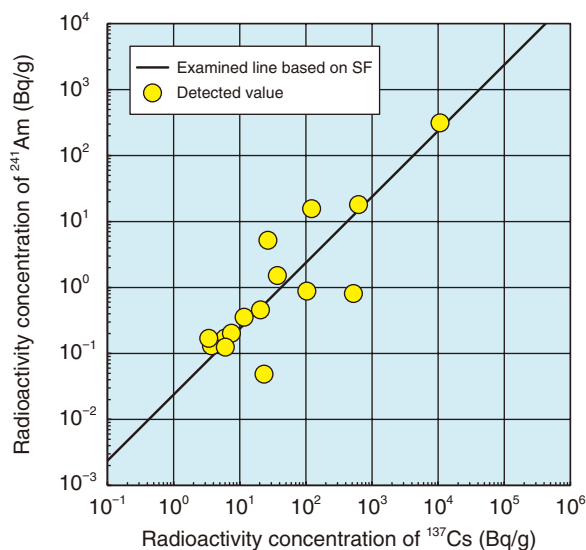


Fig.8-4 Relationship between the radioactivity concentrations of ^{137}Cs and ^{241}Am

The radioactivity concentration of ^{241}Am in the hot laboratory waste sample has good linear correlation with that of ^{137}Cs . Thus, the scaling factor method could be applied to evaluate the radioactivity concentration of ^{241}Am from that of ^{137}Cs .

Low-level radioactive wastes generated from nuclear research facilities at JAEA are planned to be disposed of in a near-surface disposal facility. Thus, a method for evaluating the radioactivity concentration contained in waste before starting disposal must be developed. However, directly determining the concentration of difficult-to-measure nuclides (DMNs), such as nuclides emitting alpha particles or beta rays, is impossible from outside the waste containers. Thus, to rapidly evaluate the concentration of DMNs, the scaling factor (SF) method or the average radioactivity concentration method was applied to the gamma-emitting nuclide (reference nuclides: cobalt-60 (^{60}Co), cesium-137 (^{137}Cs), etc.). Which method to apply consider for DMN concentration the generation mechanisms and transfer behavior of the radionuclide.

The applicability of the SF method to metal wastes from JPDR, JRR-2, and JRR-3 has been studied. In this work, the proposed method was applied to the waste from a hot laboratory (Hot Lab), a post-irradiation examination facility, focusing on 25 nuclides that are important for the evaluation of the exposure dose in near-surface disposal.

As radionuclides are in the radioactive wastes, fission products (FP), actinide elements generated from uranium, and corrosion products, produced by neutron activation on the structural materials or their corrosives during the reactor operation, are also present. In the wastes from the Hot Lab, all of these radionuclides are contained because various samples, some of

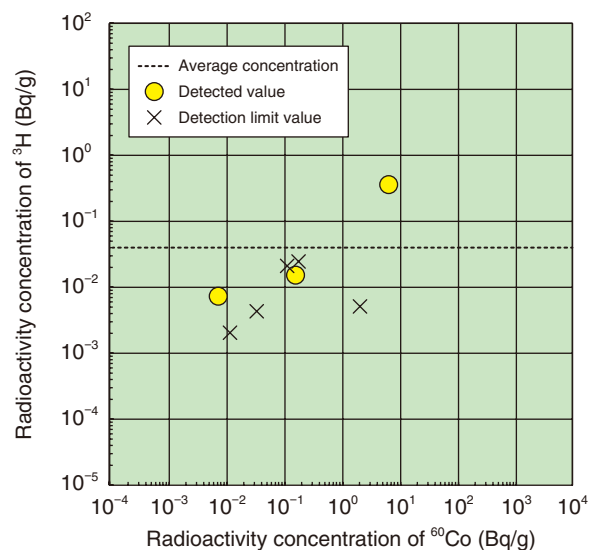


Fig.8-5 Relationship between the radioactivity concentrations of ^3H and ^{60}Co

The radioactivity concentration of ^3H in the waste sample is distributed in a certain range without correlation with ^{60}Co . The mean radioactivity concentration method could be applied for ^3H , which is calculated from the detected data and detection limits.

which were prepared by neutron irradiation in a reactor, have been treated.

An example of the relationship between radioactivity concentrations of two waste products is shown in Fig.8-4. Here, a clear relationship is found between the concentrations of ^{137}Cs (FP) and americium-241 (^{241}Am) (actinide element), thus demonstrating that the concentration of ^{241}Am can be evaluated using the SF method.

However, from the relationship between hydrogen-3 (^3H : tritium) and ^{60}Co , shown in Fig.8-5, such volatile nuclides present different transfer behaviors than ^{60}Co and ^{137}Cs and can have very small correlations with the reference nuclides. Therefore, if a nuclide does not correlate with the reference nuclide or the amount is too small to detect significant radiation signals, the average radioactivity concentration method is applied. Using this method, the concentration ratio of ^3H and ^{60}Co have a margin of 1000 times or more that of the radioactivity concentration of radionuclide corresponding to dose criterion in a near-surface disposal facility.

Based on this work, the radioactivity concentration of 25 nuclides contained in the Hot Lab waste can be evaluated using the SF and the average radioactivity concentration methods. Future efforts will focus on extending this work to develop an evaluation method for waste from a variety of facilities.

(Akina Mitsukai)

Reference

Mitsukai, A. et al., Study on the Evaluation Methodology of the Radioactivity Concentration in Low-Level Radioactive Wastes Generated from Post Irradiation Examination Facility, JAEA-Technology 2019-015, 2019, 52p. (in Japanese).

8-3 Complex Biological Effect of Low-Dose Radiation

— Feature Extraction of Multidimensional Data Using Machine Learning —

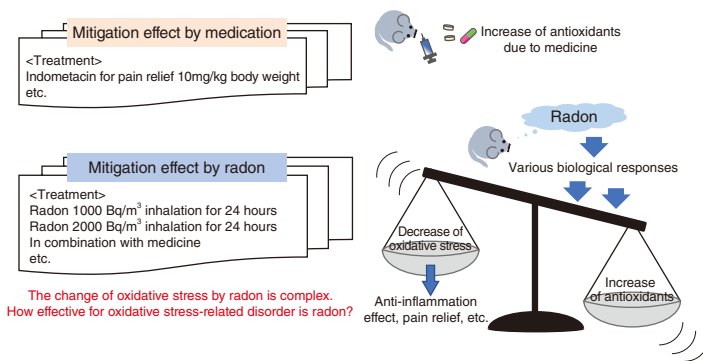


Fig.8-6 Input data for data analysis

Summary of the process and analytical data collected from reports that have shown the mitigation effect of oxidative stress-related disorders in mice by low-dose radiation or medication used to increase antioxidant ability. The condition of oxidative stress by radon exposure was more complex than that of medication.

Misasa Hot Springs in Tottori Prefecture, Japan, approximately 30 min by car from Ningyo-toe Environmental Engineering Center, is known as a radioactive hot spring containing radon. Radon hot springs have been used as alternative medicine, although their impact on human health has not been clarified. Therefore, in collaboration with Okayama University, a study focusing on clarifying the mechanism behind the low-dose radiation and how to measure its effect on human health has been performed. As a result, the increase in antioxidant ability by radon was found to inhibit oxidative stress-related disorders. However, evaluating the effectiveness of low-dose radon radiation on alleviating oxidative stress-related disorders is difficult because there are many factors of oxidative stress, not only radiation, and the biological responses are complex. The analytical data used had been collected from reports demonstrating the mitigation of the disorder in mice by low-dose radiation when compared with medication, as summarized in Fig.8-6. In particular, the state of oxidative stress is more complex due to the mix of various biological reactions that occur due to radon exposure. To clarify this data, a machine-learning approach was considered, which would allow complex information to be evaluated, given that the provided data regarding the antioxidant ability affected by radon treatments can be classified and visualized. A self-organizing map (SOM), which is a tool to place data with similar characteristics close together, was employed to visualize data similarities.

A SOM is an unsupervised artificial neural network of competitive machine learning. Briefly, the neurons, which have a vector of the same form (high dimension) as the input data, learn

Healthy, Radon-treated, medicated, treated with a combination of radon and medicine. Difference between neighborhood neurons (white: similar, black: dissimilar, black shadow indicates the separation data)

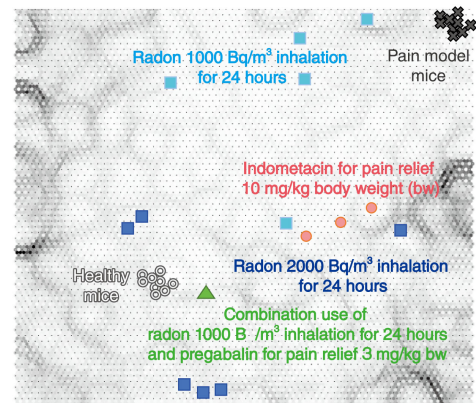


Fig.8-7 Example output map using SOM

The approximately 5000 neurons on the map correspond to each treatment condition and have a vector of the same form as the input data. As the neurons learn the input data, they self-organize as a result of similar neurons being placed close. By labeling the neurons corresponding to the input data, the complex analytical data was scattered over the entire map. However, a rough concentration dependence of radon was found.

the input data (multiplied by the learning rate) and then place data with similar characteristics close together. The resulting map output by the SOM has no axes; rather, it is a grayscale map demonstrating the regional difference between adjacent neurons, as the topology of the neurons on the map is important. SOMs allow for the comprehensive evaluation of information by dimension reduction and visualization.

The resulting output map with some data points labeled as examples is shown in Fig.8-7. Here, the space between the healthy mice and mice in pain shows little color change, indicating little change in the studied characteristic of their data. Although the plots of the mice in pain and those dosed with 1000 Bq/m³ of radon inhalation for 24 h are close together, the thin black shadow separating them indicates a greater change in their health characteristics (i.e., the mitigation effect). The complex nature of the data caused the data to be scattered across the map; however, data points representing mice treated with higher radon concentrations were closer to those representing healthy mice than untreated mice. This indicates the concentration dependence of radon, the effect of radon relative to medicine, and the combined effect of radon and medicine. Therefore, radon may be used as an alternative for pain relief and may have a combined effect with medicine.

In this study, SOM was used to evaluate the complex biological effects of low-dose radiation. Future work will focus on improving the algorithm of SOM to apply to the biological effects of various environmental factors other than radon.

(Norie Kanzaki)

Reference

Kanzaki, N. et al., Knowledge Discovery of Suppressive Effect of Disease and Increased Anti-Oxidative Function by Low-Dose Radiation Using Self-Organizing Map, RADIOISOTOPES, vol.67, issue 2, 2018, p.43-57.

8-4 Radioactive Liquid Waste Management Technologies

— STRAD Project for the Treatment of Radioactive Liquid Waste-Containing Chemicals —

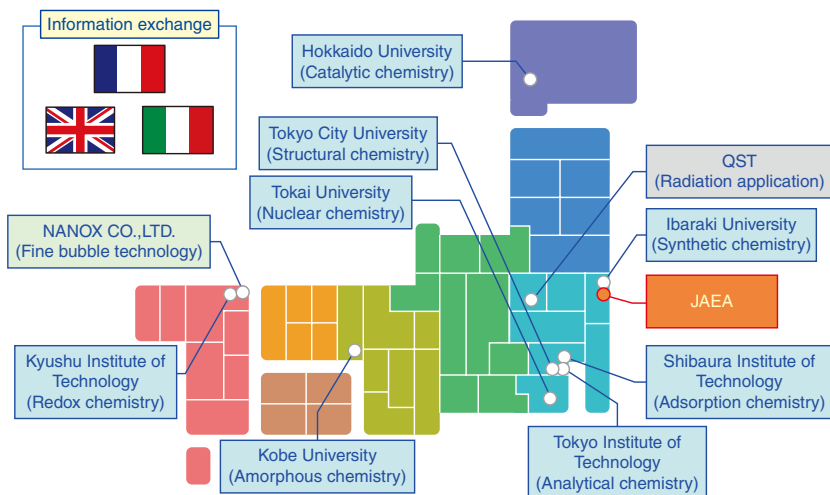


Fig.8-8 Organization of STRAD project (as of 2020)

Many scientists from universities, private companies, and a national organization contribute to the STRAD project. Information exchange with foreign facilities is also conducted under the project.



Fig.8-9 Experiments

(a) Ammonium ions in a simulated waste solution were oxidatively decomposed through catalysis.

(b) Solidification was demonstrated with MS manipulators inside a hot-cell.

Decommissioning nuclear facilities such as laboratories and medical facilities will be an important task in the near future. In particular, liquid waste accumulated inside the facilities, containing radioactive particles and various chemicals, must be treated inside the facility with special care and adherence to strict safety procedures.

JAEA is developing new technologies for treating liquid waste using genuine radioactive liquid waste accumulated in the Chemical Processing Facility (CPF) of JAEA under a collaborative research project, the Systematic Treatments of RADIOactive liquid wastes for Decommissioning (STRAD) project. Eleven organizations have joined the project, as shown in Fig.8-8, and participating members have actively performed research on and are engaged in discussions on the management of liquid waste.

As various activities in the facilities have generated many kinds of liquid wastes, an appropriate treatment procedure must be found for each liquid waste containing hazardous chemicals. One particularly difficult target is the aqueous solution generated by analyses on experimental samples. Reactive chemicals e.g., ammonium salts are often added to the sample during pretreatment; however, ammonium ions should be removed from

the solution to prevent the formation of explosive ammonium nitrate. As such, a method for decomposing the ammonium ion using ozone oxidation with a homogeneous CoCl_2 catalyst was developed (Fig.8-9(a)). Ammonium ions were successfully decomposed without high temperatures or pressures; thus, this method presents a safer alternative to previously reported methods. Other chemically reactive compounds are expected to be treated with a similar procedure.

As the recovery of U and Pu from spent solvent also presents a challenge, specialized adsorbents have been developed and tested. Phosphoric acid and lactic acid in the waste solutions of CPF were appropriately treated inside a hot-cell (see Fig.8-9(b)). The treatment procedures of liquid wastes at the CPF will be completed by the end of FY2022. The STRAD project will be further promoted based on the information exchange with foreign countries.

The STRAD project is conducted through several collaborative studies by JAEA with other organizations on, e.g., “Separation and decomposition of ammonium ion for treatment of radioactive liquid waste”.

(Sou Watanabe and Haruka Aihara)

Reference

Watanabe, S., Aihara, H. et al., STRAD Project for Systematic Treatments of Radioactive Liquid Wastes Generated in Nuclear Facilities, *Progress in Nuclear Energy*, vol.117, 2019, p.103090-1–103090-8.

8-5 Assessing Underground Fracture Connectivity from the Surface — Development of a Single Borehole Investigation Method —

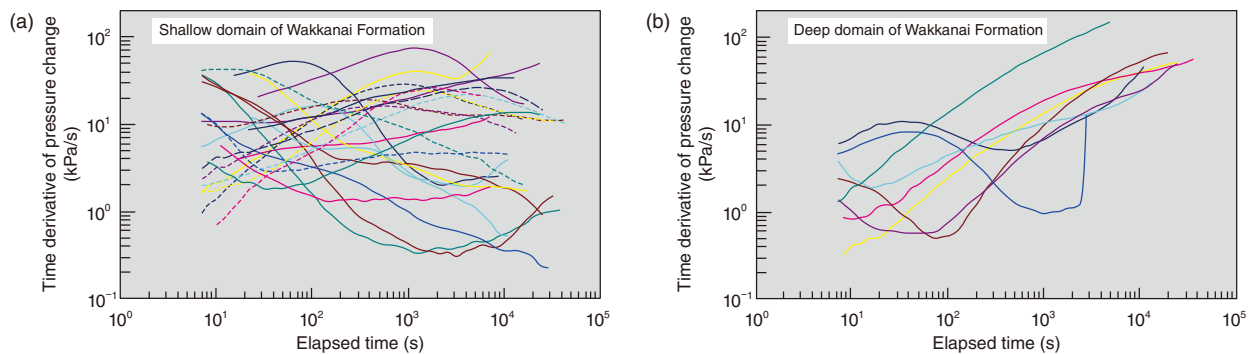


Fig.8-10 Time derivatives of pressure changes during packer tests of fractures in the Wakkanai Formation (from 32 points in 10 boreholes)

Stable or decreasing derivatives during the middle to late period of the elapsed time indicates a high fracture connectivity, whereas, an increasing derivative suggests low connectivity. The former and latter derivatives characterize the (a) shallow and (b) deep domains of the Wakkanai Formation, respectively.

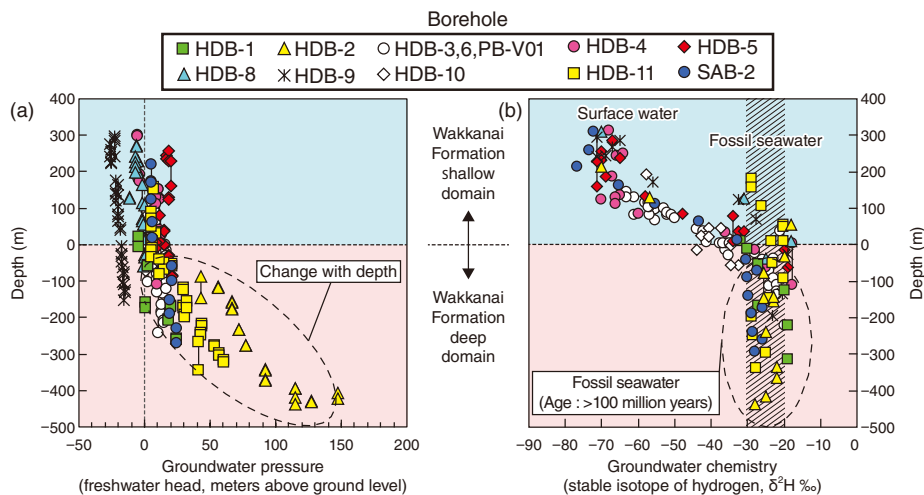


Fig.8-11 Depth distributions of groundwater pressure and chemistry measured in boreholes

(a) The change of freshwater head with depth in the deep domain of the Wakkanai Formation indicates low permeability.
(b) In the deep domain, fossil seawater also remains, although the surface water admixes near the boundary with the shallow domain. The boundary is denoted as 0 m in depth.

For radioactive waste disposal, it is important to efficiently detect low-permeability rock domains deep underground. Although water-conducting fractures may exist locally in rocks, the macroscopic permeability is low if the fracture connectivity is low.

Although assessing the connectivity of underground fractures by single-borehole investigations has been difficult, this work presented a methodology that allows the fracture connectivity to be efficiently assessed using single-borehole investigations. In the methodology, rocks are first divided into two depth domains using the rock-mechanical indicator, as fractures tend to connect when the effective mean rock-stress normalized to the tensile rock-strength is less than 2. The fracture connectivity in each domain is then assessed by analyzing pressure changes during hydraulic packer tests in each domain. Finally, this result is verified by comparison with water pressure, chemistry, and age.

This methodology was then applied to the Wakkanai Formation (a several-million-year-old marine bed) in northern Hokkaido to divide the formation into shallow and deep domains where the fractures mechanically tended to connect and not, respectively. Confirmed pressure changes during hydraulic packer tests indicated high- and low-fracture connectivity for the shallow and deep domains, respectively (Fig.8-10). These results for the deep domain were consistent with data on groundwater pressure, chemistry, and age, which exhibited a pressure distribution indicating low permeability and fossil seawater, which implies the presence of stagnated groundwater (Fig.8-11).

Thus, the methodology was confirmed feasible. The application of the method to other formations will assist in efficiently detecting low-permeability rock domains deep underground through single-borehole investigations.

(Eiichi Ishii)

Reference

Ishii, E., Assessment of Hydraulic Connectivity of Fractures in Mudstones by Single-Borehole Investigations, *Water Resources Research*, vol.54, issue 5, 2018, p.3335–3356.

8-6 Change in Permeability after Backfilling a Research Tunnel — Change in Hydraulic Conductivity in the Simulated Realistic Disposal Environment —

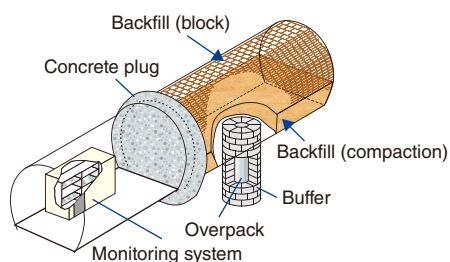


Fig.8-12 Illustration of the in situ engineered barrier system

The emplacement of the steel overpack, buffer material block, and backfilling were simulated.

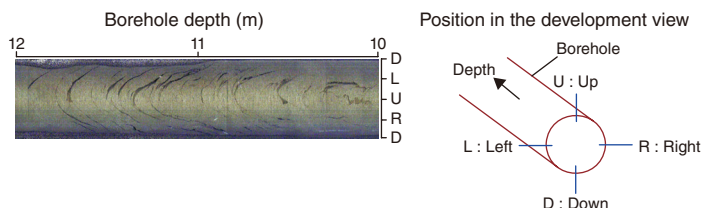


Fig.8-13 Development view of borehole wall image

Fractures were developed around the test pit in Section 2 (from 10 to 12 m).

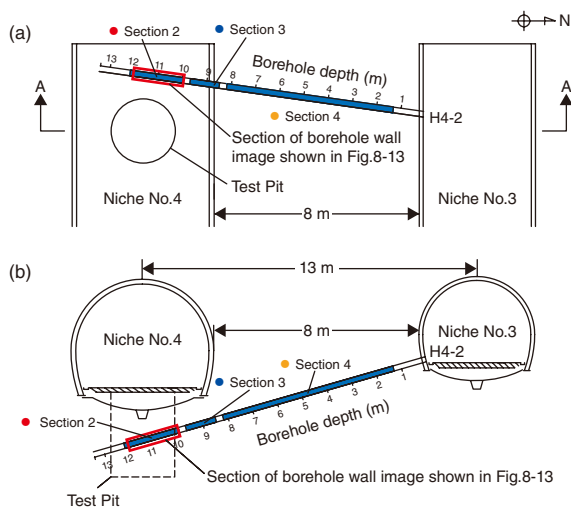


Fig.8-14 Layout of the hydraulic test: (a) plan view and (b) cross section

The construction of underground facilities induces fractures in the rock mass around the underground repository. This has particular implications for high-level radioactive waste (HLW) disposal projects, where fracture development creates an excavation-damaged zone (EDZ) that increases the hydraulic conductivity of the surrounding rock mass and can provide a pathway for migrating radionuclides from the disposal facilities. It is therefore necessary to develop a model that can estimate the future hydraulic conductivity of an EDZ and perform a comprehensive HLW-disposal safety assessment. In the Horonobe Underground Research Laboratory, an in situ engineered barrier experiment was designed to simulate a realistic disposal environment. In this experiment, which occurred from October 2014 to December 2014, the steel overpack and buffer material were placed and the gallery was partially backfilled (see Fig.8-12). Groundwater injections then began in January 2015. Additionally, hydraulic tests were performed for the following four years around the test pit to investigate the change in hydraulic conductivity.

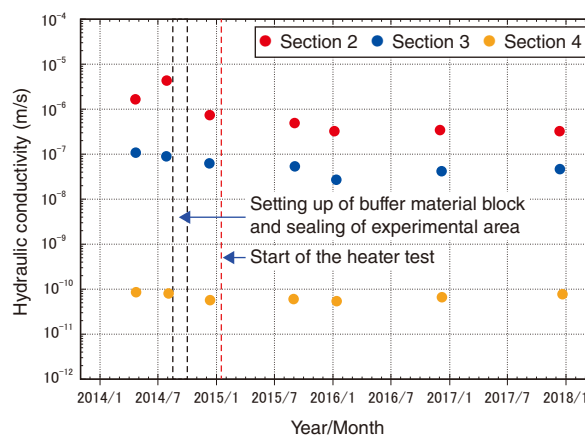


Fig.8-15 Simulated hydraulic conductivity

In Sections 2 and 3, the hydraulic conductivity slightly decreased from January 2014 to January 2016, but then remained constant.

A camera was installed in one of the drilled boreholes (H4-2; see Fig.8-13); camera imaging indicated fractures around the test pit. Therefore, the hydraulic conductivity of the EDZ around the test pit included Sections 2 and 3; Section 4 was maintained as an unfractured section, as indicated in Figs.8-13 and 8-14.

The EDZ hydraulic conductivity in Sections 2 and 3 after the excavation of the test pit was $1.7\text{--}4.3 \times 10^{-6}$ and 8.9×10^{-8} to 1.1×10^{-7} m/s, respectively, representing values 3–5 orders of magnitude higher than those in the unfractured zone ($8.0\text{--}8.6 \times 10^{-11}$ m/s), as shown in Fig.8-15. In Sections 2 and 3, the hydraulic conductivity decreased by approximately one order of magnitude with time for the first two years, but then remained constant from January 2016. This suggests that the aperture of the EDZ fracture was not changed significantly, although the swelling of the buffer material did cause compression stress around the test pit. Therefore, these results provide fundamental data that will be instrumental in developing a model to predict the hydraulic conductivity of the EDZ.

(Nobukatsu Miyara)

Reference

Aoyagi, K., Miyara, N. et al., Evolution of the Excavation Damaged Zone Around a Modelled Disposal Pit: Case Study at the Horonobe Underground Research Laboratory, Japan, Proceedings of 13th SEGJ International Symposium, Tokyo, Japan, 2018, 5p., in USB Flash Drive.

8-7 Chemical Signatures Suggesting Recent Fault Activity

— Detection of Elemental Changes due to Fault Activity —

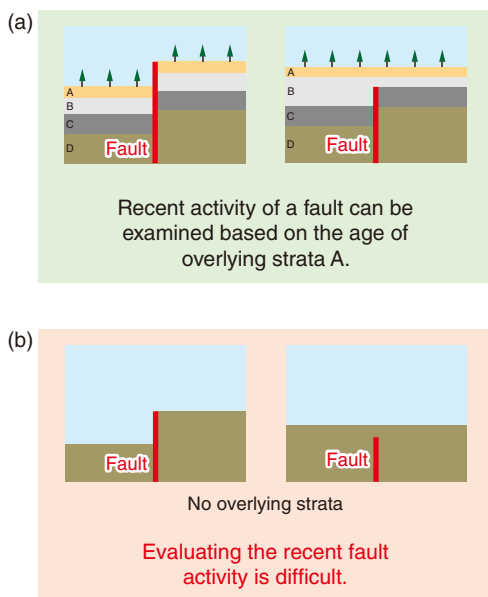


Fig.8-16 Identification of recent fault activity (a) with and (b) without overlying strata

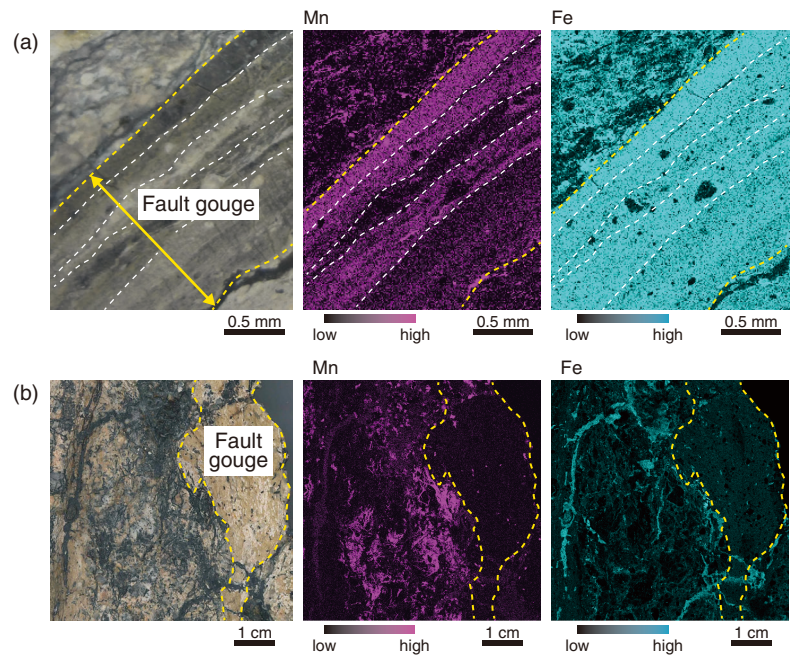


Fig.8-17 Photographs of polished sample surfaces and X-ray microscopy images showing spatial distribution of Mn and Fe from fault gouges of (a) capable and (b) incapable faults
Mn and Fe are concentrated in the gouge of the capable fault.

A fault, which is a fracture in a rock mass that has experienced displacement and can generate earthquakes, is classified as a capable or incapable fault based on the existence of any displacement over the past several hundred millennia. Identification of capable faults is crucial for reliable seismic hazard assessments and for assessing the safety of geological disposal, as they are considered to have a significant potential for displacement in the near future. Generally, recent fault activity is identified based on the occurrence of any displacement in the strata overlying the fault. However, when such overlying strata are absent or when faults are newly found during underground tunnel excavation, alternative methods for identifying fault activity are needed (see Fig.8-16).

Faults are generally associated with a fracture zone, i.e., a zone with numerous fractures and/or breccia. A fracture zone often includes a clay-rich “fault gouge” developed by grain-size reduction owing to repetitive fragmentation and clay mineral formation caused by water–rock interaction during faulting. In this study, the mineral and chemical compositions of fault gouges from known capable and incapable faults were analyzed using multiple approaches such as X-ray diffraction and X-ray fluorescence analyses. Consequently, elemental mapping for polished sample surfaces using an X-ray analytical microscope

revealed that the concentrations of several elements such as manganese (Mn) and iron (Fe) in fault gouges were clearly different between capable and incapable faults (see Fig.8-17).

Mn and Fe, discovered to be concentrated in the gouges of a capable fault, can form oxides that are insoluble in water. A fault gouge is generally impermeable because it is filled with fine-grained fragments and clay minerals. However, groundwater can migrate into the gouge of a capable fault when fault activity causes the formation of new fractures. As water from deep underground is reductive, Mn and Fe remain dissolved in the water. The migration of the reductive water to the subsurface during faulting results in its mixing with near-surface water that is rich in oxygen, leading to the subsequent precipitation of insoluble Mn and Fe oxides in the fault gouge.

In contrast, as a fault gouge of an incapable fault remains impermeable, no opportunities for the concentration of Mn and Fe are presented. These findings will aid in the identification of capable faults using chemical signatures as well as the structures and mineralogical characteristics of faults, especially when geological features formed by recent near-surface faulting are obscured due to the absence of overlying strata.

(Masakazu Niwa)

Reference

Niwa, M. et al., Identification of Capable Faults Using Fault Rock Geochemical Signatures: A Case Study from Offset Granitic Bedrock on the Tsuruga Peninsula, Central Japan, *Engineering Geology*, vol.260, 2019, p.105235-1–105235-15.

8-8 Visualization of Long-Term Variability in Groundwater Flow Conditions

— Development of Evaluation Method for Variability of Groundwater Flow Conditions —

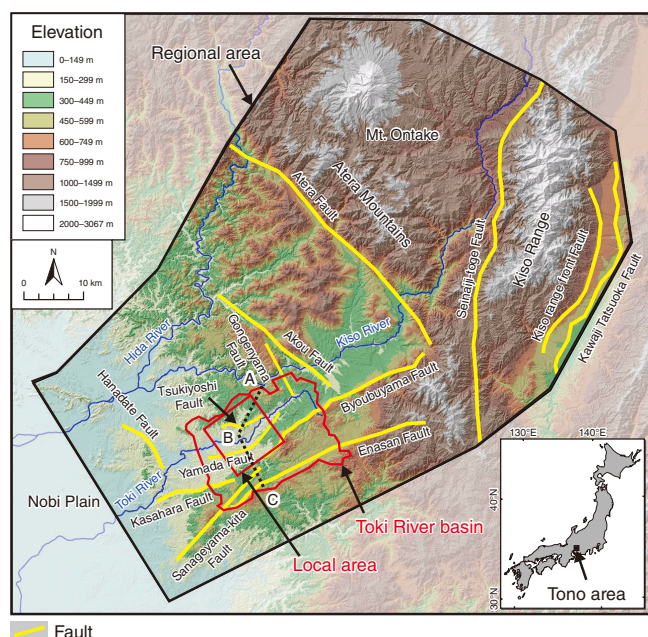


Fig.8-18 Regional setting of the case study

In this regional area, the long-term topographic changes and climate perturbations over the past million years are studied and steady-state simulations considering those conditions are performed. In the local area, the effects of topographic changes and climate perturbations on groundwater flow conditions are estimated using the simulated results from the regional area.

Safety assessments of the geological disposal of high-level radioactive waste are performed on a time scale of more than tens of thousands of years after the closure of the facility. As part of this assessment, the effects of long-term topographic change and climate perturbations on the geological environmental characteristics must be estimated. Therefore, a quantitative evaluation method of the effects of long-term geological phenomena on groundwater flow conditions, such as the velocity and travel time of groundwater, was developed.

In this method, the coefficient of variation is calculated based on steady-state groundwater flow simulations for quantifying the effects of long-term geological phenomena. The coefficient of variation is the standard deviation of data divided by the average value; a lower value indicates a lesser relative variation with respect to the average value of the data. Further, it is not affected by the influence factors.

First, a steady-state simulation was first conducted using a present-day hydrogeological model of the Tono area (Fig.8-18). As a result, a region with a slow groundwater flow was estimated to be distributed in the deep underground of the Toki River surrounded by the Tsukiyoshi Fault and the Yamada Fault (see Fig.8-19(a)). Second, topographic changes and climate perturbations over the past one million years were estimated, and hydrogeological models of 1 Ma (million years ago), 0.45 Ma,

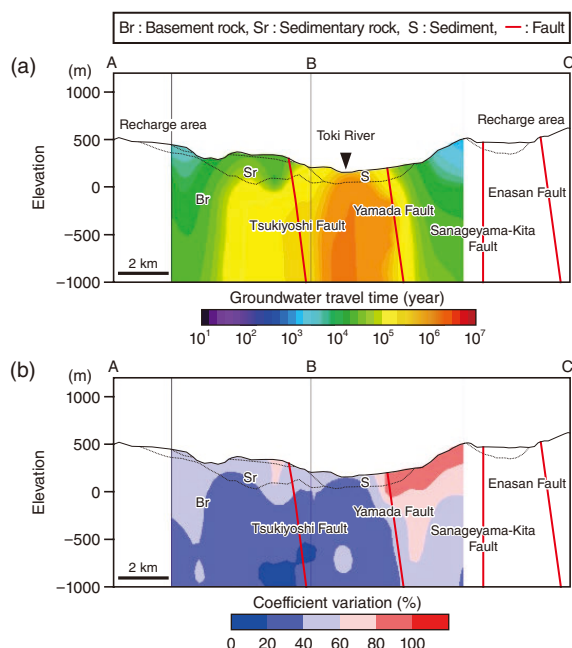


Fig.8-19 Modeled groundwater flow conditions in the deep underground

(a) Spatial distribution of the groundwater travel time from the recharge area to the discharge area, and (b) spatial distribution of the effects of topographic change and climate perturbations on the groundwater travel time. The vertical cross section corresponds to the dashed A–B–C line in Fig.8-18.

and 0.14 Ma were constructed. Two recharge rate patterns were estimated for each model considering climate perturbations. The coefficient of variation was calculated based on the steady-state simulation results of eight hydrogeological models. The results indicated that the region with slow groundwater flow is distributed in the area where the coefficient of variation is relatively small (see Fig.8-19(b)), thus suggesting that the deep underground area below the Toki River has not been susceptible to topographic change and climate perturbations over the past 1 Ma. It was also estimated that the groundwater flow in the deep underground of the Toki River is slow, based on the groundwater chemistry data. The validity of the results of this study was then confirmed.

This proposed evaluation method, which can quantitatively estimate the effect of topographic changes and climate perturbations on groundwater flow conditions, is an effective technique for assessing geological disposal, as it requires the evaluation of long-term changes in the geological environment characteristics over tens of thousands of years.

This study is part of the results entrusted in FY2016, supported by the Agency for Natural Resources and Energy (ANRE), the Ministry of Economy, Trade and Industry (METI), Japan.

(Hironori Onoe)

Reference

Onoe, H. et al., Development of Evaluation Method for Variability of Groundwater Flow Conditions Associated with Long-Term Topographic Change and Climate Perturbations, *Journal of Nuclear Fuel Cycle and Environment*, vol.26, issue 1, 2019, p.3–14 (in Japanese).

8-9 Mechanical Modeling of Buffer Materials

— Applicability of Elasto-Plastic Constitutive Model under Saltwater Conditions —

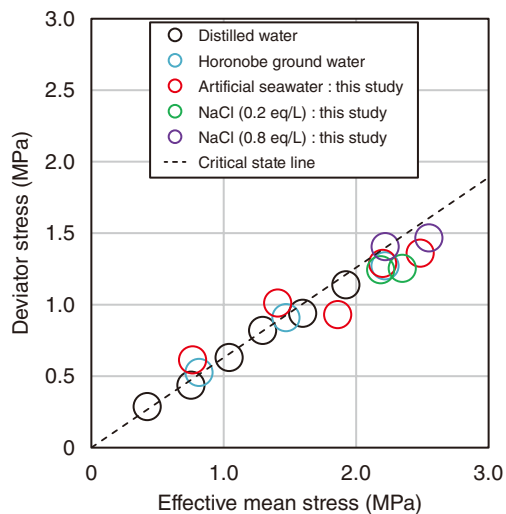


Fig.8-20 Consolidation undrained triaxial compression test results

This graph shows the stress state at the end of shear in the \overline{CU} test for examining shear deformation characteristics. Here, strength does not depend on salt concentration. The critical state line used in the MCC model could be used to assess the stress state at the end of shear.

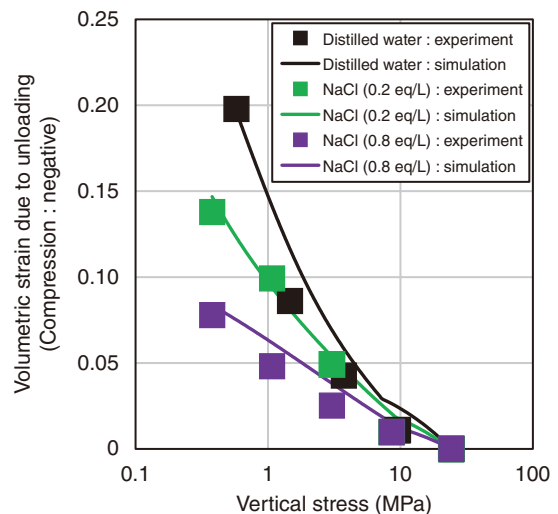


Fig.8-21 Relationship between the vertical stress and volumetric strain

The volumetric strain due to unloading under saltwater conditions during the consolidation test, which is used to examine loading/unloading deformation characteristics, is lower than that under distilled water conditions. By estimating the parameter values, it was confirmed that the MCC model can be applied to various saltwater conditions.

Bentonite is planned to be used as a buffer material in repositories for the geological disposal of radioactive waste. However, as the mechanical properties of bentonite depend on the salinity of the groundwater, the mechanical properties of the buffer material under various salinity conditions must be characterized. Furthermore, an appropriate mechanical constitutive model corresponding to the groundwater conditions and appropriate corresponding parameters should be selected to evaluate the mechanical behavior of the buffer material using numerical simulation techniques.

In this study, the applicability of the existing constitutive model to the buffer material under various salinity conditions was examined. The widely used modified Cam-clay (MCC) model was used as the constitutive model, as this model has been phenomenologically formulated based on the elastoplastic response under loading and unloading processes and deformation characteristics during shearing. Consolidation tests and consolidated undrained triaxial compression tests with pore water pressure measurements (\overline{CU} test) were then conducted to understand these characteristics. In preparing the data sets for the consolidation and \overline{CU} test under various salt concentration conditions, the \overline{CU} test was discovered to have been conducted with different salinity conditions and thus did not have sufficient data. Based on these results and the existing consolidation test data, the differences in the mechanical properties of the buffer material under distilled water and saltwater conditions

were clarified. Additionally, the applicability of this model under various salt concentration conditions was examined by comparing the simulated and experimental data.

No clear differences were present in the \overline{CU} test results, as shown in Fig.8-20, thus confirming that the main difference in the mechanical properties of the buffer material under distilled water and saltwater conditions is the unloading behavior in the consolidation test, which is shown in Fig.8-21. Additionally, the relationship between the swelling index, which is a model parameter, and the equivalent ion concentration (eq/L) was defined so that the parameter values can be set according to the water condition. Furthermore, the simulated consolidated results using these parameters agreed well with the experimental data, thus confirming that the model could be applied to various salt concentration conditions (see Fig.8-21).

Future work will include the development of simulation methodologies for evaluating the mechanical behavior of bentonite that applies to more comprehensive site conditions and obtaining experimental data under groundwater conditions with variations in ion species other than NaCl.

This study was conducted as part of the project on “Development of enhancing the disposal system in the coastal regions (JFY2018)”, funded by the Agency for Natural Resources and Energy (ANRE), the Ministry of Economy, Trade and Industry (METI), Japan.

(Yusuke Takayama)

Reference

Takayama, Y. et al., A Study on Applicability of Elasto-Plastic Constitutive Model to Mechanical Behavior of Buffer Material in Salt Water Conditions, Journal of Nuclear Fuel Cycle and Environment, vol.27, issue 1, 2020, p.12–21 (in Japanese).

8-10 Unveiling the Interaction Mechanism of Fe (II) and Si — Characterization of Ferrous Silicate Co-Precipitates under Reducing Conditions —

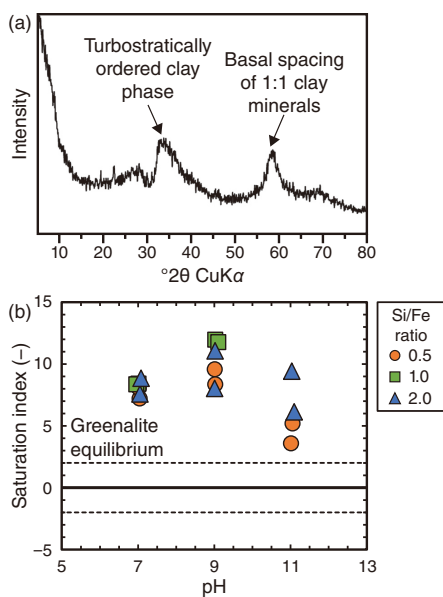


Fig.8-22 Solid mineralogy and solution chemistry
(a) A typical XRD pattern showing the poorly crystalline character of the precipitates; however, the two broad peaks suggest the presence of a turbostratically ordered clay phase. (b) Thermodynamic calculations predict saturation of the ferrous clay phase greenalite.

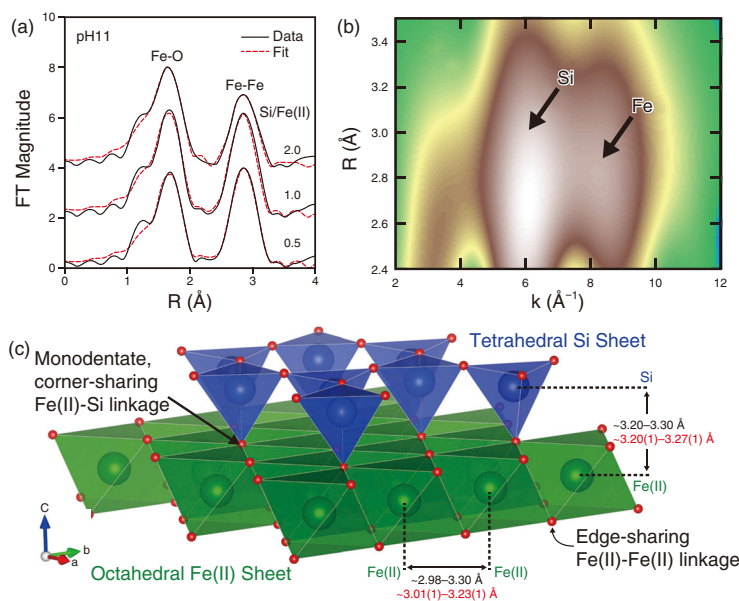


Fig.8-23 Local structure analyses using EXAFS
(a) Fourier transform of Fe K-edge EXAFS; fitting the spectra yields information on bond lengths and coordination numbers. (b) Wavelet transform of EXAFS showing bonding between Si and Fe. (c) Structural details derived from EXAFS analysis confirm the presence of a clay structure in the solids.

In the geological disposal of radioactive wastes, Fe (II)-Si interactions occur at the interface between the vitrified waste and steel overpack under reducing conditions. The resulting ferrous silicate phases regulate vitrified waste solubility, and serve as a diffusive and chemical barrier against the release of radionuclides from the waste. Understanding the role of ferrous silicates is critical for long-term repository safety assessments; this necessitates fundamental knowledge of ferrous silicate precipitates and their structure and what factors influence them.

In this work, we carried out ferrous silicate synthesis experiments under low-temperature (25 °C), anoxic, and reducing conditions. We examined the role of solution chemistry, particularly Si/Fe(II) ratio and pH, on the structural characteristics of ferrous silicate co-precipitates. The precipitates that formed from the interaction of Fe (II)- and Si-rich solutions – simulating solutions from the overpack and vitrified waste – were characterized using X-ray diffraction (XRD), infrared (IR) spectroscopy and extended X-ray absorption fine structure (EXAFS) spectroscopy. These techniques provide information on phase assemblage, silicate structure, and Fe (II) local environment. We then correlated the structural results with thermodynamic calculations of solution saturation.

Our results show that Fe (II)-Si interactions readily result in the rapid precipitation of amorphous to poorly crystalline ferrous

silicate phases (Fig.8-22(a)). Thermodynamic calculations predict the precipitation of ferrous clay phases (Greenalite: $\text{Fe}_3\text{Si}_2\text{O}_5(\text{OH})_4$) (Fig.8-22(b)). This is supported by IR and EXAFS spectroscopy that reveal structures consistent with ferrous clay phases at all conditions (Fig.8-23); however, we observed significant variability in solid structure and phase assemblage with pH and Si/Fe (II) ratios. Ferrous clay formation is most pronounced at low-Si and high pH conditions; higher Si and lower pH reduces ferrous clay crystallinity, and results in amorphous silica precipitation.

These results offer insights on the structural variability of alteration zones at the glass/steel interfaces in a multibarrier system. These may be used to: (1) interpret the mineralogy observed in glass alteration studies; (2) refine thermodynamic datasets used to model secondary mineral formation during glass alteration; (3) and predict their impacts on long-term glass dissolution and radionuclide migration in the safety assessment of geological repositories.

This work was supported by the Agency of Natural Resources and Energy (ANRE), the Ministry of Economy, Trade and Industry (METI) of Japan, under “The project for validating assessment methodology in geological disposal (FY2017)”.

(Paul Clarence M. Francisco)

Reference

Francisco, P. C. M. et al., Interaction of Fe^{II} and Si under Anoxic and Reducing Conditions: Structural Characteristics of Ferrous Silicate Co-Precipitates, *Geochimica et Cosmochimica Acta*, vol.270, 2020, p.1–20.

8-11 Analysis of Radioactive Samples by Plasma Generated in the Microchannel

— Determination of Cesium in Highly Radioactive Liquid Waste by Liquid Electrode Plasma Optical Emission Spectrometry —

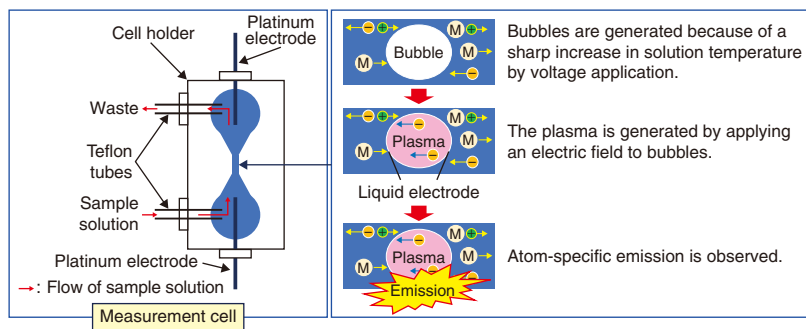


Fig.8-24 Liquid electrode plasma optical emission spectrometry (LEP-OES)

Bubbles are generated as a voltage application. The LEP is generated by applying an electric field to the bubbles. An emission is observed when the element in the sample solution enters the LEP.

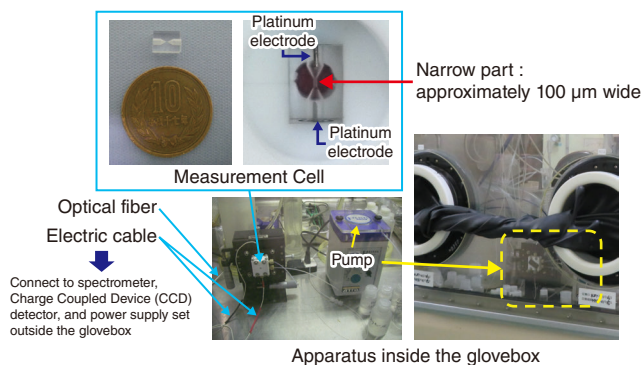


Fig.8-25 LEP-OES apparatus installed inside the glovebox

A quartz glass measurement cell was installed inside the glovebox; the emission of elements by the LEP was measured by a spectrometer and CCD detector set outside the glovebox with an optical fiber.

Highly radioactive liquid waste (HLW), which is generated by the reprocessing of spent nuclear fuel, contains fission products (e.g., Cs and Sr), and reagent additives from the process such as Na. Elemental concentrations in HLW should be accurately determined because they affect the immobilization of radioactive materials in the vitrified glasses after the treatment of HLW. Radioactive samples including HLW are analyzed inside an airtight shielded cell or glovebox to protect the operator from radiation exposure. Inductively coupled plasma optical emission spectrometry (ICP-OES) and inductively coupled plasma mass spectrometry (ICP-MS), which are often used for elemental analysis, require plasma gas, cooling water, and a large-capacity power supply. Thus, the specific design and manufacturing of the glovebox and instrumental modification are required before their installation into the shielded cell and glovebox. Remote operated maintenance inside the shielded cell would be another issue.

This study therefore used liquid electrode plasma (LEP), which is generated in a microchannel, and LEP-based optical emission spectrometry (LEP-OES) to deliver a safe, compact, remote operated elemental analysis method. As shown in Fig.8-24, LEP is generated by applying pulsed direct current voltage when a sample solution is introduced into the narrow part of a microchannel 100 μm wide. The atom-specific emission line is observed when the element in the sample enters the LEP. This method spectroscopically analyzes the emission line (i.e., LEP-OES) and has been applied to elemental analysis. Since LEP-OES does not require plasma gas, cooling water, and a

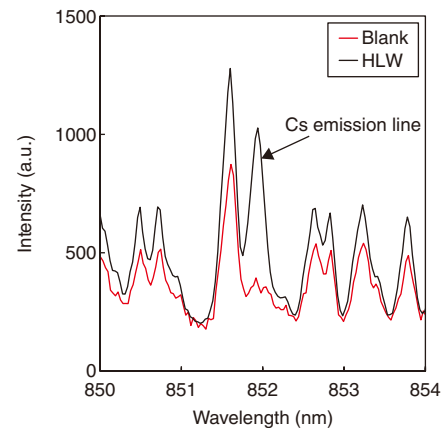


Fig.8-26 LEP emission spectra of HLW

The black line indicates the emission spectrum of HLW with 10000-fold dilution by nitric acid. The red line indicates the emission spectrum of blank nitric acid. The Cs concentration of HLW was determined by using the Cs emission line observed at 852.1 nm.

large-capacity power supply, the apparatus is more compact than that of ICP-OES or ICP-MS, and is more easily installed into a generic glovebox. Also, the generation of liquid waste and radiation exposure to the operator may be reduced because the sample is treated in the microchannel.

Therefore, as shown in Fig.8-25, an LEP-OES system was designed by combining the optimized apparatuses for spectrometer resolution and grating to measure radioactive sample. The emission spectrum of a Cs standard solution was obtained, where emission lines were observed at 852.1 and 894.3 nm. Furthermore, the detection and quantification limits of Cs at the strongest emission line of 852.1 nm were 0.005 mg/L and 0.02 mg/L, respectively, thus indicating that the proposed method has sufficient sensitivity for Cs determination in HLW. No spectral interferences from co-existing elements were observed at this wavelength from the measured emission spectrum of the simulated sample, which imitated elemental compositions of HLW. Therefore, HLW from the Tokai Reprocessing Plant was measured using the developed LEP-OES system. The measured Cs concentration was 3.61 ± 0.47 g/L, showing good agreement with the calculated value of 3.60 g/L, as demonstrated in Fig.8-26. The proposed method allows the analytical apparatus inside the glovebox to be downsized and can be used to determine the concentration of Cs in HLW; future efforts will extend usage to the determination of Sr and Na concentrations in HLW.

(Noriyasu Kodaka)

Reference

Do, V-K. et al., Quantitative Determination of Total Cesium in Highly Active Liquid Waste by Using Liquid Electrode Plasma Optical Emission Spectrometry, *Talanta*, vol.183, 2018, p.283–289.

Computational Science for Nuclear Research and Development

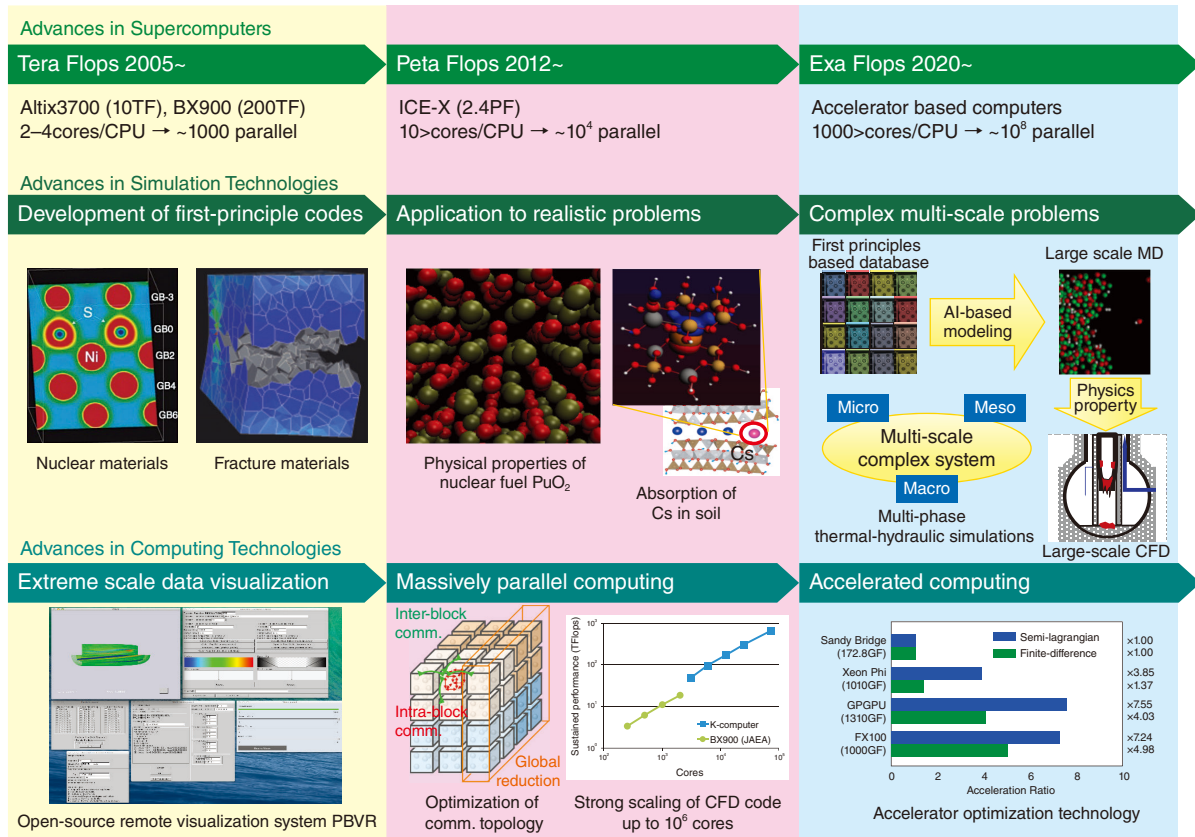


Fig.9-1 Computational science research at the Center for Computational Science and e-Systems

To analyze complex systems in nuclear research and development, exascale simulations are being developed by advancing the simulation and computational technologies that were devised for tera/petascale simulations.

Simulation techniques for analyzing complex phenomena comprising various physics effects are essential for resolving issues created by the accident at the TEPCO's Fukushima Daiichi NPS (1F), such as the environmental dynamics of radioactive substances, the volume reduction of polluted soil, and the study of severe accidents. They are also required for the research and development (R&D) of future nuclear systems. Severe-accident analyses require macroscale thermal-hydraulic simulations of the melt–relocation behavior of nuclear fuels and structural materials as well as state-of-the-art multi-scale and multi-physics simulation technologies. These technologies enable the AI-based integration of mesoscale simulations used for evaluating complicated interface formations caused by the mixing of molten debris and fracture events such as crack growth and microscale atomic/molecular simulations to estimate the diffusion, chemical reactions, and phase transitions occurring in extreme environments at high temperatures and pressures. In addition to these simulation technologies, computational technologies that support high-performance computing on exascale machines, such as the supercomputer Fugaku, are required.

Simulation techniques including atomic/molecular simulations and fluid simulations, which are the basis for analyzing complex phenomena, and computational technologies such as numerical algorithms and visualization systems have been developed. Efforts to further improve these techniques and develop new simulation and computational technologies to enable exascale

simulations of complex phenomena are ongoing, as summarized in Fig.9-1. Such simulation techniques for complex phenomena will become a foundation for future nuclear R&D.

In FY2019, as a computer-science contribution to the reconstruction and revitalization of Fukushima Prefecture, the concentration of radioactive cesium on mushrooms was addressed via quantum chemical calculations (Topic 1-13), and the amount of radioactive cesium released in the port of 1F was estimated via detailed computational fluid dynamics (CFD) simulations (Topic 1-14). In this chapter, some recent developments in micro and mesoscale simulations needed for the analysis of complex phenomena are reviewed. This includes the development of a thermal hydraulic model for the lattice Boltzmann method, which enables multi-scale thermal-hydraulic simulations of the reactor container in 1F (Topic 9-1), a design study of a superconducting neutron microscope system via the particle and heavy ion transport code system (PHITS; Topic 9-2), and the clarification of the mechanism behind the plastic deformation of iron via atomic simulations (Topic 9-3). On the exascale computing front, a communication-avoiding matrix solver was developed, which enables extreme-scale multi-phase CFD simulations using accelerator (GPU)-based supercomputers (Topic 9-4).

We steadily promote research of simulation and computational techniques, which are a common foundation for nuclear R&D, and provide them to the community.

9-1 CFD Simulation of a Fuel Debris Air-Cooling Experiment

— Validation of a Thermal-Hydraulic Model Using the Lattice Boltzmann Method —

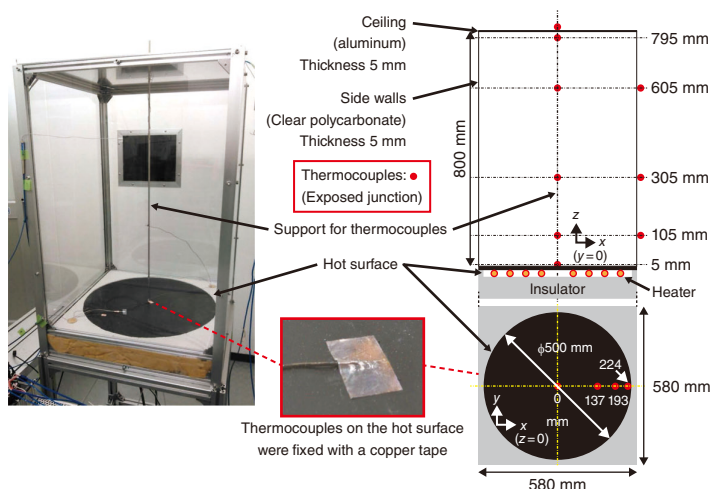


Fig.9-2 Experimental setup

A disk-shaped heater was installed at the bottom of the case (580 × 580 × 795 mm) and the steady-state temperature was measured with a thermometer placed on a pillar in the center of the experimental apparatus (The experiment referred to previous research)*.

Thermal-hydrodynamics analyses based on detailed computational fluid dynamics (CFD) simulations are important for nuclear design and safety and are an essential tool for decommissioning the TEPCO's Fukushima Daiichi Nuclear Power Station. It is necessary to perform multi-scale CFD simulations that resolves from fuel debris of mm-scale to the reactor pressure vessel of m-scale. The adaptive mesh refinement (AMR) method is a key technique to accelerate multi-scale simulations. In this work, therefore, an AMR version of the detailed CFD code named CityLBM was developed and applied to thermal-hydrodynamics problems.

CityLBM is based on the lattice Boltzmann method (LBM) and suitable for high-performance computing. In the conventional thermal-hydraulic model, both the velocity and temperature equations are formulated by LBM. However, this requires a large amount of computational memory, thus making it difficult to apply to large-scale problems. Using the finite difference method (FDM) for the temperature equation can reduce the memory usage to 1/7th that of the LBM during 3D analysis. Therefore, a hybrid CFD model that combines the FDM and LBM was proposed to reduce both memory usage and calculation time. Here, the effect of temperature on the LBM was evaluated as an external force term using the Boussinesq approximation, thus allowing a consistent formulation of the velocity and thermal flow fields.

Reference

Onodera, N. et al., Locally Mesh-Refined Lattice Boltzmann Method for Fuel Debris Air Cooling Analysis on GPU Supercomputer, Mechanical Engineering Journal, vol.7, issue 3, 2020, p.19-00531_1-19-00531_10.

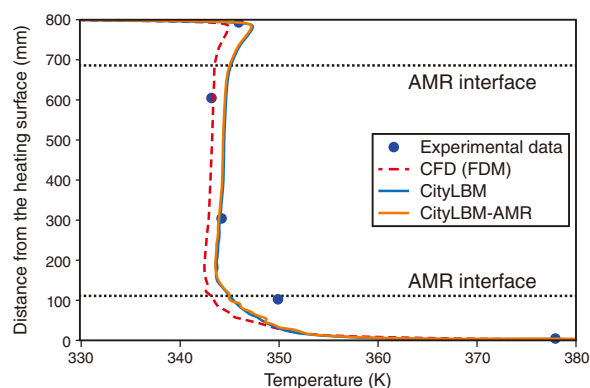


Fig.9-3 Time-averaged air temperature

CityLBM with uniform and AMR grid systems accurately reproduced the temperature profile, including rapid changes in the temperature on the bottom and top surfaces.

CityLBM was then validated against using experimental data from a natural convection problem in a 3D system shown in Fig.9-2. Here, the bottom of the test vessel was equipped with a heat transfer surface. The Rayleigh number in the experiments was approximately 2×10^9 . The data was obtained along the z-axis by taking the time average for 5 minutes. Although CityLBM showed slightly higher temperatures than did the conventional FDM, both models reproduced the experiments within an error range of 10 K, as seen in Fig.9-3. Furthermore, when operating with 4 GPUs (NVIDIA® V100), CityLBM completed the calculations (total elapsed time) 6.7 times faster than did the conventional FDM with 36 CPUs (Intel Broadwell). CityLBM was thus concluded to be an efficient tool to simulate large-scale thermal convection problems that are required for decommissioning processes.

This study was supported by Joint Usage/Research Center for Interdisciplinary Large-scale Information Infrastructures (JHPCN) (jh180041-NAH, jh190049-NAH).

(Naoyuki Onodera)

* Uesawa, S. et al., Development of Numerical Simulation Method to Evaluate Heat Transfer Performance of Air Around Fuel Debris, 2: Validation of JUPITER for Free Convection Heat Transfer, Proceedings of 25th International Conference on Nuclear Engineering (ICONE-25), Shanghai, China, 2017, 7p.

9-2 Using Computer Simulations to Design a Superconducting Neutron Microscope

— Simulating All Radiation Types inside the Neutron Microscope and Predicting Its Behavior —

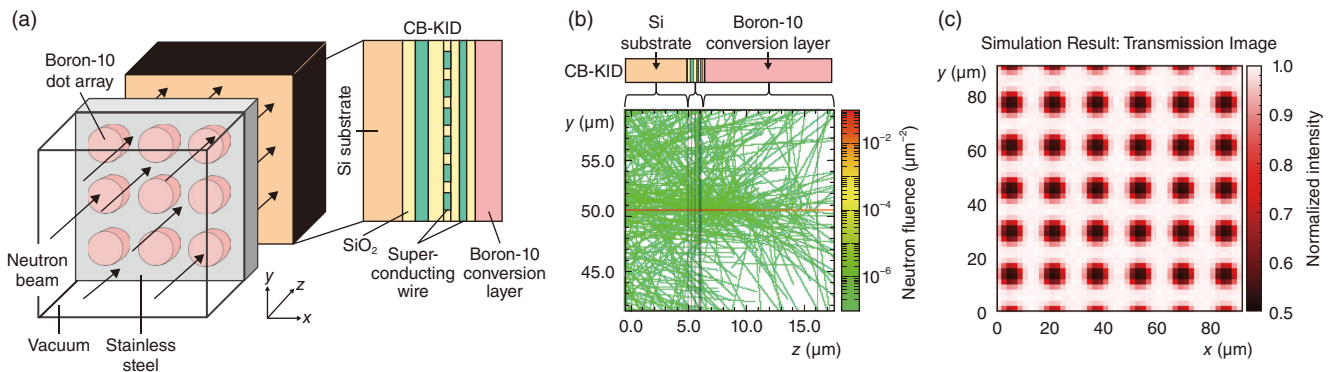


Fig.9-4 (a) Model of the CB-KID superconducting neutron microscope, (b) PHITS simulation of radiation tracks inside the CB-KID, and (c) simulated neutron transmission image from the CB-KID

(a) Schematic showing the boron-10 dot array test sample and a model of the CB-KID superconducting neutron microscope. The CB-KID is a stack of different layers of materials. The incident neutron beam undergoes nuclear reactions in the boron-10 conversion layer, which releases ⁴He and ⁷Li particles that are then detected by the superconducting wires. (b) Simulated neutron tracks, where the colors indicate the neutron fluence, or the number of neutrons per unit area. The horizontal red line in the figure shows the focused neutron beam which was simulated incident to the center of the detector. (c) Simulation results of a neutron transmission image from the CB-KID of the boron-10 dot array test sample (left side of panel (a)), where a uniform neutron beam was simulated incident on the CB-KID. Only a small number of neutrons could pass through the boron-10 dots; these show up as dark regions in the image.

As neutrons can penetrate deeply into matter, neutron beams can be used for imaging inside substances. Few facilities currently produce high-intensity neutron beams capable of neutron imaging, though various particle accelerators are being planned and constructed. However, further developments in high-resolution neutron microscopy technologies are necessary to take full advantage of high-intensity neutron beams.

The current-biased kinetic inductance detector (CB-KID) is one type of neutron microscopy technology that is under development in Japan. This innovative technology for micron-scale microscopy has improved upon existing neutron imaging technologies. In the CB-KID, incident neutrons undergo nuclear reactions in a thin film of boron-10 (the conversion layer), which converts the neutrons into helium-4 (⁴He) and lithium-7 (⁷Li) particles. The CB-KID then detects the positions of these individual particles using superconducting wires.

However, it is not possible to perform enough experiments to design the CB-KID, as there are a limited number of neutron beam facilities worldwide. Therefore, the Center for Computational Science and e-Systems developed a simulation model, shown in Fig.9-4(a), to support the detector's design in collaboration with Osaka Prefecture University and Japan Proton Accelerator Research Complex (J-PARC). In this model, the PHITS simulation code was used for simulating tracks and nuclear reactions of neutrons within the CB-KID. A representative example of the resulting simulated neutron tracks inside the CB-KID under irradiation by a focused neutron beam is shown in Fig.9-4(b). Here, the neutrons were tracked,

the ⁴He and ⁷Li particles were produced from the nuclear reactions, and the maximum penetration lengths of these particles were calculated. The results demonstrated that only the ⁴He and ⁷Li particles produced in the boron-10 conversion layer caused a detectable signal, and therefore neither the ⁴He and ⁷Li particles produced in the test sample nor the gamma rays from nuclear reactions significantly affected the transmission images. This represents the first demonstration that gamma rays do not affect the transmission images, thus indicating that the CB-KID design is only sensitive to neutrons incident on the microscope, therefore making it suitable for neutron imaging.

A representative result of the simulated neutron transmission image of a test sample is shown in Fig.9-4(c). The result corresponded well with microscopy imaging of the test sample (an array of microscopic boron-10 dots 6 μm in diameter), thus validating the potential of the CB-KID neutron microscope for imaging sub-10 μm microscopic test samples. Future work will include the simulation of various modified designs for the neutron microscope to increase the resolution of its transmission images. Such numerical experiments are expected to accelerate the development of CB-KID by significantly reducing project costs and labor.

This study was conducted on “Neutron detection efficiency improved by employing dual current-biased kinetic inductance detectors”, supported by the Japan Society for the Promotion of Science (JSPS) KAKENHI Grant-in-Aid for Scientific Research (A) (No.16H02450).

(Alex Malins)

Reference

Malins, A. et al., Monte Carlo Radiation Transport Modelling of the Current-Biased Kinertic Inductance Detector, Nuclear Instruments and Methods in Physics Research Section A, vol.953, 2020, p.163130-1–163130-7.

9-3 Understanding the Deformation of Iron from the Movement of Atoms

— Analysis of Screw-Dislocation Motion and Slip-Plane Transition by Atomistic Simulations —

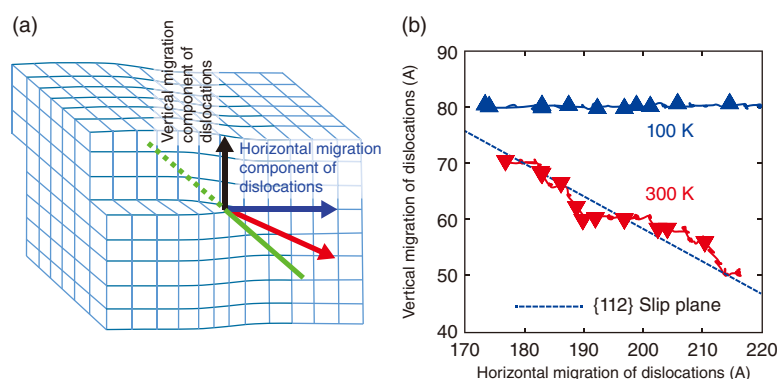


Fig.9-5 Migration of screw dislocations due to iron crystal slip

(a) Schematic of a screw dislocation (--- line) and the slip in iron crystals. Here, the screw dislocations proceed in the direction of the blue arrow at low temperatures; however, as the temperature increases, the direction of travel changes as shown by the red arrow, causing slip-plane transition. (b) Temporal developments in the location of screw dislocations at low and room temperatures obtained from the atomistic simulations, reproducing the slip-plane transition observed in the experiments.

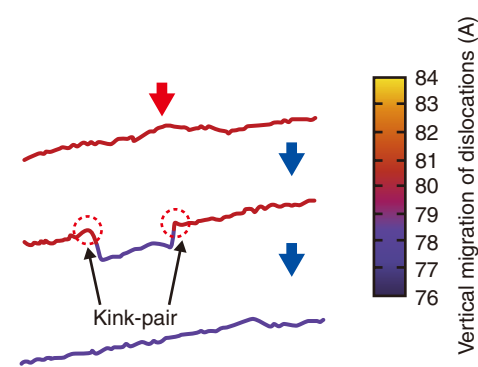


Fig.9-6 Atomistic simulation of the temporal development of screw dislocations in an iron crystal (blue arrow indicates the time change)

As the temperature increases, the dislocation line fluctuates as shown by the red arrow, triggering the short part of the dislocation to project to the crystal plane below; eventually, the entire dislocation line moves downward. This is called a kink-pair mechanism and is the origin of the vertical movement, which is called a cross-slip motion.

Deformation in metals is categorized into two types: elastic and plastic deformations. In the case of elastic deformation, the deformation is restored when the force applied to the metal disappears. In the case of plastic deformation, the crystal plane slips and the deformation is never restored. Iron is known to be brittle at low temperatures; this is because plastic deformation is less likely to occur. The plastic deformation of iron at low temperatures occurs mainly by the motion of screw dislocations along the slip-plane, as shown in Fig.9-5(a). The high activation energy of the movement of screw dislocations causes the low likelihood of plastic deformation of iron at low temperatures.

The slip-plane of iron can be obtained by quantum mechanical calculation, and the result agrees with the experimental result at low temperatures. However, the slip-plane is known to deviate from the theoretical value as the temperature is raised to room temperature. At low temperatures, screw dislocations travel horizontally, as shown by the blue arrow in Fig.9-5(a); as the temperature increases, the direction changes, as indicated by the red arrow. Despite the ubiquitous nature of iron, the mechanism of this phenomenon is not yet understood. Therefore, atomistic simulations were performed using a supercomputer to clarify this phenomenon.

The simulation results accurately reproduced the experimental data; as shown in Fig.9-5(b), at 100 K, the screw dislocations proceeded horizontally, whereas they proceeded obliquely along the {112} plane at 300 K. On average, the dislocation position moved to the lower layer once every two times. This type of slip, called cross slip, is the cause of the vertical migration component of dislocations observed at high temperatures and occurs due to the increase in lattice vibration by the temperature rise. A detailed investigation of the cross slip indicated that only the short part of the dislocation moves to another layer due to fluctuations, as shown in Fig.9-6; this motion then triggers the movement of the entire screw dislocation to this layer.

These results may aid in the understanding of the mechanical properties of aging nuclear material, which becomes brittle with use.

This study is the result of joint research with the University of Fukui conducted on “The research of interaction between irradiation defects and dislocation for evaluating mechanical degradation of nuclear structural materials”, supported by the Japan Society for the Promotion of Science (JSPS) KAKENHI Grant-in-Aid for Scientific Research (C) (No.26420865).

(Tomoaki Suzudo)

Reference

Suzudo, T. et al., Analyzing the Cross Slip Motion of Screw Dislocations at Finite Temperatures in Body-Centered-Cubic Metals: Molecular Statics and Dynamics Studies, Modelling and Simulation in Materials Science and Engineering, vol.27, no.6, 2019, p.064001-1-064001-15.

9-4 Multi-Phase Fluid Simulations Using the World's Largest GPU Supercomputer — Development of Communication-Avoiding Matrix Solvers on GPU —

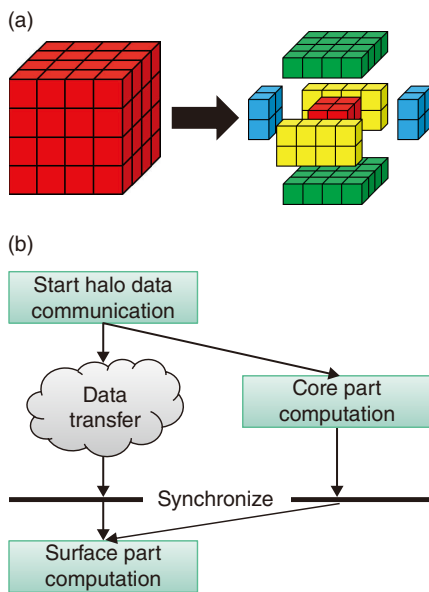


Fig.9-7 Communication overlap technique
(a) A computational domain on each GPU is decomposed into core and surface parts; (b) communication and core computation are processed simultaneously by splitting these processes on each GPU and processing them in parallel.

Existing computational fluid dynamics (CFD) simulations must be improved to analyze complex thermal-hydraulic phenomena in nuclear reactors. Whereas conventional CFD codes have been developed on petascale CPU-based computers, exascale GPU-based computers are essential for future simulations with ~ 100 billion grids. However, GPU-based computers have a significantly different performance gap between computation and communication than do conventional CPU-based computers because communication and computation are accelerated by several and several tens of times, respectively; the development of new matrix solvers capable of working at such a performance profile is thus required. In this study, GPU-computing technologies were developed for matrix solvers, which occupy a dominant cost of CFD codes. Additionally, extreme-scale multi-phase CFD simulations were accelerated using 7680 GPUs on Summit, which is the world's largest GPU supercomputer operated at the Oak Ridge National Laboratory in the United States.

CFD codes compute extreme-scale matrices that are obtained by discretizing a fluid model using a finite difference method. Conventionally, an iterative matrix solver based on the conjugate gradient (CG) method has been used. Parallel computation of the CG method requires two types of communication processes per iteration, i.e., halo data communication for finite difference computation on decomposed computational domains, and reduction communication for inner product

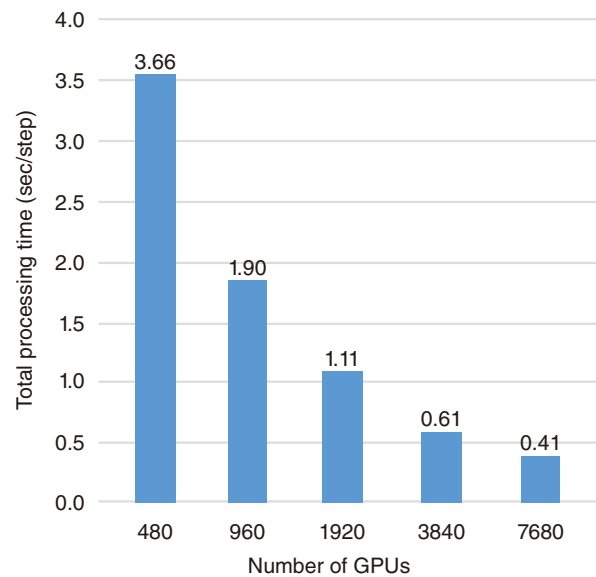


Fig.9-8 Scaling of computational performance on the GPU supercomputer Summit

Relationship between the total processing time per time step and number of GPUs in multi-phase fluid simulations (~ 7.5 billion grids) using 7680 GPUs of Summit (Oak Ridge National Laboratory).

operations of distributed vector data. Two approaches were used in this work to reduce these communication processes, including a communication and computation overlap technique and the communication-avoiding CG (CA-CG) method. In the communication and computation overlap technique, shown in Fig.9-7, a computational domain on each GPU is decomposed into core and surface parts. The halo data communication and the finite difference computation for the core, which does not require the halo data, are processed simultaneously to reduce the communication cost. In the CA-CG method, inner product operations for multiple iterations are processed at once by improving the mathematical algorithm of the CG method, thus reducing the number of reduction communications by an order of magnitude.

The performance of the developed method was evaluated in a multi-phase CFD simulation (approximately 7.5 billion grids, corresponding to the scale of four fuel assemblies) on the melt relocation of fuel assemblies on Summit. As shown in Fig.9-8, the total processing time was reduced nine-fold between 480 and 7680 GPUs, thus demonstrating scaling close to the target performance.

This study was conducted on “Exascale CFD Simulations at JAEA (CSC367)”, supported by the Oak Ridge Leadership Computing Facility (OLCF) Director’s Discretion Project.

(Yasuhiro Idomura)

Reference

Ali, Y., Idomura, Y. et al., GPU Acceleration of Communication Avoiding Chebyshev Basis Conjugate Gradient Solver for Multiphase CFD Simulations, Proceedings of 10th Workshop on Latest Advances in Scalable Algorithms for Large-Scale Systems (ScalA 2019), Denver, U.S.A., 2019, p.1–8.

Development of Technology and Human Capacity Building in the Nuclear Nonproliferation and Nuclear Security Fields to Support the Peaceful Use of Nuclear Energy

The Integrated Support Center for Nuclear Nonproliferation and Nuclear Security (ISCN) has been conducting a variety of activities in the areas of technology development and human-resources development related to nuclear nonproliferation and security in cooperation with affiliated domestic and overseas institutions toward a world without the threat of nuclear weapons or nuclear terrorism, as summarized in Fig.10-1.

Technology Development for Japanese and International Applications

A variety of technologies are under development to strengthen nuclear nonproliferation and security in accordance with domestic and international trends. Current projects in nuclear material detection and measurement technology include the development of a non-destructive assay technology to measure nuclear material retaining high radiation levels by irradiating neutrons from an external pulsed neutron source. Another involves the development of non-destructive assay technology to measure nuclear material with delayed gamma spectroscopy, outlined in Topic 10-1. A workshop was also organized in January 2020 regarding the technology developed for detecting nuclear materials in heavily shielded containers using nuclear resonance fluorescence (NRF); this work has received positive feedback by domestic and foreign experts. Nuclear forensics technology used to identify the origin and processing history of nuclear materials used in criminal acts has been improved. Small and low-cost detectors for first responders following nuclear terrorism events and artificial intelligence (AI) for analyzing nuclear forensic signatures are also under development. These developments contribute to the improvement of international nuclear forensic capabilities through international joint sample analysis exercises. Furthermore, methodologies to evaluate and reduce attractiveness of nuclear or radioactive material for nuclear security are being developed in collaboration with the United States of America (US).

Policy Research Based on Technical Expertise

Based on requests from the relevant administrative agencies, factor analysis affecting denuclearization has been studied through case studies, of denuclearized countries such as South Africa, Ukraine, Belarus, Kazakhstan, countries attempted to possess nuclear weapon such as Libya, Iran, Iraq, North Korea, and Syria, from the view point of the incentive for the development of nuclear weapons, domestic and international context, progress

in development, and effectiveness of sanctions. The technical procedures related to the disarmament, disabling, dismantlement, and verification have also been investigated and considered in view of the peaceful use of nuclear energy.

Support for Human Resources Development

ISCN has conducted capacity building support activities targeting Asian countries since 2011. As of March 2020, about 4600 participants from Asian countries including Japan have joined ISCN training activities on nuclear nonproliferation (safeguards) and nuclear security. ISCN's capacity building support activities have contributed to human-resource development in Asia and have drawn high praise from the US and Japanese governments.

Contributions to the International Verification Regime for CTBT

To establish a global verification regime for nuclear testing, the international monitoring system of the Comprehensive Nuclear-Test-Ban Treaty (CTBT) and a related national data center have been under provisional operation. A joint radioactive noble-gas measurement project began with as a way to strengthen the CTBT Organization's (CTBTO's) capability of detecting nuclear tests based on a voluntary contribution made to the CTBTO by the Government of Japan in February 2017 at Horonobe-Cho of Hokkaido and at Mutsu City of Aomori. This project aims to monitor behavior of background radioactive Xenon in the East Asia region and has been extended until 2022.

Support for JAEA's Nuclear-fuel Transportation and Procurement of Research Reactor Fuels

ISCN coordinates and provides support of nuclear transportation performed by JAEA's research and development centers and dealing with fresh fuels demand of JAEA research reactors and spent fuel after use. ISCN has been contributing to the Global Threat Reduction Initiative (GTRI), which has been strengthening global nuclear security, by promoting the systematic return of highly enriched uranium to the US.

Efforts to Promote Understanding

ISCN promotes understanding of nuclear nonproliferation and nuclear security at home and abroad by delivering the ISCN News Letter with articles on international trends and analysis of nuclear nonproliferation and nuclear security and ISCN activities, and by holding the International Forum on Peaceful Use of Nuclear Energy.

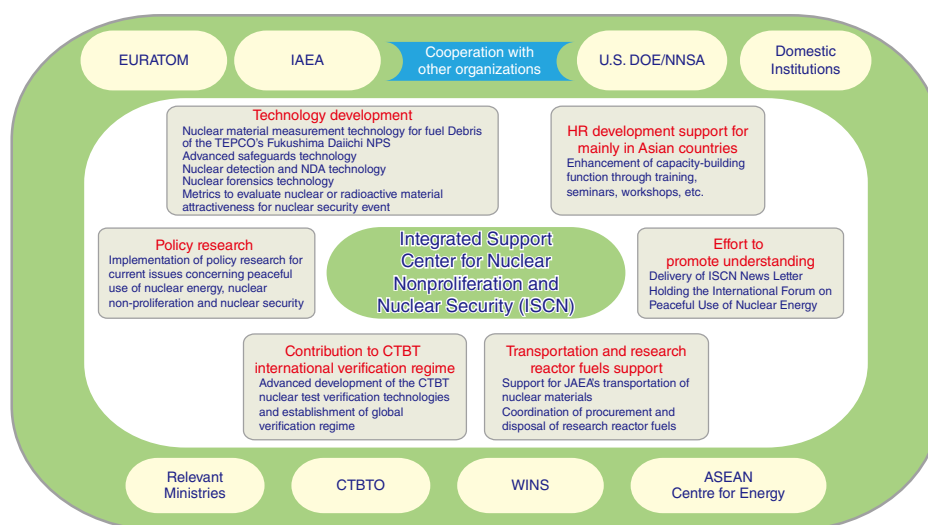


Fig.10-1 Summary of ISCN's activities and affiliated institutions

ISCN has played an active role in strengthening nuclear nonproliferation and nuclear security in cooperation with affiliated domestic and overseas institutions.

10-1 Nondestructive Assay of Nuclear Materials for Safeguards

— Developing Practical Delayed Gamma-ray Spectroscopy Using PUNITA —

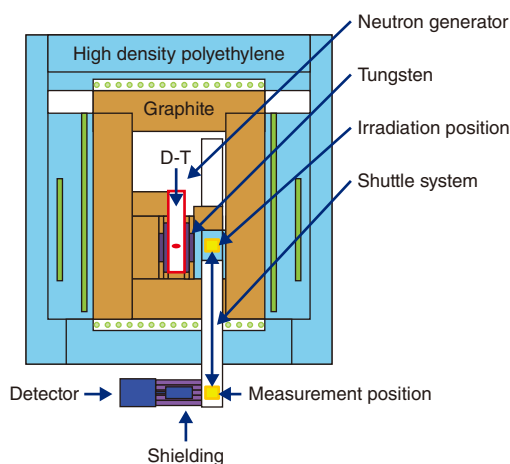


Fig.10-2 Schematic of PUNITA for delayed gamma-ray tests
Fission products are generated in the sample by neutrons from the deuterium-tritium (D-T) generator, which are moderated by the tungsten, graphite, and polyethylene. The sample is transferred to the detector to observe gamma rays from the decaying fission products.

ISCN has been developing delayed gamma-ray spectroscopy (DGS) to supplement present verification methods for nuclear material safeguards. DGS is useful for determining the fissile content in mixed-material samples for which current passive non-destructive assay (NDA) verification methods have challenges, like for spent nuclear fuel.

DGS is an active NDA technique wherein neutrons are used to induce fission in a sample. This generates fission products in proportion to the fissionable content, fission cross-section, and fission yield. The fission products subsequently emit unique sets of gamma rays as they decay with unique expected half-lives. These gamma rays are collected in a spectrum unique to the sample and interrogation procedure. The spectrum is subsequently deconvoluted to determine the fissionable nuclide ratios and, ideally, their mass.

However, since the long-lived fission products in spent fuel emit low-energy gamma rays at significant rates, shielding must be applied for reasonable verification times. As such, only high-energy gamma rays (above 2500 keV) can be used for evaluation and these must be emitted at significant rates to overcome the low-energy filter.

A DGS instrument requires an external neutron source and

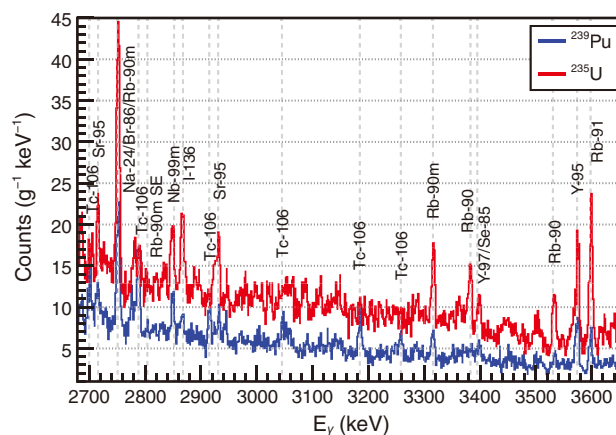


Fig.10-3 ^{235}U and ^{239}Pu fission product gamma-rays

Gamma rays from the noted fission products were observed from interrogations of standard sealed samples. These can be analyzed to determine the nuclide fractions in mixed-material samples. [Testing pattern: 50 cycles (Irradiation: 50 sec + Measurement: 50 sec)].

moderator for fission product creation and a gamma-ray detector to observe the spectrum over time. Ideally the sample is transferred between the neutron irradiation and measurement positions (see Fig.10-2). This interrogation cycle is repeated until statistically sufficient gamma-ray peaks are obtained.

ISCN conducted a joint experiment to demonstrate the safeguarding applicability of this technique using the Pulsed Neutron Interrogation Test Assembly (PUNITA), which is a non-destructive assay instrument that uses a D-T neutron generator at the Joint Research Center of the European Commission in Ispra, Italy. Preliminary experiments show clear distinctions between ^{235}U and ^{239}Pu that can be used to evaluate mixed-material samples (see Fig.10-3).

Future work will focus on optimizing the interrogation timing pattern and number of cycles to best evaluate the composition and associated mass. Additionally, the use of various neutron sources, neutron moderators, and neutron monitoring methods in compact instruments is being investigated.

This study was supported by the Ministry of Education, Culture, Sports, Science and Technology (MEXT), Japan.

(Tomoki Yamaguchi and Douglas Chase Rodriguez)

Reference

Rodriguez, D. C. et al., Utilizing PUNITA Experiments to Evaluate Fundamental Delayed Gamma-Ray Spectroscopy Interrogation Requirements for Nuclear Safeguards, *Journal of Nuclear Science and Technology*, vol.57, issue 8, 2020, p.975-988.

JAEA R&D Review 2020-21

Published by

Japan Atomic Energy Agency in January 2021

Editorial Board

Chief editor: Michio Yoshizawa

Editors: Kenji Tatematsu, Yoshio Suzuki, Mitsuo Koizumi, Tadahiro Washiya,
Kazuki Iijima, Taro Shimada, Hiroyuki Koura, Hideo Harada, Yasuji Morita,
Terufumi Yokota, Takuro Sakai, Kenji Sakai, Takashi Takata, Etsuo Ishitsuka,
Hirotsugu Hamada, Takashi Mizuno, Kazuhiko Sato

This publication is issued by Japan Atomic Energy Agency (JAEA) on a yearly basis. Inquiries about availability and/or copyright of the contents in this publication should be addressed to Institutional Repository Section, Intellectual Resources Management and R&D Collaboration Department, JAEA.

Address: 2-4 Shirakata, Tokai-mura, Naka-gun, Ibaraki-ken 319-1195, Japan

Phone: +81-29-282-6387, **Facsimile:** +81-29-282-5920, **e-mail:** ird-seika_shi@jaea.go.jp

All Rights Reserved by JAEA ©2021

About the Cover Design

The cover design uses white hexagons that are similar to the pattern on the shell of a tortoise, which represents an ancient Japanese symbol of the desire for long life. Coincidentally, this shape is also that of the core fuel assemblies in the high-temperature engineering test reactor, “HTTR”.

The top left figure shows the air dose rate maps around the TEPCO’s Fukushima Daiichi Nuclear Power Station (NPS), from 2011–2016. The bottom right figure shows the mercury target vessel which adopted double-walled structure.

The air dose rate maps were created based on measurements collected using survey meters at thousands of points that were non-paved and less artificial disturbance. More details can be found on page 30 in Chapter 1, Topic 1-17.

The interior of the mercury target vessel at the time of proton beam injection is illustrated schematically. The vessel adopts the double-walled structure with a narrow mercury channel for the high-pressure region at the front part of the vessel. More details can be found on page 58 in Chapter 5, Topic 5-3.



Other Publications

Industrially applicable patented technology and know-how within the intellectual property owned by JAEA can be found on “JAEA Technology Seeds”.

The activity status of the whole agency, including CSR, can be found in the annual report, “Japan Atomic Energy Agency 2020 (Business Report FY2019)”.